Hypervelocity Shock Tunnel Studies of Blunt Body Aerothermodynamics in Carbon Dioxide for Mars Entry

Thesis by

Matthew Gregory Leibowitz

In Partial Fulfillment of the Requirements for the
Degree of
Doctor of Philosophy

CALIFORNIA INSTITUTE OF TECHNOLOGY
Pasadena, California

2020
Defended January 16, 2020

ACKNOWLEDGEMENTS

I would like to express my special appreciation and thanks to my advisor and mentor, Professor Joanna Austin for her constant encouragement. I am indebted for her guidance and support.

I would particularly like to thank my committee members; Prof. Hans Hornung, Prof. Joe Shepherd, and Prof. Guillaume Blanquart. I consider myself lucky to have daily interaction with such prolific scientists. This work has greatly benefited from their expertise, criticisms, advice, and enthusiasm.

My graduate experience would not have been complete without the support from the NASA Aerothermodynamics groups. Dr. Dinesh Prabhu, Dr. Aaron Brandis, and Dr. Brett Cruden at Ames, and Dr. Brian Hollis and Dr. Chris Johnston at Langley have provided invaluable advice and discussions. This collaboration was possible due to the support of the NASA Space Technology Research Fellowship. I particularly want to thank to Brett and Brian for serving as excellent fellowship advisors.

I would like to thank many members of the Caltech staff. Bahram Valiferdowsi provided guidance in experimental design and testing. Denise Ruiz, Barbara McKinzie Slater, Bihn Cheng, and Christine Ramirez handled a large amount of administrative issues. Ali Kiani machined many parts on short to no notice.

Additionally, I would like to thank my undergraduate mentor at SUNY Buffalo, Professor Paul DesJardin for introducing me to research and leading me to the path of grad school.

Many graduate students helped along the way. Andrew Knisely, and Galina Shpuntova were graduate student mentors and taught me how to operate in a lab. Joel Lawson, Mallory Neet, Nelson Yanes, and Wesley Yu from the Hypersonics Group and Silken Jones, Jean-Christophe Veilleux, and Conor Martin from the Explosion Dynamics Lab provided both help and friendship.

This thesis is dedicated to my family: Mom, Dad, and sister, Jenn, who have given me the love and support needed to chase my dreams.

ABSTRACT

A low mass and reliable thermal protection system for Martian atmospheric entry requires an accurate prediction of the aerothermal environment encountered by the spacecraft. In order to move forward with predictive models for larger vehicles needed for manned and sample return missions, anomalous data needs to be resolved. This work aims to address two critical problems relevant for Mars missions.

I) We investigate significant discrepancies between experimental and simulated blunt body bow shock standoff distance in ground test facilities. Experiments using high-speed and high-resolution schlieren imaging are conducted in the T5 reflected shock tunnel and the Hypervelocity Expansion Tube (HET) to examine facility independence of the measurements. A recently-developed model for sphere and sphere-cone behavior is in good agreement with experiments, and with predictions from Navier-Stokes simulations with thermal and chemical nonequilibrium. The need to account for the divergence of the streamlines in conical nozzles is highlighted. The contributions of vibrational and chemical nonequilibrium to the stagnation-line density profile are quantified using the simulation results in order to compare different reaction rate models.

II) We measure and characterize CO_2 mid-wave infrared radiation in hypervelocity flow. Initially assumed negligible in the design of the Mars Science Laboratory (MSL) mission heat shield, this mechanism of heating must be considered for accurate predictions of the heating environment. Specifically, CO_2 radiation can be a dominant source of heating in the afterbody, particularly later in the trajectory at lower velocities. Presented are spectral measurements of the 4.3 µm fundamental band of CO_2 radiation measured using fiber optics embedded on the surface of an MSL scaled heat shield model. When comparing experiments and simulations, good agreement is found when running the HET in shock tube mode where the shock layer is optically thick, while discrepancies are observed in expansion tube mode where the shock layer is optically thin. A thorough analysis of flow features in the line-of-sight including freestream uncertainties is performed to explore possible reasons for this discrepancy. After developing the spectroscopic calibration technique and obtaining forebody measurements in the expansion tube, an experimental campaign is completed in the T5 Reflected Shock Tunnel to measure spectral radiation in the forebody and afterbody. The accompanying T5 simulations needed for radiation predictions are being carried out by NASA Ames.

PUBLISHED CONTENT AND CONTRIBUTIONS

[1] M. G. Leibowitz and J. M. Austin. Assessment of reflected shock tunnels for Mars entry vehicle ground testing. *2018 AIAA Aerospace Science Meetings*, AIAA Paper 2018-1721, 2018. doi: 10.2514/6.2018-1721.
M.G.L. participated in the conception of the project, performed the experiments and simulations, analyzed the data, and wrote the manuscript.

[2] M. G. Leibowitz and J. M. Austin. Hypervelocity measurements of mid-wave infrared CO_2 radiation impinging on blunt bodies. *2019 AIAA Aerospace Science Meetings*, AIAA Paper 2019-1555, 2019. doi: 10.2514/6.2019-1555.
M.G.L. participated in the conception of the project, performed the experiments and simulations, analyzed the data, and wrote the manuscript.

TABLE OF CONTENTS

LIST OF ILLUSTRATIONS

LIST OF TABLES

Chapter 1

INTRODUCTION

To date, there have been 45 spacecraft missions to Mars, of which only 19 have been deemed successful, a lower success rate than any of our other planetary targets [82]. With a density less than 1% of Earth's atmosphere, Mars' thin atmosphere lacks sufficient drag to substantially slow down a spacecraft entering at high speeds yet is thick enough to cause substantial heating. The thermal protection system (TPS) that protects the spacecraft from intense heat loads generated during entry needs to be properly optimized in design and weight to ensure a low-risk landing [122]. This challenge will become increasingly more difficult as we look to launch larger-mass payloads such as those required for sample return and human missions. To properly design the TPS, accurate prediction of the thermal and aerodynamic loads are needed. Since flight measurements are scarce and may not predict the heating loads of future trajectories, we are reliant on ground testing to ensure the physics of the problem are properly captured in simulations.

In this work, experiments are completed in shock tunnel facilities appropriate for reproducing heating conditions experienced by an entry spacecraft vehicle. Shock tunnels are aerothermodynamic testing facilities capable of achieving flow at hypervelocity speeds (greater than 2.5 km/s) and high temperatures (post-shock temperatures greater than 4000 K). Unlike the supersonic regime which is distinctly determined when the gas velocity exceeds the speed of sound ($\mathrm{Ma} > 1$), the definition of hypersonic flow can be vague and is typically denoted by Mach numbers greater than 5. We distinguish the term hypervelocity from hypersonic by conditions in which high Mach number are achieved from high speeds as opposed to low temperatures (and thus low speed of sound). In hypervelocity flow, the perfect gas assumption is no longer valid and departure from thermal and chemical equilibrium frequently occurs.

While these impulse facilities certainly have their advantages, they will never fully reproduce the exact environment experienced during spacecraft entry. For this reason, it is paramount to understand the underlying physics when tracing ground test results to flight as extrapolation could have catastrophic results [119]. A common technique to match physical phenomena between flight and ground tests is the use of scaling parameters. For example, it is commonly desired to match the total enthalpy h_0 and the product of freestream density ρ_∞ and characteristic length scale D known as the binary scaling parameter $\rho_\infty D$. When those two parameters are matched, the binary chemical processes such as dissociation are scaled appropriately [81]. With Reynolds number matching, the relative importance of viscous effects are also properly scaled. Other phenomena such as radiation can be harder to scale in ground testing, so a range of conditions must be explored to properly capture flight physics.

For Mars (and Venus) entry, accurate modeling of carbon dioxide (CO_2) flows, a principal component of their atmospheres, >95% by volume, is particularly important and will be the focus of this work. Recent studies have found several problems relevant for Mars entry in need of resolving or investigating [119, 122]. This work examines the following two identified topics. i) An experimental and theoretical study of bow shock standoff distance and stagnation streamline analysis is motivated by the CUBRC LENS experiments that observed anomalously-large shock standoff distance [65]. The LENS data called into question the validity of using shock tunnels for evaluating nonequilibirum phenomena in CO_2. Previous CO_2 campaigns for Mars missions in T5 [47] did not observe anomalously-large standoff distance in flows with freestream densities 2-3 times higher than LENS tests. ii) An investigation of CO_2 mid-wave infrared radiation in hypervelocity flow fields is motivated by recent work that found that CO_2 radiative heating, not considered prior to the 2012 Mars Science Laboratory mission, is significant [60]. This heating can account for up to 30% of total heat flux in the forebody and can exceed convective heat flux in the afterbody [9].

Figure 1.1 displays common flow features relevant to the aforementioned topics. Carbon dioxide radiation is present in the shock layer as well as around the afterbody after the flow is processed by a bow shock and expanded through an expansion fan around the shoulder of the vehicle. In addition, depending on the conditions of ground tests, radiation may be present in the free stream.

In this work, experiments are performed in two complementary impulse facilities. A total of 113 experiments are completed in the Hypervelocity Expansion Tube as well as 20 experiments in the T5 Reflected Shock Tunnel. Two blunt body geometries are used as test articles; the sphere and the spherically-blunted cone. The diagnostics include non-intrusive optical measurements such as high-speed and single-shot imaging to measure shock shape, as well as surface measurements

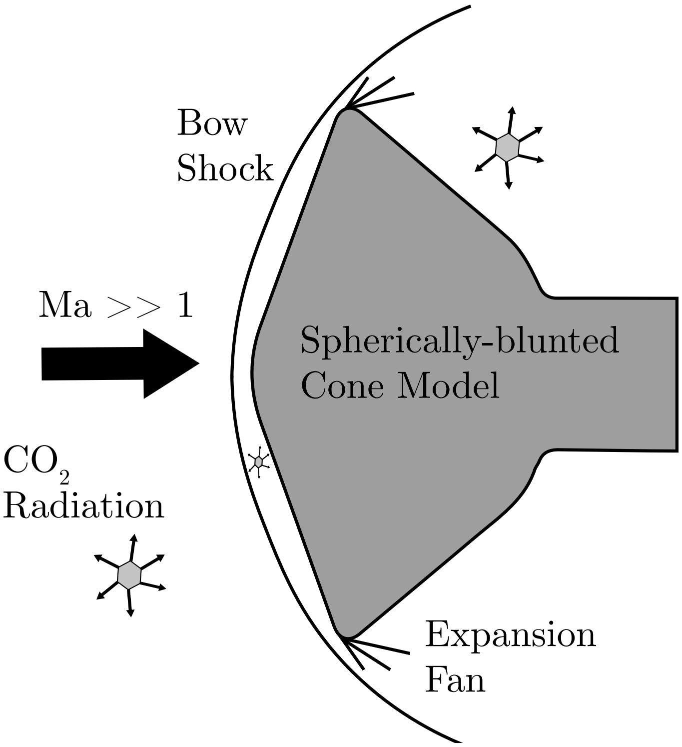

Figure 1.1: Flow features in hypersonic CO_2 flow over a spacecraft model.

such as infrared spectroscopy to measure spectral radiance. These experiments are complemented by theoretical considerations and Navier-Stokes simulations capable of modeling nonequilibrium and radiative processes.

1.1 Thesis outline

This work is organized into seven chapters.

- Chapter 1 serves as an introduction providing historical and theoretical background on standoff distance and radiation in high-enthalpy carbon dioxide flows.
- Chapter 2 compares and contrasts the two experimental facilities, HET and T5, describes the procedure for determining freestream conditions, and provides a discussion of freestream uncertainties.
- Chapter 3 describes the numerical and experimental setup for the analysis in chapters 4 to 6 including the CFD and radiation codes and their implementation of carbon dioxide modeling, the test-article geometries, diagnostics, and calibration methods used in this work.

- Chapter 4 presents the results of analysis of sphere and sphere-cone stagnation streamlines and standoff distance in reacting flows. Experimental measurements obtained in the two facilities are compared against stagnation streamline theory and simulations considering three reaction-rate models. The results are compared to the anomalous data observed in other facilities.
- Chapter 5 presents the results of spectrally-resolved radiation measurements obtained in HET and comparisons to simulations. Reported are shock tube measurements in optically thick conditions, expansion tube measurements in optically thin conditions at different model orientations, and direct measurements of the free stream. There is a discussion of any discrepancies between experimental and numerical simulations.
- Chapter 6 presents spectrally-resolved radiation and shock shape measurements obtained in the T5 Reflected Shock Tunnel. Both forebody and afterbody measurements are made at 0° and 16° angle of attack for freestream conditions that emulate a point on the ExoMars and MSL mission trajectories.
- Chapter 7 discusses the conclusions and future work.

1.2 Historical Background

1.2.1 Standoff Distance in High Enthalpy CO_2 Flows

For Mars missions, high stagnation-enthalpy ground-test campaigns for blunt body geometries in CO_2 have been conducted in reflected shock tunnel facilities such as LENS I at CUBRC [65], T3 at the Australian National University [92], and T5 at Caltech [121], as well as in expansion tube/tunnel facilities such as LENS X at CUBRC [66], Hypervelocity Expansion Tube (HET) at Caltech [103], and LENS XX at CUBRC [67].

The acceleration process of the test gas differs between the two types of facilities. In a reflected shock tunnel, the test gas is twice shocked and stagnated in the reservoir and then accelerated through a nozzle. In an expansion tube, the test gas is shocked and then further accelerated by an unsteady expansion wave.

A series of interferometric images of the shock layer in CO_2 flows at a stagnation enthalpy of 9.0 MJ/kg over circular and elliptical cylinders were obtained in the T3 free piston shock tunnel [92]. Additionally, interferometric images over spheres at stagnation enthalpies of 4 to 12 MJ/kg in carbon dioxide flows and 10 to 22 MJ/kg in air and nitrogen flows were obtained in the T5 facility [118, 121]. Comparisons obtained in the T3 facility showed good agreement with computations with the 1991 Park two-temperature model [86].

More recently, a significant discrepancy (a factor of 2.25) between the experimentally measured and numerically obtained shock standoff distance was observed for a Mars Science Laboratory (MSL) heat-shield scaled model (70° sphere-cone) at an enthalpy of 5.6 MJ/kg in the LENS I reflected shock tunnel facility and the corresponding DPLR simulation [65]. The authors believed this was due to a large amount of vibrational freezing (up to 42%) in the reservoir that was not accounted for in the prediction of the freestream. They postulated that previous experiments in T5 did not show obvious evidence of thermal nonequilibrium due to a lower freestream Mach number (4.2 vs. 5.7) as a result of less expansion in a lower geometric-area ratio nozzle used in the T5 study as compared to the LENS I [65] experiments. The sphere-cone tests previously carried out in the T5 facility [121] used a nozzle with a geometric area ratio of 100:1, while LENS I used their D-nozzle with a geometric-nozzle area ratio of nearly 1000:1 [65]. This discrepancy motivated the present study, in which different nozzle area ratios are used in the T5 facility.

A compilation of shock standoff ground-test data for sphere-cone geometries in different facilities at 0° angle of attack was made by Hollis and Prabhu [40]. Comparisons with LAURA simulations with a five-reaction chemistry model and the Park two-temperature model for CO_2-CO-O_2-O-C showed both over and underprediction of the experimental values obtained in four different impulse facilities, including the two used in the current study. No systematic source of this discrepancy was identified across data from all facilities.

Comparisons of the same shock-shape measurement over sphere-cone and sphere geometries in HET with US3D simulations carried out previously resulted in sphere standoff distances agreeing to within 7% [103]. For both studies, perfect gas predictions of the HET free stream were used, although the equilibrium and perfect gas freestream predictions for the RC5 test condition used in that study do not differ significantly. The RC5, h_0 = 5.6 MJ/kg test condition, was chosen to achieve an approximate match in freestream velocity, but not Mach number, with the expansion tube experiments of CUBRC LENS X [66]. Comparisons of shock shape for tests carried out at an angle of attack using schlieren images obtained in experiments in the two expansion facilities also yielded good agreement.

Doraiswamy et al. addressed the issue of increased shock standoff distance observed in the LENS I facility by using a state-specific vibrational model for the first few vibrational states for the species considered in their nozzle simulation and comparing to the Park two-temperature model with the Landau-Teller model for vibrational relaxation [21]. All of the models investigated predicted that the flow is close to vibrational equilibrium in the test section. The state-specific vibrational model reduced the shock standoff distance from the standard two-temperature model and could not reproduce the increase in standoff distance observed in the LENS I tests.

1.2.2 CO_2 Radiative Heating

Past predictions of heat flux for Mars missions such as the Mars Science Laboratory (MSL) mission have calculated negligible heating loads due to radiation [23]. It was only recently proposed that heating due to mid-wave infrared (MWIR) CO_2 and CO, bands that were previously neglected could be a significant cause of heating [60].

When velocities are lower, later in the entry trajectory, radiative heating can exceed convective heating [9]. The IR radiation component could have an even bigger impact in the design of new, larger entry systems, particularly if the vehicle enters the Martian atmosphere from orbit at lower speeds [122]. Brandis et al. included the mid-wave infrared bands in their simulations and observed that radiative heat loads have a non-negligible effect for the Phoenix geometry in the forebody (~5% of total heat load) and a substantial effect in the afterbody (~47% of total heat load).

Experiments in the Electric Arc Shock Tube at NASA Ames Research Center characterized two of the bands that are the largest contributors to mid-wave infrared radiation (MWIR), the 2.7 µm overtone band and the 4.3 µm fundamental band by measuring the radiation behind a moving shock wave using optical emission spectroscopy [17]. The average radiance behind the shock was measured. The 2.7 µm and 4.3 µm radiance band were bounded by simulations using the frozen and equilibrium thermochemistry post-shock states in all cases for shock velocities between 3.1 km/s and 4.9 km/s except for the 2.7 µm band at 3.1 km/s where the experimental radiance band exceeded the frozen limit.

Comparisons of simulations of the flight trajectory to experimental heat flux measured during flight missions have shown that accounting for radiative heating is necessary for accurate predictions of heat loads during entry. For the MSL mission, accounting for radiation reduced the error in heat load in the forebody from 33% to 19% [18]. For the recent ExoMars mission, measured total heat flux on the afterbody agreed with NASA CFD and radiation simulations within the uncertainty of the measurement.

MWIR band integrated and spatially resolved measurements were made in the HVET expansion tube facility at the JAXA Chofu Aerospace Centre in the wake of a scaled heat shield model as well as around the corner of wedge flow in the X2 facility at the University of Queensland. JAXA measurements observed MWIR radiation near the afterbody of the model [111]. Simulations of the 5.68 km/s freestream concluded agreement with a homogeneous spatial model, suggesting a common vibrational temperature of all modes of CO_2 and CO of 2200 K and a rotational temperature of 1700 K in their freestream. University of Queensland measurements [36] between 2.8 km/s and 4 km/s found that the ratio of experimental to simulated integrated radiance was between 0.4 to 1.9 depending on the freestream condition tested.

Below 4 km/s, radiation from the IR CO_2 bands, specifically at 4.3 µm and 2.7 µm, are the dominant sources of radiative heating. Both bands require improved predictive capabilities. The current uncertainties accessed for flight missions are 30% for the 4.3 µm band in the shock layer where the flow is in compression [17]. The uncertainty is larger in expanding flow where strong departures from the Boltzmann distribution have been observed from a state-to-state simulation in the backshell region [99].

1.3 Theoretical Background

1.3.1 Bow Shock Standoff Distance

A well-known feature of supersonic flow over a blunt body is that the bow shock standoff distance Δ is correlated with the density ratio across the shock [38, 61, 115]. In hypervelocity flows, strong shock compression and high post-shock temperatures lead to significant chemical dissociation and vibrational excitation in the shock layer, particularly near the stagnation region. A correlation with the integrated density ratio along the stagnation streamline for bow shock shape and standoff distance in nonequilibrium flows was proposed by Stulov on the basis of extensive numerical simulations for various body shapes [107] .

Independently, Wen and Hornung applied conservation of mass to a control volume as shown in Figure 1.2 [118]. The mass flow rate entering the control volume is $\pi u_\infty \rho_\infty b^2$ or $u_\infty \rho_\infty b$ depending on whether the flow is axisymmetric or planar, respectively. For small b, the mass flow rate leaving the control volume is $2\pi u_b b \bar{\rho} \Delta$ or $u_b \bar{\rho} \Delta$, respectively, where $\bar{\rho}$ is the average density in the shock layer and u_b is the velocity leaving the control volume. With simplifications $u_b \approx u_\infty \cos\phi$ and

$b = R_s \cos\phi$, mass balance results in

$$\frac{\Delta}{R_s} = L \frac{\rho_\infty}{\bar{\rho}} \tag{1.1}$$

where R_s is the shock radius of curvature. This derivation highlights the importance of the average density $\bar{\rho}$ along the stagnation streamline in nonequilibrium flows. Stulov and Hornung's results indicate that for spheres, the body radius R can be used as the length scale and the correlation of Equation 1.1 can be applied to nonequilibrium flows using the average streamline density and a value of $L = 0.82$ [118] to 0.83 (interpolated from [107], Figure 2).

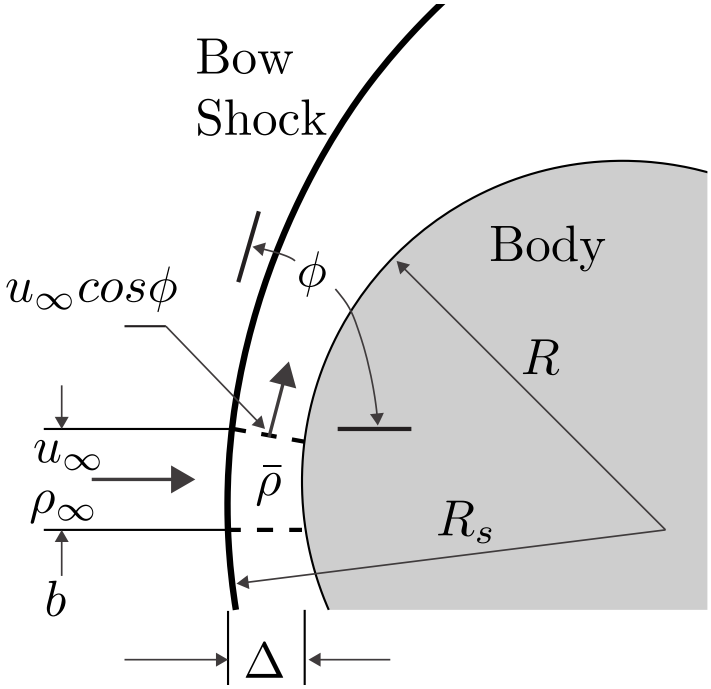

Figure 1.2: Control volume analysis applied to hypervelocity flow over a blunt body. Adapted from Wen and Hornung [118].

1.3.2 Stagnation Streamline Modeling

The previous section described how in hypervelocity blunt body flows the bow shock standoff distance is inversely proportional to the average density in the region between the shock and the body. The flow in this region is subsonic and requires numerical solution of the multidimensional flow [6, 43, 107] but a useful approximation is to neglect the transverse motion and consider only the flow on the stagnation streamline. The following discussion is based on continuum flow. The continuum-flow model is appropriate for the higher densities used in the ground testing discussed in this thesis.

Intermolecular Collisions

When particles collide, intermolecular processes occur at a finite rate that can be characterized by a relaxation time τ for each individual process. The principal finite-rate processes [8] are i) thermal energy exchange between the molecular energy modes: τ_{tr}, τ_{rot}, τ_{vib}, τ_{el} (translational, rotational, vibrational, and electronic) and ii) chemical reactions: τ_{d}, τ_{i} (dissociation and ionization). In general, there is a ranking of the number of collisions $Z_x = \tau_x/\tau_{tr}$ required for process x to reach equilibrium:

$$Z_{\mathrm{tr}} = 1 < Z_{\mathrm{rot}} \sim 5 < Z_{\mathrm{vib}} \sim 10^6 - 10^8 < Z_{\mathrm{el}} < Z_{\mathrm{d}} < Z_{\mathrm{i}}. \tag{1.2}$$

In the shock itself for continuum flow, it is usually assumed that sufficient collisions for translational and rotational energy rapidly increase while the vibrational and electronic energy and vibration-dissociation coupling lags behind. The post-shock gas is then in a state of chemical and thermal nonequilibrium and will evolve towards an equilibrium state. An example density profile along the stagnation streamline in hypervelocity blunt body flow with representative length scales is displayed in Figure 1.3. The numerical shock region width in simulations in the continuum regime is determined by the numerical solution method and spatial resolution, as well as the models for the molecular transport and nonequilibrium processes.

Two-Temperature Model

One approach that is commonly used in shock wave and engineering applications to model the relaxation processes is to use the two-temperature kinetic model [7, 85]. This model assumes that one temperature T describes the distribution of translational and rotational (rotranslational) energies and that a second temperature T_V describes the distribution of vibrational and electronic (vibronic) energies [28].

Additionally, this model assumes rotational modes are fully excited, so that according to the theorem of equipartition of energy, the rotranslational heat capacity for a given species i is

$$C_{p,tr,i} = R_i \left(\frac{f_{tr,i}}{2} + 1 \right) \tag{1.3}$$

where $f_{tr,i}$ is the number of degrees of freedom in translation (3) plus rotation (0 for atoms, 2 for diatomic and linear molecules, and 3 for non-linear molecules). The rotranslational enthalpy is defined as

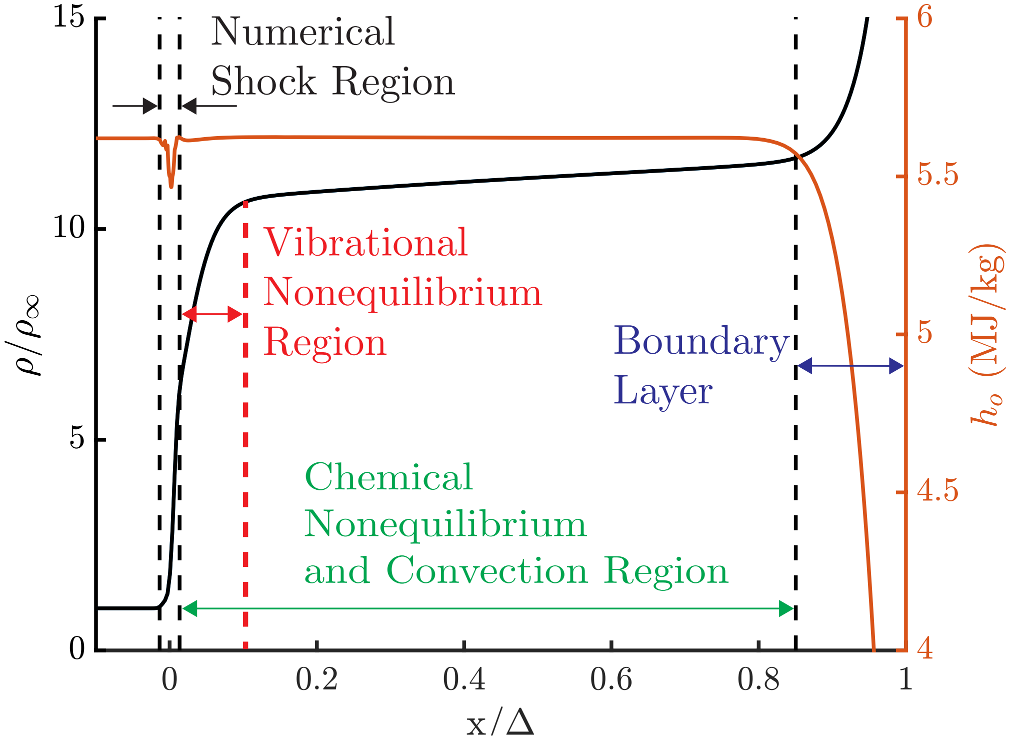

Figure 1.3: Density profile along the stagnation streamline in hypervelocity blunt body flow.

$$h_{tr,i} = C_{p,tr,i}\,(T - T^\circ) + \Delta h_i^\circ \tag{1.4}$$

where the enthalpy of formation Δh_i° is the enthalpy at the standard temperature of $T^\circ = 298.15$ K.

Molecular vibrations contribute two additional degrees of freedom per vibrational mode if the particular mode is fully excited at temperatures exceeding the characteristic vibrational temperature θ_v. The energy in partially-excited vibrational modes is defined using the temperature-dependent formulation derived from the rigid-rotor, harmonic-oscillator (RRHO) model. RRHO models molecules as hard spheres connected by springs free to rotate and vibrate. The specific heat capacity and energy for one vibrational mode v using the RRHO model is

$$C_{v,v,i} = R\left(\frac{\theta_{v,i}}{T}\right)^2 \frac{e^{\frac{\theta_{v,i}}{T}}}{\left(e^{\frac{\theta_{v,i}}{T}} - 1\right)^2}, \tag{1.5}$$

$$e_{V,i} = \frac{R\theta_{v,i}}{e^{\frac{\theta_{v,i}}{T}} - 1}. \tag{1.6}$$

When all modes of excitation (translational, rotational, vibrational, and electronic) are in equilibrium and described by a common temperature, the thermodynamic properties can be computed by a detailed statistical thermodynamic model for the partition function based on spectroscopic data and molecular structure. Polynomial data fits such as the NASA9 formulation [72] are used to evaluate individual species properties in numerical simulations. Electronic excitation, flexing of the structure, and anharmonic motion are particularly important to include at the highest temperatures encountered in hypervelocity flow. These polynomial fits to the data are implemented into software such as Cantera [31]. The energy in vibrational and electronic modes for species i is given by

$$e^*_{V,i}(T) = h^*_i(T) - [h_i(T^\circ) + C_{p,tr,i} \cdot (T - T^\circ)] \tag{1.7}$$

where the superscript $*$ represents the thermal equilibrium value found from the thermodynamic data sets. The vibrational energy $e_{V,i}$ in the two-temperature model is defined as the energy in thermal equilibrium at the vibrational temperature T_V,

$$e^*_{V,i}(T_V) = e_{V,i}. \tag{1.8}$$

Carbon Dioxide Vibrational Modes

For polyatomic molecules, there are $3N - 5$ and $3N - 6$ vibrational modes for linear and nonlinear molecules, respectively, where N is the number of atoms in the molecule. Carbon dioxide is a linear molecule with four vibrational modes. These modes are known as the symmetric stretch (ν_1), the double-degenerate bending (ν_2), and the asymmetric stretch (ν_3), Figure 1.4. The characteristic vibrational temperatures θ_v for each mode ν_{1-3} are 1890 K, 954 K, and 3360 K [8]. Figure 1.5 compares the specific heat C_v calculated with the RRHO approximation against the NASA9 polynomial fit. The RRHO is a good approximation for CO_2 until temperatures greater than 4000 K where electronic excitation starts to be significant and deviations of C_v/R from the two models are greater than 0.1. When comparing the RRHO to the NASA9 fits for the other molecular species using this metric, the RRHO approximation is valid up to 2000 K for O_2 and 4000 K for CO.

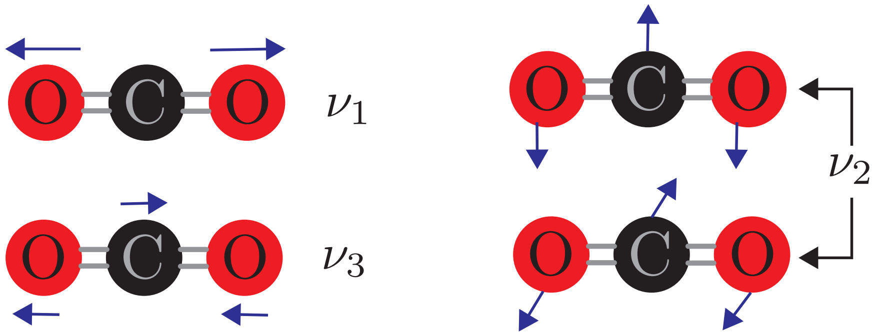

Figure 1.4: Vibrational modes of carbon dioxide.

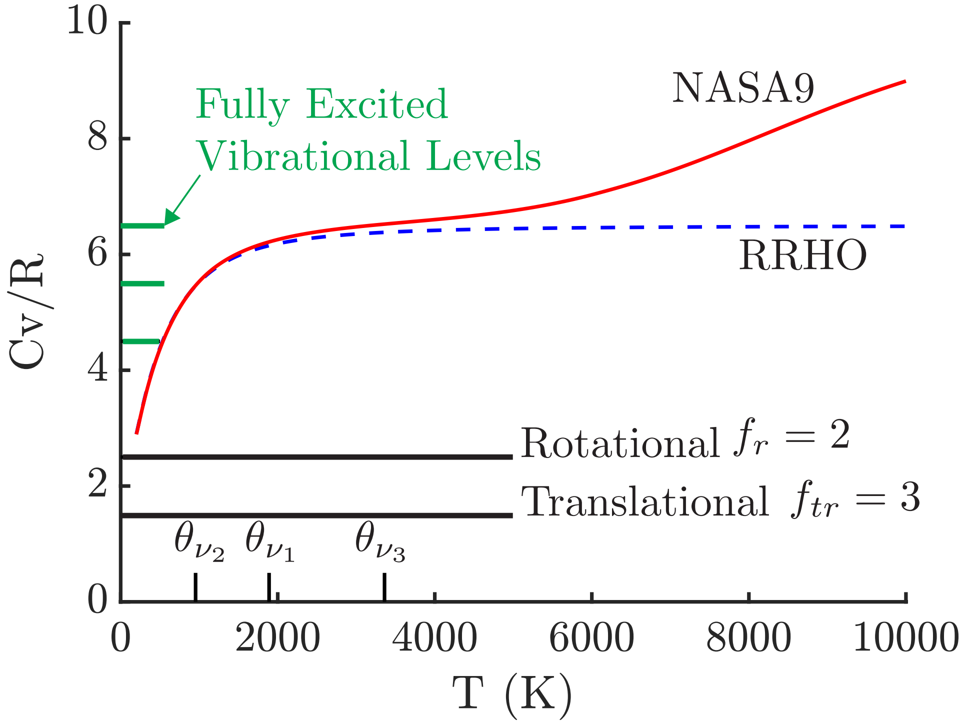

Figure 1.5: Specific heat of carbon dioxide disregarding dissociation.

Post-Shock State

The shock wave is treated as vibrationally frozen meaning that the vibrational and electronic energy in the freestream is equal to the post-shock state, $e_{V,\infty} = e_{V,s}$. Rotational and translational motions are assumed to equilibrate sufficiently quick that they are in equilibrium in the post-shock state. The post-shock state can be found using the conservation laws for 1D shock waves and the equation of state

$$\rho_\infty u_\infty = \rho_s u_s, \tag{1.9}$$

$$P_\infty + \rho_\infty u_\infty^2 = P_s + \rho_s u_s^2, \tag{1.10}$$

$$h_\infty + \frac{u_\infty^2}{2} = h_s + \frac{u_s^2}{2}, \tag{1.11}$$

$$P = \rho R T \tag{1.12}$$

where u is velocity, P is pressure, h is specific enthalpy, T is temperature, and R is the specific gas constant. The specific enthalpy h is related to the specific energy e of the gas by $h = e + P/\rho$. The change in temperature across the shock is related to the change in enthalpy by

$$h_s - h_\infty = C_{p,tr}\left(T_s - T_\infty\right) \tag{1.13}$$

where the translational-rotational specific heat capacity is $C_{p,tr} = \gamma R/(\gamma - 1)$ with γ = 7/5 for linear molecules.

Thermal Nonequilibrium

In hypervelocity blunt body flows, the translational temperature peaks right after the shock and then rapidly decreases as energy is transferred from the translational modes to the vibrational modes (Figure 1.6). Energy transfer between the vibrational and translational modes is conventionally modeled [7, 8] using the Landau-Teller equation given by

$$\frac{de_{V,i}}{dt} = \frac{e_{V,i}^*(T) - e_{V,i}}{\tau_{V,i}(P,T)} \tag{1.14}$$

where $e_{V,i}^*$ denotes the equilibrium vibrational value at temperature T and $\tau_{V,i}$ is the vibrational relaxation time constant. An empirical relation for the vibrational relaxation for a collision pair $\tau_{V,ik}$ is presented by Millikan and White [75]

$$P\tau_{V,ik} = \exp[A(T^{-\frac{1}{3}} - 0.015\mu^{1/4}) - 18.42] \tag{1.15}$$

where $P\tau_V$ has units of atm-s, μ is the reduced mass of the colliding pair in atomic units, and A is related to the molecular constant of the colliding species. For a multispecies gas mixture, the equivalent $\tau_{V,i}$ can be approximated with a simple mixture rule

$$\tau_{V,i} = \left[\sum_{i=1}^{k} \frac{X_k}{\tau_{V,ki}}\right]^{-1} \tag{1.16}$$

where X_k is the mole fraction of species k.

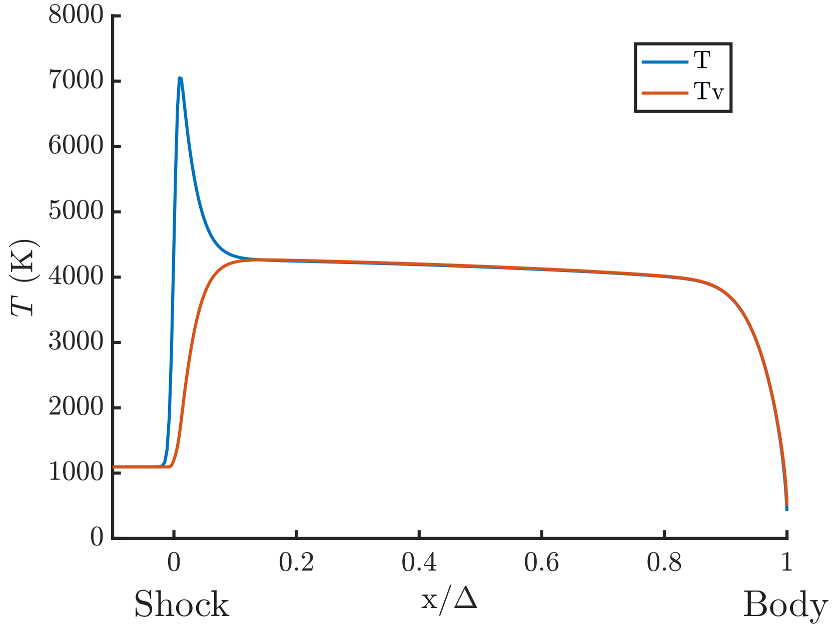

Figure 1.6: Two-temperature profile along the stagnation streamline in hypervelocity blunt body flow.

Chemical Nonequilibrium

Chemical nonequilibrium can be modeled by accounting for the rates of production and (and consequently) destruction of chemical species. Consider the general chemical reaction of form

$$\sum_{i=1}^{n} \nu_i' X_i \leftrightarrow \sum_{i=1}^{n} \nu_i'' X_i \tag{1.17}$$

where ν_i' and ν_i'' represent the stoichiometric mole numbers of the reactants and products, respectively and n represents the number of different species, X_i, in the reaction [3]. The net molar rate of production of a species $\dot{\omega}_i$, expressed in units of kmol/m^3· s, is defined as the difference between the contributions of the forward and reverse rates

$$\dot{\omega}_i \equiv \frac{d[X_i]}{dt} = \left(\nu_i'' - \nu_i'\right)\left(k_f \prod_i [X_i]^{\nu_i'} - k_b \prod_i [X_i]^{\nu_i''}\right) \tag{1.18}$$

where k_f and k_b are the forward and backward rate constants expressed in units of m^3/kmol· s or m^6/kmol^2· s depending on the order of reactants or products, respectively, and $[X_i]$ is the concentration of species i in units of kmol/m^3. Typically the forward rate constant is expressed in modified Arrhenius form and given by

$$k_f = A T_a^{\eta} \exp(-D/T_a) \tag{1.19}$$

where A is the pre-exponential constant expressed in units of m^3 / kmol· s or m^6 / kmol· s depending on the number of reactants, η is the temperature exponential constant, and D is the activation energy expressed in units of K. The constants A, η, and D are all found from experimental data. The conventional [85] empirical approach used to apply one-temperature reaction rates to the two-temperature model is to evaluate the rates with a geometrically-averaged effective temperature

$$T_a = T^s T_V^{s-1} \tag{1.20}$$

where s is between 0 to 1. For thermodynamic consistency, the forward reaction rate constant k_f is usually specified and the backward rate constant k_r is determined from the equilibrium constant based on concentration K_c

$$\frac{k_f}{k_r} = K_c. \tag{1.21}$$

The equilibrium constant based on concentration is related to the equilibrium constant based on pressures K_p,

$$K_c = \frac{K_p}{R_u T} = \frac{1}{R_u T} \prod_i P_i^{\nu'} \tag{1.22}$$

where R_u is the universal gas constant and $P_i = X_i P$ is the partial pressure of species i. The evolution of a species mass fraction along a streamline is computed using the steady, species-evolution equation

$$u\frac{dY_i}{dx} = \frac{W_i\dot{\omega}}{\rho} \tag{1.23}$$

where W_i is the molecular weight of species i, and Y_i is the mass fraction of species i. In a detailed mechanism, the number of equations needed are equal to the number of species being considered.

Computations of the Stagnation Streamline

Computations of the full flow field can be obtained through computational fluid dynamic simulations such as the NASA LAURA code [1] that uses the multidimensional Navier-Stokes conservation equations to model the thermal and chemical relaxation processes. A useful 1D model was recently developed and implemented in the Shock and Detonation Toolbox [11] which uses the quasi-one-dimensional flow equations to solve for the evolution of processes along the stagnation streamline

$$\frac{d}{dx}(\rho u A) = 0, \tag{1.24}$$

$$\rho u\frac{du}{dx} = -\frac{dP}{dx}, \tag{1.25}$$

$$\frac{dh}{dx} = -u\frac{du}{dx}. \tag{1.26}$$

The mass flux along the stagnation streamline has been observed through numerical simulations by Hornung [43] and Stulov [107] to linearly decrease from the shock front to the body

$$\rho u = \rho_s u_s \left(1 - \frac{x}{\Delta}\right). \tag{1.27}$$

From conservation of mass, $\rho u A$ = constant, the area change through the stagnation line stream tube can be related to the standoff distance

$$\frac{1}{A}\frac{dA}{dx} = \frac{1}{\Delta - x}. \tag{1.28}$$

1.3.3 Radiative Processes

Key Parameters

Electromagnetic radiation can be decomposed into a spectrum of waves. These waves can be defined in terms of key parameters such as wavelength (λ, m), wavenumber ($\bar{\nu}$, 1/m^{-1}), frequency (ν, Hz), and energy (E, J). There parameters can be used interchangeably to describe spectra and are related by the speed of light $c = 3.00 * 10^8$ m/s and Planck's constant $h = 6.626 * 10^{-34}$ J $\cdot$ s. The energy carried by a single photon is defined as $\Delta E = h\nu = hc/\lambda$. Wavelength is inversely related to wavenumber by $\bar{\nu} = 1/\lambda$

The spectrum can be divided into various regions, with this work focusing on the mid-wave infrared (MWIR) ranging from λ = 3-5 µm. Discussions can be found in Anderson [3] for definitions of radiative intensity and flux, Rybicki and Lightman [98] for radiative transfer, Boyd and Schwartzentruber for quantum mechanics [8], Hanson, Spearrin, and Goldenstein [37] for molecular spectra, and Stuart [106] for infrared spectroscopy.

Definition of Radiative Intensity and Flux

Radiation will travel at the speed of light in straight lines called rays in free space or in a homogeneous media. Consider an individual-ray incident on a surface at point P as shown in Figure 1.7. Since a single ray carries virtually no energy, we consider a set of rays within an infinitesimal solid angle $d\Omega$ carrying energy E in the wavelength interval between λ and $\lambda + d\lambda$. The spectral radiative intensity I_λ crossing area dA at point P in time dt is given by

$$I_\lambda \equiv \frac{dE}{dA d\Omega d\lambda dt}. \tag{1.29}$$

Spectral radiance describes intensity at a point and is dependent on direction. Total radiative heat flux q_{rad} (also referred to as radiative heating) describes the intensity coming from all directions and frequencies. If a set of rays are obliquely incident as opposed to normally incident, the net heat flux on the area dA in the direction normal to the surface is reduced by a factor of cosθ

$$q_{\text{rad}} = \int_0^\infty \int_\Omega I_\lambda(\Omega) \cos\theta d\Omega d\lambda. \tag{1.30}$$

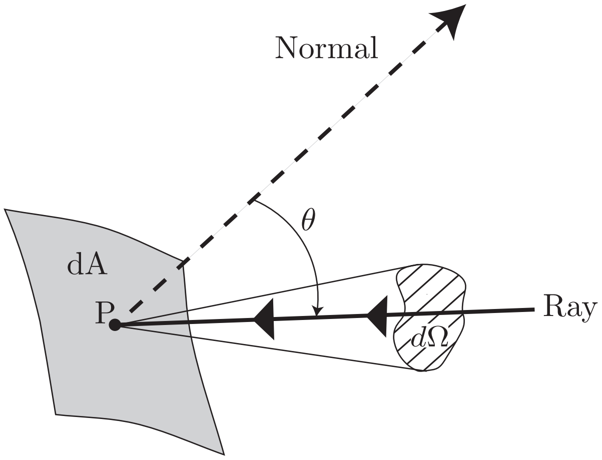

Figure 1.7: Geometry for obliquely incident rays.

Radiative flux q_{rad} is a measure of the energy carried by all rays passing through a given area dA for a time dt expressed with units of W/m^2. The solid angle can be converted to spherical coordinates and the total heat flux expressed as

$$q_{\text{rad}} = \int_0^\infty \int_0^{2\pi} \int_0^\pi = I_\lambda(\theta, \phi)\cos\theta\sin\theta d\theta d\phi d\lambda \tag{1.31}$$

where ϕ is the azimuthal angle.

Radiative Transfer Equation

In free space, the intensity I_λ is constant along a ray. If a ray passes through matter, energy can be added or subtracted through processes such as scattering, emission, and absorption. Scattering can be assumed negligible if the size of particles is small compared to the wavelength of light. This will be the case in shock tunnel testing where the diameter of the gas molecules are on the order of angstroms compared to infrared radiation on the order of microns. If particulates are present in the flow, scattering may be present. This work assumes scattering is negligible and considers only emission and absorption.

The intensity added to a ray across a distance dx is given by spontaneous emission $dI_\lambda = \epsilon_\lambda dx$ where ϵ_λ is the emission coefficient. When discussing radiative transfer, absorption includes the processes proportional to the intensity of the incoming ray; "true absorption" and stimulated emission. These processes are illustrated in Figure 1.8. While this seems counter intuitive, this convention is convenient. A phenomenological law can then be defined for the intensity taken out of the ray $dI_\lambda = -\alpha_\lambda I_\lambda dx$ where α_λ is the absorption coefficient. If stimulated emission exceeds "true absorption", the absorption coefficient will be negative.

A combined expression for the effect of emission and absorption can be written as

$$\frac{dI_\lambda}{dx} = -\alpha_\lambda I_\lambda + \epsilon_\lambda. \tag{1.32}$$

This equation can be integrated from $I_\lambda(x = 0)$ to $I_\lambda(x)$ to arrive at the equation for radiative transfer assuming constant values for ϵ_λ and α_λ

$$I_\lambda = I_{\lambda,0}e^{-\alpha_\lambda x} + \frac{\epsilon_\lambda}{\alpha_\lambda}\left(1 - e^{-\alpha_\lambda x}\right). \tag{1.33}$$

Optical Thickness

Common limits of radiative transport are discussed in terms of optical thickness τ_λ given by

$$\tau_\lambda = \alpha_\lambda x. \tag{1.34}$$

In the optically thin limit, $\tau_\lambda \longrightarrow 0$, the radiative transport equation simplifies to

$$I_\lambda = I_{\lambda,0} + \epsilon_\lambda x. \tag{1.35}$$

The optically thin limit implies photons travel through a transparent medium without getting absorbed. In the optically thick limit, $\tau_\lambda \longrightarrow \infty$, the radiative transfer equation simplifies to

$$I_\lambda = \frac{\epsilon_\lambda}{\alpha_\lambda} = B_\lambda \tag{1.36}$$

where B_λ is the blackbody radiation intensity. Under the assumption of local thermodynamic equilibrium (LTE), matter is considered to be in thermal equilibrium with itself uninfluenced by the magnitude of incident radiation. LTE implies Kirchoff's law relating emission and absorption through the blackbody function $B_\lambda = \frac{\epsilon_\lambda}{\alpha_\lambda}$. The blackbody function is given by Planck's law

$$B_\lambda(T) = \frac{2hc^2/\lambda^5}{e^{\frac{hc}{\lambda kT}} - 1}. \tag{1.37}$$

The optically thick limit implies photons can not travel without getting absorbed and reemitted.

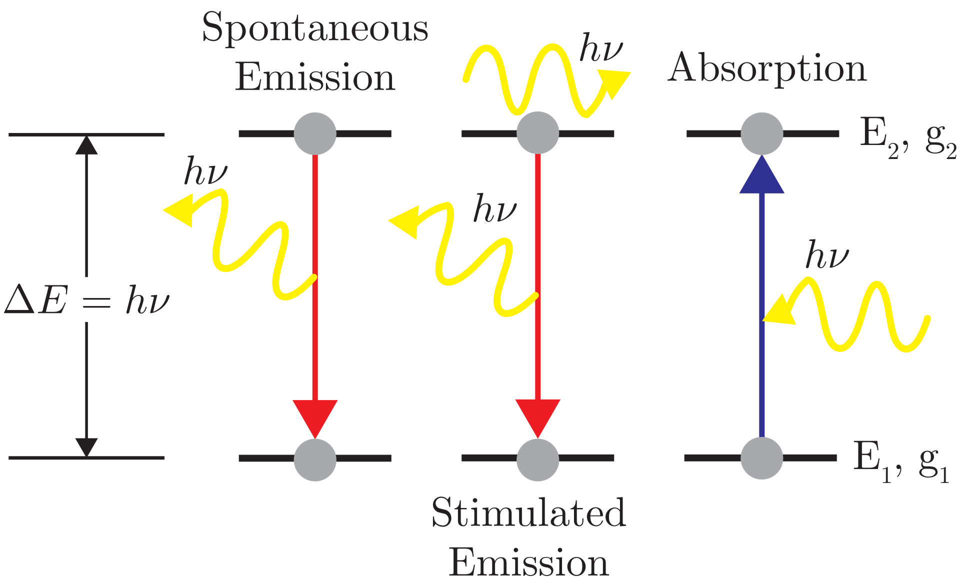

Figure 1.8: Emission and absorption processes between two energy levels.

Einstein Coefficients

Einstein recognized that there is a relationship between emission and absorption at the microscopic level. He considered thermodynamic equilibrium in an atom with two quantized electronic-energy levels. Each level has population n with degeneracy g. The population of a state represents the average number of molecules in a state at any given time and degeneracy represents the number of states with the same energy that are indistinguishable.

Balancing the flux of transitions out of state 1 into state 2 with the flux of transitions into state 1 from state 2, Einstein derived atomic properties known as the Einstein A and B coefficients that measure the probability of a given transition. The Einstein A-coefficients signify spontaneous emission and the Einstein B-coefficients signify the processes proportional to the mean spectral intensity; absorption and stimulated emission. The subscripts represent the direction of the transition, i.e. A_{21} represents a transition from level 2 to level 1. The Einstein-coefficients are related by the Einstein relations

$$g_1 B_{12} = g_2 B_{21}, \tag{1.38}$$

where g_1 and g_2 are the multiplicity or degeneracy of the levels and

$$A_{21} = 2\frac{hc}{\lambda} B_{21}. \tag{1.39}$$

Detailed-balance relations connect microscopic processes with the macroscopic processes of emission and absorption. In the assumption of LTE, the populations between two given energy levels are described by the Boltzmann distribution given by

$$\frac{n_1}{n_2} = \frac{g_1}{g_2} e^{\frac{\Delta E}{kT}}. \tag{1.40}$$

Using the Einstein relations, the respective absorption and emission coefficients for a single transition are given by

$$\alpha_\lambda = \frac{hc}{4\pi\lambda} n_1 B_{12} \left(1 - e^{-\frac{\Delta E}{kT}}\right) \phi(\lambda), \tag{1.41}$$

$$\epsilon_\lambda = \alpha_\lambda B_\lambda. \tag{1.42}$$

Spectral Line Shape

In reality, the energy difference between two levels is not infinitely sharp but can be broadened according to the line profile function $\phi(\lambda)$ given by

$$\int_0^\infty \phi(\lambda) d\lambda \equiv 1. \tag{1.43}$$

Broadening can occur naturally, due to thermal effects known as Doppler broadening, or due to collisional effects known as pressure broadening. The spectral lineshape is commonly described in terms of its line position λ_0, the max height of the line, and the full width at half max (FWHM). In the assumption of LTE, the spectral line shape can be determined using a Guassian profile for thermal broadening and a Lorentzian profile for natural or pressure broadening. A combination of these mechanisms results in a convolution of the Guassian and Lorentzian known as a Voight profile. Additionally, the observed line shape from spectroscopic measurements is broadened by the instrument line shape (ILS) function.

Molecular Spectra

While the Einstein relations above consider an electronic transition in a two-level atom, these equations hold for transitions between any two energy levels stored in rotational, vibrational, or electronic modes. For a diatomic molecule, the difference in energy levels in the different modes can be approximated using the rigid-rotor, harmonic-oscillator (RRHO) model. Changes in electric dipole moments are responsible for interactions with light, emitting and absorbing photons at the frequency of the motion.

From quantum mechanics, the rigid-rotor model predicts the quantized rotational energy is given by

$$e_{\text{rot}} = \frac{h^2}{8\pi^2 \mu r_e^2} J(J+1) \tag{1.44}$$

where r_e is the distance between atoms, μ_e is the reduced mass, $J = 0, 1, 2...$ is the rotational quantum number and the degeneracy for the rigid rotor is $g_J = 2\text{J} + 1$.

The harmonic-oscillator model predicts the quantized vibrational energy is given by

$$e_{\text{vib}} = \left(n + \frac{1}{2}\right) \frac{h}{2\pi} \omega \tag{1.45}$$

where n = 0,1,2,... is the vibrational quantum number, ω is the single vibrational frequency, and degeneracy is 1 for all levels. These predictions can be improved using the Non-rigid Rotor and the Anharmonic Oscillator (AHO) models.

Just as there is a hierarchy for the number of collisions of each mode to reach equilibrium, this same ranking holds for the difference in energy between levels in different modes:

$$\Delta e_{\text{rot}} < \Delta e_{\text{vib}} < \Delta e_{\text{elec}}. \tag{1.46}$$

This is illustrated by a potential well of a diatomic molecule (Figure 1.9). Absorption and emission of rotational, vibrational, and electronic transitions occur at frequencies in the microwave, infrared, and UV to visible, respectively. Only transitions that obey selection rules are allowed to occur. According to the RRHO model, transitions may only occur when the quantum numbers $\Delta J = \pm 1$ for rotational transitions and and $\Delta n = \pm 1$ for vibrational transitions. During vibrational transitions, rotational transitions may occur simultaneously producing an infrared rovibrational band such as the MWIR CO_2 4.3 µm fundamental band.

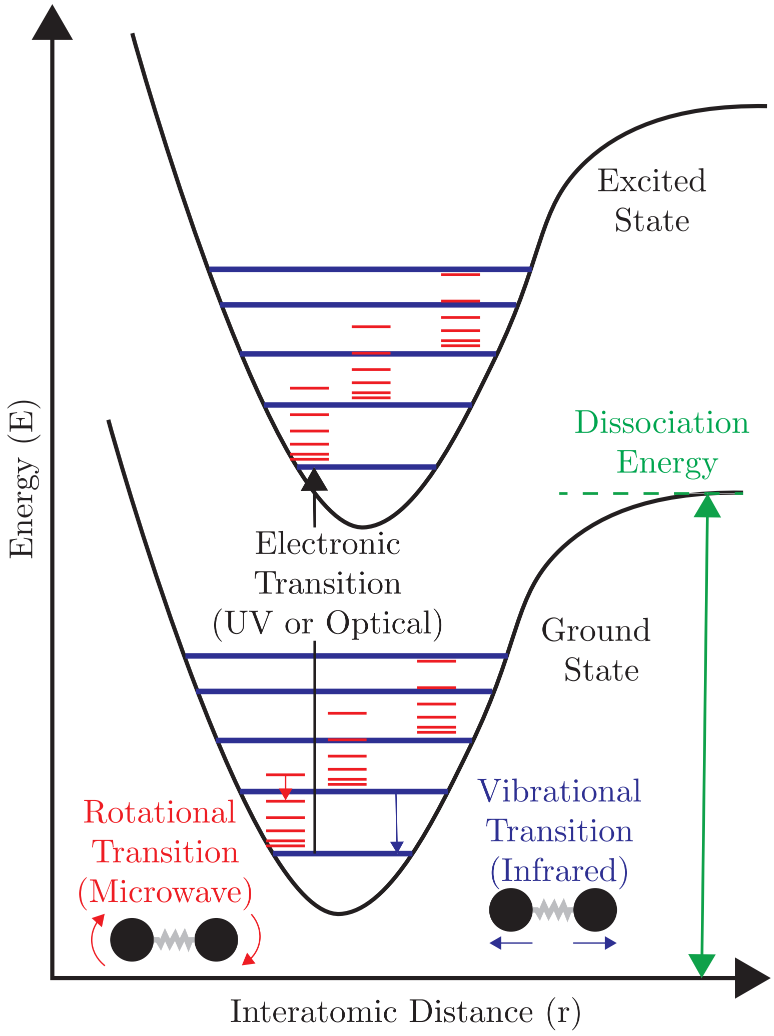

Figure 1.9: Molecular transitions between energy levels depicted by the potential energy well.

Chapter 2

FACILITIES

2.1 Comparison of the Facilities

Expansion tube and reflected shock tunnels are impulse facilities that differ in their acceleration processes. A primary shock accelerates the initial test gas in both facilities. For a reflected shock tunnel, a reflected shock stagnates the post-primary shock test gas state before steady acceleration through a converging diverging (CD) nozzle to its final state. For an expansion tube, an unsteady expansion fan accelerates the post-shocked test gas state to its final state. Having access to both the T5 Reflected Shock Tunnel and the Hypervelocity Expansion Tube (HET) allows a larger range of conditions and utilities to be achieved. A comparison of the two facilities is shown in Table 2.1. The HET has a fast turn around time that allows for diagnostic development and freestream conditions that are undissociated, while T5 allows larger models to be tested for longer test times with access to higher-enthalpy conditions.

The important flight to lab scaling relations for radiating flows in impulse facilities are discussed in Morgan et al. [81]. If radiation changes the macroscopic properties, the flow field and radiation is coupled and the assumption that the inviscid shock layer is adiabatic is no longer valid. The ratio of adiabatic radiative energy flux to total energy flux, also known as the Goulard number Λ [32], is given by

$$\Lambda = \frac{2q_r}{\frac{1}{2}\rho_\infty u_\infty^3}. \tag{2.1}$$

If the Goulard number is greater than 0.01, the flow is considered strongly coupled

Table 2.1: Comparing and contrasting the facilities.

	T5	**HET**
Acceleration Process	Steady CD Nozzle	Unsteady Expansion Fan
Test Time (ms)	1 to 5	0.1 to 0.5
Max Model Diameter (in.)	7	2
CO_2 Freestream	Dissociated	Undissociated (in this work)
Time Between Shots	≈1 day	≈2 hours

with radiation [120]. For the conditions in this work, the Goulard number has been calculated to be a maximum of 3E-4 and 5E-3 in the HET and T5, respectively, therefore the calculation of the flow field can be safely decoupled from radiation.

In this case, provided total enthalpy h_0 is matched, a match in the binary scaling parameter $\rho_\infty D$ (where D is the characteristic length scale taken to be the diameter of the body) will properly scale the effect of binary chemical reaction rates such as chemical dissociation. The radiation spectrum and intensity observed in the test facility is not the same as in flight. If the flow is optically thin, there is no absorption and the emitted radiation is imaged without interference from the surrounding flow. As opposed to flight, the free stream may radiate in a facility, and must be accounted for in simulations. In optically thick conditions, shock layer radiation can be calculated by Planck's law as a function of temperature. Outside the limiting cases in the optical thickness, the absorption along the line of sight must be considered and the radiation measurements require careful interpretation. Additionally, in the case of non-continuum or highly nonequilibrium flow, experiments at flight densities should be performed [104].

For the freestream conditions in this work, the binary scaling parameter (Figure 2.1a) and density (Figure 2.1b) can be plotted as a function of total enthalpy. These plots also include conditions for the 2012 MSL [23] and 2019 ExoMars [10] spacecraft-entry trajectories. In this study we are able to match the total enthalpy and the binary scaling parameter with the spacecraft-flight conditions in both facilities, while the flight densities are typically 1 to 2 orders of magnitude lower than the facility values. The rest of this chapter will discuss how the facility freestream conditions are characterized and the uncertainties involved.

2.2 T5 Reflected Shock Tunnel

The T5 reflected shock tunnel [42] uses a free piston to adiabatically compress a mixture of monatomic driver gases to high pressure up to 120 MPa and temperature up to 4000 K (Figure 2.2). The rupture of a steel diaphragm creates a primary shock wave that propagates through a 90 mm diameter shock tube containing the test gas. The shock then reflects from the end wall of the reservoir where the test gas is stagnated before being accelerated through a converging-diverging nozzle. Test times are typically one to two milliseconds, terminated by driver gas contamination [108].

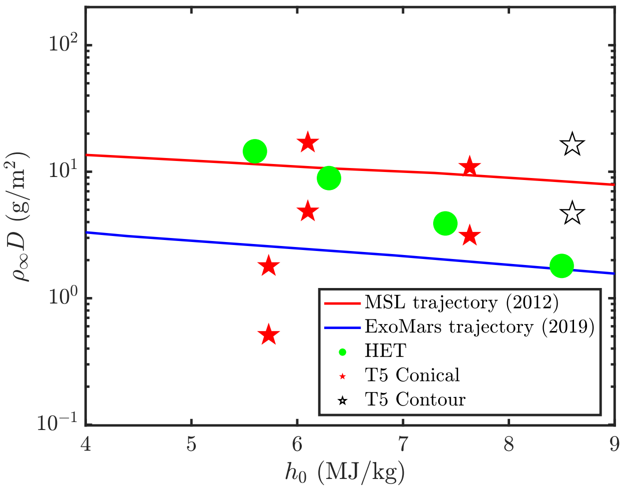

(a) Binary scaling parameter vs. total enthalpy.

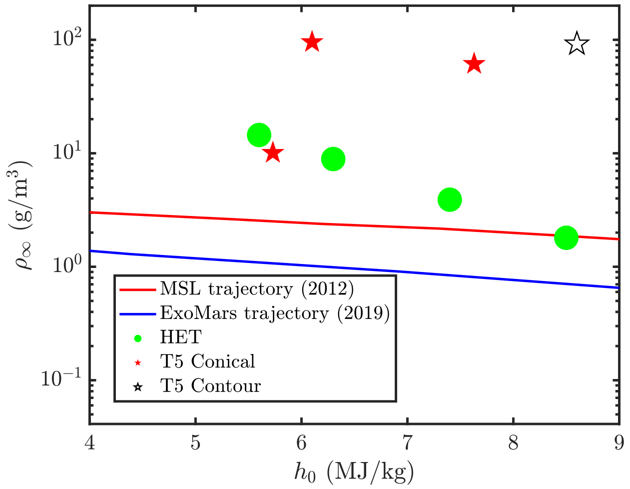

(b) Density vs. total enthalpy.

Figure 2.1: The (a) binary scaling parameter and (b) freestream density plotted against the total enthalpy for the experimental freestream conditions and entry trajectories of the MSL and ExoMars spacecrafts.

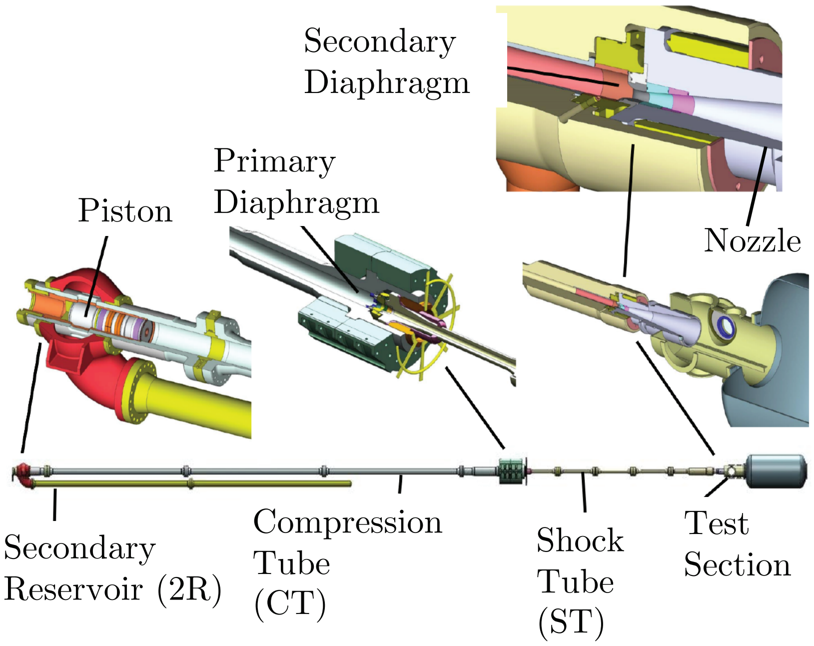

Figure 2.2: Schematic of the T5 Reflected Shock Tunnel.

2.2.1 T5 Freestream Calculations

The procedure for determining and validating the freestream conditions in T5 post experiment is summarized in the flowchart in Figure 2.3.

Reservoir Conditions

The nozzle reservoir conditions are determined using the experimental measurements of shock speed, reservoir pressure, and initial fill pressure. Pressure along the shock tube is measured using five PCB119M44 transducers. The primary shock speed for the reservoir calculation is extracted from the time of arrival of the primary shock traveling 2.4 m between stations 3 and 4 (Figure 2.4). This shock location is the approximate starting location of the slug of gas corresponding to test time determined from previous method of characteristic simulations in the T5 shock tube [5]. The reservoir pressure is the average of the two pressure traces located immediately upstream from the nozzle end wall (Figure 2.5). The transducers are labeled north reservoir and south reservoir and located on opposite ends of the shock tube diameter.

The reservoir conditions at the end of the shock tube are determined by calculating the stagnated equilibrium condition behind the primary and reflected shocks and isentropically expanding the post-reflected shock state to the experimentally measured pressure. The Shock and Detonation Toolbox and Cantera are used for the thermodynamic calculations [11, 31, 52]. The assumption of thermal and chemical equilibrium for the reservoir conditions shown in Table 2.2 were checked in Leibowitz and Austin [59]. The vibrational time constant τ_i calculated from the collisional rates presented in Doraiswamy et al. [21] ranged from 0.8 to 3.0 ns for the species CO_2, CO, and O_2. Given a reservoir speed of 100 m/s, thermal equilibrium is reached within 30 μm. Chemical equilibrium, estimated using zero-dimensional models in the Shock and Detonation Toolbox, is reached within 1 mm for all species. With a test gas slug on the order of meters, thermochemical equilibrium can safely be assumed.

Table 2.2: Select T5 reservoir conditions.

Shot	**2886**	**2889**
ρ (kg/m^3)	45.0	41.6
T (K)	3541	3503
P (MPa)	33.9	30.8
h_0 (MJ/kg)	5.73	5.63
Y_{CO_2}	0.767	0.774
Y_{CO}	0.148	0.144
Y_{O_2}	0.081	0.079
Y_O	0.004	0.004

Nozzle Code

A chemically reacting, axisymmetric Navier-Stokes solver with a structured-grid developed by the Candler group at the University of Minnesota is used to obtain the freestream conditions at the test section [13]. Previously, this code was used for the T5 nozzle to study boundary layer transition on a slender cone in various gases including carbon dioxide [52]. For a carbon dioxide mixture, chemical nonequilibrium is modelled using a 5 species (CO_2, CO, O_2, O, and C), 6 reaction kinetic mechanism and the vibrational nonequilibrium is modelled using the Camac vibrational energy relaxation model [117].

T5 has two interchangeable nozzles; a contour geometry that produces uniform flow at the exit plane when operated on-design and a conical geometry that results in a

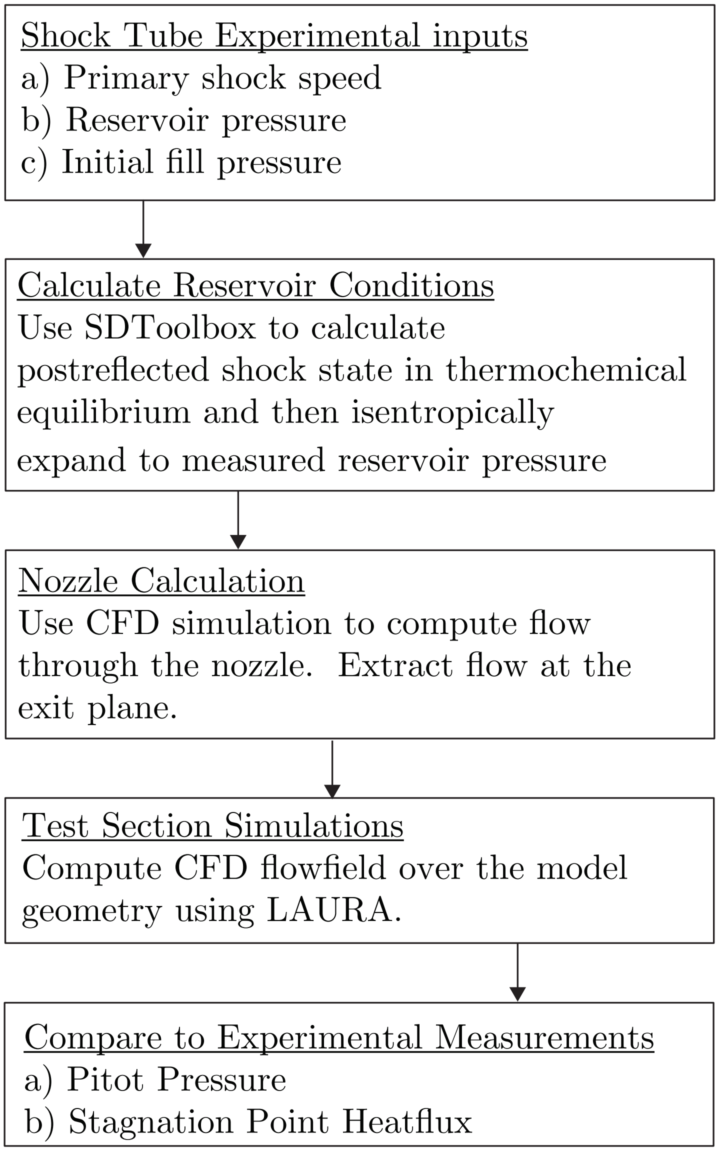

Figure 2.3: Flowchart for determining and validating the T5 freestream conditions.

slightly diverging flow at the nozzle exit. Both nozzles have an exit diameter of 300 mm. The contour nozzle throat to exit area ratio is 100:1 and the conical nozzle has interchangeable inserts at the throat to allow for different area ratio nozzles. The original Nozzle Code grid was generated by Wagnild [117] for the contoured nozzle and contains 490 x 217 cells in the stream wise and wall-normal directions, respectively.

To generate the conical nozzle grids, the previous grid cell locations were modified to convert the contour cell locations to the dimensions of the conical nozzle while

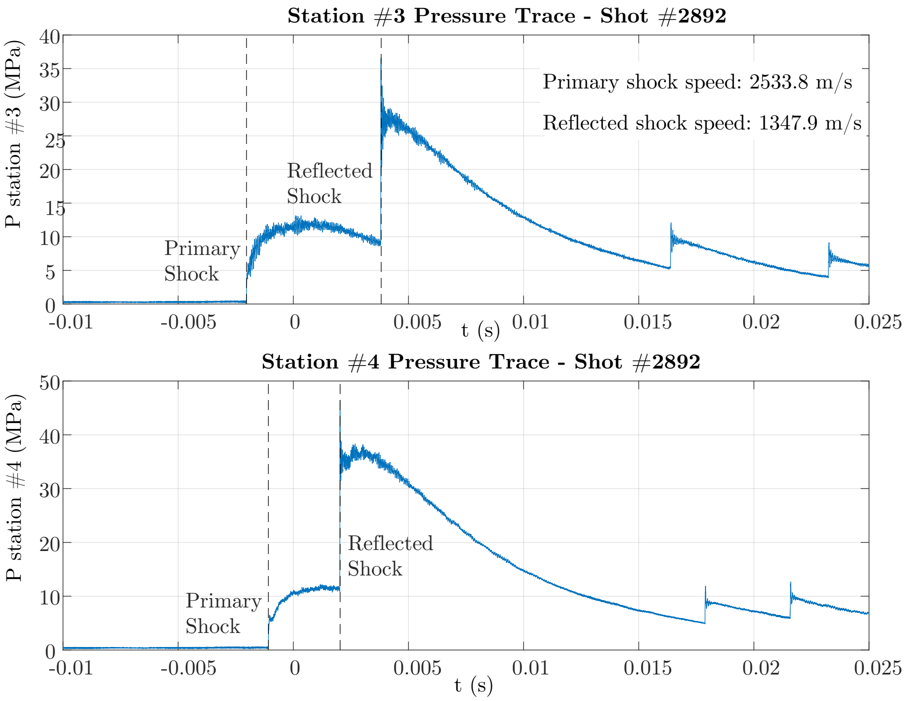

Figure 2.4: Shock arrival pressure traces from shot T52892 located along the shock tube.

ensuring the grid is similarly refined close to the wall. Two grids were constructed with 100:1 and 900:1 geometric area ratios. Resulting density contours for simulations with the contoured and 900:1 conical nozzle are shown in Figure 2.6. The freestream conditions are extracted from the output of the nozzle simulation at the exit plane. While the contour nozzle produces nominally uniform flow, Section 4.2 discusses the effect of the divergence of streamlines produced by the conical nozzle.

2.2.2 T5 Experimental Input Sensitivity Analysis

Leibowitz and Austin [59] presented a sensitivity study where the shot T52886 experimental uncertainties of the primary shock speed, reservoir pressure, and fill pressure were separately propagated following the flowchart in Figure 2.3 to see the resulting effect on sphere standoff distance and heat flux. The uncertainty of the fill pressure produced negligible effects (<0.1%) and so is omitted. The nominal shock speed is found using the time of arrival between stations 3 and 4 while the speed increase and decrease correspond to the polynomial fit shock speed at stations 3 and 4 found using the arrival time data along the shock tube. The nominal reservoir

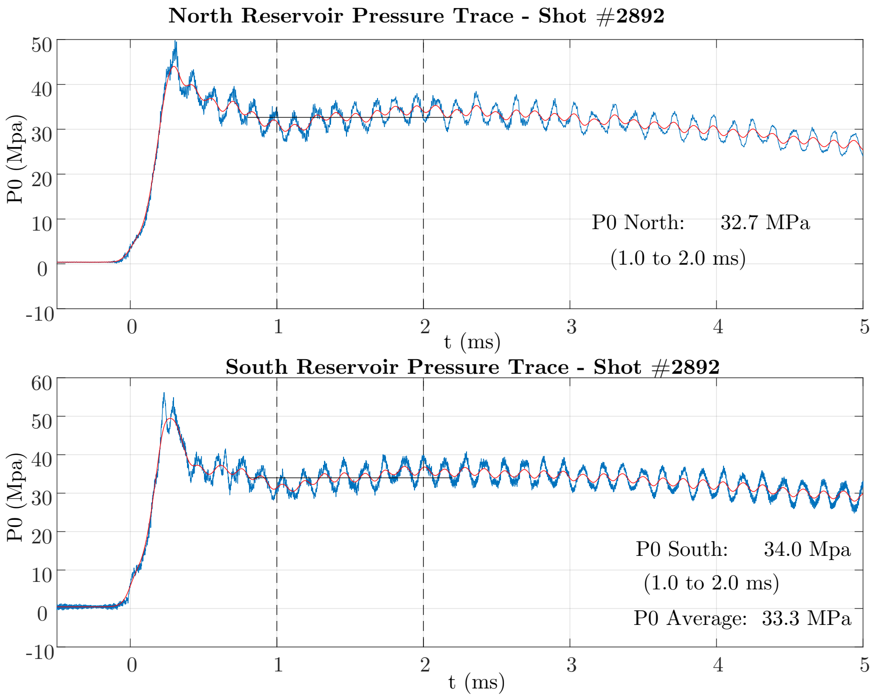

Figure 2.5: Reservoir pressure traces from shot T52892.

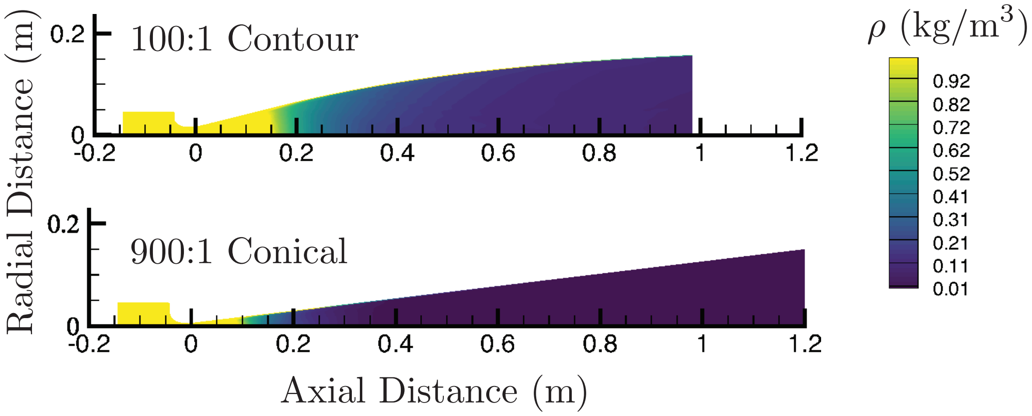

Figure 2.6: Nozzle density contours for shots T52866 (top) and T52889 (bottom).

pressure is the average of the two reservoir pressure traces during test time and the increase and decrease in pressure correspond to the standard deviation of the two reservoir pressure traces during test time. The standoff distance and stagnation point heat flux from flow over a 1" sphere are extracted from CFD simulations using the LAURA code [1] with a fully catalytic wall [41] specified. The results are summarized in Table 2.3. The corresponding RMS values for the uncertainty in experimental inputs are ±2.1% in sphere standoff distance and ±5.4% in stagnation-point heat flux.

Table 2.3: Results of the sensitivity study to understand how uncertainties in primary shock speed and reservoir pressure affect sphere standoff distance and stagnation point heat flux.

Input —-	**Shock Speed** m/s	**Reservoir P** MPa	**Standoff Distance** mm (+/-%)	**Heat Flux** MW/m^2 (+/-%)
Nominal	2451	33.86	1.282	12.63
Speed Inc.	2606	Nominal	1.257 (-2.0%)	12.59 (-0.3%)
Speed Dec.	2324	Nominal	1.304 (+1.7%)	12.13 (-4.0%)
Reservoir Inc.	Nominal	35.86	1.276 (-0.5%)	13.04 (+3.3%)
Reservoir Dec.	Nominal	31.86	1.298 (+1.2%)	12.18 (-3.6%)

2.3 Hypervelocity Expansion Tube (HET)

The HET facility consists of three sections: a driver, a driven, and an accelerator tube of lengths of 1.22, 5.18, and 9.14 m, respectively, all with a 152.4 mm inner diameter. The driver section is typically filled with helium up to a pressure of 3.5 MPa to burst an aluminum diaphragm, propagating an initial shock wave through the test gas in the driven section. The incident shock ruptures a second thin Mylar diaphragm at the driven/accelerator gas interface. An unsteady expansion fan is generated and provides the secondary acceleration of the test gas to the freestream condition without stagnating the flow. Test times are on the order of 100 to 500 μs. The facility can also be operated in shock tube mode by removing the secondary diaphragm. A more detailed description of this facility can be found in Dufrene et al. [22].

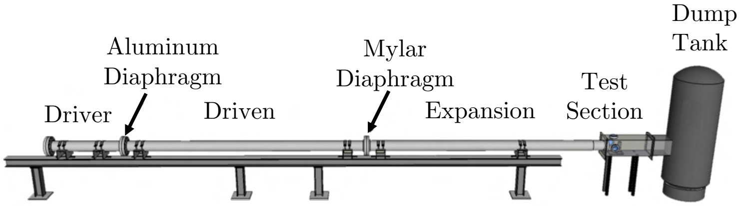

Figure 2.7: Schematic of the HET.

2.3.1 HET Freestream Calculations

The freestream conditions for the HET are calculated using the MATLAB Expansion Tube Solver (METS). METS is developed to understand how different chemistry assumptions for individual processes affect the calculated freestream. The underlying algorithms of METS find the shock and expansion pressure-velocity relations assuming either perfect gas or calling Cantera [31] to find the equilibrium state. There are seven gas states as labelled on the x-t diagram for the MSL1 condition shown in Figure 2.8.

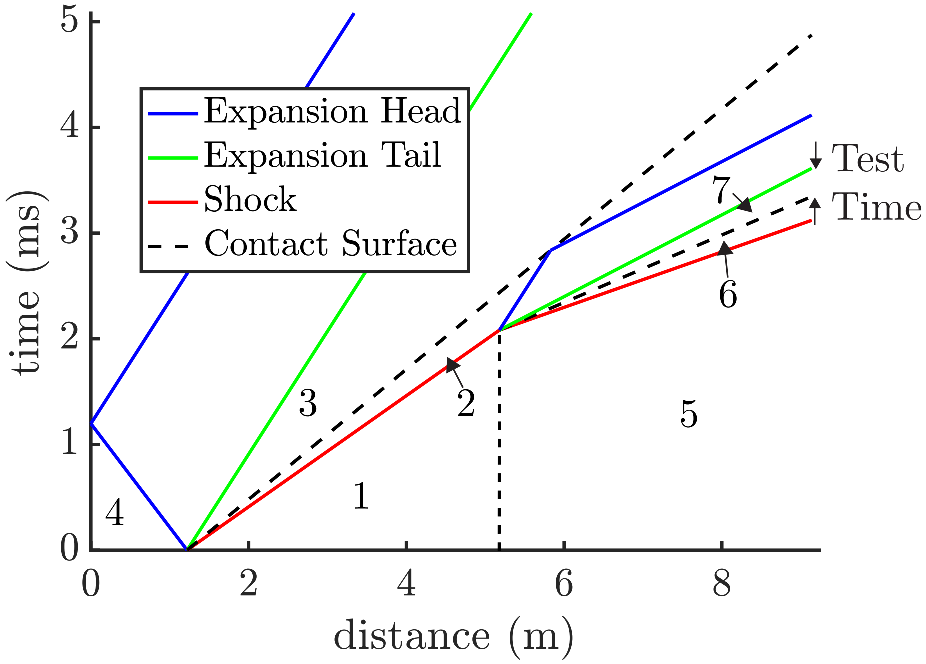

1. Initial test gas
2. Post-incident shock test gas
3. Post-expanded driver gas
4. Initial driver gas
5. Initial accelerator gas
6. Post-transmitted shock accelerator gas
7. Accelerated freestream test gas

Figure 2.8: x-t diagram with labelled states for the MSL1 condition.

The code is written to allow for maximum flexibility in choosing the desired thermochemical assumption for each shock or expansion process. For perfect gas calculations, the shock jump equation is given by

$$\frac{P_1}{P_0} = 1 + \gamma \frac{\Delta u}{a_0} \left(\frac{\gamma + 1}{4} \frac{\Delta u}{a_0} + \sqrt{1 + \left(\frac{\gamma + 1}{4} \frac{\Delta u}{a_0} \right)^2} \right), \tag{2.2}$$

and the non-steady isentropic flow equation is given by

$$\frac{P_1}{P_0} = \left(1 - \frac{\gamma - 1}{2}\frac{\Delta u}{a_0}\right)^{\frac{2\gamma}{\gamma-1}}, \tag{2.3}$$

where $\Delta u = u_1 - u_0$ is the difference in velocity between state 1 (post-process) and state 0 (pre-process) in the lab frame of reference, a is the sound speed, P is the pressure, and γ is the ratio of specific heats. The equilibrium shock pressure-velocity relations are calculated by stepping through a range of shock speeds, calling the Shock and Detonation Toolbox [11] routines PostShock_fr for chemically frozen/thermal equilibrium calculations or PostShock_eq for thermochemical equilibrium calculations. The equilibrium expansion states are calculated by iterating on pressure, using Cantera to find the corresponding equilibrium state at constant entropy and pressure and then calculating the corresponding velocity along a J+ characteristic:

$$u_{i+1} = u_i - \frac{P_{i+1} - P_i}{\rho_i a_i}. \tag{2.4}$$

The initial pressures and gases for the four expansion tube conditions analyzed in the sensitivity analysis in this chapter are shown in Table 2.4. The first condition, MSL1, is the same as the RC5 condition characterized by Sharma et al. [103] except with a higher burst pressure of 3.0 MPa vs. 2.5 MPa. The accelerator gas is changed from air to helium for MSL3 and MSL4 to reach higher velocity and total enthalpy in the free stream.

Table 2.4: Initial pressures and gases for each section for the four expansion tube test conditions.

Label	**Driver, P4: He**	**Driven, P1: CO_2**	**Accelerator, P5 (Gas)**
—-	MPa	kPa	mTorr
MSL1	3.0	1.2	180 (Air)
MSL2	3.0	1.2	75 (Air)
MSL3	3.0	1.2	150 (He)
MSL4	3.0	1.2	50 (He)

2.3.2 Vibrational Nonequilibrium in the Expansion Fan

For a mixture of diatomic and linear molecules such as N_2 and O_2 or CO_2, CO, and O_2, the number of degrees of freedom in rotranslational modes is given by

$f_{tr,i} = 5$ for all species. The resulting ratio of specific heat γ_{tr} for a chemically and vibrationally frozen process is $\gamma_{\mathrm{tr}} = 1.4$. This value is used for a CO_2 vibrationally frozen process in the thermochemical sensitivity study presented in Section 2.3.2.

Additionally, the heat capacities can be assumed to remain frozen at the initial facility temperature of 300 K resulting in a constant $\gamma = 1.29$ perfect gas. This was the assumption made for the RC5 condition calculation [103].

Sensitivity to Thermochemistry

METS lets the user specify each individual shock or expansion process as i) perfect gas (thermally and chemically frozen) defined by a constant ratio of specific heat γ, ii) thermal equilibrium and chemically frozen, or iii) thermochemical equilibrium. METS then calculates the corresponding pressure-velocity relationships as shown in Figure 2.9. The intersection of the pressure-velocity relationships for the waves define the pressure and velocity at the interface allowing the corresponding states 1-7 to be calculated. The pressure-velocity diagram illustrates the fact that the thermochemical assumption for the secondary expansion fan results in a larger difference in pressure and velocity than any other process.

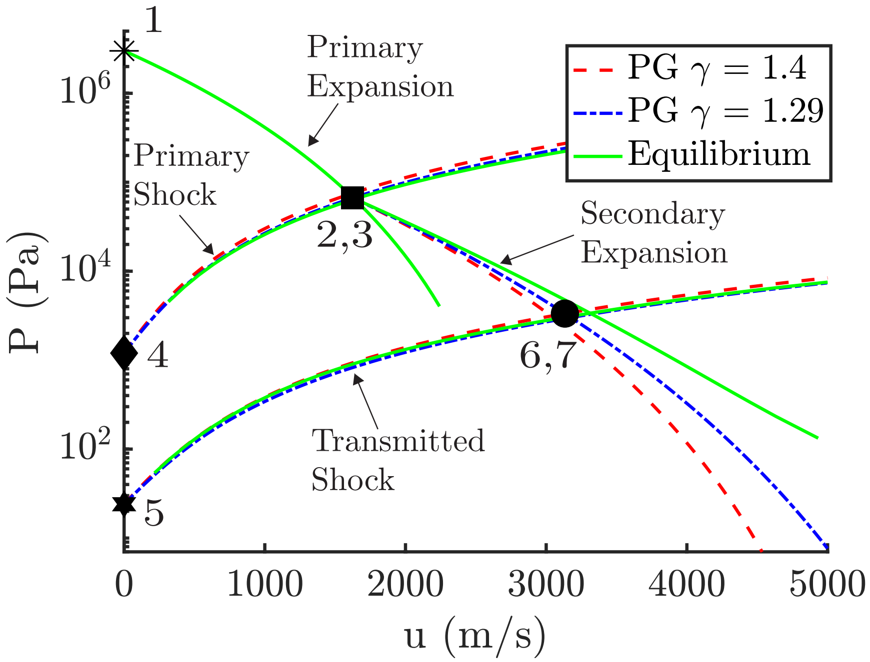

Figure 2.9: Perfect gas and equilibrium shock and expansion pressure-velocity relationships for the MSL1 condition.

The computed freestream conditions for the MSL1-4 conditions for a range of assumptions about the gas state are shown in Table 2.5. Insight can be gained when one assumption about the gas process is changed at a time. Qualitatively, for the CO_2 test gas, assuming a perfect gas model with $\gamma = 1.29$ or equilibrium shocks and expansion fans resulted in very similar freestream conditions, however, the sequence of gas states are drastically different. A perfect gas incident shock results in higher post-shock temperatures, but the temperature then decreases more rapidly through a perfect gas expansion fan when compared to an endothermic equilibrium shock and exothermic equilibrium expansion fan.

Calculations show that for the conditions in this work, assuming chemically frozen or chemical equilibrium in the post-incident shock has little impact on the freestream conditions because of the small amount of dissociation post-incident shock (Y_{CO_2} = 0.995).

A simulation using a state-to-state air numerical model developed by Massa [70] showed that the accelerator gas for the MSL1 condition, while not fully in equilibrium will be much closer to equilibrium than thermally and chemically frozen for the accelerator gas duration, which was was experimentally measured with a pitot probe to be 50-100 μs. Assuming a chemically frozen or chemical equilibrium transmitted shock has a small impact on the freestream conditions but the assumption of a perfect gas for the air accelerator does result in a freestream pressure increase of 8% compared to the equilibrium air accelerator gas assumption.

The vibrational nonequilibrium assumptions in the secondary expansion fan makes a large difference on the freestream conditions. For example, in the case of an equilibrium incident and transmitted shock assumption, the temperature of the freestream gas ranges from 668 K to 1081 K depending on if the expansion fan processes are assumed to be vibrationally frozen or in thermochemical equilibrium. Recent work in carbon dioxide in expansion tubes have ranged from assuming the expansion fan is vibrationally frozen in X2 at UQ [36] and HVET at JAXA [111] to perfect gas at $\gamma = 1.29$ in previous HET work [22]. Since the reasonable assumptions are highly dependent on facility dimensions, operation, and initial conditions, we were motivated to write a vibrational nonequilibrium fan solver to investigate possible effects of nonequilibrium in the expansion fan.

Nonequilibrium Expansion Tube Solver

Between 1957 to 1968, many experiments were conducted to investigate carbon dioxide vibrational relaxation times in compressive flow behind a shock wave [12,

Table 2.5: Study of different thermochemical assumptions for each process for run conditions MSL1-4. Equil. represents a thermochemical equilibrium process, Chem. Fr. represents a chemically frozen, thermal equilibrium process, and γ = constant defines the perfect gas process.

	Pri. Shock	**Exp. Fan**	**Trans. Shock**	h_0 MJ/kg	T K	P Pa	ρ g/m^3	u m/s
MSL1	γ = 1.4	γ = 1.4	γ = 1.4	6.2	1404	3580	13.50	3246
	γ = 1.29	γ = 1.29	γ = 1.4	6.0	1231	3351	14.42	3139
	Equil.	γ = 1.4	Equil.	4.6	668	2566	20.33	2869
	Equil.	γ = 1.29	Equil.	5.1	824	2722	17.49	2960
	Equil.	Equil.	Equil.	6.1	1081	2956	14.48	3092
	Equil.	Equil.	γ = 1.4	6.1	1093	3186	15.43	3060
	Chem. Fr.	Chem. Fr.	Chem. Fr.	6.1	1087	3067	14.93	3076
MSL2	γ = 1.4	γ = 1.4	γ = 1.4	7.0	1148	1768	8.16	3539
	γ = 1.29	γ = 1.29	γ = 1.4	6.8	1051	1659	8.36	3426
	Equil.	γ = 1.4	Equil.	5.1	540	1220	11.95	3081
	Equil.	γ = 1.29	Equil.	5.7	700	1314	9.94	3202
	Equil.	Equil.	Equil.	6.9	971	1462	7.97	3384
	Equil.	Equil.	γ = 1.4	6.8	983	1587	8.54	3350
	Chem. Fr.	Chem. Fr.	Chem. Fr.	6.9	977	1523	8.25	3367
MSL3	γ = 1.4	γ = 1.4	γ = 1.67	8.1	877	690	4.20	3885
	γ = 1.29	γ = 1.29	γ = 1.67	7.8	852	653	4.10	3773
	Equil.	γ = 1.4	Equil.	5.7	421	510	6.41	3302
	Equil.	γ = 1.29	Equil.	6.5	577	557	5.11	3464
	Equil.	Equil.	Equil.	7.9	852	636	3.95	3718
	Equil.	Equil.	γ = 1.67	7.9	852	635	3.95	3718
	Chem. Fr.	Chem. Fr.	Chem. Fr.	7.9	852	635	3.94	3717
MSL4	γ = 1.4	γ = 1.4	γ = 1.67	9.2	688	265	2.10	4193
	γ = 1.29	γ = 1.29	γ = 1.67	8.9	689	253	1.90	4091
	Equil.	γ = 1.4	Equil.	6.4	318	191	3.18	3520
	Equil.	γ = 1.29	Equil.	7.3	465	213	2.43	3729
	Equil.	Equil.	Equil.	9.2	734	254	1.83	4092
	Equil.	Equil.	γ = 1.67	9.2	734	254	1.83	4092
	Chem. Fr.	Chem. Fr.	Chem. Fr.	9.2	734	253	1.82	4087

33, 34, 53, 105, 124]. Combining the available low-temperature data and their own experiments looking at the shape of the radiation profile behind a shock wave as well as electron-beam interferometry to look at the density profile, Camac [12] calculated the CO_2-CO_2 vibrational relaxation time. Camac postulated that all four modes of carbon dioxide relax simultaneously with a relaxation time valid up to temperatures of 6000 K in the form

$$P\tau = e^{(36.5T^{-\frac{1}{3}}-3.9)} \text{ atm-}\mu\text{s} \tag{2.5}$$

Later interest in CO_2 vibrational relaxation stemmed from its value as a laser medium. While Camac concluded that all vibrational modes of CO_2 relax at the same rate, work in 1975 found that the symmetric-stretch and bending modes are highly coupled due to Fermi resonance [50]. Lopez et al. [62] devised a state-to-state model for CO_2 and found vibrational-translational (V-T) relaxation rate of the symmetric modes may be five times faster than vibrational-vibrational (V-V) rates between the asymmetric mode and the coupled symmetric modes [62]. Doraiswamy et al. [21] simplified the full state-to-state CO_2 model by assuming that the symmetric modes are in thermal equilibrium with translation. They devised a state-to-state model for V-T and V-V transitions for the first four vibrational levels of the asymmetric stretch mode as well as interactions with O_2 and CO. Their state-to-state model was then simplified into a $P\tau$ model where they extracted collision rates in Millikan and White form. The extracted rate for V-T transitions of $CO_2(\nu_3)$ with CO_2 colliding partners is given by

$$P\tau = e^{(40.58T^{-\frac{1}{3}}-17.50)} \text{ atm-s.} \tag{2.6}$$

The relaxation times for the two different models are plotted in Figure 2.10. While the Camac model relaxes faster, there is more total energy in the four degenerate modes compared to just the asymmetric stretch mode.

The Nonequilibrium Expansion Tube Solver (NETS) uses the Landau-Teller equation to implement the Camac and asymmetric stretch models in a vibrational nonequilibrium simulation of the expansion fan. NETS solves the Euler equations with a source term for vibrational relaxation using the explicit MacCormack finite-difference technique that is second order accurate in both space and time. The numerical method implemented follows sections 6.3 and 10.3 in Anderson [2] as well as sections 5.6-5.7 and 6.1 - 6.3 in Pletcher, Tannehill and Anderson, [88]. The MacCormack method is a variant of the Lax-Wendroff approach but is simpler in its application. It is an explicit finite-difference technique that is second-order accurate in both space and time. Unlike first-order upwind schemes, the MacCormack method doesn't introduce diffusive errors, however it does introduce dispersive errors in the regions where gradients are high. This results in Gibbs phenomenon near the interface

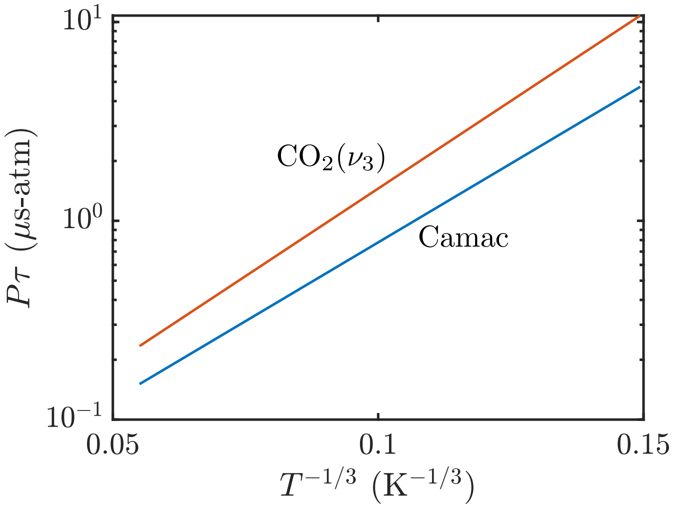

Figure 2.10: V-T relaxation times for the vibrational nonequilibrium CO_2 modes deactivated by collisions with CO_2.

between the fan and the inflow. Equilibrium simulations assuming no source term are compared to the equilibrium output from the METS code for verification of the simulation.

Results from simulations for the MSL1 to MSL4 conditions with driver pressure of 3.5 MPa are shown in Table 2.6. To be able to start the simulation on a uniformly spaced grid, the fan is assumed frozen for the first $t_0 = 10$ µs before iterating with time steps of 1 µs for 2 ms. The grids have between 4500 to 8000 spatial grid points in the 3.96 m length accelerator section. The largest difference in the resulting translational and vibrational temperatures is 18 K for the MSL1, MSL2, and MSL3 conditions, and 72 K for the MSL4 condition. These results suggest that for the conditions tested in this work, assuming equilibrium thermodynamics is more accurate than assuming perfect gas for the secondary expansion fan process.

2.3.3 Sources of Freestream Uncertainty

In addition to thermochemistry effects, we also examine the sensitivity of the freestream conditions to uncertainty in fill pressures, air contamination, viscous effects, and diaphragm effects. Analysis is performed using the METS tool.

Uncertainty to Initial Pressures

A sensitivity analysis to initial pressures in the tube is shown in Table 2.7. Equilibrium gas dynamics are assumed and pressure ranges are chosen to illustrate

Table 2.6: Freestream conditions extracted from the NETS simulation testing the Camac and asymmetric stretch (ν_3) nonequilibrium models, equilibrium model, and a comparison to the METS equilibrium output.

MSL1				
Free stream	**Camac**	ν_3	**Eq.**	**METS**
T (K)	1126	1115	1115	1119
T_v (K)	1144	1127	1115	1119
P (Pa)	3242	3155	3145	3174
ρ (g/m^3)	15.3	15.0	14.9	15.0
u (m/s)	3110	3124	3127	3130
MSL2				
Free stream	**Camac**	ν_3	**Eq.**	**METS**
T (K)	1018	1002	1001	1007
T_v (K)	1034	1012	1001	1007
P (Pa)	1625	1560	1554	1576
ρ (g/m^3)	8.5	8.2	8.2	8.3
u (m/s)	3396	3414	3417	3426
MSL3				
Free stream	**Camac**	ν_3	**Eq.**	**METS**
T (K)	884	909	875	878
T_v (K)	897	926	875	878
P (Pa)	626	629	645	656
ρ (g/m^3)	3.8	3.7	3.9	4.0
u (m/s)	3768	3772	3757	3783
MSL4				
Free stream	**Camac**	ν_3	**Eq.**	**METS**
T (K)	770	754	752	758
T_v (K)	806	826	752	758
P (Pa)	258	252	251	262
ρ (g/m^3)	1.8	1.8	1.8	1.8
u (m/s)	4087	4093	4095	4160

sensitivities. Differences in pressure of 500 kPa in the driver are chosen to compare the MSL1 (3.0 nominal burst pressure) to RC5 [103] (2.5 MPa nominal burst pressure). The driven and accelerator section sensitivity shown is 10% of the nominal initial pressure. The uncertainty for the accelerator section is also provided in the sensitivity table.

The burst pressure in the driver is measured using a Setra 206 static pressure gauge with an accuracy rated at ±27 kPa in the range of 0.2 to 20.7 MPa. The average burst pressure and standard deviation calculated from 19 shots between HET Shots 1500 - 1553 results is 3140 ± 140 kPa. The primary diaphragm material is 5052 aluminum with a thickness is 0.05" ± 0.004". This shot-to-shot variation is most likely due to the uncertainty in the thickness.

The driven section pressure is measured using a MKS Baratron type 626 pressure gauge rated up to 133 kPa with an accuracy of ±0.3 kPa. The accelerator section fill pressure is monitored using a MKS 626 Baratron rated up to 2 Torr with an accuracy of ±5 mTorr. Using table 2.7 and linear interpolating, the shot-to-shot variations in driver and driven pressure due to gauge accuracy results in freestream condition uncertainties of less than 1% for the conditions in this work.

In the spring of 2019, a manufacturer calibrated 2 Torr full scale MKS Baratron 626A was installed. Both gauges were monitored while the accelerator tube was evacuated and filled to 11 pressures ranging from 25 to 300 mTorr. The resulting gauge calibration using a linear fit is

$$P_{\text{new}} = 1.04221 P_{\text{old}} + 4.5399 \tag{2.7}$$

where units are in mTorr. The resulting freestream conditions due to this accelerator section gauge calibration is shown in Table 2.7. For the MSL1 to MSL4 conditions, the freestream condition uncertainty due to the accelerator initial pressure is 8.2% in pressure and 1.2% in temperature.

Sensitivity to Gas Leaks

Air contamination due to leaks in the accelerator section has been suspected in the past when using helium as an accelerator gas. McGilvray et al. found for an air test gas condition with 200 mTorr helium in the accelerator section, assuming 8% - 10% contamination of air (by volume) would best agree with experimental pitot measurements [73]. A leak rate of air into the tube of 4.2 ± 1.1 mTorr every minute is observed over a 30 minute rise time when averaged over 3 tests (Shots 1525, 1528,

Table 2.7: Sensitivity study of the freestream conditions to different initial pressures. The column labelled section indicates which initial pressure is changed. The freestream conditions are calculated assuming equilibrium chemistry with nominal pressures shown in Table 2.4.

	Section –	**Initial *P***	**M** (–)	***h_0*** MJ/kg	***T*** K	***P*** Pa	***ρ*** g/m^3	***u*** m/s
MSL1	Nominal	—	6.3	6.1	1081	2956	14.48	3092
	Driver	3.5	6.3	6.4	1112	3058	14.55	3147
	(MPa)	2.5	6.3	5.9	1044	2839	14.39	3026
	Driven	1.3	6.4	6.1	1055	2952	14.81	3089
	(kPa)	1.1	6.2	6.2	1110	2962	14.12	3095
	Accelerator	216	6.1	6.0	1105	3417	16.37	3030
	(mTorr)	144	6.5	6.3	1052	2474	12.44	3167
		192.1	6.2	6.1	1089	3113	15.13	3070
MSL2	Nominal	—-	7.3	6.9	971	1462	7.97	3384
	Driver	3.5	7.3	7.2	1000	1513	8.01	3443
	(MPa)	2.5	7.2	6.6	937	1403	7.92	3313
	Driven	1.3	7.3	6.9	947	1457	8.15	3378
	(kPa)	1.1	7.2	7.0	998	1467	7.78	3390
	Accelerator	90	7.1	6.7	993	1695	9.03	3323
	(mTorr)	60	7.5	7.1	944	1219	6.84	3457
		82.7	7.2	6.8	983	1582	8.52	3351
MSL3	Nominal	—-	8.5	7.9	852	636	3.95	3718
	Driver	3.5	8.5	8.2	878	656	3.96	3783
	(MPa)	2.5	8.5	7.6	822	611	3.94	3641
	Driven	1.3	8.6	7.9	830	632	4.03	3708
	(kPa)	1.1	8.4	8.0	877	639	3.85	3728
	Accelerator	180	8.3	7.7	873	740	4.48	3657
	(mTorr)	120	8.8	8.2	827	527	3.37	3792
		160.9	8.4	7.9	860	674	4.15	3695
MSL4	Nominal	—-	10.0	9.2	734	254	1.83	4092
	Driver	3.5	10.1	9.5	758	262	1.83	4161
	(kPa)	2.5	10.0	8.8	707	243	1.82	4004
	Driven	1.3	10.1	9.1	714	252	1.87	4076
	(kPa)	1.1	9.9	9.3	757	255	1.78	4106
	Accelerator	60	9.8	9.0	753	295	2.07	4026
	(mTorr)	40	10.4	9.5	711	210	1.56	4163
		56.7	9.8	9.0	747	282	2.00	4047

Table 2.8: Sensitivity study of the freestream conditions to air contamination by volume in the helium filled accelerator section. The rise time is calculated from the leak rate.

MSL3: Accelerator Pressure of 150 mTorr			
Freestream	**0% Air**	**10% Air**	**20% Air**
Rise time (min)	0	3.6	7.1
M	8.9	8.0	7.7
h_0 (MJ/kg)	7.9	7.5	7.3
T (K)	852	897	928.6
P (Pa)	636	876	1096
ρ (g/m^3)	3.9	5.2	6.2
u (m/s)	3718	3590	3500
u_t (m/s)	5159	4597	4289
MSL4: Accelerator Pressure of 50 mTorr			
Freestream	**0% Air**	**10% Air**	**20% Air**
Rise time (min)	0	1.2	2.4
M	10.0	9.5	9.1
h_0 (MJ/kg)	9.2	8.7	8.4
T (K)	734	775	804
P (Pa)	254	352	442
ρ (g/m^3)	1.8	2.4	2.9
u (m/s)	4092	3956	3863
u_t (m/s)	5640	5043	4713

1553). The time that the accelerator section is evacuated to the initial pressure to the time that the primary diaphragm bursts is about 1.5 minutes. During that time, it is expected that the accelerator section leak rate would result in 4% and 13% air by volume for the MSL3 and MSL4 conditions, respectively.

Table 2.8 shows the MSL3 and MSL4 freestream conditions assuming equilibrium thermochemistry with 0%, 10%, and 20% air contamination. Large observable changes are observed in the transmitted shock speed. Transmitted shock speed measurements are presented in Section 2.4.2.

Diaphragm Effects

Thin secondary diaphragm modeling is a difficult problem for the simulation of expansion tubes. While ideal operation assumes the secondary diaphragm ruptures instantaneously on impact by the primary shock, it has been proven in some cases that a shock reflection occurs at the diaphragm before rupture.

While testing in the Langley HYPULSE expansion tube, Bakos and Morgan [4] observed a reflected shock using a static pressure measurement at 76 mm downstream from the secondary diaphragm. They ran a test where the primary shock speed is 2670 m/s with initial pressures of 3.45 kPa and 0.072 kPa in the driven and expansion section. Coincidentally HYPULSE [112] has a 6" shock tube section and a 12.7 µm polyester diaphragm; the same dimensions as in the HET.

In order to compare the HYPULSE experiment to the HET experiments, we will model the diaphragm by assuming the Mylar diaphragm acts like a metal diaphragm with petals opening as hinged doors, as is commonly done for the primary diaphragm [95]. In this model, the rupture time, t_R, for shock tube diaphragms is estimated as

$$t_R = K\left(\frac{L\rho t}{P_R}\right)^{\frac{1}{2}} \tag{2.8}$$

where K is a constant with a large uncertainty (0.6 to 1.5), L is the petal base estimated as the tube radius (r = 0.0762 m), ρ is the diaphragm material density (1400 kg/m^2 for Mylar), t is the diaphragm thickness (12.7 µm), and P_R is the reservoir pressure. The equilibrium reflected shock condition for the HYPULSE condition is calculated to be 2170 kPa.

The MSL1 to MSL4 conditions have a calculated primary shock speed of 1835 and an initial driven pressure of 1.2 kPa resulting in an equilibrium reflected shock pressure of 71 kPa. For K= 1, the rupture time t_r is estimated to be 138 µs in the HET and 25 µs in the HYPULSE facility. For a primary shock speed of 1835 m/s, the reflected shock speed from a solid wall is calculated to be 283 m/s. Following a test gas particle at the end of the initial test gas slug estimated to be 0.6 m in length, the time for the particle to reach the diaphragm is 30 µs. The estimated hold time in the HET is 4.6 times longer than this calculate time. The results of these calculations indicate that a reflected shock off of the secondary diaphragm could plausibly affect the freestream gas state.

James et al. [51] describes two diaphragm models in the cases where the diaphragm inertia and opening or "hold time" affects the flow condition. The inertial diaphragm models treat the diaphragm as a piston driving the transmitted shock with the reflected shock gas behind it. As the diaphragm starts accelerating, the reflected shock loses its strength until it decays to a Mach wave. The hold time model assumes that the diaphragm remains closed for a period of time, causing some of the gas to be processed by a reflected shock before it opens fully and the effect is removed from the flow.

In the X2 facility at UQ, Gu [35] observed an opening time between 150 to 200 µs by fitting shock speeds to their time of arrival measurements. Gu calculated their freestream conditions assuming the test gas is twice shocked and stagnated before expanding to its final state [51]. This method was implemented into the METS code. The secondary expansion polar calculation is changed from starting at state 2 to starting at a post-reflected shock, stagnated state 2R. State 2R is found by calling the SDToolbox [11] reflected_eq function with state 2 inputted. Starting from state 2R, the equilibrium expansion pressure-velocity relationship is calculated using the same method described in Section 2.3.1. The intersection of the equilibrium expansion pressure-velocity curve with the equilibrium transmitted shock pressure-velocity curve defines the freestream pressure and velocity allowing the corresponding freestream state to be calculated.

The resulting non-ideal diaphragm, equilibrium freestream conditions for MSL1 to MSL4 are compared to perfect gas and equilibrium calculations assuming an ideal diaphragm break as shown in Table 2.9. Large differences from the ideal solution can be observed in temperature and density, resulting in a 35% increase in temperature and a 22% decrease in density for the MSL1 condition for the non-ideal diaphragm model.

Core Flow and Viscous Effects

In the mid-1950s, several researchers investigated the reduction of test time observed in low-pressure shock tube experiments compared to inviscid calculations. Test time is reduced due to the boundary layer starting behind the shock wave and growing along the tube wall until the contact surface is reached. Work by Roshko [94] and Mirels [76–80] applied conservation of mass in the shock fixed frame between the shock and the contact surface.

The wall boundary layer acts as a sink, removing mass and decelerating the shock until the shock and contact surface move at the same speed. The contact surface also slows down due to friction but at a slower rate as discussed by Hornung [44].

A similar control volume analysis can be used to study the viscous effects in the low-pressure accelerator section in an expansion tube. Figure 2.11 shows the control

Table 2.9: Freestream conditions calculated with METS using ideal diaphragm operation as well as an equilibrium reflected shock at the secondary diaphragm.

	Assumption	**Ma**	h_0	T	P	ρ	u
	—	–	MJ/kg	K	Pa	g/m^3	m/s
MSL1	Perfect gas	5.7	5.9	1221	3345	14.5	3129
	Equilibrium	6.3	6.1	1081	2956	14.5	3092
	Reflected Shock	5.6	7.0	1455	3106	11.3	3173
MSL2	Perfect gas	6.8	6.7	1042	1655	8.4	3414
	Equilibrium	7.3	6.9	971	1462	8.0	3384
	Reflected Shock	6.5	7.9	1321	1567	6.3	3505
MSL3	Perfect gas	8.3	7.8	850	653	4.1	3765
	Equilibrium	8.5	7.9	852	636	4.0	3718
	Reflected Shock	7.6	9.1	1172	691	3.1	3889
MSL4	Perfect gas	10.0	8.9	687	253	2.0	4082
	Equilibrium	10.0	9.2	734	254	1.8	4092
	Reflected Shock	9.0	10.6	1024	281	1.5	4318

volume defined by Roshko and Mirels applied to an expansion tube. Their expressions are valid for perfect gas flows in air or argon. In an expansion tube, Erdos and Bakos [24] predicted a transitional-unit Reynolds number of 3.7E6 1/m. The unit Reynolds number (1/m) calculated for the expansion tube CO_2 conditions are a maximum of 3.3E5 1/m for the MSL1 condition therefore we expect a laminar boundary layer in the expansion tube.

The initial expansion tube state 5 and post transmitted shock state 6 are transformed into the shock fixed frame: $u_w = u_t$, $u_e = u_t - u_6$, $T_e = T_6$, $T_w = T_5$, $P_e = P_6$, $\rho_e = \rho_6$, and $T_w\rho_w = \rho_e T_e$. The subscripts w and e represent the wall and edge conditions, respectively. Instead of a uniform state 6, viscous effects cause state 6 to change as a function of distance l behind the shock from $l = 0$ to $l = l_m$.

For a laminar boundary layer, Roshko [94] derived an expression for the characteristic displacement thickness given by

$$\delta(l) = \beta\left(\frac{\mu_w l}{\rho_w(u_w - u_e(0))}\right)^{\frac{1}{2}}. \tag{2.9}$$

An estimate for the parameter β, a parameter that accounts for the variations in the boundary layer and edge conditions was improved by Mirels [80] and expressed as

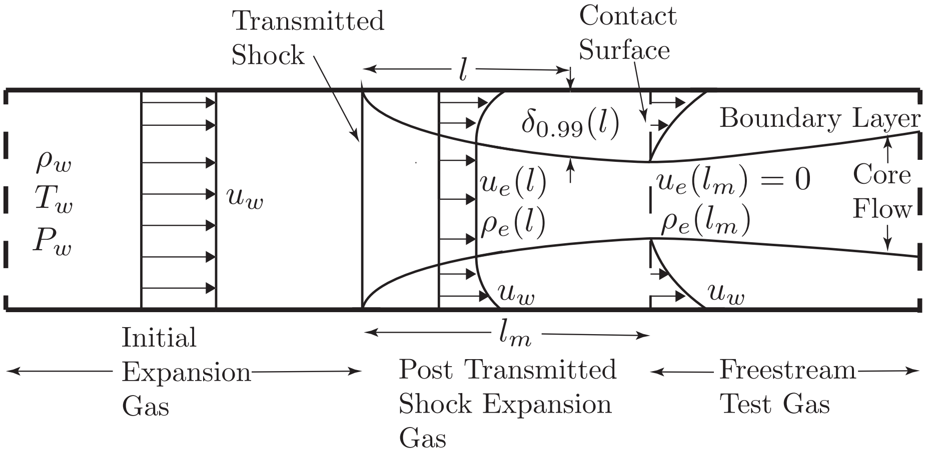

Figure 2.11: Schematic of a portion of the accelerator tube in an expansion tube in the transmitted shock fixed frame. Adapted from Mirels [80]

$$\beta_1 = C_{e,0}^{0.37} 1.59 \left[1 + \frac{1.796 + 0.802W}{W^2 - 1} \right]. \tag{2.10}$$

where the constants are $C_{e,0} = (\rho_e \mu_e / \rho_w \mu_w)_0$, $W \equiv u_w / u_e(0)$. When the mass flow rates are equal, the separation length will reach a maximum length, l_m, defined as

$$l_m = \frac{d^2}{16\beta_1^2} \left(\frac{\rho_e(0)}{\rho_w} \right)^2 \frac{u_e(0)}{u_w - u_e(0)} \frac{u_e(0)}{\nu_w}, \tag{2.11}$$

where d is the tube diameter and ν is the kinematic viscosity. Mirels [79] estimated the flow nonuniformity between the shock and contact surface to be

$$\rho_e(l) u_e(l) = \rho_e(0) u_e(0) \left(1 - \sqrt{\frac{l}{l_m}} \right). \tag{2.12}$$

The relationship between l, l_m, and time t can be determined by assuming a strong shock where $\rho_e(l) \approx \rho_e(0)$, and transforming Equation 2.12 using $u_e(l) = dl/dt$, and non-dimensional variables $L = l/l_m$ and $T = t u_e(0)/l_m$

$$\frac{dL}{dT} = 1 - \sqrt{L}. \tag{2.13}$$

Integrating Equation 2.13, the solution is given by

$$T = -2 \left(\ln[1 - \sqrt{L}] + \sqrt{L} \right). \tag{2.14}$$

Equations 2.11 and 2.14 can be used to solve for the separation between the contact surface and the shock when the contact surface reaches the test section at the accelerator tube length $l = 3.96$ m.

The boundary layer thickness $\delta_{0.99}$ can be determined by estimating the value of y at which $(u_w - u(y))/(u_w - u_e(0))$ is 0.99 where y is the distance normal from the wall.

Mirels [79] defined an explicit value of $\delta_{0.99}$ at l as

$$\delta_{0.99} = \left[\frac{\rho_w}{\rho_e(0)} \left(\frac{2l\nu_w}{u_e(0)} \right)^{\frac{1}{2}} \right] (\eta_u - I_\infty)_0, \tag{2.15}$$

where

$$(\eta_u - I_\infty)_0 = C_{e,0}^{0.48} \left(\frac{3.20}{[1 + 0.543W]^{\frac{1}{2}}} - I_{\infty,0} \right), \tag{2.16}$$

$$\frac{I_{\infty,0}}{(f - \eta)_{\infty,0}} = \frac{1 + 0.431[(1 + 1.665W)(1 + 1.022W)]^{1/2}}{W^2 - 1}, \tag{2.17}$$

$$(f - \eta)_{\infty,0} = 1.135 \frac{(W - 1)}{[1 + 1.022W]^{\frac{1}{2}}}. \tag{2.18}$$

At l_m

$$\left(\frac{2\delta_{0.99}}{d} \right)_{l_m} = \frac{(\eta_u - I_\infty)_0}{\beta_1 \, [2(W - 1)]^{\frac{1}{2}}}. \tag{2.19}$$

These formulas are implemented into METS and the computed boundary layer thickness $(2\delta_{0.99}/D)$ at l_m is verified using the plot predictions on Figure 12 from Mirels [79]. For the MSL1 condition assuming a perfect gas accelerator gas, the calculated transmitted shock Mach number is 10.7 and the calculated boundary layer thickness $(2\delta_{0.99}/D)$ at l_m is 0.116. These values fall on the curve, verifying the METS calculation.

An expression for the attenuation of a strong shock in the lab frame can be derived from conservation of momentum. Hornung, derived the formula (See pg. 226 of [44])

$$\frac{\Delta U_t}{U_t} = -\frac{l}{d} C_f, \tag{2.20}$$

where C_f is the coefficient of skin friction and the 3.96 m length, 0.1524 m diameter HET has a length to diameter l/d of 26.0.

Table 2.10: Results from the viscous study presenting the expected transmitted shock slow down, displacement thickness, and pressure rise due to viscous effects from Mirels theory as well as the expected transmitted shock attenuation from the conservation of momentum [44].

	ΔU_t m/s	$\delta_{0.99}$ mm	$P_e(l_m)/P_e(0)$ –	ΔU_t [44] m/s
MSL1	556	7.1	1.11	183
MSL2	698	8.2	1.11	312
MSL3	1444	13.7	1.20	625
MSL4	1556	13.7	1.20	1164

For laminar flow, the coefficient of friction can be estimated using the Blausius solution

$$C_f = \frac{0.664}{\sqrt{Re_x}}. \tag{2.21}$$

The calculated attenuation for the various test conditions is presented in Table 2.10. The Mirels analysis is performed in the shock fixed frame and does not indicate the rate of deceleration of both the shock and contact surface. The value of the shock velocity deficit is calculated when the contact surface arrives at the test section. The pressure rise due to negative displacement thickness is calculated at l_m to be 11% for the MSL1 and MSL2 conditions and 20% for the MSL3 and MSL4 conditions. The shock attenuation calculated using conservation of momentum is much less than predicted by Mirels theory but shows similar trends. The boundary layer thickness is calculated at the time when the contact surface arrives at the tube exit.

2.4 Experimental Freestream Diagnostics and Measurements

Efforts to experimentally characterize the T5 and HET freestream conditions are presented using 1" sphere stagnation point heat flux and pitot probe measurements. Staggered pitot probes are used to measure transmitted shock speed in the HET.

2.4.1 Fast Response Surface Mounted Thermocouples

The surface heat flux is measured using a 2.4 mm diameter, type E, Constantan-Chromel coaxial thermocouple manufactured in-house. The gauge type was designed and tested by Sanderson [100]. These gauges take advantage of the thermoelectric effect where a temperature rise at the junction of two dissimilar metals result in a measurable voltage rise which is converted back to temperature using

NIST standards. The thermocouples have a tapered center pin and a sharp edged out conductor to form a robust, thin surface junction with a fast response time of <1 μs. The gauge can be modeled as a one-dimensional semi-infinite solid with linear conduction given by

$$\frac{\partial^2 T(x,t)}{\partial x^2} = \frac{1}{\alpha}\frac{\partial T(x,t)}{\partial t} \tag{2.22}$$

where T is temperature, x is the distance normal to the surface into the solid, t is time, k is the thermal conductivity, ρ is the density of the material, c is the specific heat of the material, and α is the thermal diffusivity given by $\alpha = k/\rho c$.

The boundary conditions for a uniform temperature applied are

$$T(x, t = 0) = T_\infty, \tag{2.23}$$

$$\frac{\partial T}{\partial x}_{|x=0} = -q_w/k, \tag{2.24}$$

$$T(x, 0) = T_i, \tag{2.25}$$

$$T(0, t) = T_i + \Delta T(t). \tag{2.26}$$

The solution for the surface temperature rise given the heat flux is given by the convolution integral

$$\Delta T = \int_0^t g(x, t - \tau) q_w(\tau) d\tau \tag{2.27}$$

where the impulse function g(x,t) is defined as

$$g(x,t) = \frac{\partial \Delta T(x,t)}{\partial t} = \sqrt{\frac{\alpha}{\pi k^2 t}} e^{-\frac{x^2}{4\alpha t}}. \tag{2.28}$$

Equation 2.27 has to be inverted in order to compute heat flux from the measured temperature rise. One challenge is that the temperature rise is modest and contaminated by noise. Following the suggestions of Davis [20], a low pass filter with a cutoff of 20 kHz is applied to the temperature signal to reduce high frequency noise. The chosen filter is a 4th order Butterworth filter applied to the raw temperature following the work of Flaherty [26]. The heat flux is calculated using the convolution theorem in the frequency domain and fast Fourier transforms of the post-filtered temperature signal s(t) and impulse function g(t) denoted by upper case symbols

$$q_w = FFT^{-1}\left[\frac{S(f)}{G(f)}\right]. \tag{2.29}$$

Marineau and Hornung [69] simulated and calibrated the thermocouples using an instrumented shock tube end wall plate in T5. Simulations showed that the geometry at the thin junction strongly affects the measurement. Specifically, the epoxy used during the manufacturing process acts as an insulator to create a local overheating that increases with the step height between the inner and outer electrodes. At time scales of 30 μs, the effective thermal product $\sqrt{k\rho c}$ was found to be ≈30% lower than the average of chromel and constantan. This discrepancy decreases with time but may still appear on millisecond time scales.

Improvements to the Manufacturing Process

To maintain consistent gauge-to-gauge variation of the junction geometry, we introduced the use of a torque wrench to measure the level of torque applied on the set screw holding the inner and outer probe together during the epoxy setting manufacturing process. Using a 1" diameter, 3" span cylinder, we tested three different torque levels of 0.5, 1, and 2 in-oz for thermocouples labeled 1, 2, and 3.

The experimental results are compared to LAURA simulation heat flux using Johnston chemistry with the expected fully catalytic level as well as the non-physical super catalytic level. LAURA, the kinetic models implemented, and the grids for the sphere geometry are further described in Section 3.1.1. Fully and super catalytic recombination models force the atoms to recombine at the wall. The fully catalytic model forces recombination into diatomic molecules such as O to O_2 and C to C_2 and the super catalytic model forces recombination to the freestream levels. Recent investigations have concluded that fully catalytic wall boundary conditions should provide a realistic bound on metal models [41]. Simulations assuming a non-catalytic wall boundary condition resulted in similar values of heat flux at the stagnation point compared to simulations assuming a fully catalytic wall boundary condition.

The results of the HET MSL1 run condition experiment are shown in Figure 2.12a. Thermocouples 2 and 3 approach the fully-catalytic simulation while the 0.5 in-oz torqued thermocouple measured a heat flux level 21% higher than the 2 in-oz torqued thermocouple. This suggests there was epoxy at the junction surface after setting and is consistent with the observations of Marineau and Hornung. When the thermocouples were examined under a microscope (Figure 2.12b), a ring can be seen on thermocouple 1 suggesting the inner probe was protruding above the surface when set. A protrusion at the junction was imaged in micrographs of thermocouple cross-sections taken by Davis [20] and reproduced in Marineau and Hornung [68] confirming this hypothesis.

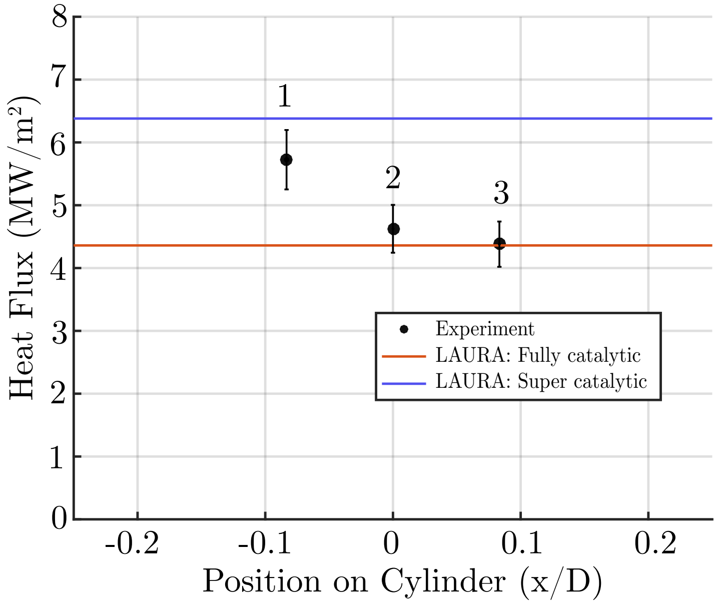

(a) Shot 1491 MSL1 experimental heat flux compared to simulated heat flux.

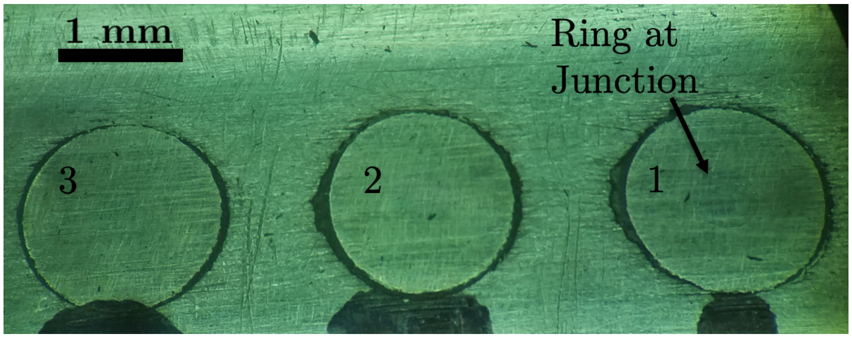

(b) Thermocouples under a microscope.

Figure 2.12: Cylinder experiment where thermocouples 1 to 3 (bottom plot) are manufactured with a torque on the set screw of 0.5, 1, and 2 in-oz, respectively, during the setting process. The resulting HET MSL1 condition experimental heat-flux level is shown on the top plot.

Stagnation Point Heat Flux Theory

Two models are considered in comparison to the experimental measurements and CFD predictions: the Fay and Riddell correlation [25] and the empirical correlation of Sutton and Graves [110]. Fay and Riddell derived a heat transfer rate of

$$q_w = 0.76\sqrt{2}\mathrm{Pr}^{-0.6}(\rho_e\mu_e)^{0.4}(\rho_w\mu_w)^{0.1}\sqrt{\left(\frac{du_e}{dx}\right)_s}(h_0 - h_w)\left[1 + (\mathrm{Le}^{0.52} - 1)\frac{h_D}{h_0}\right] \tag{2.30}$$

where q_w is the stagnation point wall heat flux, Pr is the Prandtl number, ρ is the density, μ is the viscosity, Le is the Lewis number, and h_0 is the total enthalpy. The subscripts e, w, and s refer to the location behind the shock but external to the boundary layer, the location at the wall, and the stagnation point, respectively. These parameters are extracted from LAURA simulations. Equation 2.30 assumes an equilibrium boundary layer while the authors note that if the boundary layer was frozen, the Lewis number exponent is changed from 0.52 to 0.63. The Lewis number is assumed to be 1.4, commonly accepted for engineering applications of carbon dioxide high speed flow [15]. The stagnation point velocity gradient can be estimated using Newtonian flow theory to be

$$\left(\frac{du_e}{dx}\right)_s = \frac{1}{R}\sqrt{\frac{2(P_e - P_\infty)}{\rho_e}} \tag{2.31}$$

where P is pressure, R is the radius of the sphere, the subscript ∞ refers to the free stream, and the "dissociation enthalpy" is defined as

$$h_D = \sum_i Y_i h_i^\circ . \tag{2.32}$$

where Y_i is the mass fraction for species i and h_i° is the reference enthalpy at 298.15 K for species i.

The second model examined is the empirical model of Sutton and Graves [110] given by

$$q_w = K\sqrt{\frac{P_s}{R}}(h_0 - h_w) \tag{2.33}$$

where P_s is the stagnation pressure at the wall, R is the radius of the sphere, h_0 and h_w are the total and wall enthalpies respectively, and the constant K is defined for a specific gas mixture. For CO_2, K = 0.121 kg/s-m$^{3/2}$-atm$^{1/2}$.

Experimental T5 Heat Flux Results

Three 1" diameter spheres with heat flux gauges flush mounted at the stagnation point were tested in T5 for four shots, 2886 to 2889, with two conical nozzle area ratios, 100:1 and 900:1. The distance between each sphere on the sphere rake is 5.8 cm. For shot 2886, only the middle sphere heat flux is reported and the error bars are the root mean square of the standard deviation in signal, material uncertainty of 8%, and NIST voltage to temperature uncertainty of 1.7% [20]. For shots 2887-2889, the average heat flux on the three spheres are reported and the error bars are the sample standard deviation of the three heat flux measurements. A 1 ms window of data during test time is used to extract the heat flux from the voltage trace.

Comparison of the experimental heat flux measurements are made to heat flux extracted from LAURA [1] simulations with a fully catalytic recombination model at the wall and Johnston chemistry rates. Additionally, the simulation data are used to obtain heat flux values from the Fay and Riddell [25] and Sutton and Graves models [110].

See Figure 2.13 and Table 2.11 for stagnation point heat flux results. For the 100:1 nozzle area ratio experiments, shots 2886 and 2887, the LAURA simulation, Sutton and Graves, and Fay and Riddell predicted heat flux are within the uncertainty of the experiment except shot 2886 where the LAURA simulation predicted heat flux is 12% below the experiments. For the 900:1 nozzle area ratio, shots 2888 and 2889, the LAURA simulation and Sutton and Graves prediction are within the uncertainty of the experiment while the Fay and Riddell prediction is 8% and 2%, respectively, below the lower bound of the experiment.

Table 2.11: T5 experimental heat flux measurements. All units are MW/m^2

Shot Number	**2886**	**2887**	**2888**	**2889**
Experiment	16.5	14.9	5.6	5.4
Uncertainty (±)	2.3	4.1	0.7	0.9
LAURA	12.6	12.2	5.0	5.0
Fay and Riddell	15.2	14.2	4.5	4.4
Sutton and Graves	15.2	14.2	5.1	5.1

Experimental HET Heat Flux Results

1" diameter sphere stagnation point heat flux experiments are performed for the CO_2 test conditions with pressures for each run condition from Table 2.4. Table 2.12 shows the different accelerator gases tested along with the results of the HET heat flux measurements compared to Sutton and Graves predictions.

The difference between the air and nitrogen experiments, while up to 11% higher than the Sutton and Graves predictions, show reasonable agreement. Since these tests were all completed without changing the thermocouple, any uncertainty due to the junction geometry would be systematic. When helium is used an accelerator

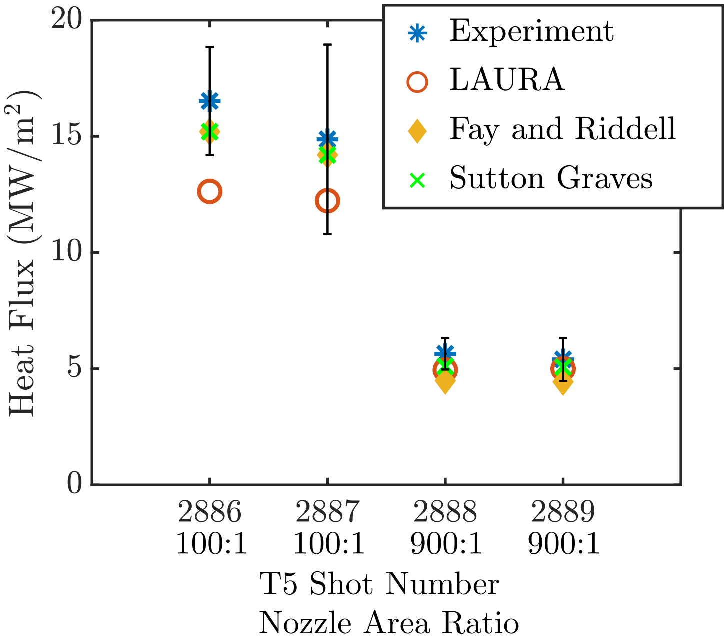

Figure 2.13: Shot 1491 MSL1 experimental heat flux measurements compared to simulated and theoretical heat flux predictions.

gas, the measurements are ≈25% higher than Sutton and Graves predictions based on inviscid perfect gas freestream calculations.

Table 2.12: Results of the HET sphere stagnation heat flux experiments compared to the empirical model of Sutton and Graves (SG). The nominal test conditions are from Table 2.4. The accelerator gas is changed for some of the experiments. Units are in MW/m^2.

	Acc. Gas	**Shot #**	**Experiment**	**Uncertainty**	**SG**	**% Diff.**
RC5 [103]	Air	NA	6.73	0.55	6.55	2.7
MSL1	Air	1454	7.75	0.63	6.98	9.9
MSL1	Air	1455	7.73	0.60	6.98	9.7
MSL1	N_2	1450	8.56	0.70	7.35	10.7
MSL1	He	1456	8.00	0.65	6.06	24.3
MSL2	N_2	1451	7.95	0.65	6.65	16.4
MSL3	He	1441	8.06	0.66	5.98	25.8
MSL4	He	1442	7.32	0.60	5.42	26.0

2.4.2 Pitot Measurements

T5 Pitot Measurements

The T5 pitot rake and probe mount was developed by Rousset in 1995 [96] and resurrected in preparation for the T5 radiation campaign presented in Chapter 6. Three PCB113B26 pressure sensors are mounted in the pitot rake at a distance of +7, -31, and -69 mm relative to the centerline of the nozzle. Experimental measurements are obtained for the T5 ExoMars condition (Shot 2893) and MSL condition (Shot 2894). The pressure trace for Shot 2893 is shown in Figure 2.14. The pressure was averaged between 1 to 2 ms and compared to DPLR simulations (with Johnston's rate constants) carried out by Dinesh Prabhu at NASA Ames and shown in Figure 2.15. The comparisons suggest that the pitot probe was about 5 cm inside the nozzle during the ExoMars condition and between 5 and 10 cm outside the nozzle during the MSL condition. This is within the uncertainty of the recoil. Future tests should record the recoil of the nozzle and the beginning position of the model relative to the nozzle.

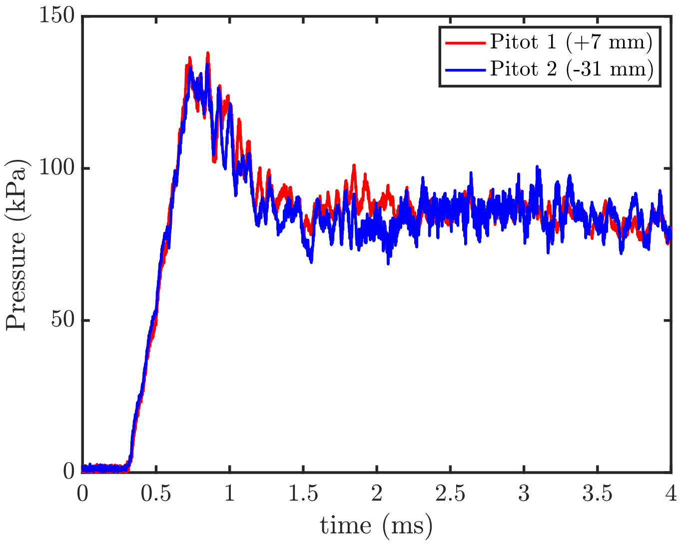

Figure 2.14: Pitot measurements for T5 Shot 2893, 900:1 Nozzle Area Ratio, ExoMars test condition.

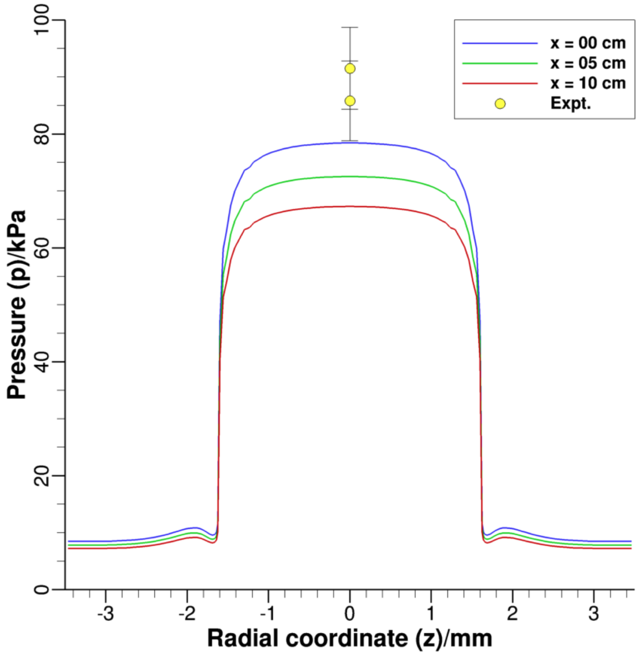

(a) T5 ExoMars condition.

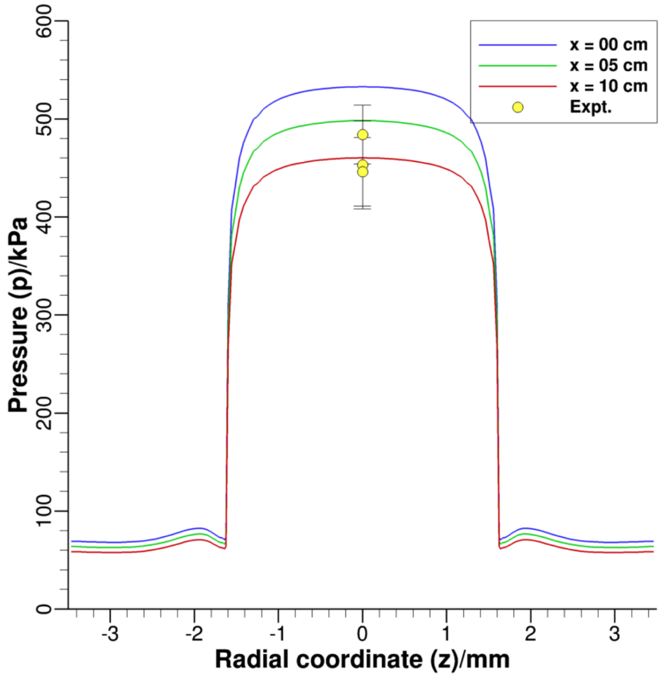

(b) T5 MSL condition.

Figure 2.15: T5 Pitot Measurements for the two conditions used in Chapter 6. Simulations and plots were made by Dinesh Prabhu and reproduced with permission.

HET Pitot Measurements

The HET pitot probe mount design is based on the work of Neely, Stalker, and Paul [83]. Two different types of pressure transducers were tested; the PCB113B26 used in the T5 tests and new PCB112A22 transducers. Compared to the PCB113B26, the PCB112A22 is 10 times more sensitive (100 mV/psi vs. 10 mV/psi), has a lower resonant frequency (>250 kHz vs. >500 kHz), a higher low frequency response (0.5 Hz vs. 0.01 Hz), and a longer rise time (≤ 2.0 μs vs. ≤ 1.0 μs).

The resulting pitot traces for two tests acquired at 1 MHz at the MSL1 condition are offset in time and displayed in Figure 2.16. The predicted equilibrium and perfect gas pitot pressure calculations for this condition are 135.9 kPa and 138.4 kPa, respectively. The pitot measurement with the PCB113B26 transducer is overpredicted by ≈40 kPa. It was initially suspected that the measurement with the PCB113B26 was either incorrectly mounted or no longer calibrated correctly but the same discrepancy was observed in the measurements of Sharma et al. [103] in 2010 for the RC5 condition where they reported a pitot pressure of 82.0 kPa ± 4.0 kPa and a prediction of 128.3 kPa. It is unknown why the PCB113B26 measurements were a lower value than expected. Measurements for the MSL1 and MSL3 conditions using the PCB112A22 transducers are compared to predictions of perfect gas and equilibrium chemistry in Table 2.13. The predictions are within the uncertainty of the measurement for the MSL1 condition test gas and are closer to the equilibrium accelerator gas while the predictions are lower for the MSL3 condition test and accelerator gas by 14% and 43%, respectively.

Table 2.13: Experimental pitot pressure experiments using PCB112A22 transducers inside the mount compared to theoretical predictions assuming perfect gas and equilibrium chemistry. Units are in kPa.

Shot #	**Gas**	**Experiment**	**Perfect Gas**	**Equilibrium**
MSL1	Test	146.2 ± 14.0	138.4	135.9
(1551)	Accelerator	32.5 ± 3.5	12.2	27.2
MSL3	Test	64.9 ± 8.3	56.0	52.3
(1553)	Accelerator	3.0 ± 0.3	1.7	1.6

HET Transmitted Shock Measurements

A staggered pitot rake with a distance between transducers of 150 mm are used to obtain time of arrival for the transmitted shock wave. An AMRITA simulation

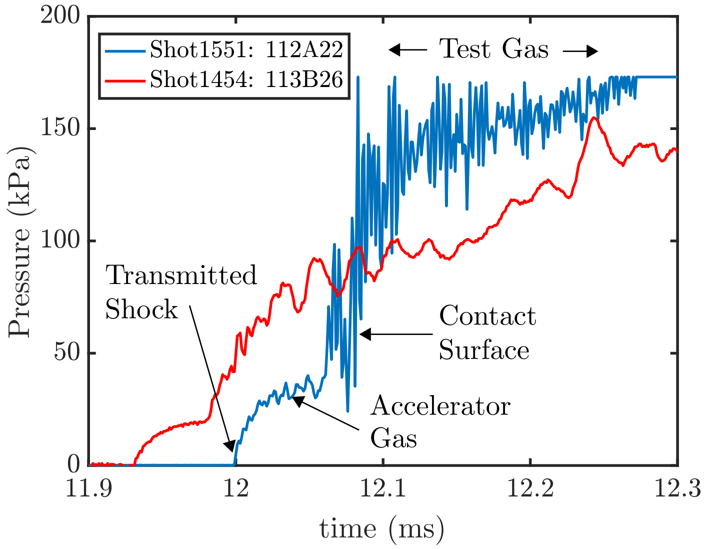

Figure 2.16: Comparison of HET pitot measurements for the MSL1 condition using two different transducer types. The time offset between pressure traces is arbitrary.

showed that the shock interference effects between the two gauges will not play a role in measuring the transmitted shock speed [46]. The uncertainty is found from the propagation of uncertainty of the caliper measurement uncertainty between probes and the difference of shock arrival time uncertainty of 2 μs. The results for the MSL1 and MSL3 condition are seen in Table 2.14. The MSL1 measurement agrees well with the measurement for the RC5 condition of [103] and is bounded by the perfect gas and equilibrium chemistry predictions. The MSL3 measurement is 21% slower than the equilibrium chemistry prediction.

Table 2.14: Transmitted shock speed measurements compared to theory predictions of perfect and equilibrium chemistry. Units are in m/s

	Experiment	Perfect	Equilibrium
RC5	3644 ± 41	3710	NA
MSL1	3643 ± 191	3795	3410
MSL3	4229 ± 260	5219	5126

2.5 Conclusions of the T5 and HET Characterization Efforts

T5 and HET are complementary impulse facilities with some overlap in operating envelopes and reach flight trajectories in important scaling parameters such as total enthalpy and the binary scaling parameter. The method for determining the freestream conditions in T5 is discussed and a sensitivity study propagating experimental uncertainties to sphere standoff distance and heat flux was completed. The experimental uncertainties in sphere standoff distance measurements was ±2.1% and stagnation point heat flux was ±5.4%. Experimental stagnation point heat flux and pitot measurements were made and compared to CFD and theoretical predictions. The heat flux predictions are within the uncertainty of the measurements for both the 100:1 and 900:1 geometric nozzle area ratio experiments. The pitot probe measurements agree with simulations performed by Dinesh Prabhu to within the uncertainty of the nozzle recoil. The experiments and analysis shown provides confidence in the prediction of the T5 freestream conditions.

The METS numerical tool was devleloped for analysis of the HET freestream conditions to test sensitivities to uncertainties in thermochemistry, initial presssures, diaphragm effects, and viscous effects. The NETS vibrational nonequilibrium expansion fan solver tested two models of vibrational relaxation for CO_2 and concluded that a reliable assumption for the carbon dioxide test gas is vibrational-translational equilibrium for the conditions in this work. The highest uncertainty in initial facility conditions is due to the accelerator section pressure uncertainty. The largest percentage freestream condition uncertainty was observed in the MSL2 freestream condition that showed at most an 8% change in pressure and 1.2% in change in temperature. The possibility of a reflected shock was examined and the calculations assuming the secondary diaphragm acts as a metal diaphragm with hinged pedals indicate a reflected shock would fully process the test gas. The resulting freestream conditions were calculated a reflected shock stagnates the test gas before accelerating through an unsteady expansion. In this case assuming equilibrium chemistry, the freestream temperature would increase by 35% and 36% for the MSL1 and MSL2 conditions, respectively, compared to ideal diaphragm calculations.

The Mirels theory for low pressure shock tubes was reviewed and predictions of shock attenuation and boundary layer thickness in the low pressure accelerator gas were calculated. Comparisons to experimental measurements of transmitted shock speed show that the attenuation is over predicted for the MSL1 condition with air as an accelerator gas. The decrease in shock speed relative to the predicted value for the MSL3 condition is most likely due to a combination of viscous effects and air contamination. Additionally, when helium was used as an accelerator gas, the stagnation point heat flux measurements resulted in a 25% difference to the comparison with the Sutton and Graves prediction based on inviscid perfect gas predictions of freestream conditions. Comparatively, The air accelerator gas conditions resulted in a 10% difference. This work was used to shift the priority of experiments to the MSL1 and MSL2 conditions where the freestream is better predicted when using air as an accelerator gas.

Chapter 3

NUMERICAL AND EXPERIMENTAL SETUP

This chapter describes the numerical and experimental setup for the diagnostics required for the analysis and results of chapters 4 to 6.

3.1 Numerical Setup

3.1.1 Reacting Flow Simulations: LAURA

The NASA Langley Aerothermodynamic Upwind Relaxation Algorithm (LAURA) is a high-fidelity, structured grid, CFD flow solver specialized for hypersonic reentry physics [1, 28]. LAURA employs a multidimensional Navier-Stokes solver capable of simulating two temperature reacting flows with vibrational and chemical nonequilibrium. The solver uses shock capturing methods such as Roe's averaging [93] and Yee's symmetric total variational diminishing formulation of second-order inviscid flux [123]. LAURA allows for grid adaptation to the shock as shown in a simulation in Figure 3.1.

The energy exchange between the translational-rotational and vibrational-electronic modes is modeled using a Landau-Teller formulation [122] with relaxation times specified for O_2 [75], CO [86], and CO_2[12]. The relaxation model for CO_2 assumes all of the vibrational modes relax at the same rate.

CO_2 Chemical Nonequilibrium Modeling

Mars entry CO_2 chemical kinetic models have been under development dating back to the mid-1960s McKenzie model [74]. In the early 1990s, Park [86] developed a two-temperature model that more accurately matched the slow vibrational relaxation and observed time to peak radiation by assuming the rate coefficients for dissociation are a function of the square root of T and T_V. Rock et al. compared these models to interferometric measurements of the bow shock in high enthalpy CO_2 flow, h_0 = 10 MJ/kg, and found good agreement with the Park model [92].

More recently, in 2014 Johnston and Brandis, developed a CO_2 chemical kinetic model with the dissociation reactions based on measurements in the Electric Arc Shock Tube (EAST) facility [54]. In the Johnston model, three dissociation reactions are functions of the geometric average temperature $\sqrt{TT_V}$ and the exchange reactions

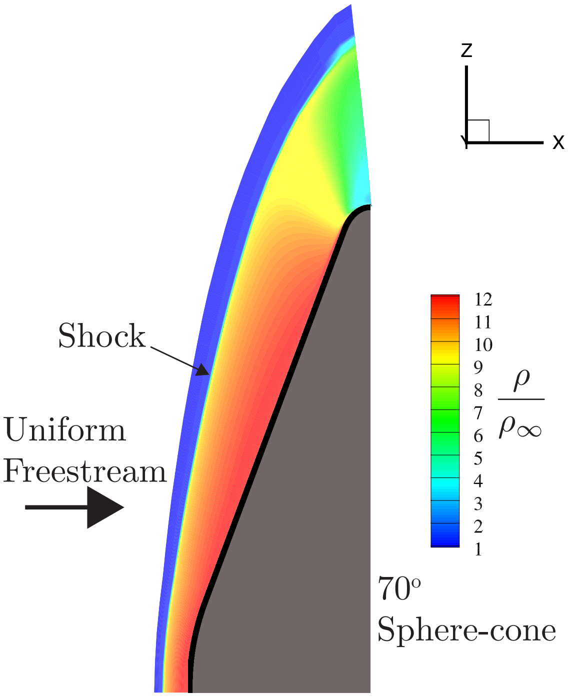

Figure 3.1: Density flow field from a LAURA simulation of CO_2 flow at MSL1 condition.

are functions of the translational temperature, T. In 2018, Cruden et al. presented an analysis of CO radiation and diode laser absorption measurements in a velocity range of 3-9 km/s and suggested two sets of kinetic rates, one for above and below 6.6 km/s [19]. The Cruden rates are fit using a single temperature. All of the experiments in this work are conducted with a freestream velocity of less than 4 km/s where ionization is negligible. The relevant neutral species are CO_2, CO, O_2, O, and C as identified by recent LENS-XX shock tunnel testing [41]. The corresponding five relevant reactions are

$$CO_2 + M \leftrightarrow CO + O + M \tag{3.1}$$

$$CO + M \leftrightarrow C + O + M \tag{3.2}$$

$$O_2 + M \leftrightarrow O + O + M \tag{3.3}$$

$$CO_2 + O \leftrightarrow O_2 + CO \tag{3.4}$$

$$CO + O \leftrightarrow O_2 + C \tag{3.5}$$

The Johnston rates are the default CO_2 kinetic rates implemented in the 2016 LAURA version used in this work. We also implement the rates specified in Cruden for below 6.6 km/s as well as the Fridman model rates that were developed in the the context of CO_2 decomposition in plasma [27]. The Fridman model is a 4 species (CO_2, O_2, CO, and O), 16 reaction mechanism. The forward dissociation reactions are controlled by T_V while the backwards dissociation reactions are dependent on T. Only the CO_2 + O -> CO + O_2 exchange reaction is a function of $\sqrt{TT_V}$. Cruden et al. compared these three models to CO_2 EAST radiation measurements noting that the key difference in the models is in the rate in which they equilibrate, with the equilibration rates ranked as Fridman > Johnston > Cruden [17]. Each kinetic model agreed with EAST measurements at select conditions, but no individual model provided a universal match to the experimental data.

3.1.2 HARA

The High-Temperature Aerothermodynamic RAdiation (HARA) model detailed in Johnston [55, 56] calculates the radiative properties for species in a known flow field and solves the radiative transport equation. Recall from Section 1.3.3, the solution to the radiative transport along a single ray of distance x in a slab of constant properties is given by

$$I_\lambda = I_{\lambda,0} e^{-\alpha_\lambda x} + \frac{\epsilon_\lambda}{\alpha_\lambda}\left(1 - e^{-\alpha_\lambda x}\right). \tag{3.6}$$

If the ray passes through N regions, the solution is given by

$$I_\lambda = \sum_{i=1}^{N} \frac{\epsilon_{\lambda,i}}{\alpha_{\lambda,i}} \exp\left(-\sum_{j=i+1}^{N} \alpha_j x_j\right)(1 - e^{-\alpha_{\lambda,i} x_i}) \tag{3.7}$$

where the body is the Nth region.

CO_2 Radiation Modeling

The radiative heating from carbon dioxide during entry is due to emission of rovibrational lines in the IR spectral ranges of 2.3, 2.7, 4.3, and 15 μm regions [97, 109]. The most extensive line list (630 million) for CO_2 presently available is the Carbon Dioxide Spectroscopic Databank (CDSD-4000) which was an extension of the CDSD-1000 model up to 5000 K [113, 114]. The database is implemented in HARA and used to calculate the spectral emission and absorption coefficients for radiative transfer calculations. To improve the efficiency of HARA, the CO_2 IR spectrum is tabulated for a range of temperatures and pressures reducing the number of spectral points to 500,000. A code-to-code comparison with the NASA Ames Non-EQuilibrium Air (NEQAIR) radiation code found agreement within 3% in spectral

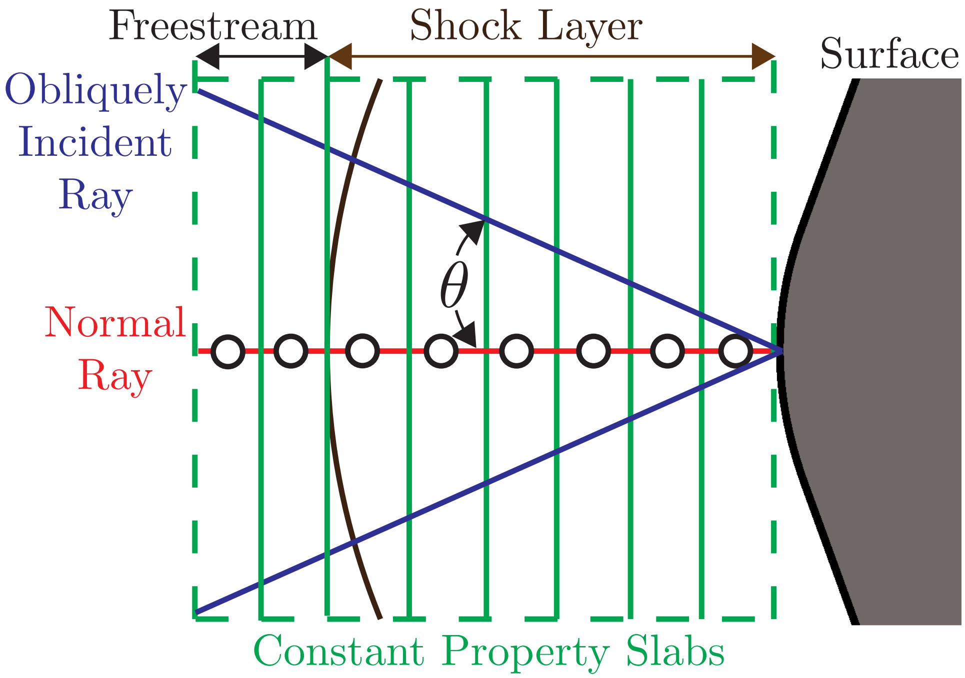

Figure 3.2: Schematic of the tangent slab approximation.

radiance when inputting the same CO_2 flow field [9]. For optically thin cases, the smeared band model [14] can be effectively used as opposed to a line-by-line approach. NEQAIR mid-wave infrared CO_2 radiation simulations have previously been validated using equilibrium shock tube and plasma torch experiments [84].

Tangent Slab Approximation

A common simplification to avoid having to compute radiative properties on multiple obliquely incident rays is to use the tangent slab approximation [57]. This approach calculates radiative properties in N regions only along the ray normal to the surface. These regions are extended tangentially to the surface into slabs of constant properties as shown in Figure 3.2. For an obliquely incident ray at angle θ from the normal, the properties in the slabs remain the same but the distance traveled through a given slab increases from $x_i(0)$ to $x_i(\theta) = x_i(0)/\cos\theta$.

In the optically thin limit, $\alpha_\lambda x \rightarrow 0$, the radiative transport equation simplifies to

$$I_{\lambda,\text{thin}}(0) = \sum_{i=1}^{N} \epsilon_{\lambda,i} x_i(0). \tag{3.8}$$

Using the tangent slab approximation, the radiative transfer equation for an obliquely incident ray can be written as

$$I_{\lambda,\text{thin}}(\theta) = \sum_{i=1}^{N} \frac{\epsilon_{\lambda,i} x_{i,0}}{\cos\theta} = \frac{1}{\cos\theta} \sum_{i=1}^{N} \epsilon_{\lambda,i} x_i(0). \tag{3.9}$$

Relating Equations 3.8 and 3.9, the radiance from an obliquely incident ray in the optically thin limit is related to the radiance from the normal ray by

$$I_{\lambda,\text{thin}}(\theta) = \frac{I_{\lambda,\text{thin}}(0)}{\cos(\theta)}. \tag{3.10}$$

In the optically thick limit, $\alpha_\lambda x \longrightarrow \infty$, the radiative transfer equation simplifies to

$$I_{\lambda,\text{thick}} = \frac{\epsilon_{\lambda,N}}{\alpha_{\lambda,N}} = B_{\lambda,N}. \tag{3.11}$$

Thus, the optically thick spectral radiance is independent of θ as expected from a Lambertian source such as a black body.

3.2 Experimental Setup

3.2.1 Facility Data Acquisition System

The T5 data is recorded using a National Instruments data acquisition system consisting of 6 PXIe-6368 data acquisition cards housed in a PXIe-1075 chassis, as well as 12 PXI-6115 data acquisition devises housed in a PXI-1045 chassis. Each PXIe-6368 card is connected to two BNC-2110 blocks capable of acquiring up to 16 analog input signals at a sample rate up to 2 MHz with a 16-bit resolution. Each PXI-6115 card is connected to one BNC-2110 card capable of acquiring 4 analog input signals at a rate up to 10 MHz with 12-bit resolution.

The PXI-6368 system collects signals from 8 dynamic PCB 199M114 pressure signals along the compression tube and shock tube, with the final 2 located next to the end wall as well as any diagnostic signals such as pitot probe, spectrometer camera, and schlieren image system timing. The PXI-6115 is used exclusively for heat flux measurements. Thermocouple signals are amplified by a custom built op-amp with a gain of 100 and 48 channels. Data is recorded on a Virtual Instrument (VI) set at a sample rate of 1 MHz, total recording time of 50 ms, 25 ms of pretrigger time, and voltage range between -5 and 5 V. The VI is triggered off the reservoir pressure signal.

The HET data is recorded using a National Instruments data acquisition system, consisting of two 14-bit PXI-6133 cards housed in a PCI-1031 chassis. Each card is connected to a BNC-2100 channel connector blocks capable of acquiring up to 8 analog input signals at a sample rate up to 3 MHz with 14-bit resolution. Data is recorded on a VI set at a sample rate of 1 MHz, and total recording time of 30 ms, 12 ms of pretrigger time, and voltage range between -5 and 5 V. The VI is triggered off a pitot probe or a PCB113B26 pressure transducer mounted along the tube. Thermocouple signals are amplified by a custom built op-amp amplifier with a gain of 1100 and 12 channels.

Both facility systems send out a TTL signal when triggered to a BNC Model 577-4C 4-Channel Digital Delay Generator. The delay generator is used to time the infrared camera exposure time and the schlieren imaging system.

3.2.2 Model Geometries

Two axisymmetric blunt body geometries are employed as test articles in this work; the sphere and the spherically-blunted cone (also referred to as a sphere-cone). All US missions to Mars to date have used sphere-cone heat shield geometries as reviewed by Prabhu and Sanders [90]. Additionally, spheres were used to measure stagnation point heat flux and bow shock standoff distance to enable comparisons with theoretical predictions. The sphere model diameter is 25.4 mm. The dimensions defining a sphere-cone are shown in Figure 3.3. The geometry in this work matches the scaled dimensions of the MSL heat shield model. For the MSL geometry, $\theta = 70°$, $\theta_{\mathrm{aft}} = 40°$ sphere-cone, $R_N/R = 0.500$, and $R_S/R = 0.056$ where R_N, R, and R_S is the nose, base, and shoulder radius, respectively. The MSL heat shield had a base radius of $R = 2.25$ m and the two scaled models used in this work have a base radius of $R = 0.0254$ m and $R = 0.0889$ m. The smaller model is tested in the HET while both models are tested in T5. Both models are designed to have the capability of testing at varying angles of attack. This work tests the model at 0° and 16° angle of attack.

3.2.3 Schlieren Flow Visualization

To visualize the flow field and measure the shock standoff distance, a Z-type schlieren setup is used. Schematics of both setups can be found in the thesis of Knisely [58]. The bow shock visualization and shock standoff distance measurements are made using schlieren in two camera configurations; high speed videos are obtained to quantify the shock steadiness during the test time and high resolution single images are used to measure the shock shape. The light source for the T5 experiments is a pulsed diode light source developed by Parziale et al. consisting of a Sony laser

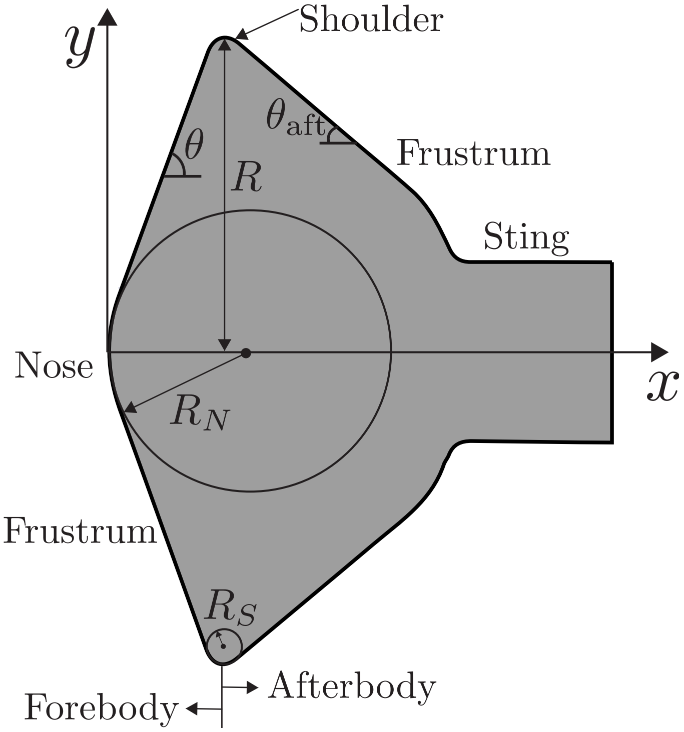

Figure 3.3: Spherically-blunted cone geometry.

diode paired with a PicoLAS driver emitting light at 670 nm [87]. A bandpass filter and an iris placed near the focal point of the system eliminate most of the self-luminosity of the flow. A graded filter schlieren cutoff as shown in Figure 3.4 is used to avoid diffraction of the laser light [101]. For the HET experiments, the light source is a Xenon 437B nanopulser with a knife edge for a cutoff. High speed videos are obtained using a Shimadzu Hyper Vision HPV-X2 (256 frames with 10-bit depth and 400x250 pixel resolution on a 12.7 mm wide sensor 240x400 pixels) camera at a frame rate between 25,000 to 100,000 frames per second. High resolution (1600x2400 pixels) single-shot schlieren images are obtained using a pco.1600 camera exposed between 0.5 to 2 µs. A focusing lens with a focal length between 300 and 500 mm, depending on magnification required is used to focus the image on the camera.

3.2.4 Spectrally Resolved Mid-wave Infrared Radiation

Spectrally resolved mid-wave infrared radiation is measured at a point on the surface of the test article using the set up shown in Figure 3.5. Radiation is collected through an infrared fiber optic cable behind a 2.5 mm diameter, 0.5 mm thick sapphire window (Edmond #43-627). The fiber is brought out of the test section

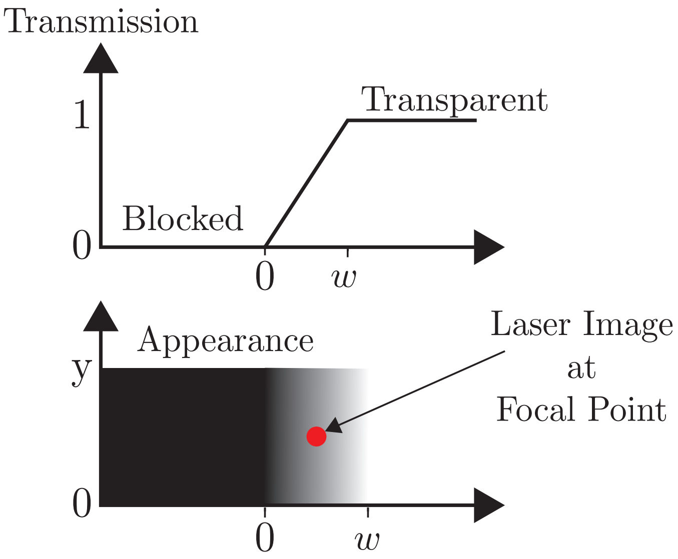

Figure 3.4: The top plot is the transmission function of a graded filter schlieren cutoff and the bottom part is the appearance.

using a Roxtec CRST25 circular cable seal sliding into a PVC vacuum flange. The output end of the fiber is positioned at the slits of a PI-Acton SP2500 spectrometer using a Princeton Instruments Model FC-446-021-U adjustable fiber coupler. The spectrometer is equipped with a 17 g/mm grating blazed at 4.3 µm. Dispersed light is imaged by an IRC800 camera equipped with a 10 mm x 12.8 mm liquid-N_2 cooled InSb array with 640 x 512 pixel resolution. The camera and spectrometer are borrowed from NASA Ames Research Center, where they were previously used to measure mid-wave infrared radiation in the Electric Arc Shock Tube [17].

By using a diagnostic where a fiber optic is embedded behind a window on the surface of the model, surface point measurements are simulated using the same ray tracing techniques used when calculating radiative heating on entry vehicles. Also, since no optics have to be aligned, the setup can be transferred between facilities with ease.

The locations of the fiber ports on the model geometries are defined by (x/R, y/R) where the coordinate system is shown on Figure 3.3. The forebody fiber locations on the HET and T5 models are at the nose (0,0) and the 16° angle of attack stagnation point (0.125,0.433). The afterbody fiber port location on the T5 model is located at (0.557, 0.861).

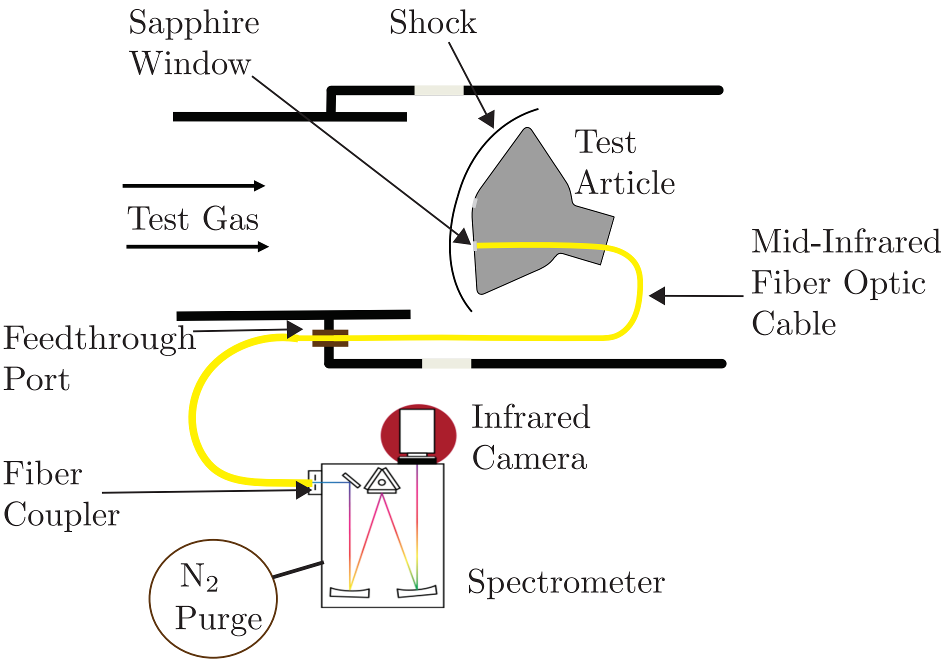

Figure 3.5: Test set up.

Fiber Optic Cables

Chalcogenide glass fibers (Art Photonics model No. CIR-500/550) are chosen for forebody measurements based on their large (500 µm) diameter core size and good transmission properties between 1.1 - 6.5 µm. Indium fluoride glass fibers (Leverre Fluore No. IFG MM (0.20) 200/260) are chosen for the afterbody measurements in T5 due to their less brittle properties, allowing the fiber to be turned inside the model and oriented towards the wake. The chalcogenide and indium fluoride cables have nominal numerical aperture (NA) specifications of 0.30 and 0.20, respectively. The numerical aperture can be related to the acceptance half angle or critical angle of the fiber θ_c given by NA = n sinθ_c. When an obliquely incident ray at an angle from the normal θ is greater than the critical angle θ_c, total internal reflection occurs and the light does not enter the fiber. Assuming n≈1, the nominal half angles of the fibers are 17.5° and 11.5° for chalcogenide and indium fluoride, respectively.

3.2.5 Spectroscopic Calibration Techniques

The calibration methods follow techniques outlined by Cruden in order to obtain absolute spectrally resolved radiation measurements [16].

Wavelength Calibration

Argon emission lines are used to calibrate the setup in wavelength space. To image the wavelengths of interest (3800 to 5300 nm), the spectrometer is centered at 5000 nm and a spectrum is obtained with a mercury-argon (HgAr) lamp (Oriel Instruments model 6035) mounted at the spectrometer slits. The grating spectrometer allows for higher order lines to be identified as shown in Figure 3.6. The four main peaks identified are the following 4th order Argon lines in nm: 811.53, 912.30, 922.45, and 925.78 as seen in Figure 3.6. By fitting a linear line through these four points, the pixels on the detector can be converted to wavelength. This fit matches the peaks of the identified lines within ± 0.8 nm.

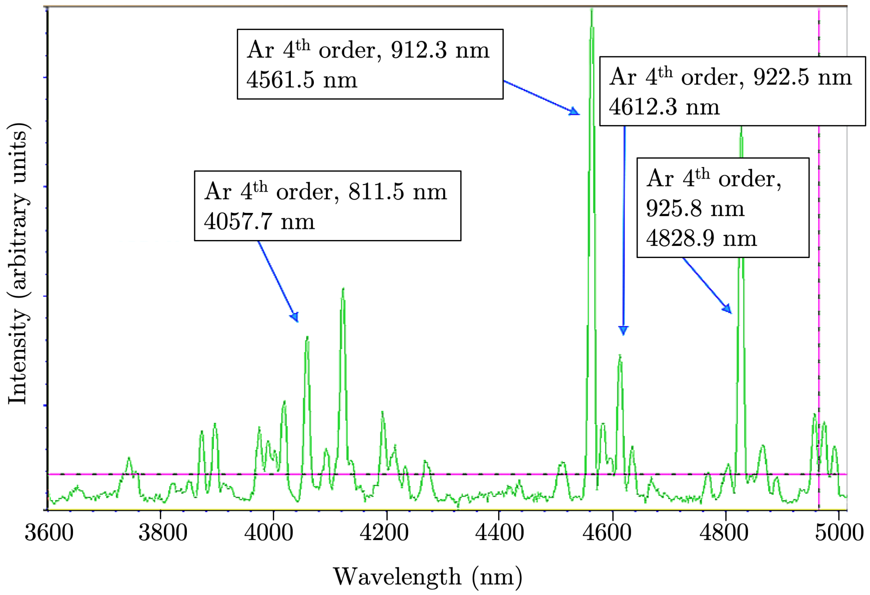

Figure 3.6: Wavelength calibration identifying higher order Argon lines with a HgAr lamp.

Instrument Line Shape Function

Spectral lines can be broadened by local effects such as thermal and collisional processes as well as experimental effects due to the resolution of the instrument. The local effects are simulated while the experimental broadening is measured by an instrument line shape (ILS) function. The ILS for the IR camera is determined by fitting a Gaussian function to emission lines from a HgAr lamp. The Guassian function is given by

$$G(\lambda_G, \Delta_x) = \sqrt{\frac{\ln 2}{\lambda_G^2 \pi}} e^{-\ln 2\left(\frac{\Delta x}{\lambda_G}\right)^2} \tag{3.12}$$

where Δx is the distance from the line center and λ_G is the half width at half max (HWHM). For a spectrometer slit width of 100 µm, the guassian fit to the zeroth-order line results in a HWHM of $\lambda_G = 6.0$ nm as shown in Figure 3.7 with the Guassian function normalized to the max intensity of the emission line. The average of multiple 4th order lines results in a HWHM of $\lambda_G = 6.4$ nm.

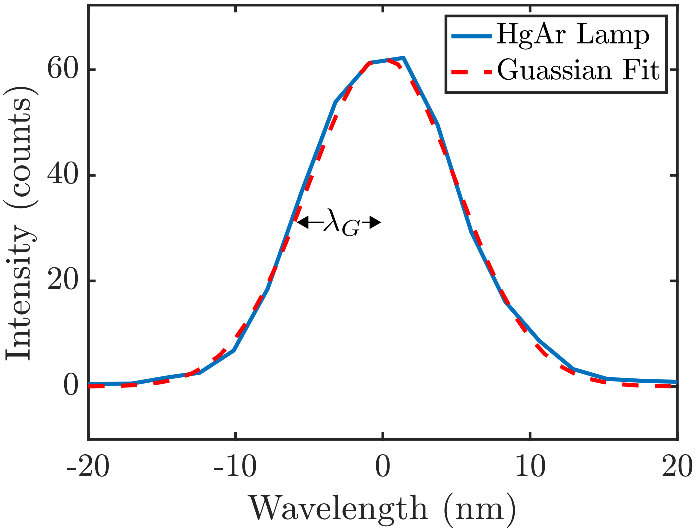

Figure 3.7: Zeroth order HgAr line compared with a Gaussian profile fit.

Instrument line shapes are also measured for slit widths of 200 µm and 20 µm. When the slit width is 20 µm, the zeroth order line is described by a Guassian function with a HWHM as $\lambda_G = 6.0$ nm, the same ILS function as the 100 µm slit confirming the slit is uniformly illuminated during measurement. When the slit width is 200 µm, the ILS changes and a flat top is observed in the instrument line shape. The ILS function is no longer a Guassian but a Smeared Guassian described by a convolution of a Guassian function and a Square function. The spectrometer slit width for all experimental spectral measurements presented in this work are obtained with a slit width of 100 µm with the exception of the three shock tube measurements presented in Section 5.4.1 that are obtained with a slit width of 20 µm. All simulations are convolved with the ILS function for direct comparison to experimental spectra. The convolution broadens the individual spectral lines. The area under the curve of the simulation before and after the convolution of the ILS function is checked to remain the same to satisfy conservation of energy. The ILS function assumed for this work is a Guassian function with a HWHM of λ_G = 6.4 nm.

Absolute Radiance Calibration

The absolute radiance calibration is performed using a constant temperature blackbody source and converting the number of counts collected on the camera to the known spectral radiance using Planck's law. The blackbody source (BBS1200) has a 1" opening and is heated to 1200.0° ± 0.2° C. To get an accurate calibration, the acceptance cone of the fiber should be probing the back of the cavity where there is a uniform radiance at a known temperature.

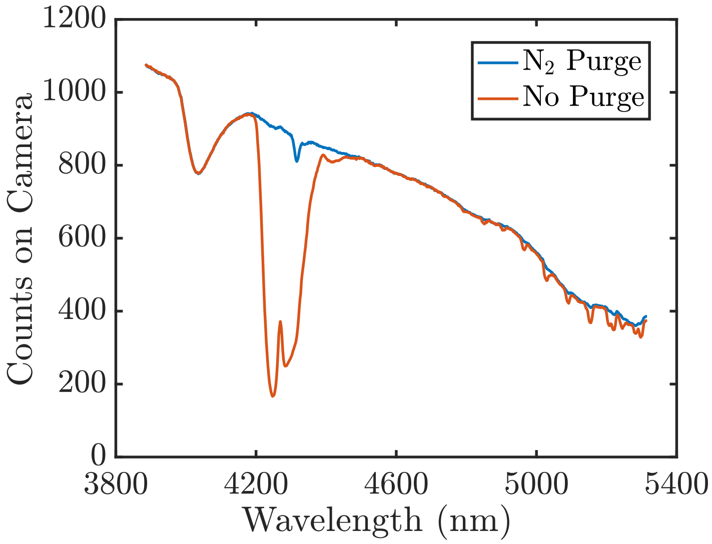

Figure 3.8: Blackbody calibration spectra with and without the spectrometer purged with N_2.

The resulting blackbody calibration spectra imaged on the IRC800 camera (640 x 512 pixel resolution) is processed through the ThermoScientific WinSpec software, Figure 3.9. The y-axis provides spatial information from the fiber location at the slits and the x-axis provides wavelength information. The white light is the intensity of the spectra. The spatial pixels along the y-axis of the detector where intensity is approximately constant is averaged and extracted for each x-axis pixel location from the WinSpec software. Seven to ten pixels are averaged when using the 500 µm core chalcogenide fiber and three pixels are averaged when using the smaller 200 µm core indium fluoride fiber. The experimental data extracted from the WinSpec software is averaged over the same spatial pixels on the camera as the calibration spectra.

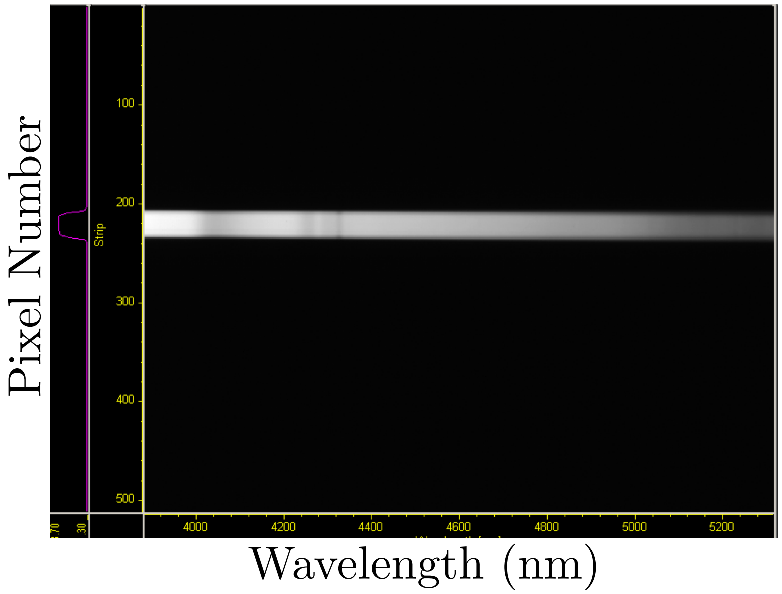

Figure 3.9: Blackbody calibration spectra imaged on the IRC800 camera.

Two methods of calibration are used. Each method uses rails and translation stages for alignment and optimized to gather the maximum number of counts. When the fiber is mounted in the model behind a window, the model can be moved to the face of the blackbody source where the fiber directly probes the back of the black body. Care is taken to quickly remove the blackbody source to prevent heating of the fiber. When the fiber is at the forebody frustum location, the model is placed on a 4° wedge to ensure the acceptance cone of the fiber is parallel with the blackbody opening. The aperture wheel plate on the BBS1200 front is removed to move the model closer to the blackbody opening.

The second method uses a 1" diameter germanium meniscus lens with a focal length of 25 mm to focus the fiber optic into the back of the blackbody source. The first method is used to avoid uncertainty due to improper alignment and the second method can be used when the fiber is not protected by the model such as the case with the freestream probe. When using the lens technique, the absorption due to carbon dioxide in the room can be observed in the spectrum. To remove this absorption from the calibration, the points at the wavelengths where the room CO_2 absorption occurred are removed and replaced by linear interpolation between the next available points.

During the experiments, a 3300 nm long pass filter is placed at the slits of the spectrometer to eliminate any lower order radiation that could appear in the test data. The introduction of the long pass filter into the system that is not used during wavelength calibration causes an additional linear shift in wavelength between 0 and 25 nm. This shift is accounted for by taking a blackbody spectra with and without the nitrogen purge. The nitrogen purged data are then divided by the purged data to obtain a plot of the CO_2 transmittance as shown in Figure 3.10. The normalized data is compared to a room temperature simulation using the Carbon Dioxide Spectroscopic Databank [113] to find the correct shift as shown in Figure 3.8. In this case, the shift is 13 nm. Good agreement between the linear shifted absorption spectra and the CDSD simulation confirms estimating the response of the filter as linear is a reasonable assumption.

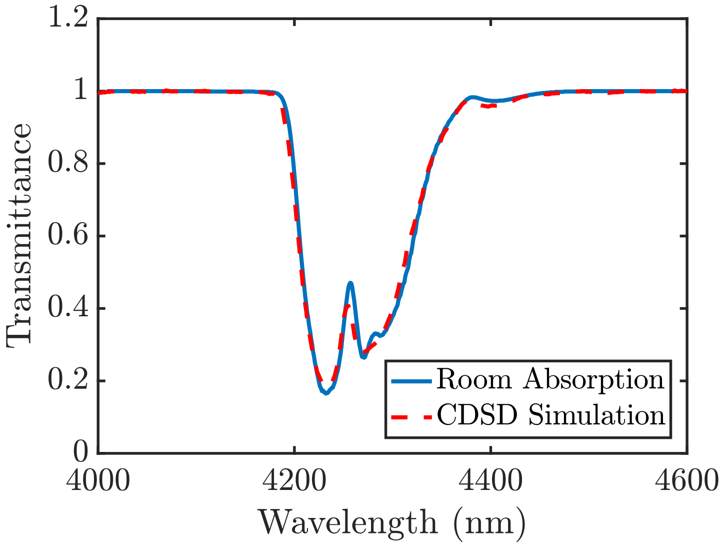

Figure 3.10: CO_2 room absorption compared to a CDSD simulation.

Calibration Transfer Function

The spectral radiative heat flux is given by the total spectral radiance collected through the fiber optic cable

$$q_\lambda = \int_0^{2\pi} \int_0^{\theta_c} I_\lambda(\theta, \phi) \sin\theta \cos\theta d\theta \tag{3.13}$$

where θ_c is the acceptance angle of the fiber. During calibration, the radiance source is a Lambertian blackbody source, $I_\lambda = B_{\lambda,\text{cal}}$ and thus independent of angle

$$q_{\lambda,\text{cal}} = 2\pi B_{\lambda,\text{cal}} \int_0^{\theta_c} \sin\theta\cos\theta d\theta = 2\pi B_{\lambda,\text{cal}} \sin^2\theta_c. \tag{3.14}$$

The number of counts detected on the camera N_λ can be related to the total heat flux through the sensitivity of the system S_λ given by

$$S_\lambda = \frac{N_\lambda}{q_\lambda} \tag{3.15}$$

The experiment and the calibration can be related through the sensitivities which are equal for a given setup by

$$\int_0^{2\pi} \int_0^{\theta_c} I_{\lambda,\text{exp}}(\theta, \phi)\sin\theta\cos\theta d\theta = \frac{N_{\lambda,\text{exp}}}{N_{\lambda,\text{cal}}} 2\pi B_{\lambda,\text{cal}} sin^2\theta_c \tag{3.16}$$

Validity of the Tangent Slab Approximation in the Shock Layer

Recall in the tangent slab approximation optically thick limit, the radiance is independent of angle (Equation 3.11). In this case Equation 3.16 simplifies to

$$I_{\lambda,\text{exp}} = \frac{N_{\lambda,\text{exp}}}{N_{\lambda,\text{cal}}} B_{\lambda,\text{cal}}, \tag{3.17}$$

and the calibration may be transferred directly.

In the tangent slab approximation optically thin limit, the radiance given by an obliquely incident ray is related to the normal ray by $I_\lambda(\theta) = I_\lambda(0)/\cos\theta$ (Equation 3.10). In this case Equation 3.16 simplifies to

$$I_{\lambda,\text{exp}}(0) \int_0^{\theta_c} \sin\theta = \frac{N_{\lambda,\text{exp}}}{N_{\lambda,\text{cal}}} B_{\lambda,\text{cal}} \sin^2\theta_c, \tag{3.18}$$

evaluating the integral, we arrive at

$$I_{\lambda,\text{exp}}(0) = \frac{N_{\lambda,\text{exp}}}{N_{\lambda,\text{cal}}} B_{\lambda,\text{cal}} \frac{\sin^2\theta_c}{2(1-\cos\theta_c)}. \tag{3.19}$$

The chalcogenide optical fiber used for the forebody experiments has an acceptance half angle $\theta_c = 17.5°$. Evaluating at the critical angle

$$I_{\lambda,\text{exp}}(0) = 0.977 \frac{N_{\lambda,\text{exp}}}{N_{\lambda,\text{cal}}} B_{\lambda,\text{cal}}, \tag{3.20}$$

in this case the radiance calibration is modified and the experimental radiance is reduced by 2.3% if the tangent slab approximation is applied to the shock layer. In this work, this modification is assumed negligible.

Chapter 4

BOW SHOCK STANDOFF DISTANCE AND STAGNATION STREAMLINE ANALYSIS

4.1 Introduction

Bow shock standoff distance for high-stagnation enthalpy, hypersonic CO_2 flows over sphere and spherically-blunted cone geometries is examined through experiments in two facilities capable of simulating Mars planetary entry conditions. Experiments using both high-speed and high-resolution schlieren imaging are conducted in the T5 Reflected Shock Tunnel and the Hypervelocity Expansion Tube to examine facility independence of the measurements.

The validation of a recently-developed unified model for sphere and sphere-cone behavior [48] is first extended to flows with both thermal and chemical nonequilibrium in CO_2 using the average shock layer density obtained from LAURA simulations. Experimental shock standoff distance measurements in both facilities are then compared to the theoretical model and found to be in good agreement. The need to account for the divergence of the streamlines in conical nozzles is highlighted and an existing model is extended to account for changes in shock curvature between parallel and conical flow. The contributions of vibrational and chemical nonequilibrium to the stagnation streamline density profile are quantified using the simulation results and three thermochemical models are compared.

4.1.1 Freestream Conditions

Seven test conditions are chosen to span the binary scaling and total enthalpy map of the anomalous LENS I Run 8 test as shown in Figure 4.1. For comparison with flight, portions of the lifting entry 2012 Mars Science Laboratory (MSL) [23] and ballistic entry 2019 ExoMars mission [10] are also indicated. The reservoir and freestream conditions for the 900:1 nozzle area ratio condition, T52892, closely match the LENS I Run 8 condition. The reservoir conditions for T52892 and LENS I are given in Table 4.1.

The HET freestream is predicted from one-dimensional gas dynamic calculations assuming equilibrium thermochemistry with an air accelerator gas. The assumption of equilibrium thermochemistry is justified in Section 2.3.2. The method of obtain-

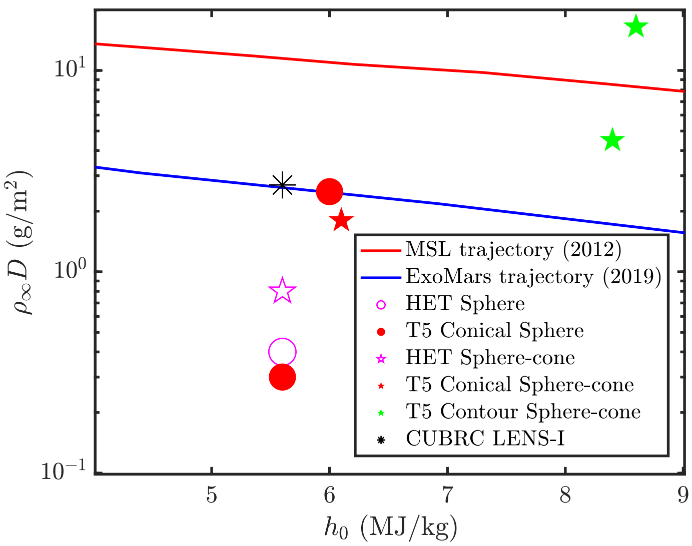

Figure 4.1: Freestream binary scaling parameter and stagnation enthalpy for test conditions analyzed in the present study together with values for portions of the ExoMars and MSL trajectories.

ing the T5 freestream is described in Section 2.2. The freestream values reported for T5 are extracted from the simulation centerline data at the nozzle exit plane. The standoff distance reported for any conical nozzle tests is corrected using the conical nozzle correction factor given in Section 4.2. The predicted freestream conditions for the three sphere tests analyzed in this study are presented in Table 4.2.

Table 4.1: Reservoir conditions for T52892 and CUBRC LENS I Run 8 [65].

Shot #	**T52892**	**LENS I Run 8**
ρ (kg/m^3)	42.7	38.3
T (K)	3623	3499
P (MPa)	33.3	29.5
h_0 (MJ/kg)	6.05	5.63
Y_{CO_2}	0.736	0.780
Y_{CO}	0.168	0.146
Y_{O_2}	0.091	0.080
Y_O	0.005	0.037

The predicted freestream conditions for the five sphere-cone tests analyzed in this study are shown in Table 4.3.

Table 4.2: Sphere freestream conditions.

Facility	**HET**	**T5**	**T5**
Shot #	1455	2886	2889
D (in.)	1.0	1.0	1.0
Nozzle	No Nozzle	Conical	Conical
Area Ratio	—	100:1	900:1
$\rho_\infty D$ (g/m^2)	0.4	2.5	0.3
u (m/s)	3080	2676	2840
T (K)	1095	1417	837
T_V (K)	1095	1418	869
P (kPa)	3.1	27.5	1.7
ρ (g/m^3)	15.1	96.6	10.0
h_0 (MJ/kg)	5.6	6.0	5.6
Ma	6.2	4.2	5.8
$\mathrm{Y}_{\mathrm{CO}_2}$	1.0	0.869	0.845
Y_{CO}	0.0	0.083	0.098
$\mathrm{Y}_{\mathrm{O}_2}$	0.0	0.048	0.056
Y_{O}	0.0	8.2E-5	1.1E-6

4.1.2 Simulations

The flow fields around sphere and sphere-cone geometries are simulated using the NASA Langley LAURA code described in Section 3.1.1. Navier-Stokes simulations are carried out for comparison with experimental results. The standoff distance, uncertainty, and average density ratio are extracted from simulations as follows, using the parameters shown in Figure 4.2. The shock standoff distance is taken to be the distance from the body to the center of the numerical shock region, x_s. x_s is defined by the length for conservation equations to be satisfied, indicated by the deviation from constant stagnation enthalpy h_0, to within ±0.05 MJ/kg.

As discussed in Section 1.3.1, theoretical predictions for shock standoff distance assume a constant velocity through the boundary of the control volume (u_b = constant), which is reasonable for an inviscid shock layer. In viscous flow, there are large gradients near the wall which can be accommodated by consideration of the displacement thickness. At the Reynolds numbers of the conditions in this study, however, the displacement thickness is calculated to be an order of magnitude less than the numerical resolution. Viscous and inviscid simulations are carried out to

Table 4.3: Freestream conditions for the sphere-cone tests analyzed.

Facility	**HET**	**T5**	**T5**	**T5**	**LENS I**
Shot #	MSL1-1467	2866	2902	2892	Run 8
MSL D (in.)	2.0	2.0	7.0	7.0	12.0
Nozzle	No Nozzle	Contour	Contour	Conical	D-nozzle
Area Ratio	—	100:1	100:1	900:1	1000:1
$\rho_\infty D$ (g/m^2)	0.8	4.5	16.5	1.8	2.7
u (m/s)	3080	3123	3160	2937	2871
T (K)	1095	1751	1793	855	892
T_V (K)	1095	1752	1793	887	896
P (kPa)	3.1	33.3	35.9	1.5	1.6
ρ (g/m^3)	15.1	88.3	92.7	8.8	9.0
h_0 (MJ/kg)	5.6	8.4	8.6	6.1	5.6
Ma	6.2	4.3	4.3	5.9	5.7
$\mathrm{Y}_{\mathrm{CO}_2}$	1.000	0.728	0.719	0.828	0.863
Y_{CO}	0.000	0.173	0.179	0.110	0.087
$\mathrm{Y}_{\mathrm{O}_2}$	0.000	0.097	0.100	0.062	0.050
Y_{O}	0.000	0.002	0.002	2.0E-5	0.0E-5

confirm that the standoff distance is the same to within the numerical accuracy.

For comparisons with theoretical predictions, the average density along the stagnation streamline $\bar{\rho}$, normalized by the freestream density ρ_∞, is calculated by integrating the density from the end of the numerical shock region $x = x_s/2$ to the edge of the thermal boundary layer, and assuming an inviscid density profile $\rho = \rho_\delta$ near the wall

$$\frac{\bar{\rho}}{\rho_\infty} = \left(1 - \frac{\delta}{\Delta}\right)\frac{\bar{\rho}_{\text{invis}}}{\rho_\infty} + \frac{\rho_\delta}{\rho_\infty}\frac{\delta}{\Delta} \tag{4.1}$$

where $\bar{\rho}_{\text{invis}}$ is the average density in the inviscid region, discussed in more detail in Section 4.5. Note, the numerical shock thickness is negligible in the normalization. The density profile is strongly modified in the thermal boundary layer δ near the wall, Figure 4.2, so the assumption of constant density will result in an underprediction of the boundary layer contribution to the average density. However, as discussed above, the boundary layer contribution is small for the conditions considered in this work.

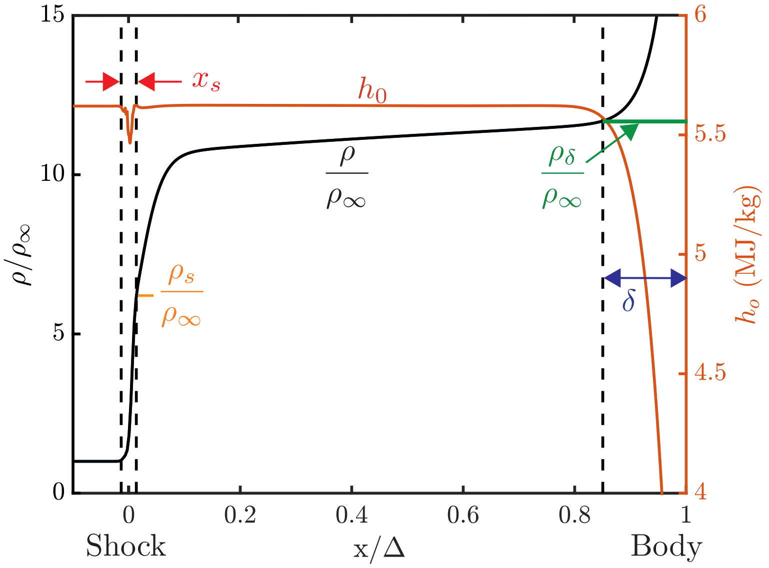

Figure 4.2: Stagnation streamline density ρ/ρ_∞ and total enthalpy h_0 profiles for reacting, viscous, hypervelocity flow over a sphere illustrating nomenclature described in the text.

4.1.3 Grid Sensitivity Study

Axisymmetric grids around sphere and sphere-cone geometries are generated and the flow field around the geometries are simulated. The final number of grid cells used in the wall normal and symmetry plane, Figure 4.3, are chosen based on the results of a grid sensitivity study, Table 4.4. This study simulates the flow field around a 25.4 mm diameter hemisphere using a constant HET perfect gas freestream inflow shown in Table 2.9.

Six cases are considered that vary the number of wall normal cells between 128 to 512 and the number of symmetry plane cells between 32 and 128. The variation in the calculated average density is $\bar{\rho}/\rho_\infty = 11.27 \pm 0.07$ or 0.6%. The extracted standoff distance for all cases agrees to within the uncertainty of the numerical shock thickness. Doubling the number of wall normal grid cells, roughly halves the numerical shock thickness. The numerical shock thickness x_s is further decreased by clustering the grid near the shock. The grid clustering is performed using a grid stretching function described in the LAURA user's manual [1]. The resulting numerical shock region thickness is 2.6% of the total standoff distance.

The final sphere grids have 64 cells in the symmetry plane and 256 cells in the wall normal direction. The final sphere-cone grids have 32 cells in the symmetry plane and 197 cells in the wall normal direction. The 197 wall normal cells doubled (from 97 cells) the number of cells from a grid provided from the NASA Langley Aerothermodynamic group [39]. For comparisons to theoretical prediction curves, the simulation grids did not have shock clustering. For comparisons to experiments, the simulation grids used shock clustering at the maximum recommended constant in the grid stretching function of 4.25 [1]. Decreasing the numerical shock region is most important for the stagnation streamline analysis in Section 4.5 that is only valid outside this region.

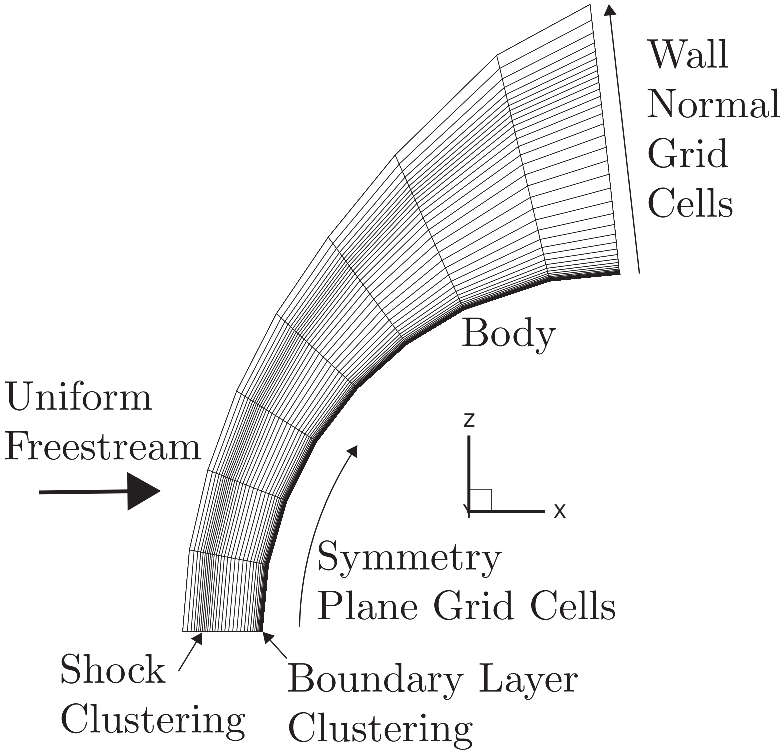

Figure 4.3: Axisymmetric sphere grid generated with 64 grid cells in the wall normal direction and 8 grid cells in the symmetry plane.

4.1.4 Standoff Distance Measurements

Experimental measurements of bow shock standoff distance are extracted from each schlieren image. The experimental standoff distance is defined as the location of the peak intensity in the images, corresponding to the maximum density gradient measured by the schlieren technique [59]. The body location is defined by the maximum gradient in intensity near the body.

The uncertainty reported for measurements obtained from high resolution images is the propagation of error of 1 pixel uncertainty at the body and at the shock,

Table 4.4: Results of number of grid cell sensitivity study. The inflow is the HET MSL1 perfect gas freestream condition and the geometry used is a 25.4 mm diameter hemisphere.

Case	**1**	**2**	**3**	**4**	**5**	**6**
Wall Normal Cells	256	256	256	128	256	512
Symmetry Plane Cells	32	64	64	128	128	128
Shock Clustering	No	No	Yes	No	No	No
Standoff Distance (mm)	0.933	0.932	0.929	0.937	0.927	0.918
Uncertainty (mm)	±0.022	±0.027	±0.012	±0.080	±0.041	±0.020
$\bar{\rho}/\rho_\infty$	11.21	11.24	11.21	11.34	11.28	11.26

and when applying the correction factor, the uncertainty in determining the shock curvature. The resulting uncertainty is greater than the shot-to-shot variation for two repeat experiments at the expansion tube freestream condition and four repeats at the T52892 condition.

Bow Shock Unsteadiness

Standoff distance measurements for three T5 experiments as a function of test time (0.8 ms to 1.8 ms after primary shock arrival at the reservoir) are shown in Figure 4.4. T52886 data are acquired at 100 kHz, and the corresponding standoff distance in test time is 9.03 ± 0.36 pixels (1.24 ± 0.05 mm). T52889 data are acquired at 25 kHz and the corresponding standoff distance in test time is 7.88 ± 0.33 pixels (1.10 ± 0.05 mm). T52866 data are acquired at 25 kHz and the corresponding standoff distance in test time is 7.56 ± 0.61 pixels (1.89 ± 0.15 mm). The standard deviations measured are taken to be the uncertainties in standoff distance for these shots.

Spheres and scaled Mars Science Laboratory (MSL) 70° sphere-cone geometries are tested in the experiments with the geometry further described in Section 3.2.2. The two sphere-cone models tested in this study are scaled with base diameters of 50.4 mm and 177.8 mm. The sphere model diameter is 25.4 mm.

4.2 Conical Nozzle Correction

Flow divergence at the nozzle exit plane caused by the acceleration process of a large-area conical nozzle geometry will result in observable differences in flow behavior when compared to parallel flow. Recently, Hornung [45] applied conservation of mass to diverging hypervelocity blunt body flow over a blunt body as shown in

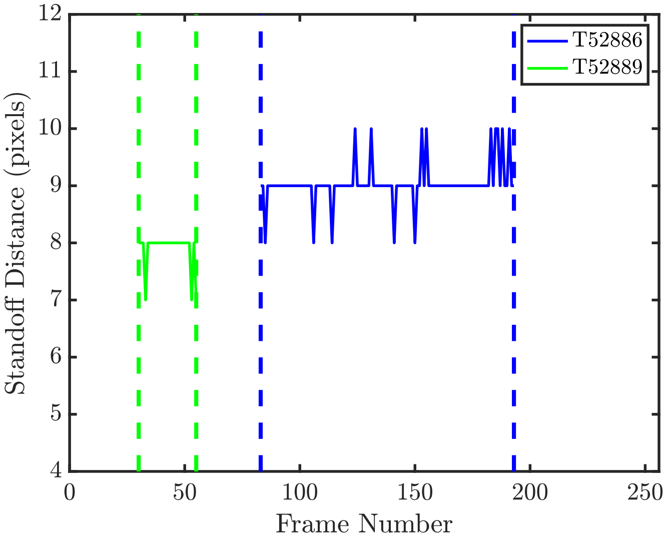

(a) Sphere videos.

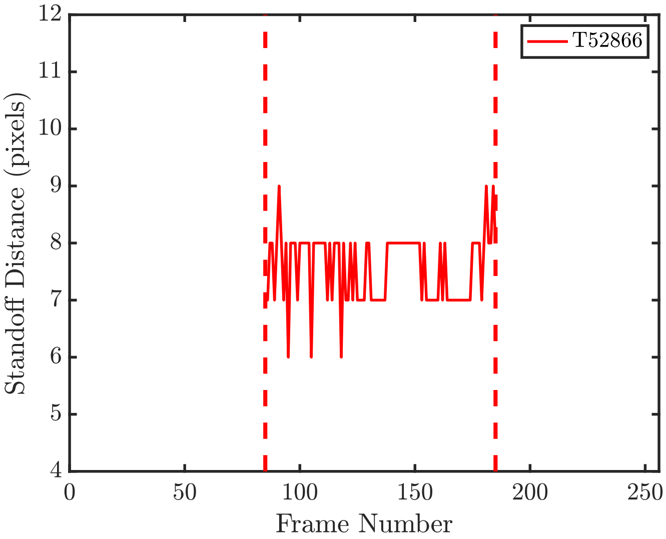

(b) Sphere-cone videos.

Figure 4.4: Shock standoff distance in terms of number of pixels extracted for each frame from high speed videos. The frames shown represent test time of each test.

Figure 4.5. The same analysis was applied to parallel flow except the mass flux out of the control volume is a function of $u_\infty \cos(\phi - \delta)$ instead of $u_\infty \cos(\phi)$ where δ is the angle the streamlines diverge.

Hornung derived that the standoff distance Δ_c in conical flow is modified by a

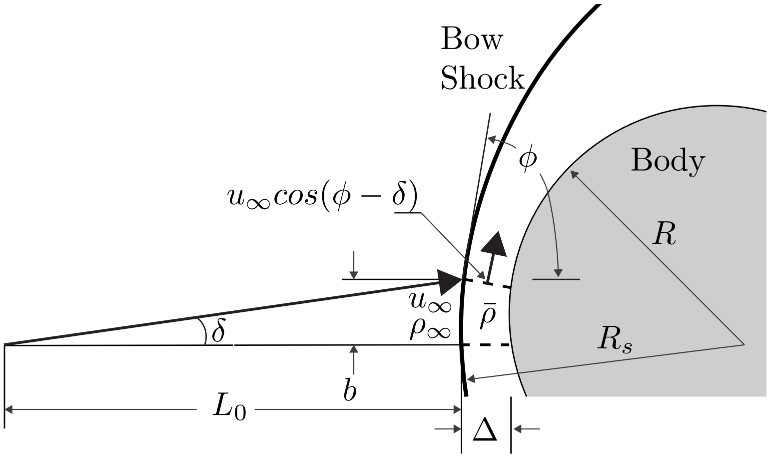

Figure 4.5: Control volume analysis of conical hypervelocity flow over a blunt body. Adapted from Hornung [45].

correction factor

$$\frac{\Delta_c}{R_s} = \frac{1}{2}\frac{\rho_\infty}{\bar{\rho}}\frac{1}{1+\frac{R_s}{L_0}} \tag{4.2}$$

where Δ_c is the standoff distance in conical flow, L_0 is the distance from virtual flow origin to the shock, and R_s is the radius of curvature of the shock. The divergence of the conical incoming flow reduces the shock standoff distance by a factor that approaches unity as L_0 approaches infinity.

R_s is found by fitting a circle radius to the experimental or numerical shock shape as suggested in Hornung [45]. Hornung validated this correction factor using a series of Euler simulations [91] for flow over a sphere where the radius of curvature of the shock in parallel and conical flow are equal, $R_{s_p} = R_{s_c} = R_s$. However for geometries such as sphere-cones, the shock curvature is not constant between parallel and conical flow as shown in Figure 4.6. Accounting for the change in curvature, the standoff distance correction factor from conical to parallel flow for sphere-cone shocks can be expressed as

$$\frac{\Delta_p}{\Delta_c} = \frac{R_{s_p}}{R_{s_c}}\left(1+\frac{R_{s_c}}{L_0}\right). \tag{4.3}$$

Using a series of Euler simulations [46] in Amrita [91], this model is validated for sphere-cones using perfect gas flows of non-dimensional diameters 10, 15, and 20 with a 15° half-angle conical nozzle, $L_0 = 1.3$ m, $\gamma = 1.4$, and freestream Mach number of $M_\infty = 8.9$. The results of the Euler simulations are shown in red circles and compared to the theoretical prediction, Figure 4.7.

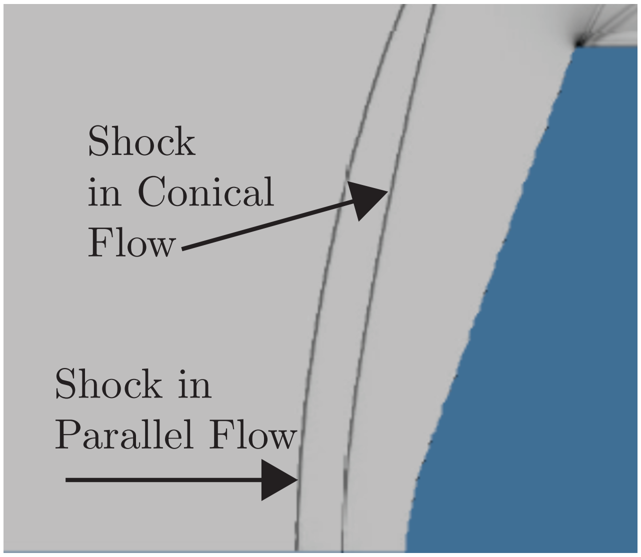

Figure 4.6: Overlay of supersonic parallel flow and conical flow in a 15° half angle nozzle over a sphere-cone geometry.

Experimentally, the T5 conical nozzle has a 7° half angle with L_0 = 1.3 m (T52886) with the 900:1 area ratio insert and L_0 = 1.2 m with the 100:1 area ratio insert (T52889). The radius of curvature is measured from the schlieren images as R_s = 17.5 ± 1.0 mm for the 1" sphere model experiments, T52886 and T52889, resulting in a conical standoff distance correction factor of 1.013 and 1.015 for sphere experiments, respectively. R_s = 110 ± 5.0 mm for the 7" MSL model experiment and R_s = 130 ± 5.0 mm for the parallel flow simulation resulting in a conical standoff distance correction factor of 1.282. These correction factors have been applied to the experimental data for conical nozzle experiments (T52886, T52889, and T52892) in order to compare to simulations assuming a uniform free stream. The uncertainty in shock curvature is accounted for in the experimental standoff distance uncertainty using the propagation of error formula.

A comparison of the LAURA prediction with a simulation completed by Dr. Dinesh Prabhu using the NASA Ames DPLR code is made for shot T52892. The standoff distance differed by 3% (LAURA: 6.3 mm vs DPLR 6.1 mm). An additional DPLR simulation which incorporated a diverging freestream is carried out to test the conical nozzle correction factor over a sphere-cone model in reacting flow. The numerically predicted standoff distance is 4.5 mm, corresponding to a correction factor of 1.355. This agrees with the predicted correction factor of 1.282 ± 0.073 to within experimental uncertainty in the curvature measurement.

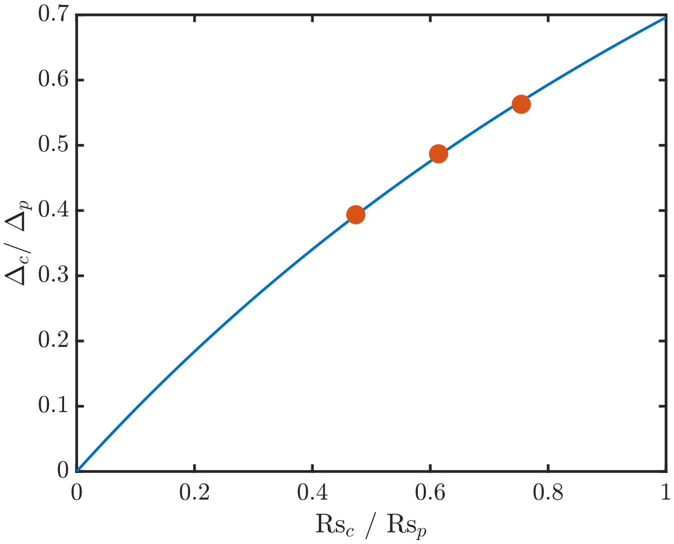

Figure 4.7: Comparison of model correction for shock standoff distance in conical vs. parallel flow with selected Euler simulations.

4.3 The Sphere

As discussed in Section 1.3.1, the shock standoff distance for flow over a sphere is well-known to be inversely proportional to the post-shock density normalized by the freestream density. This scaling was extended to reacting flows by replacing the post-shock density by the average density along the stagnation streamline [118]

$$\frac{\Delta}{R} = 0.82\frac{\rho_\infty}{\bar{\rho}}. \tag{4.4}$$

Numerical simulations of CO_2 flows over spheres at three stagnation enthalpies (h_0 = 5.9, 9.0, and 13.5 MJ/kg) and freestream densities ranging from 7 to 100 g/m^3 conditions with thermal and chemical nonequilibrium are carried out. The average density along the stagnation streamline is calculated and the shock standoff distance is compared with the theoretical scaling as shown in Figure 4.8. Simulations confirm the theoretical prediction for reacting CO_2 flows over spherical geometries. As freestream total enthalpy increases, the standoff distance becomes less sensitive to the binary scaling parameter.

The sphere experimental data and simulations with three different chemistry models are directly compared with the results summarized in Table 4.5. The density ratio is inverted to $\bar{\rho}/\rho_\infty$ so that the effects of the chemistry models on post-shock density can be observed more directly. As the post-shock density was not measured directly

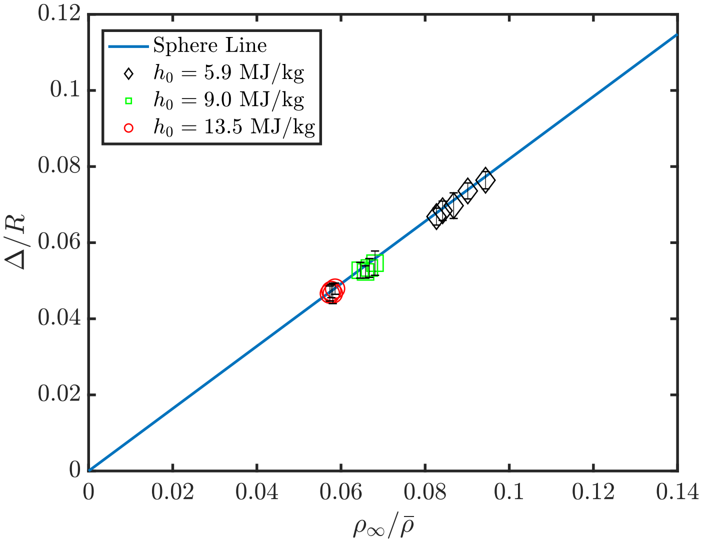

Figure 4.8: Sphere reacting flow simulations compared to the theoretical prediction, Equation 4.4.

in the experiments, the data are presented as boxes bound by frozen post-shock chemistry on the left and equilibrium chemistry on the right.

The results are shown for the HET condition (Figure 4.11), a low pressure T5 experiment (Figure 4.13) and a high pressure T5 experiment (Figure 4.12). All three experiments have comparable total enthalpies of 5.6 - 6.0 MJ/kg. The HET and T5 low pressure experiments have comparable binary scaling parameters $\rho_\infty D$ of 0.4 g/m^2 and 0.3 g/m^2, respectively. The expansion tube condition has the largest difference between chemically frozen and equilibrium post-shock density ratio due to an undissociated freestream. The simulation using the Fridman reaction mechanism is the closest match to the experimental standoff distance but is above the upper bound of the experiment by 3%. For the low pressure T52889 condition, all three simulations are within the measured uncertainty bounds on the experimental standoff distance. This condition has a similar binary scaling parameter as the expansion tube condition; however, post-shock reaction rates are slower, possibly due to the partially dissociated freestream, and differences between chemical reaction models are not significant. The high pressure T5 experiment with a larger binary scaling parameter of 2.5 showed distinguishable differences in numerical standoff distance between the different chemical reaction models. The experimental standoff distance bounds are within the numerical standoff distance using the Cruden mechanism. The Johnston mechanism numerical standoff distance is 0.7% above the upper experimental uncertainty bound.

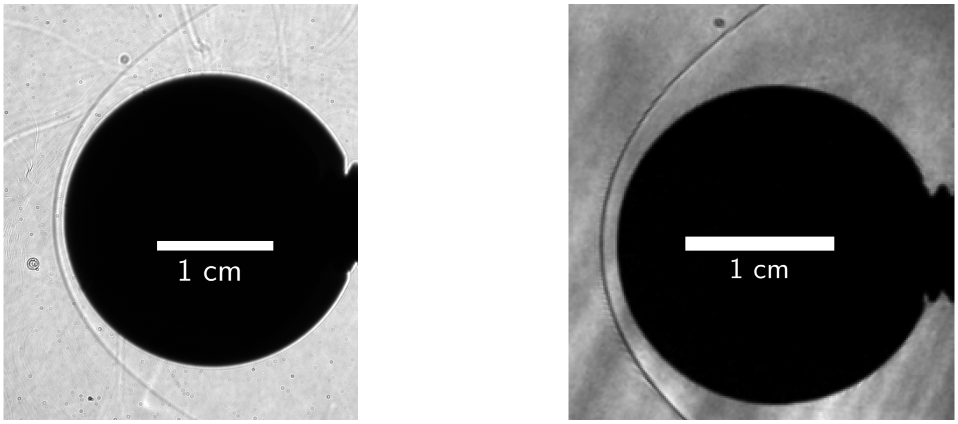

(a) HET MSL1 Shot 1455.

(b) T5 Shot 2886.

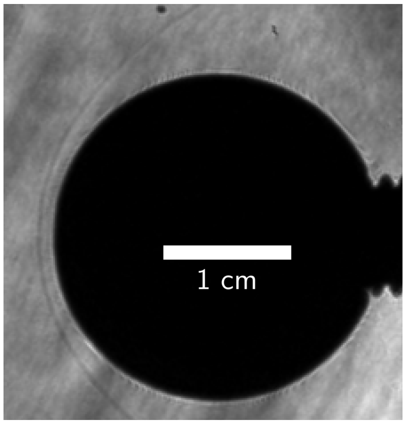

(c) T5 Shot 2889.

Figure 4.9: Schlieren images for flow over 25.4 mm sphere. The HET image is an example of a higher resolution image while the T5 images are extracted from high speed movies.

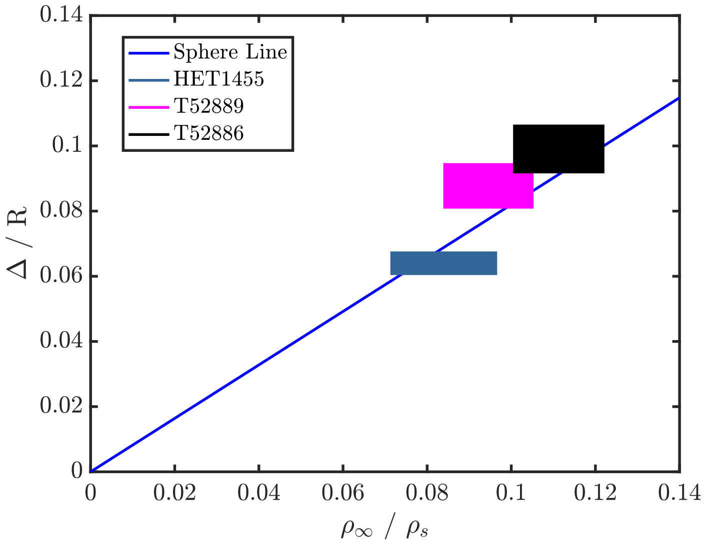

Figure 4.10: Sphere experimental measurements in T5 and HET facilities compared to the theoretical line. Boxes are bounded by the post-shock equilibrium (left) and chemically frozen (right) limits.

Table 4.5: Sphere experimental and numerical standoff distance and density ratios.

	Shot #	**HET1455**	**T52889**	**T52886**
	Experiment	0.064	0.087	0.098
	Uncertainty	±0.003	±0.007	±0.006
$\frac{\Delta}{R}$	Cruden	0.074	0.084	0.093
	Johnston	0.073	0.084	0.091
	Fridman	0.069	0.082	0.085
	Chem. Frozen	10.4	9.5	8.2
	Cruden	11.0	9.7	8.6
$\frac{\bar{\rho}}{\rho_\infty}$	Johnston	11.2	9.7	9.2
	Fridman	11.9	10.0	9.8
	Equilibrium	14.1	11.9	9.9
	Closest Model(s)	F	J, C	All 3

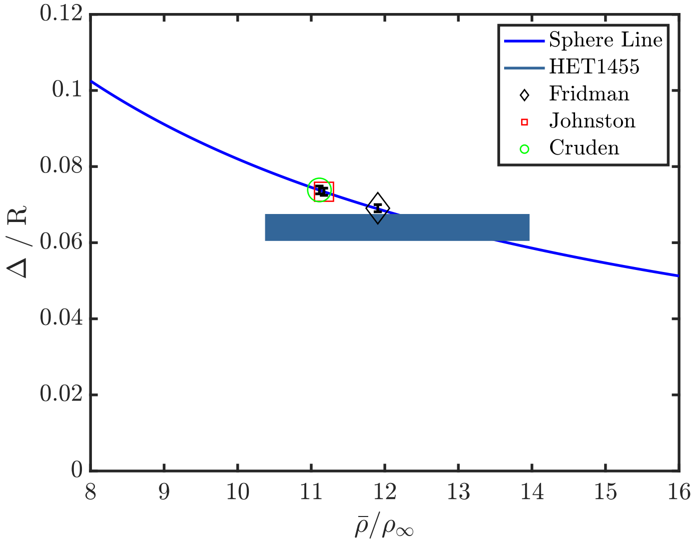

Figure 4.11: HET1455, h_0 = 5.6 MJ/kg, $\rho_\infty D$ = 0.4 g/m^2, sphere. Comparison of experiment, simulations, and empirical prediction. Boxes are bounded by the post-shock chemically frozen (left) and equilibrium (right) limits.

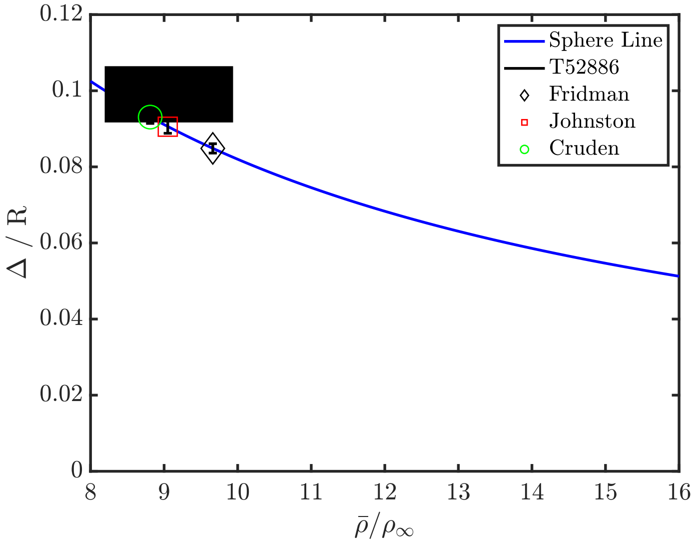

Figure 4.12: T52886, h_0 = 6.0 MJ/kg, $\rho_\infty D$ = 2.5 g/m^2, sphere. Comparison of experiment, simulations, and empirical prediction. Boxes are bounded by the post-shock chemically frozen (left) and equilibrium (right) limits.

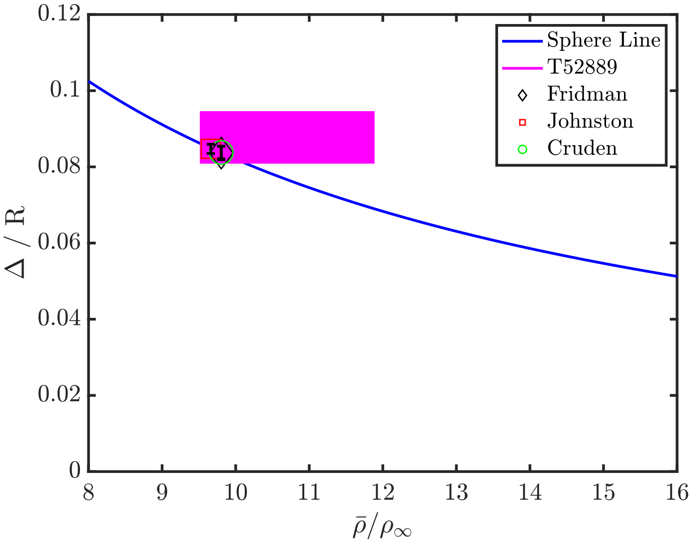

Figure 4.13: T52889, h_0 = 5.6 MJ/kg, $\rho_\infty D$ = 0.3 g/m^2, sphere. Comparison of experiment, simulations, and empirical prediction. Boxes are bounded by the post-shock chemically frozen (left) and equilibrium (right) limits.

4.4 The Spherically-blunted Cone

Spherically-blunted entry vehicle geometries exhibit a sudden transition between "sphere" and "cone" behavior corresponding to a jump in the location of the sonic line from near the sphere nose to the cone shoulder with increasing density ratio ϵ (Figure 4.14). The transition in sonic line location was predicted and observed to lead to a pitch instability in the Mars Pathfinder mission that induced wobble in the spacecraft [29, 30].

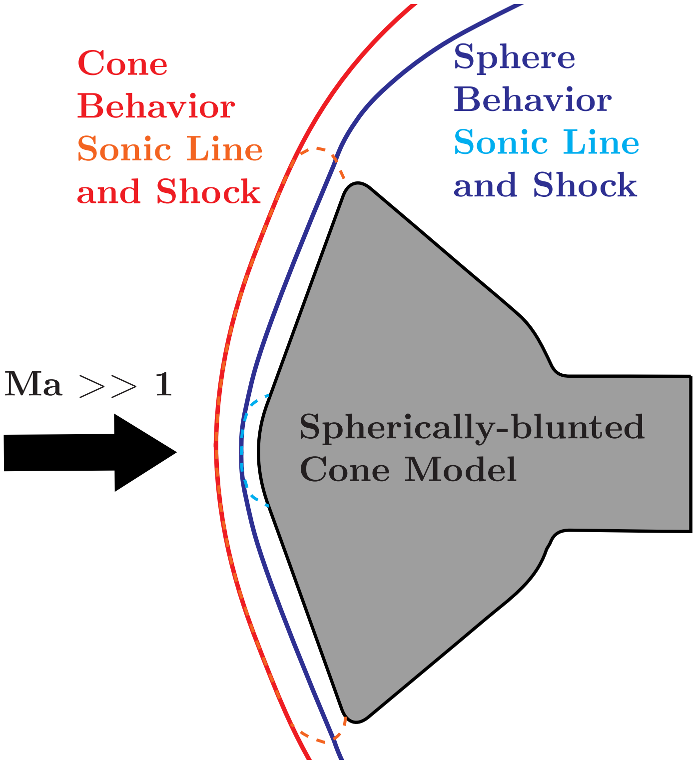

Figure 4.14: Bow shock and sonic line location for sphere and cone behavior.

Recently, an analysis of shock shape and drag coefficient for sphere-cone geometries that unifies the two limits of sphere and sharp cone behavior was developed by Hornung et al. [48]. While the analysis assumes perfect gas flow, the authors note that the results may be applied to reacting flows by using the average density along the stagnation streamline as was previously done for spheres [118]. Experimental examination of the analytical results by the same authors are in progress for high-enthalpy air flows relevant to Earth atmospheric entry [48].

During sphere behavior, the standoff distance is defined by the sphere correlation

$$\frac{\Delta}{R_N} = 0.82\frac{\rho_\infty}{\bar{\rho}} \tag{4.5}$$

where R_N is the nose radius of the spherically-blunted cone. A unifying analytical expression for the shock standoff distance as a function of two parameters for flow over sphere-cone geometries was recently derived by Hornung et al. [48]

$$\frac{\Delta}{R} = g(\epsilon)f(\eta) \tag{4.6}$$

where R is the sphere-cone body radius, ϵ is the frozen density ratio

$$\epsilon = \frac{\rho_\infty}{\rho_s}, \tag{4.7}$$

and η is a function of the half angle of the cone θ and the shock detachment angle θ_d,

$$\theta_d = 2\text{arctan}\left(\sqrt{\frac{2}{\epsilon}}\right) - \frac{\pi}{2}, \tag{4.8}$$

$$\eta = \frac{\theta - \theta_d}{\pi/2 - \theta_d}. \tag{4.9}$$

The respective functions $g(\epsilon)$ and $f(\eta)$ are given by

$$g(\epsilon) = \sqrt{\epsilon}\left(1 + \frac{\epsilon}{2}\right), \tag{4.10}$$

$$f(\eta) = 1.15(\eta - 0.075) + 0.06(\eta - 0.075)^2. \tag{4.11}$$

While the prediction was validated against perfect gas Euler simulations, the authors postulate the scaling will also apply to reacting flows if the average density along the stagnation streamline replaces the post-shock density, as was the case for spheres.

We perform reacting Navier-Stokes simulations under conditions of thermal and chemical nonequilibrium using LAURA. Shock standoff distances and average density profiles are extracted from the simulations and compared with the analytical expression from Hornung et al., Figure 4.15. The nose radius to sphere-cone body radius $R_N/R = 0.5$ for all computations and experiments replicating the MSL heat shield geometry [90] shown in Figure 3.3. The curve chosen for comparison from Hornung et al. [48] is the result for no shoulder radius ($R_S/R = 0$). The transition from sphere to cone behavior is reproduced by the simulations, validating the prediction of Hornung et al. for reacting CO_2 flows over sphere-cones.

Experiments are performed in both the T5 and HET facilities. The predicted freestream conditions for the five sphere-cone experiments analyzed in this study are shown in Table 4.3. Schlieren images from this work are presented in Figure 4.16.

Experimentally measured shock standoff distances are compared with the analytical predictions of Hornung et al. in Figure 4.17. As the density is not measured independently in the experiments, the boxes again represent bounds given by the equilibrium (left) and chemically frozen (right) post-shock values. The upper and lower bounds represent the experimental uncertainty in the standoff distance measurement. The CUBRC LENS I Run 8 data point is also included.

As with the sphere experiments, experimental data are in good agreement with the analytical prediction, with the exception of the the data from LENS I Run 8. MacLean and Holden's analysis suggested that 42% of the reservoir total enthalpy in the vibration mode would need to be artificially frozen in the reservoir to match the numerically predicted shock stand off distance for this experiment [65]. The T5 and HET data span the binary scaling parameter of LENS I Run 8, with the 900:1 nozzle experiment (T52892, pink box) as the closest match.

The sphere-cone experiments and simulations with three different kinetic mechanisms are directly compared with the results are summarized in Table 4.6. As with the sphere comparisons, the density ratio is inverted to $\bar{\rho}/\rho_\infty$ so that the effects of the chemistry models on post-shock density can be interpreted more directly.

The two conditions at similar enthalpies (5.6 to 6.1 MJ/kg) as the LENS I Run 8 condition are the HET1476 2" MSL experiment (Figure 4.18) and the T52892 7"

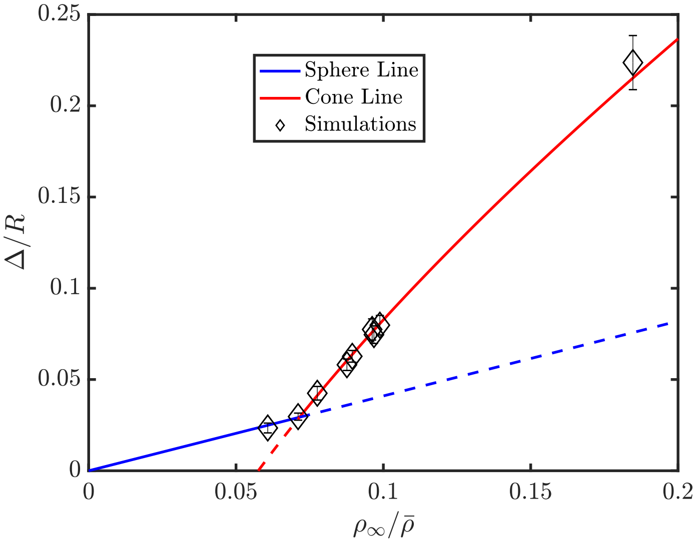

Figure 4.15: Spherically-blunted cone reacting flow simulations compared to the theoretical prediction [48].

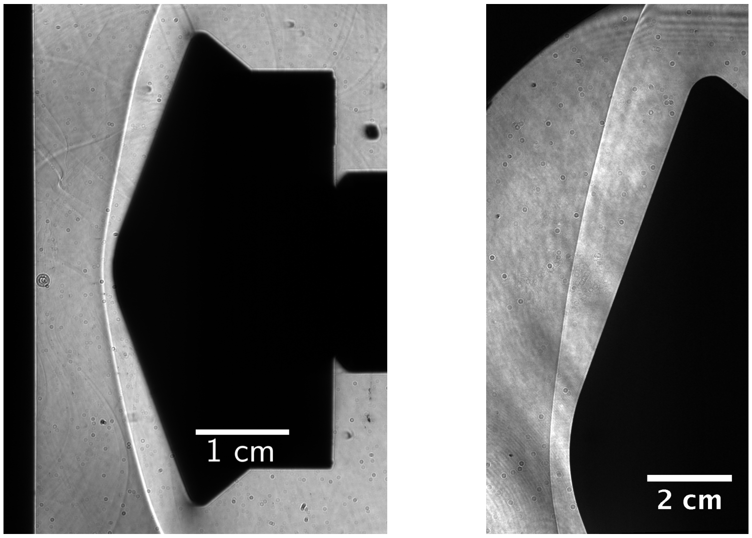

(a) HET1467. (b) T52892.

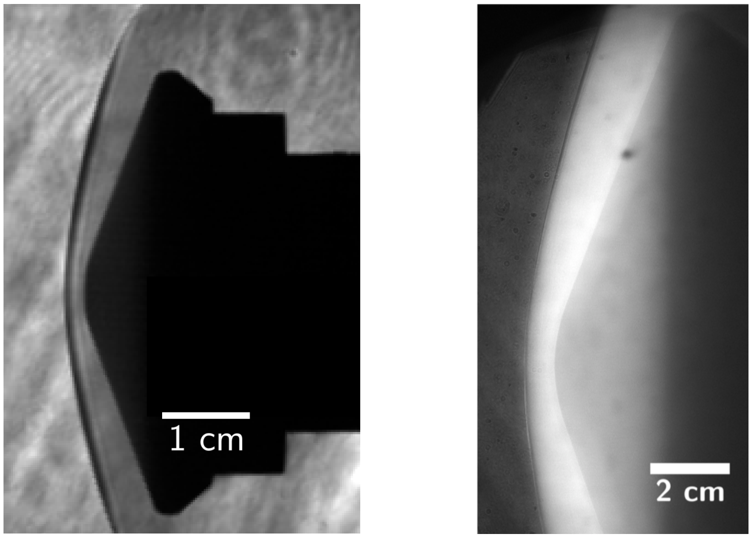

(c) T52866. (d) T52902.

Figure 4.16: Sphere-cone schlieren images from HET and T5. The T5 Shot 2866 schlieren image shown is the average of 100 frames during test time while the others are high-resolution images.

MSL experiment (Figure 4.19). For the expansion tube sphere-cone experiment HET1476, the simulation using the Fridman rates is the closest match to the experimental standoff distance as is observed in sphere flows. The numerical standoff distance is 11% greater than the upper bound of the experimental measurement. In the T52892 experiment, the 7" sphere-cone experimental measurement is corrected using the correction factor of 1.282, Section 4.2. After correction, as for sphere experiments at the similar lower density condition (T52889), all three simulations are within the experimental uncertainty for T52892. These results suggest that at

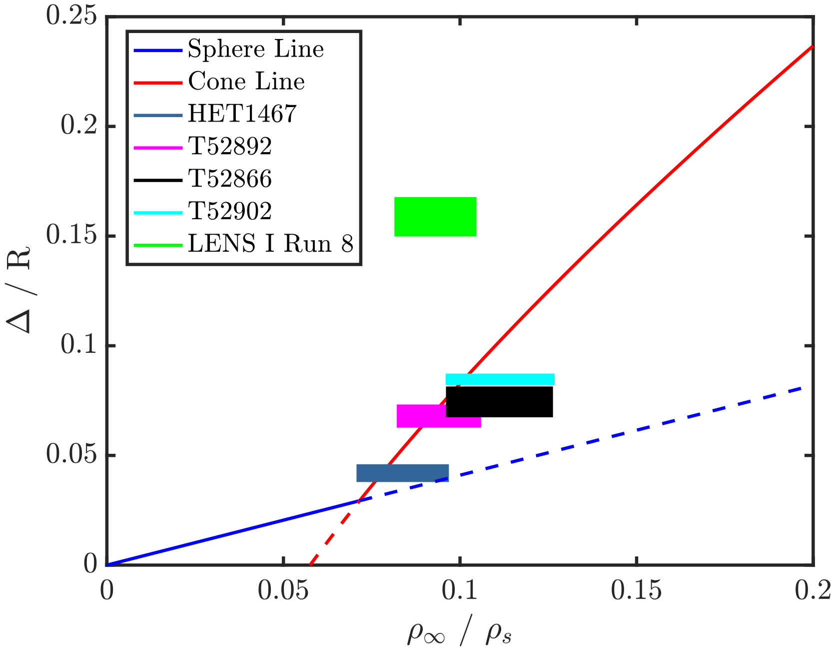

Figure 4.17: Sphere-cone experiments compared to the theoretical predictions. The boxes are bounded by the post-shock equilibrium (left) and chemically frozen (right) limits.

Table 4.6: Sphere-cone experimental and numerical standoff distance and density ratios.

	Shot #	**HET1476**	**T52892**	**T52866**	**T52902**
	Experiment	0.042	0.068	0.074	0.085
	Uncertainty	±0.003	±0.004	±0.006	±0.002
$\frac{\Delta}{R}$	Cruden	0.060	0.072	0.077	0.079
	Johnston	0.059	0.071	0.077	0.077
	Fridman	0.050	0.065	0.058	0.058
	Chem. Frozen	10.4	9.5	8.0	7.9
	Cruden	11.1	10.3	10.1	10.3
$\frac{\bar{\rho}}{\rho_\infty}$	Johnston	11.4	10.6	10.3	10.6
	Fridman	12.2	11.1	11.2	11.9
	Equilibrium	14.0	12.1	10.3	10.4
	Closest Model(s)	F	All 3	J, C	J, C

reflected shock tunnel conditions with a lower binary scaling parameter ($\rho_\infty D = 0.3$ to 1.8 g/m^2), the degree of reaction is sufficiently low that differences between the three chemical reaction models are not large enough to discern.

The high-enthalpy (8.4 to 8.6 MJ/kg), high-density condition tested with a 2" sphere-cone model, T52866 (Figure 4.20), and a 7" sphere-cone model, T52902 (Figure 4.21), showed much greater differences between the chemical reaction models, with reasonable agreement in numerical standoff distance using the Johnston and the Cruden rates, while numerical standoff distance using the Fridman rates are above the bounds of the experimental data at both binary scaling parameters ($\rho_\infty D$ = 4.5 and 16.5).

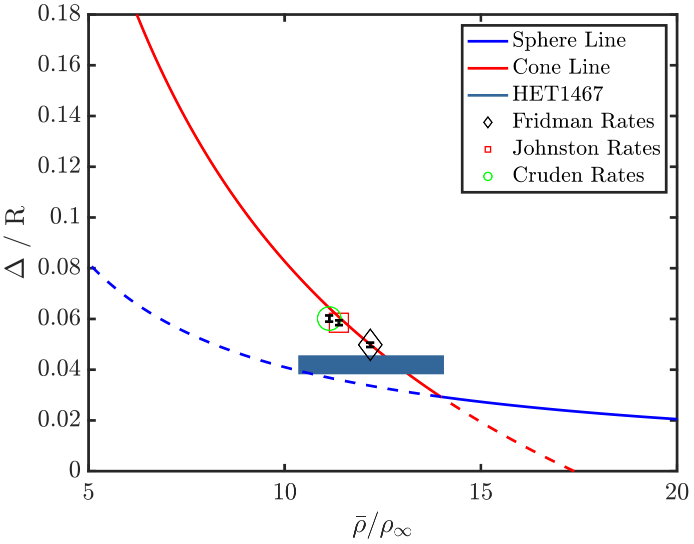

Figure 4.18: HET1467, h_0 = 5.6 MJ/kg, $\rho_\infty D$ = 0.8 g/m^2, sphere-cone. Comparison of experiment, simulations, and empirical prediction. Boxes are bounded by the post-shock frozen (left) and equilibrium (right) limits.

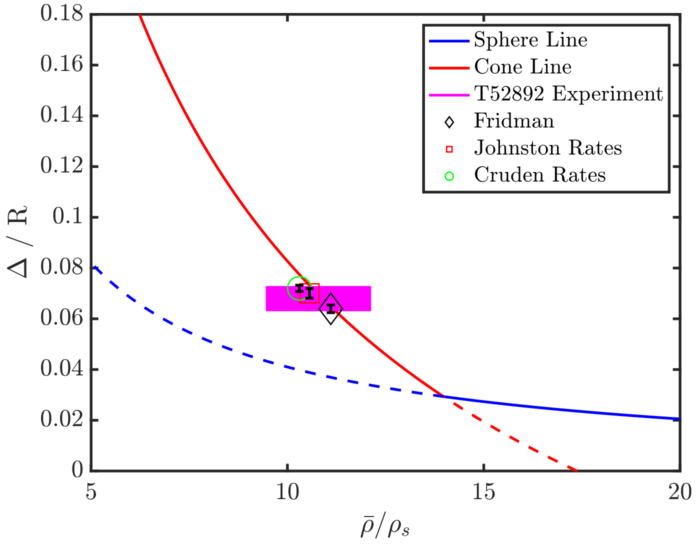

Figure 4.19: T52892, h_0 = 6.1 MJ/kg, $\rho_\infty D$ = 1.8 g/m^2, sphere-cone. Comparison of experiment, simulations, and empirical prediction. Boxes are bounded by the post-shock frozen (left) and equilibrium (right) limits.

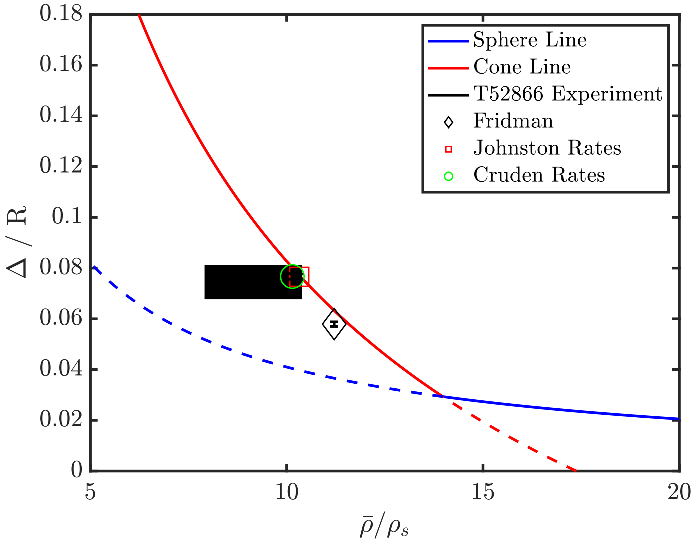

Figure 4.20: T52866, h_0 = 8.4 MJ/kg, $\rho_\infty D$ = 4.5 g/m^2, sphere-cone. Comparison of experiment, simulations, and empirical prediction. Boxes are bounded by the post-shock frozen (left) and equilibrium (right) limits.

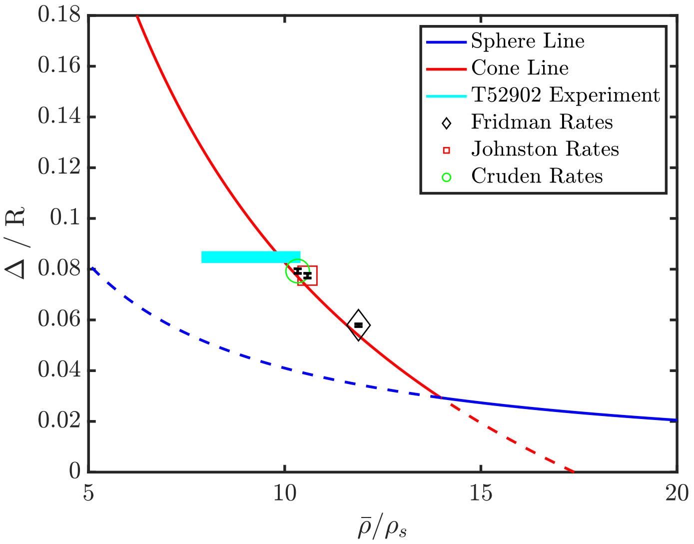

Figure 4.21: T52902, h_0 = 8.6 MJ/kg, $\rho_\infty D$ = 16.5 g/m^2, sphere-cone. Comparison of experiment, simulations, and empirical prediction. Boxes are bounded by the post-shock frozen (left) and equilibrium (right) limits.

4.5 Stagnation Streamline Analysis

In reacting flow, the density behind a vibrationally frozen shock wave can change due to three inviscid effects: chemical nonequilibrium, vibrational nonequilibrium, and the velocity profile along the stagnation streamline. Additionally, the density can change due to viscous effects in the boundary layer. Between the shock and the boundary layer, the flow is assumed to be inviscid and adiabatic. The caloric equation of state can be written in the general form

$$h = h(P, \rho, q) \tag{4.12}$$

where q is a general nonequilibrium variable [116]. Wen and Hornung considered the case of chemical nonequilibrium behind strong shock waves where vibrational equilibrium is reached quickly and the nonequilibrium effects are given by the chemical composition change, $q = Y_i$ [118]. Houwing et al. followed this analysis for ballistic range experiments where composition is frozen and vibrational nonequilibrium dominates with $q = e_V$ [49]. In high-enthalpy hypervelocity experiments at relatively low densities both chemical and vibrational nonequilibrium can occur simultaneously. A common simplification to model flow in this regime is to use the two-temperature flow model where the vibrational and electronic energies are grouped together at a common temperature T_V. Considering both chemical and vibrational nonequilibrium, the conditions on the stagnation streamline between the shock and stagnation point on the symmetry axis can be written as

$$h(P, \rho, Y_i, e_V) = \sum_{i=1}^{n} Y_i h_i^* + \left(e_V - e_V^*\right) \tag{4.13}$$

where n is the number of species, and the superscript, *, represents thermal equilibrium defined by the translational temperature T.

The change in enthalpy along the stagnation streamline can be written as

$$\frac{dh}{dx} = \frac{dh^*}{dx} + \frac{d(e_v - e_v^*)}{dx} \tag{4.14}$$

where $h^* = f(P, \rho, Y_i)$ and the total derivative of h^* is defined as

$$\frac{dh^*}{dx} = \frac{\partial h^*}{\partial P}\frac{dP}{dx} + \frac{\partial h^*}{\partial \rho}\frac{d\rho}{dx} + \frac{\partial h^*}{\partial Y_i}\frac{dY_i}{dx}. \tag{4.15}$$

Substituting Equation 4.15 into Equation 4.14 and solving for $d\rho/dx$

$$\frac{d\rho}{dx} = -\frac{1}{\frac{\partial h^*}{\partial \rho}}\left(-\frac{dh}{dx} + \frac{\partial h^*}{\partial P}\frac{dP}{dx}\right) - \frac{1}{\frac{\partial h^*}{\partial \rho}}\left(\frac{\partial h^*}{\partial Y_i}\frac{dY_i}{dx} + \frac{d(e_v - e_v^*)}{dx}\right). \tag{4.16}$$

Using the inviscid, adiabatic flow conservation equations along a streamline for momentum

$$\frac{dP}{dx} = -\rho u \frac{du}{dx}, \tag{4.17}$$

and energy

$$\frac{dh}{dx} = -u \frac{du}{dx}. \tag{4.18}$$

as well as the definition of the thermal equilibrium sound speed [116]

$$(a^*)^2 = \frac{-\frac{\partial h^*}{\partial \rho}}{\frac{\partial h^*}{\partial P} - 1/\rho} \tag{4.19}$$

we can write Equation 4.16 as

$$\frac{d\rho}{dx} = \rho \left[-\left(\frac{u}{(a^*)^2} \right) \frac{du}{dx} \right] - \frac{1}{\frac{\partial h^*}{\partial \rho}} \left(\frac{\partial h^*}{\partial Y_i} \frac{dY_i}{dx} + \frac{d(e_v - e_v^*)}{dx} \right). \tag{4.20}$$

Using the thermodynamic equation of state

$$P = \rho R T \tag{4.21}$$

where the average specific gas constant for a gas mixture R is defined as

$$R = \sum_{i=1}^{n} Y_i R_i, \tag{4.22}$$

the partial derivatives in Equation 4.20 can be evaluated as

$$\frac{\partial h^*}{\partial Y_i} \frac{dY_i}{dx} = \sum_{i=1}^{n} \frac{\partial \sum_{j=1}^{n} Y_j h_j^*}{\partial Y_i} \frac{dY_i}{dx} = \sum_{i=1}^{n} \left(-C_p^* T \frac{R_i}{R} + h_i^* \right) \frac{dY_i}{dx}, \tag{4.23}$$

$$\frac{\partial h^*}{\partial \rho} = \frac{\partial h^*}{\partial T} \frac{\partial T}{\partial \rho} = -\frac{C_p^* T}{\rho}. \tag{4.24}$$

Equations 4.23 and 4.24 are substituted into Equation 4.20 and the rise in density along the stagnation streamline can be written in a form that splits the contributions due to convection, chemical nonequilibrium, and vibrational nonequilibrium

$$\frac{d\rho}{dx} = \rho \left[\left(-\frac{u}{(a^*)^2} \right) \frac{du}{dx} \right] + \rho \left[\sum_{i=1}^{n} \left(-\frac{R_i}{R} + \frac{h_i^*}{C_p^* T} \right) \frac{dY_i}{dx} \right] + \rho \left[\frac{1}{C_p^* T} \frac{d\left(e_V - e_V^*\right)}{dx} \right]. \tag{4.25}$$

By grouping terms in this manner, the rise in density along the stagnation streamline from the shock to the edge of the boundary layer can be split into individual contributions in the brackets from convection, chemical nonequilibrium, and vibrational nonequilibrium, respectively.

The stagnation streamline flow field profile is extracted from the full-field LAURA simulations. While the LAURA simulations calculate all of the thermodynamic variables, the output file did not contain all of the variables needed for this analysis. Since LAURA uses the NASA9 thermodynamic database [72], e_V, e_V^*, C_p^*, a^*, and h_i^* are calculated using the same database, implemented into the thermodynamic software Cantera [31]. The Cantera calculations are verified by calculating the mass weighted energy $e(T, T_V) = e_{tr}(T) + e_V(T_V)$ and comparing the result to the the mass-weighted energy output from the LAURA simulations. The vibrational energy is calculated as follows. The two-temperature model assumes rotational modes are fully excited and the rotranslational heat capacity is defined as

$$C_{p,tr,i} = R_i \left(\frac{f_{tr,i}}{2} + 1 \right) \tag{4.26}$$

where $f_{tr,i}$ is the number of degrees of freedom in translation (3) plus rotation (0 for atoms, 2 for diatomic and linear molecules, and 3 for non-linear molecules).

The rotranslational enthalpy is defined as

$$h_{tr,i}(T) = C_{p,tr,i}(T)\,(T - T^\circ) + \Delta h_i^\circ \tag{4.27}$$

where the enthalpy of formation Δh_i° at the standard temperature of $T^\circ = 298.15$ K.

The mass weighted vibrational-electronic energy is defined as

$$e_V(Y_i, T_V) = \sum_{i=1}^{n} Y_i e_{V,i}(T_V). \tag{4.28}$$

The vibrational-electronic energy is then calculated

$$e_{V,i}(T_V) = h_i(T_V) - h_{tr,i}(T_V). \tag{4.29}$$

Similarly,

$$e_{V,i}^*(T) = h_i^*(T) - h_{tr,i}(T). \tag{4.30}$$

Equation 4.25 is valid for the adiabatic, inviscid portion of the shock layer. The extraction of data from simulations originates at the end of the numerical shock region x_s as shown in Figure 4.2. The input and output to this region is listed in Table 4.7 comparing three different chemistry models. The numerical shock region x_s is found by locating when the total enthalpy deviates from the freestream value of 5.6 MJ/kg by ±0.05 MJ/kg. The post-shock conditions, denoted by subscript s, is calculated at the output location of the numerical shock region. While significant

Table 4.7: HET MSL1 1" sphere simulation conditions at the exit of the numerical shock region. Froz. shock represents the post-shock condition calculated assuming a vibrationally frozen shock wave in the context of the two-temperature model. A one-temperature model case is also considered.

	Freestream	**Froz. Shock**	**Fridman**	**Cruden**	**Johnston**	**Johnston 1-T**
u_s/u_∞	1.00	0.19	0.16	0.15	0.15	0.10
$Y_{\mathrm{CO}_2,s}$	1.000	1.000	1.000	0.982	0.999	0.997
T_s	1107	7817	6825	6363	6621	4451
$\mathrm{T}_{V,s}$	1107	1107	2308	2439	2495	NA
ρ_s/ρ_∞	1.0	5.2	6.3	6.7	6.5	10.4

vibrational excitation occurs in the numerical shock region, the chemical reactions are negligible, as evidenced by the change in mass fraction of CO_2 from 1.00 to 0.98 (Cruden mechanism).

Equation 4.25 is integrated from the shock (downstream of the numerical shock thickness) to the edge of the boundary layer to extract contributions to the density profile from LAURA simulation data. An example of these profiles are shown in Figure 4.22. Illustrated are the density profiles for the HET1455 1" high-resolution sphere experiment with the Johnston and Fridman chemistry models. The density profiles are similar for the convection and vibration terms but are distinguished by the differences in the chemical term. The density profiles are sensitive to the reaction rates of the different chemistry models.

Directly behind the shock wave, the density rise in simulations using the Fridman chemical reaction model occurs over a longer distance compared to the density rise in simulations with Johnston and Cruden models because the Fridman dissociation reaction rates are controlled by the vibrational temperature. Once thermal equilibrium is reached, the Fridman model predicts the density profile reaches chemical equilibrium in a shorter distance than the Johnston and Cruden models. The overall non-dimensional density increase due to chemistry $\bar{\rho}_{dY_i}/\rho_\infty$ is 0.49, 1.17, 2.00 from simulations using the Cruden, Johnston, and Fridman models, respectively.

The average density along the stagnation streamline that defines the standoff distance in viscous reacting flow can be written in terms of the individual density contributions

$$\frac{\bar{\rho}}{\rho_\infty} = \frac{\rho_s}{\rho_\infty} + \frac{\bar{\rho}_{d(e_V - e_V^*)}}{\rho_\infty} + \frac{\bar{\rho}_{dY_i}}{\rho_\infty} + \frac{\bar{\rho}_{du}}{\rho_\infty} + \frac{\bar{\rho}_{bl}}{\rho_\infty}. \tag{4.31}$$

After the numerical shock region, the total average density $\bar{\rho}$ is composed of the

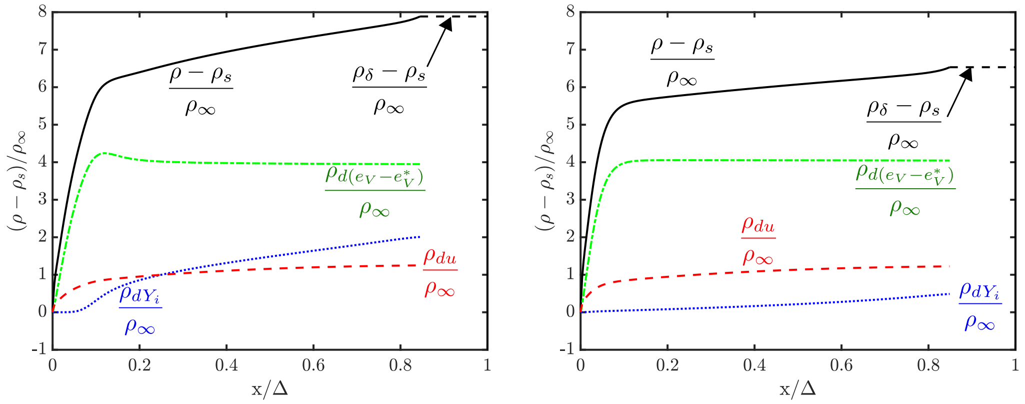

(a) Fridman rates, Δ = 0.88 mm.

(b) Cruden rates, Δ = 0.94 mm.

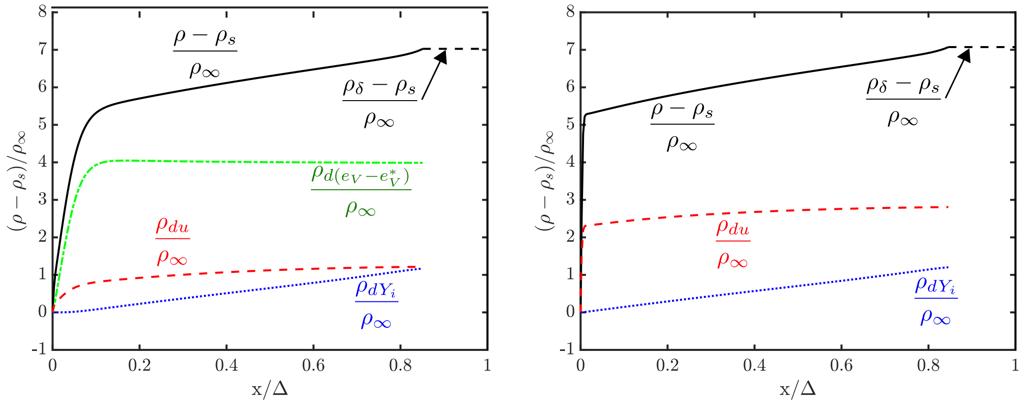

(c) Johnston rates, Δ = 0.93 mm.

(d) 1-T with Johnston rates, Δ = 0.91 mm.

Figure 4.22: Comparing chemistry models through rise in density due to individual contributions for HET, MSL1-1455 1" Sphere. The three inviscid contributions add up to the total density profile. $\rho_s/\rho_\infty = 5.2$, the frozen shock jump condition.

post-shock density ρ_s, the inviscid contributions: average density from vibrational nonequilibrium $\bar{\rho}_{d(e_V-e_V^*)}$, average density from chemical nonequilibrium $\bar{\rho}_{dY_i}$, and average density from convection $\bar{\rho}_{du}$, as well as the contribution from the viscous boundary layer region $\bar{\rho}_{bl}$. The cumulative inviscid contributions are calculated by integrating the density profiles due to individual contributions shown in Figure 4.22 from the end of the numerical shock region $x_s/2$ to the edge of the boundary layer $\Delta - \delta$.

The numerical error $\bar{\rho}_{\text{error}}$ accumulated during this term-by-term integration is found by calculating the difference between the average density in the post-shock inviscid flow region directly extracted from the simulation

$$\frac{\bar{\rho}_{\text{invis}}}{\rho_\infty} = \frac{1}{(\Delta - \delta) - \frac{x_s}{2}} \left(\int_{\frac{x_s}{2}}^{\Delta - \delta} \frac{\rho}{\rho_\infty} dx \right) \tag{4.32}$$

and the sum of the average individual contributions

$$\frac{\bar{\rho}_{\text{error}}}{\rho_\infty} = \frac{\bar{\rho}_{\text{invis}}}{\rho_\infty} - \left(\frac{\rho_s}{\rho_\infty} + \frac{\bar{\rho}_{d(e_V - e_V^*)}}{\rho_\infty} + \frac{\bar{\rho}_{dY_i}}{\rho_\infty} + \frac{\bar{\rho}_{du}}{\rho_\infty} \right). \tag{4.33}$$

The contribution to the total average density due to the boundary layer region $\bar{\rho}_{bl}$ is found by calculating the difference between the average density profile including the approximation for the boundary layer, Equation 4.1, and the average density profile in the inviscid region, Equation 4.32.

4.5.1 Results of the Stagnation Streamline Analysis

The stagnation streamline analysis is used to show the relative importance of the contributions to the average density for comparison of different chemical reaction models. This analysis is performed using the stagnation streamline extracted from simulations of flow over 25.4 mm diameter hemispheres with HET freestream condition inflow, Table 4.2, examining the two-temperature (2-T) chemistry models of Fridman, Cruden, and Johnston, as well as the Johnston chemistry model assuming the one-temperature (1-T) model. The results are presented in Table 4.8 and Figure 4.23.

The numerical shock region density rise can be largely attributed to the vibrational excitation occurring as shown in Table 4.7. The combination of the numerical shock region, vibrational nonequilibrium, and convection contributions to the total average density are within $\bar{\rho}/\rho_\infty = 0.2$ for the three different chemistry models. The largest difference in total average density contributions between the three chemistry models is observed in the chemical nonequilibrium contribution. The simulations using the Cruden chemistry model result in a chemical nonequilibrium contribution of $\bar{\rho}/\rho_\infty = 0.2$ compared to an increase of $\bar{\rho}/\rho_\infty = 1.2$ from simulations using the Fridman chemistry model. The chemical nonequilibrium contribution from the Johnston chemistry model is closer to the contribution from the Cruden model with an increase of $\bar{\rho}/\rho_\infty = 0.6$.

The contributions explain the difference in standoff distance observed in the different chemistry models, with a 0.5% and 6.4% decrease in standoff distance extracted from the simulation using the Cruden mechanism compared to the standoff distance extracted from the simulation using the Fridman and Johnston mechanisms, respectively. The average density extracted from the Johnston mechanism using the two-temperature model and one-temperature model resulted in a difference of $\bar{\rho}/\rho_\infty = 0.1$. The standoff distance from the simulation decreases by 2.3% when the Johnston 1-T model is used instead of the Johnston 2-T chemistry model.

Table 4.8: Contribution to the total density, $\bar{\rho}/\rho_\infty$.

Kinetic Model	**Fridman**	**Cruden**	**Johnston 2-T**	**Johnston 1-T**
Frozen Jump	5.2	5.2	5.2	10.4
Numerical Shock Region	1.1	1.5	1.3	0.0
Vibrational Nonequilibrium	3.5	3.3	3.3	0.0
Convection	0.8	0.7	0.7	0.3
Chemical Nonequilibrium	1.2	0.2	0.6	0.6
Boundary Layer	0.1	0.1	0.1	0.1
Numerical Error	0.1	0.1	0.1	0.0
Total	12.0	11.1	11.3	11.4
Δ/R (Simulation)	0.0691	0.0738	0.0734	0.0717

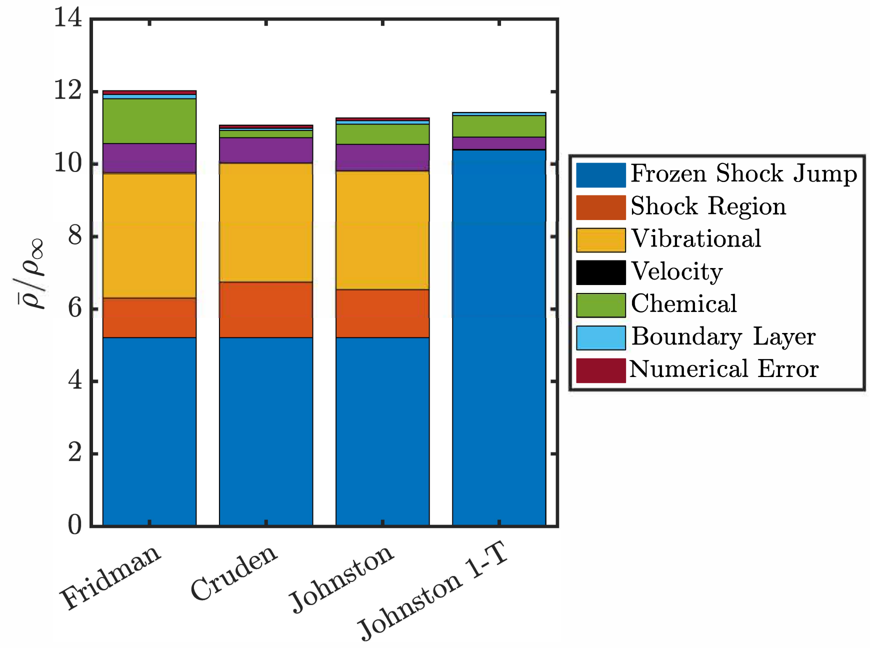

Figure 4.23: HET sphere simulation bar chart displaying the individual contributions to the total density.

4.6 Conclusions

The standoff distance over sphere and spherically-blunted cone geometries have been examined through theory, simulations, and experiments in two hypervelocity facilities with different gas acceleration processes. The theoretical predictions by Hornung et al. derived from perfect gas simulations have been validated using Navier-Stokes simulations for reacting carbon dioxide flow, replacing the frozen post-shock density ρ_s with the average density $\bar{\rho}$ along the stagnation streamline as well as accounting for the boundary layer through the displacement thickness δ^*.

Three experiments for spheres and four for sphere-cones were analyzed using both high-speed and high-resolution images. The effect of using the conical nozzle was observed and a correction factor was derived to account for this phenomena. A correction for heat flux is suggested but not considered in this work. All of the experiments agree with the analytical predictions to within experimental uncertainty.

The simulation data were analyzed along the stagnation streamline and the contributions to the total density ratio from vibrational nonequilibrium, convection, chemical nonequilibrium, and the boundary layer were extracted. The largest difference between three mechanisms was observed in the chemical contribution. The Fridman mechanism predicts a larger post-shock density rise than the Johnston mechanism, with the Cruden mechanism resulting in the smallest post-shock density rise.

Simulations using the Fridman mechanism produced the best agreement with the HET data. At comparable values of the total enthalpy h_0 and the binary scaling parameter $\rho_\infty D$, simulations of T5 experiments showed good agreement with experimental data with small difference between model predictions due to less dissociation at the lower pressure conditions. At higher pressure, the closest agreement with experiments was obtained using the Cruden mechanism. These comparisons held for both sphere and sphere-cone experiments.

There was no evidence that vibrational freezing in the T5 nozzle significantly affects the shock standoff distance at any of the conditions tested. Experiments were designed to span the value of the binary scaling parameter of the LENS I Run 8 test, however the standoff distance discrepancy between Run 8 data and DPLR simulations was not reproduced [65].

A possible explanation for the standoff discrepancy found in LENS I is early onset of driver-gas contamination due to the shock tunnel being run over-tailored. With a mix of light driver gas and CO_2, the standoff distance would increase. Sudani et al.

studied the effect of driver gas contamination in T5 and experimentally showed that a slightly over-tailored condition reduces the test time significantly and can induce early onset of driver-gas contamination [108].

Chapter 5

HET CO_2 RADIATION MEASUREMENTS

5.1 Introduction

Spectrally resolved 4.3 μm band mid-wave infrared CO_2 radiation measurements are presented for radiation impinging on the surface of a 88.6:1 scaled Mars Science Laboratory (MSL) heat shield model. Experimental measurements are made in the HET facility. The facility is run in shock tube mode to obtain measurements in optically thick conditions. Expansion tube mode operation results in conditions that are closer to optically thin, as discussed in more detail in Section 5.3.1.

Table 5.1: Summary of the experimental spectral 4.3 μm measurements obtained. The start and end of the exposure time of the camera is referenced to the start of test time.

Measurement Location	**Condition**	**Shot #**	**Exposure (μs)**
16° AOA Stag. Pt.	ST0_4	1544	100 - 180
	ST1_2	1541	100 - 180
	ST14_6	1543	100 - 180
	MSL1	1546	70 - 150
	MSL2	1527	50 - 130
16° Lee Side	MSL1	1531	70 - 150
0° AOA Stag. Pt.	MSL1	1786	70 - 150
	MSL2	1787	50 - 130
Freestream Probe	MSL1	1724	50 - 130
		1722	170 - 250
	MSL2	1725	50 - 130
		1723	160 - 240

The MSL model measurements are obtained in three different configurations. Measurements that directly probe the free stream are also made. The line-of-sight (LOS) of the rays inside the fiber probe acceptance cone for the different geometries are illustrated on a cross-sectional schematic of the accelerator and test section for each configuration.

Measurements are directly compared to CFD (LAURA) and radiation (HARA) simulations, conducted along different ray lengths that bound the rays inside the acceptance cone. Uncertainties in freestream conditions, post-shock chemistry, and flow-field features such as the expansion fan and tube-wall boundary layer in the line-of-sight are considered as possible experimental explanations for the difference between simulated and measured spectra. A summary of the presented experimental spectral measurements are shown in Table 5.1.

5.1.1 Freestream Conditions

For all conditions, the nominal driver pressure is P_4 = 3.0 MPa. When the facility is in expansion tube mode, the initial driven pressure is P_1 = 1.2 kPa and the initial accelerator pressure is P_5 = 180 mTorr for the MSL1 condition and P_5 = 75 mTorr for the MSL2 condition. For the three shock tube conditions, the initial driven pressure is P_1 = 0.4, 1.2, and 14.6 kPa, respectively. The condition name specifies the initial pressure. For example, for the shock tube condition labelled ST1_2, the initial pressure is P_1 = 1.2 kPa. The predicted freestream conditions for the corresponding shock tube and expansion tube conditions are shown in Table 5.2. Equilibrium chemistry is assumed for shock tube mode and perfect gas (γ = 1.29 for CO_2) is assumed for expansion tube mode. The perfect gas freestream assumption was initially based on the work of Sharma et al. [103] and predates the conclusions drawn in Section 2.3.2 that the test gas is expected to be in thermochemical equilibrium. The perfect gas and equilibrium chemistry freestream conditions are shown in Table 2.9. The equilibrium chemistry freestream temperature is 11% and 7% lower than the perfect gas freestream temperature for the MSL1 and MSL2 condition, respectively.

Table 5.2: Table of HET radiation measurement freestream conditions.

Condition -	M_∞ -	h_o MJ/kg	T_∞ K	P_∞ kPa	ρ_∞ g/m^3	U_∞ m/s	t_{test} µs	P_{pitot} kPa	YCO_2 —
MSL1	5.7	5.9	1221	3.35	14.5	3129	267	134	1
MSL2	6.8	6.7	1042	1.66	8.4	3414	201	93	1
ST0_4	2.9	2.1	1939	27.4	74.3	1862	>300	267	0.984
ST1_2	2.7	1.7	2410	64.6	204	1638	>300	561	0.997
ST14_6	2.3	0.8	991	353	1890	1065	>300	2210	1

5.1.2 Experimental Setup

The general experimental setup and calibration technique is described in Section 3.2.4. A section view of the MSL model oriented at a 16° angle of attack

(AOA) in the HET test section is shown in Figure 5.1. For the experiments presented in this chapter, the spectrometer slit width is 100 µm for the expansion tube conditions and 20 µm for the shock tube conditions. This change in slit width did not change the Instrument Line Shape function determined to be a Guassian function with a half width at half max of $\lambda_g = 6.4$ nm as discussed in Section 3.2.5.

Each fiber port has a 2.5 mm diameter, 0.5 mm thick sapphire window that is flush mounted on the surface of the model. The coordinates of the two fiber port locations (x/R, y/R) are (0, 0) for the 0° AOA measurements and (0.125, 0.433) for the 16° AOA measurements. The coordinate system origin (shown in Figure 3.3) is located at the nose of the sphere, where x is the distance into the body along the model centerline and y is the distance in the radial direction. The two 16° AOA measurement locations are obtained by rotating the forebody 180°. A chalcogenide fiber cable is mounted directly behind the sapphire window. The chalcogenide fiber has a 500 µm core diameter and a 17.5° acceptance cone half angle.

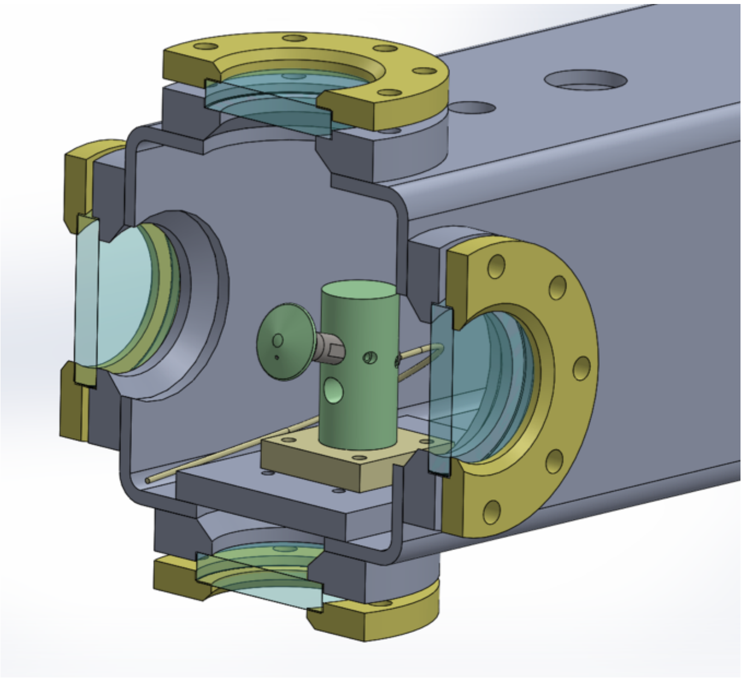

Figure 5.1: Section view of the test section with the model mounted at a 16° angle of attack.

5.1.3 Experimental Timing

The radiation data acquisition is triggered using the pressure trace obtained from a pitot probe mounted in the test section. The pitot probe is located directly underneath the model or at the centerline for the freestream probe. In expansion tube mode, the test time starts when the contact surface between the accelerator and test gas is detected by the pitot probe. In shock tube mode, the test time starts after the primary shock reaches the pitot probe. The infrared camera is exposed for 80 µs for all experiments with the delay time listed in Table 5.1 referenced from the start of test time. All of the model measurements have camera exposure times referenced from the start of test time of 100-180 µs in shock tube mode, 70-150 µs for MSL1 condition measurements, and 50-130 µs for MSL2 condition measurements. This is within the predicted test times of greater than 300 µs in shock tube mode, and 267 µs and 201 µs for the MSL1 and MSL2 conditions, respectively.

The freestream probe is located at the NPT port 0.3 m upstream of the tube exit plane. Direct freestream measurements are obtained at two different camera exposure time windows for the MSL1 and MSL2 conditions. Experimental shots 1724 (MSL1) and 1725 (MSL2) are timed using a pitot probe extended into the tube, 6.6 cm downstream from the freestream probe location. The travel time of the slug of test gas, assumed to be propagating with the freestream velocity, between the freestream probe and the pitot probe is approximately 20 µs for MSL1 and MSL2. A further 30 µs delay is added, such that the radiation measurement acquisition begins 50 µs after the contact surface arrives at the pitot probe.

The x-t diagrams showing the model and freestream probe line-of-sight for the start and end of test time bounding the measurement are shown on the x-t diagrams for the MSL1 condition, Figure 5.2 and the MSL2 condition, Figure 5.3. For the model measurements, the line-of-sight observed by the fiber probe 1.0 m upstream (representative of the 16° AOA stagnation point normal line-of-sight, red-dashed line, Figure 5.9) at the beginning and end of test time is represented by the red lines on the x-t diagrams. For the freestream probe measurements, the line-of-sight during the exposure time at the probe location shown in Figure 5.27 is represented by the vertical blue lines on the x-t diagrams . The blue-dashed lines on the x-t diagrams show the freestream probe line-of-sight exposure time bounds when projected from the probe location to the test section location, accounting for the the travel time of the slug of test gas.

Experimental shots 1722 (MSL1) and 1723 (MSL2) are obtained with the pitot probe located 37 cm away from the freestream probe location. The long separation distance is due to simultaneous measurements with a double FLDI set up attempting freestream velocity measurements. The data from these two experiments are obtained 170 µs and 160 µs after the arrival of the contact surface at the pitot probe in the test section and thus include underexpanded gas outside the test gas slug. These data are included and discussed only in Section 5.7.1.

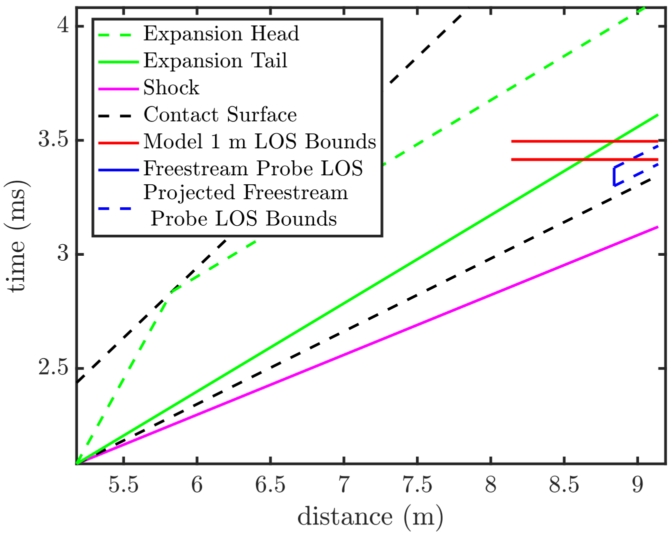

Figure 5.2: MSL1 condition accelerator section x-t diagram, x = 5.18 m to 9.14 m. Freestream probe location, x = 8.84 m.

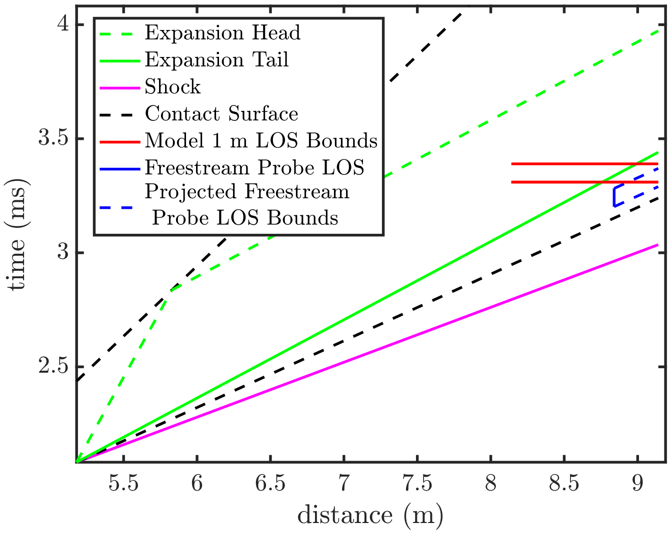

Figure 5.3: MSL2 condition accelerator section x-t diagram, x = 5.18 m to 9.14 m. Freestream probe location, x = 8.84 m.

5.1.4 Pitot Measurements

Pitot measurements are made using the pitot probe design described in Section 2.4.2 with PCB model 112A22 pressure transducers installed. The pitot pressure traces are shown in Figure 5.4 for the MSL1 condition and Figure 5.5 for the MSL2 condition. The pitot pressure measurements are obtained in the same experimental shots as the freestream radiation probe measurements of Shot 1724 (MSL1) and Shot 1725 (MSL2). The pitot probe is mounted along the tube centerline and extended 23.4 cm into the tube referenced from the tube exit plane. The black-dashed lines represent the exposure time bounds of the freestream data acquisition of 70-150 µs for the MSL1 condition and 50-130 µs for the MSL2 condition. The red line is the average pitot pressure during measurement time. The corresponding measured pitot pressures is 158.4 kPa ± 5.8 kPa for the MSL1 condition and 87.8 kPa ± 5.5 kPa for the MSL2 condition. This shows decent agreement with the perfect gas calculations of 134 kPa and 93 kPa for the MSL1 and MSL2 conditions, respectively. These measurements give confidence that the time windows chosen for camera exposure is within test time.

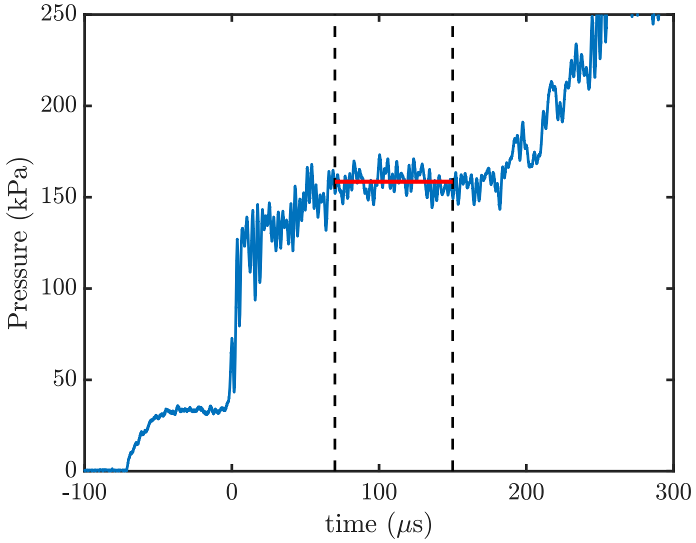

Figure 5.4: MSL1 pitot pressure measurement, Shot 1724.

5.2 Shock Shape Measurements

The HET schlieren system is described in Section 3.2.3. Shock shape measurements are obtained for the MSL1 and MSL2 conditions at 0° AOA and 16° AOA using a single shot, high resolution pco.1600 camera (1600x2400 pixels). The presented

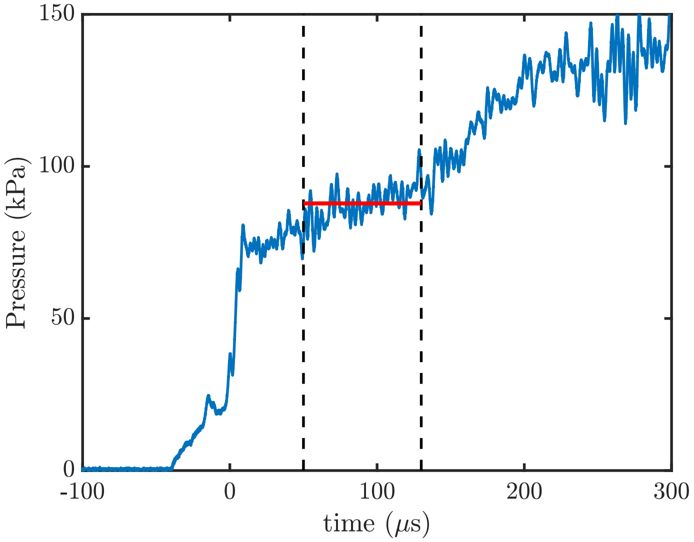

Figure 5.5: MSL2 pitot pressure measurement, Shot 1725.

images are obtained with a camera exposure time of 0.5 µs, starting 80 µs after the arrival of the contact surface at a pitot probe mounted directly underneath the model. The MSL1 condition, 0° AOA (HET1467, Figure 4.16a) bow shock standoff distance is Δ = 1.066 ± 0.053 mm. The MSL2 condition, 0° AOA (HET1455, Figure 5.6c), bow shock standoff distance is Δ = 0.970 ± 0.050 mm. The 16° AOA schlieren images are shown for the MSL1 condition, Figure 5.6a, and MSL2 condition, Figure 5.6b.

5.3 Shock Layer Simulations

The 3D steady flow-field around the MSL scaled model is computed using the NASA LAURA Navier-Stokes solver described in Section 3.1.1 [1]. The CFD simulations assume laminar flow and use a two-temperature model with five species (CO2, CO, O2, C, and O) and the five reaction CO_2 subset of the Johnston rates [54]. The 3D grid for the MSL has 1,087,758 total grid points including 97 grid points in the wall-normal direction. The grid was previously used for simulations of laminar carbon dioxide hypervelocity flow in various high-enthalpy facilities [40].

The grid is adapted until the bow shock is captured at 80% of the distance between body and inflow boundary condition. The flow-field properties are extracted along the line-of-sight normal to the fiber port location approximately every 0.02 mm from the body to the inflow boundary condition. The flow properties are then

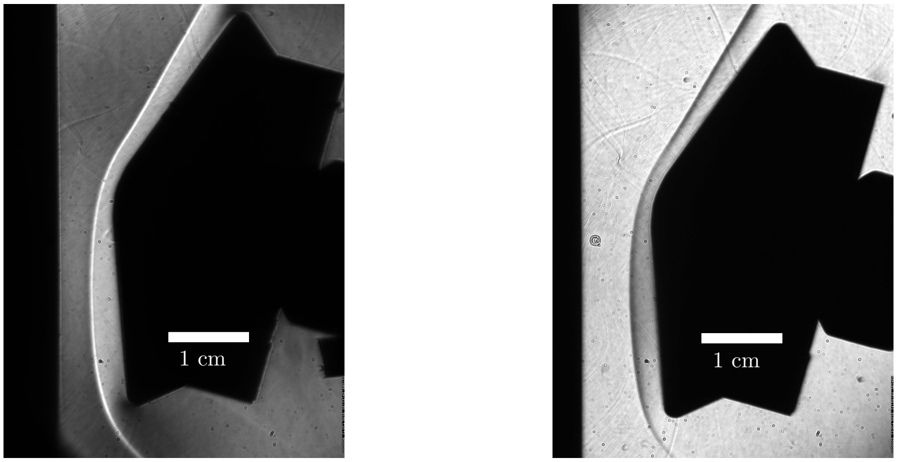

(a) HET1465, MSL1 16° AOA.

(b) HET1459, MSL2 16° AOA.

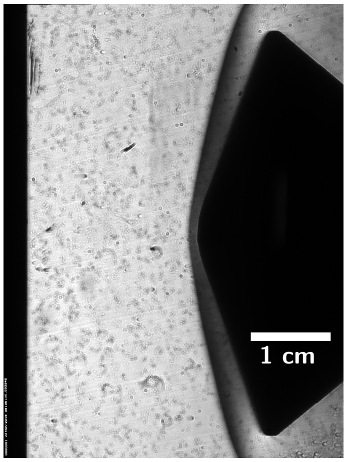

(c) HET1788, MSL2 0° AOA.

Figure 5.6: 50.8 mm MSL scaled model schlieren images for the MSL1 and MSL2 conditions from HET.

imported into HARA (described in Section 3.1.2) where a line-by-line model is implemented to simulate the CO_2 and CO infrared radiation in the flow field. The simulation output is convolved with the experimental instrument line shape function for direct comparison of simulations to experiments. In Section 3.2.5, the tangent slab approximation is used to conclude the spectral radiance for the normal line-of-sight compared to the obliquely incident ray at the fiber probe acceptance cone half angle of 17.5° is within 2.3% of the spectral radiance for the optically thin limit and equal in the optically thick limit.

The integrated radiance along the 16° AOA stagnation line-of-sight is extracted from simulations and shown in Figure 5.7 for the expansion tube tests and Figure 5.8 for the shock tube tests. Comparisons to the optically thin limit $\alpha_\lambda \rightarrow 0$ are shown to examine absorption in the shock layer. The smeared rotational band (SRB) model is used for these computations, applying a simplified and efficient treatment of each molecular band system [1]. This approach does not properly capture wall boundary layer absorption but is useful for evaluating the appropriate optical thickness regime. The MSL2 integrated intensity at the wall is 1.1% below the optically thin limit while the MSL1 integrated intensity at the wall is 9.1% below the optically thin limit indicating there are more photons absorbed and reemitted in the shock layer for the MSL1 condition compared to the MSL2 condition. The shock tube simulations deviate significantly from the optically thin limit, approaching the optically thick blackbody limit.

For expansion tube measurements, the "tail" of the spectra approximately between 4900 nm to 5300 nm can be used to assess the match in shock-layer predictions as the spectral emission in this range is predominately from shock-layer gas. Freestream probe measurements at 5000 nm are discussed in Section 5.7 for the MSL1 condition, Figure 5.28 and the MSL2 condition, Figure 5.29. At 5000 nm, the experimental freestream radiance is 0.0198 W/cm^2-µm-sr or 1.7% of the peak radiance and 0.020 W/cm^2-µm-sr or 4.4% of the peak radiance. The simulated radiance at 5000 nm accounting for a Mirels calculated boundary layer is less than 0.1% of the peak radiance.

5.3.1 Accounting for Freestream Radiation

In the shock layer, the tangent slab approximation is used to show that the radiance calibration is modified by at most 2.3% for an obliquely-incident ray at the acceptance half angle $\theta_c = 17.5°$ in the optically-thin limit, Section 3.2.5. In this work, this modification has been assumed negligible.

The freestream radiation is accounted for by extending the calculated free stream as a constant slab to a distance determined by the length of the ray inside the tube, from the shock to the tube wall. If flow features such as expansion fans or tube-wall boundary layers are considered in the line-of-sight, the freestream slab is no longer constant but affected by the conditions calculated for the flow feature. This method is useful to determine when flow features and accurate distances are important to take into account before a future algorithm to average the radiance of all rays in the acceptance cone is developed.

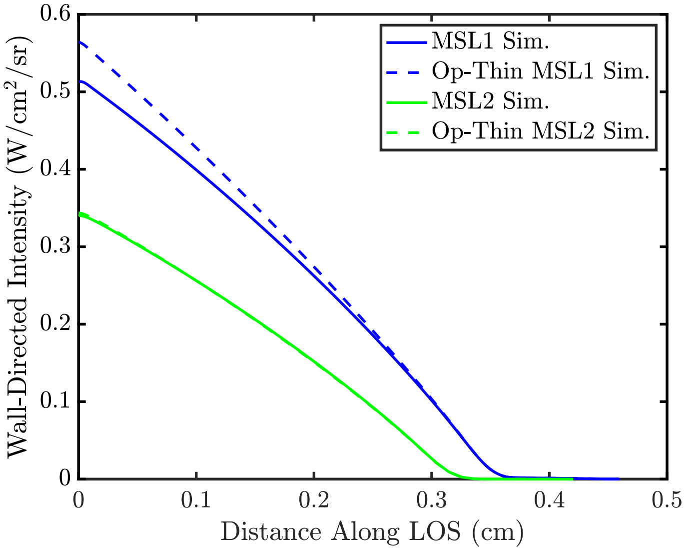

Figure 5.7: Expansion tube 16° AOA stagnation LOS shock layer simulations compared to optically thin limit simulations.

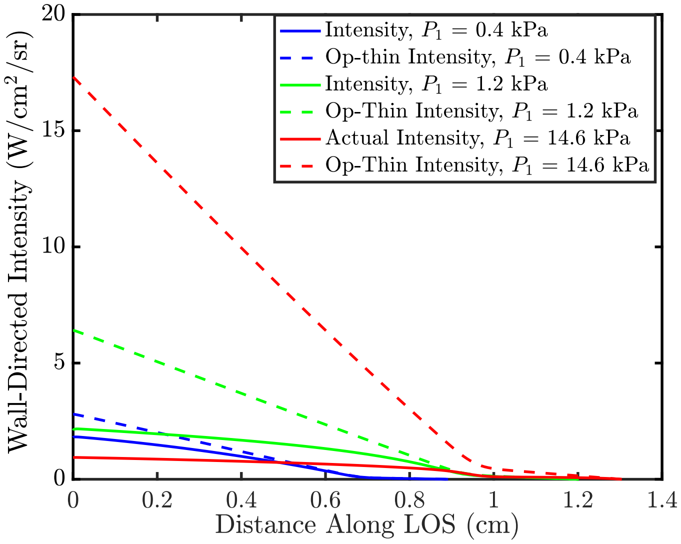

Figure 5.8: Shock tube 16° AOA stagnation LOS shock layer simulations compared to optically thin limit simulations.

5.4 16° AOA Stagnation Point Measurements

Figure 5.9 shows a schematic of the collection volume for the tests measuring radiation at the 16° AOA stagnation point. The red-dashed line has a divergence angle of 4° from the tube exit plane centerline and represents the normal line-of-sight for this probe location. The normal-line-of sight is approximated in the simulations by a ray 1.0 m in length. The orange and green lines represent the outer rays of the fiber collection volume corresponding to the chalcogenide fiber half angle of 17.5°. The simulation radiance lower bound is given by the radiation along the shortest ray, the 0.2 m long green line.

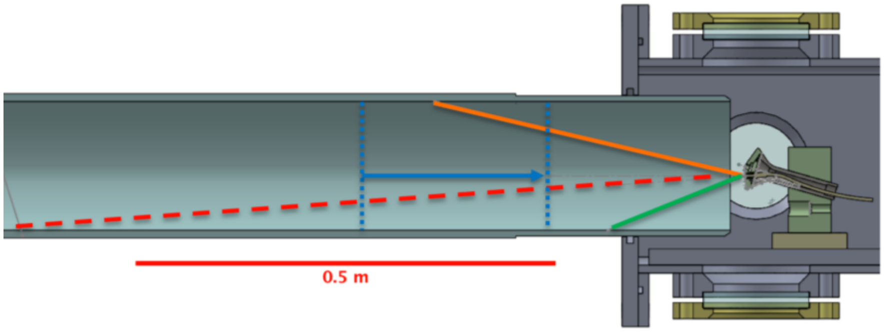

Figure 5.9: Schematic of the fiber collection volume when the probe is mounted at the 16° AOA stagnation point location on the MSL model.

5.4.1 Shock Tube 16° AOA Stagnation Point Measurements

Radiance data obtained in this configuration for three shock tube conditions with increasing freestream pressure are shown in Figures 5.10, 5.11, and 5.12. Peak radiance is equal to within 0.07% between the 0.2 m ray and the 1.0 m ray simulations indicating the shock layer radiation is approaching the optically thick limit. In this limit, all of the photons emitted in the free stream are absorbed and reemitted in the shock layer.

Good agreement is observed between the simulations and experiments with the exception of the absorption feature between 4200 nm and 4600 nm. Peak experimental radiance shows good agreement with the peak simulation radiance with a difference of 1.2%, 1.3%, and 2.1% for the ST0_4, ST1_2, and ST14_6 conditions, respectively.

In the optically thick limit, the spectral radiance approaches the temperature dependent blackbody function. Shown in Figure 5.13, the experimental data is bounded by the Planck curves calculated at the post-shock equilibrium and post-shock frozen temperatures. For the highest pressure condition ST14_6, the calculated post-shock temperature and post-shock equilibrium temperature are equal at T_s = 1406 K and the peak radiance at 4550 nm agrees with the spectral blackbody radiance B_λ within 3%.

The strong absorption feature is more prominent as the boundary layer pressure increases due to the extremely thin boundary layer at the model wall at high pressures. With a thin (<0.1 mm) boundary layer and a large temperature gradient (1000 K over a 20 µm distance for the shocktube14_6 condition), more points in the boundary layer is needed to better resolve the absorption feature. Agreement can be further improved by clustering the boundary layer extraction points. The overall good correspondence between experiments and simulations in the shock tube results provide confidence in the technique used to measure the spectral radiance under optically thick conditions.

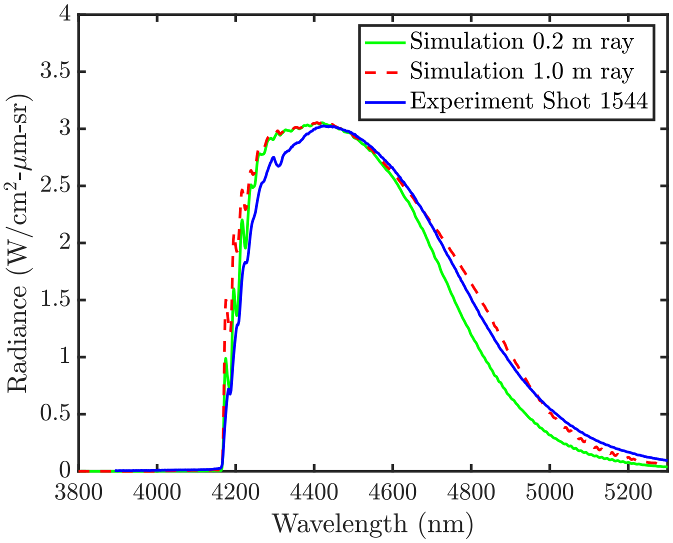

Figure 5.10: Shocktube0_4 test condition spectral radiance measured at the 16° AOA stagnation point.

5.4.2 Expansion Tube 16° AOA Stagnation Point Measurements

Experimental radiance measurements for the MSL1 and MSL2 conditions during tests in the configuration shown in Figure 5.9 are presented in Figures 5.14 and 5.15. Line-of-sight spectral radiance is simulated with a 0.2 m path length (green line) and a 1.0 m path length (red-dashed line). In contrast to the shock tube results where the shock layer is optically thick, there is significant deviation between the simulated spectra with different path lengths. For the MSL1 condition, the peak radiance of the 1.0 m ray and 0.2 m simulation rays are 3.1% and 14.5% below the

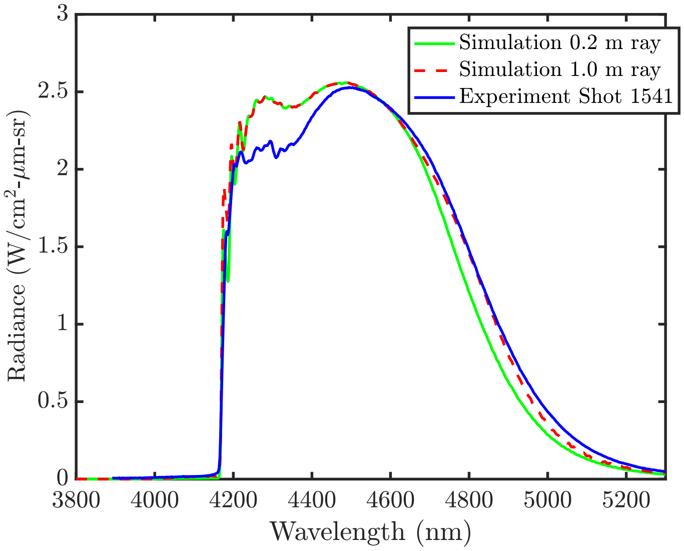

Figure 5.11: Shocktube1_2 test condition spectral radiance measured at the 16° AOA stagnation point.

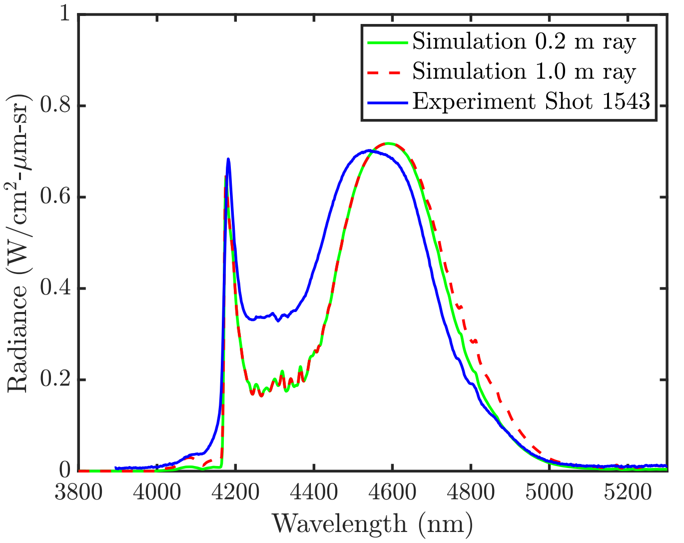

Figure 5.12: Shocktube14_6 test condition spectral radiance measured at the 16° AOA stagnation point.

experimental peak radiance, respectively. The MSL2 condition has a worse match in peak radiance, with the peak radiance of the 1.0 m ray and 0.2 m ray simulations 28.6% and 38.9% below the experimental peak radiance, respectively. At 5000 nm, the experimental spectral radiance is 7.1% and 15.2% above the simulated spectral

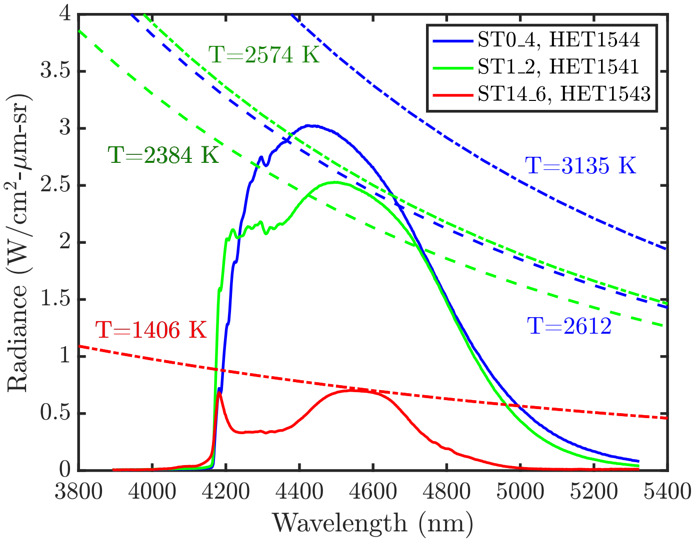

Figure 5.13: The three shock tube experimental data (solid line) and corresponding blackbody curves at the calculated post-shock equilibrium (dashed line) and post-shock chemically frozen (dash-dot line) temperatures.

radiance for the MSL1 and MSL2 conditions, respectively, Figure 5.16.

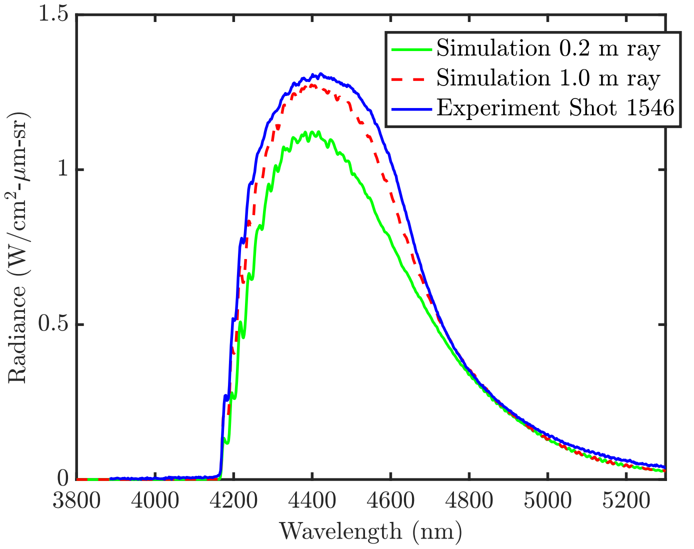

Figure 5.14: MSL1 test condition spectral radiance measured at the 16° AOA stagnation point.

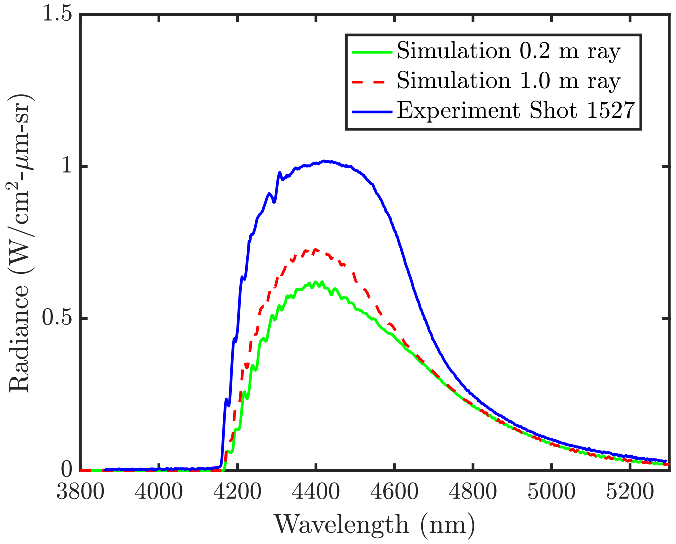

Figure 5.15: MSL2 test condition spectral radiance measured at the 16° AOA stagnation point.

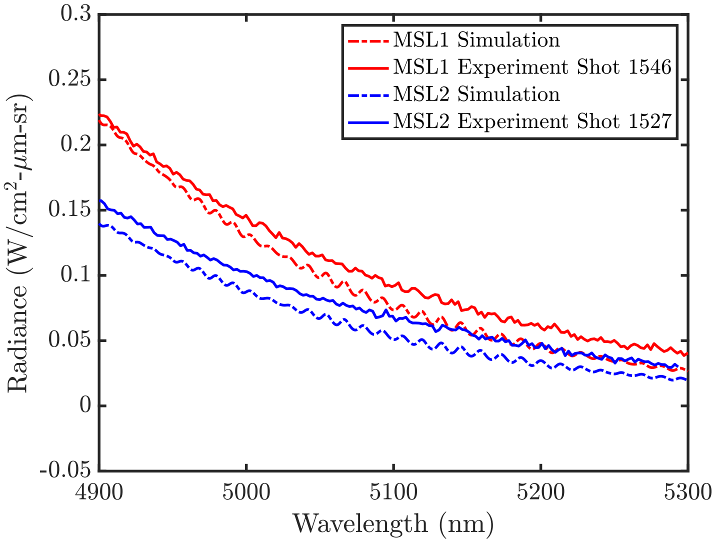

Figure 5.16: 16° AOA stagnation point spectral radiance between 4900 nm to 5300 nm for the MSL1 and MSL2 test condition experiment and simulation (1.0 m ray length).

5.4.3 Expansion Fan in the Line-of-sight

Not accounting for freestream variations in spectral radiance contributions from the upstream, unsteady expansion fan is a possible cause for the simulation underprediction. The accelerator x-t diagrams for the MSL1 condition, Figure 5.2, and MSL2 condition, Figure 5.3 shows the 1D perfect gas dynamic processes during facility operation. The expansion tail traveling down the tube during the exposure time of the camera is illustrated by the blue-dashed lines in Figure 5.9. The location of the intersection of the expansion tail and fiber probe line-of-sight, noted by the red lines on the x-t diagrams, is 0.51 m and 0.30 m at the start and end of the spectral measurement, occurring 70 μs and 150 μs after the arrival of the contact surface. For the MSL2 condition, the expansion tail is 0.44 m and 0.21 m away from the tube exit plane at the start and end time of the spectral measurement, 50 μs and 130 μs after the arrival of the contact surface at the probe location, respectively.

Perfect gas temperature and pressure profiles are calculated through the expansion fan at the times and distances representative of the start and end of the measurement using the method of characteristics (MOC), perfect gas, analytical solution. The MOC calculations for a 1.0 m ray length are input into HARA with the resulting radiation simulations shown in Figure 5.17 for the MSL1 condition and Figure 5.18 for the MSL2 condition. These simulations are compared to the experimental measurement and to simulations not accounting for the expansion fan in the probe line-of-sight.

For the MSL1 condition, the peak spectral radiance increases by 2.2% and 5.0% for the fan simulations at the start and end of the measurement, respectively, compared to the baseline simulation that did not account for the expansion fan. The value of the experimental peak radiance of 1.30 W/cm^2-μm-sr falls between the simulations of peak radiance which include the expansion fan location at two limiting locations.

For the MSL2 condition, the peak spectral radiance increases by 7.8% and 15.5% for the fan simulations at the start and end of the measurement, respectively, compared to the baseline simulation that did not account for the expansion fan. The expansion fan has a larger impact for the MSL2 condition that is closer to the optically thin limit compared to the MSL1 condition as discussed in Section 5.3. The wavelength of the peak radiance increases and the shape around the peak better matches the experiment when the expansion fan is accounted for in the simulation, however the measured peak radiance is 22.6% (start of measurement) and 17.1% (end of measurement) higher in experiments than simulations even when the expansion fan is included.

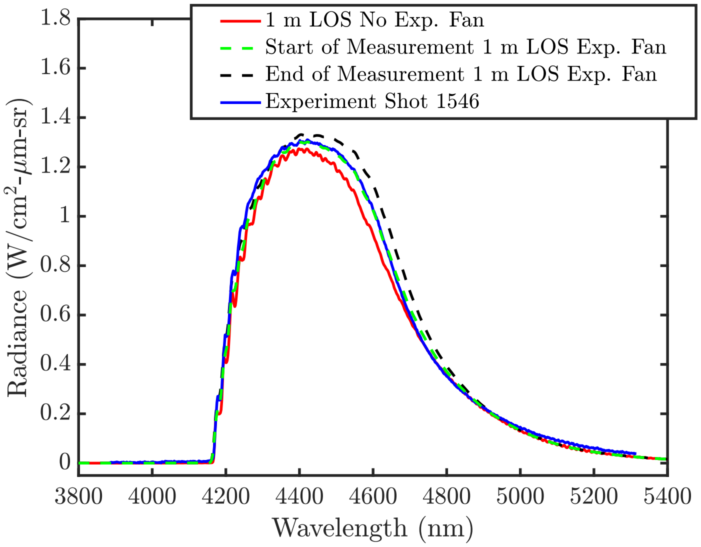

Figure 5.17: MSL1 condition, 16° AOA stagnation point measurement compared to the normal LOS ray simulations accounting for the expansion fan.

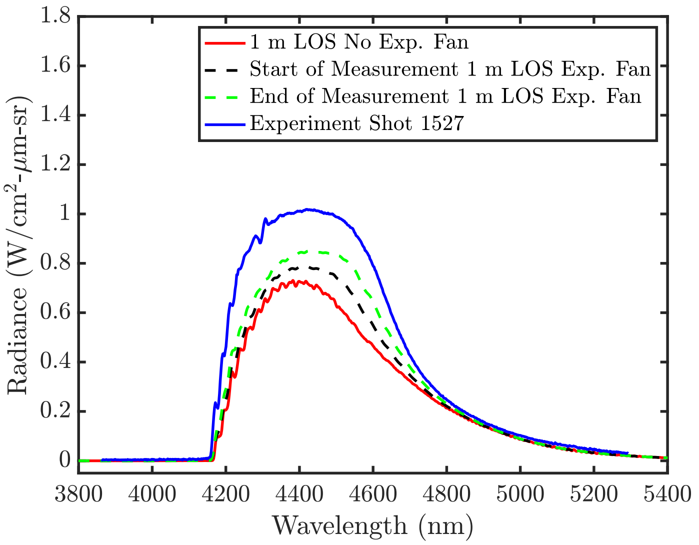

Figure 5.18: MSL2 condition, 16° AOA stagnation point measurement compared to the normal LOS ray simulations accounting for the expansion fan.

5.5 Expansion Tube 16° AOA Lee Side Measurements

To avoid any possible contributions due to the upstream, unsteady expansion fan in the line-of-sight, the forebody is turned 180° from the stagnation point to the lee side resulting in the collection volume shown in the schematic, Figure 5.19. The green and purple lines represent the outer rays of the fiber collection volume. The length from the probe to the wall is 0.095 m for the green line and 0.254 m for the purple line. The red-dashed line is the wall-normal ray. The MSL1 condition lee side experimental measurement and simulation results for the outer rays of the collection volume are shown in Figure 5.21.

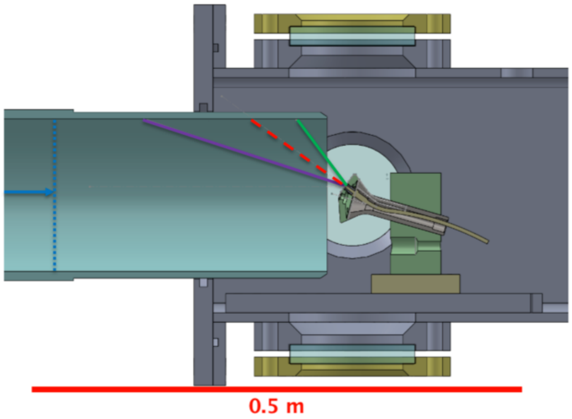

Figure 5.19: Schematic of the fiber collection volume when the probe is mounted at the 16° AOA lee side location on the MSL model.

The simulated peak radiance for the purple (longest) and green (shortest) rays underpredict the experimental peak radiance by 15.2% and 25.1%, respectively. Both the shock distance from the model surface and post-shock density in the line-of-sight will be lower for the lee side compared to the 16° AOA stagnation point, thus the shock layer optical thickness $\tau_\lambda = \alpha_\lambda \Delta$ is expected to be closer to the optically thin limit for the lee side than for the stagnation point location resulting in less shock layer absorption. This is consistent with the radiation measurement showing worse agreement for the 0.254 m ray simulation of the lee side (25.1% underprediction) compared to the 0.2 m ray simulation of the stagnation point (14.5% underprediction).

5.5.1 Tube-Wall Boundary Layer in the LOS

An analysis of the tube-wall boundary layer behind the transmitted shock wave is presented in Section 2.3.3. Based on unit Reynolds number, the MSL1 and MSL2 conditions are expected to have a laminar boundary layer develop along the tube wall. Predictions in Section 2.3.3 using the the theory of Mirels calculated a boundary layer size of 7.1 mm and 8.2 mm for the MSL1 and MSL2 conditions, respectively. Sharma estimated for the RC5 condition, which has the same initial conditions as

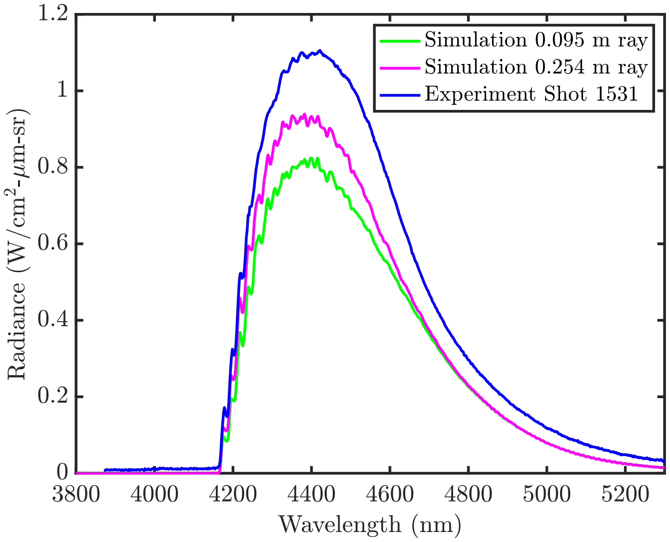

Figure 5.20: MSL1 condition lee side measurement compared to simulations with the shortest and longest ray length in the collection volume.

the MSL1 condition except with a lower burst pressure of P_4 = 2.5 MPa, that the boundary layer thickness is ~25 mm for laminar and turbulent boundary layers [102].

To examine the effect of the boundary layer that develops along the tube behind the transmitted shock wave, a laminar Blausius velocity profile is calculated. Using Crocco-Busemann relations, a temperature profile is estimated and a 25 mm laminar boundary layer is projected onto the 0.095 m ray for the MSL1 condition radiation measurement. No MSL2 condition radiation measurement is obtained for the lee side probe location. Figure 5.21 shows the results of the simulation with a 25 mm laminar boundary layer projected on the shortest ray distance to observe an upper bound on increase in radiance for the MSL1 condition due to the tube-wall boundary layer. This simulation increases the peak spectral radiance by 7.6% compared to the simulation without a wall-boundary in the line-of-sight.

5.6 Expansion Tube 0° AOA Measurements

Figure 5.22 shows the collection volume of the MSL model mounted at a 0° AOA with the probe located on the nose, at the stagnation point. The green lines represent the outer rays of the fiber collection volume and are 0.25 m in length. The red-dashed line is the wall-normal ray that probes upstream along the tube centerline. Two centerline rays of lengths of 1.0 m and 2.0 m are simulated. The 0.25 m length ray represents the shortest ray distance in the collection volume given by the green

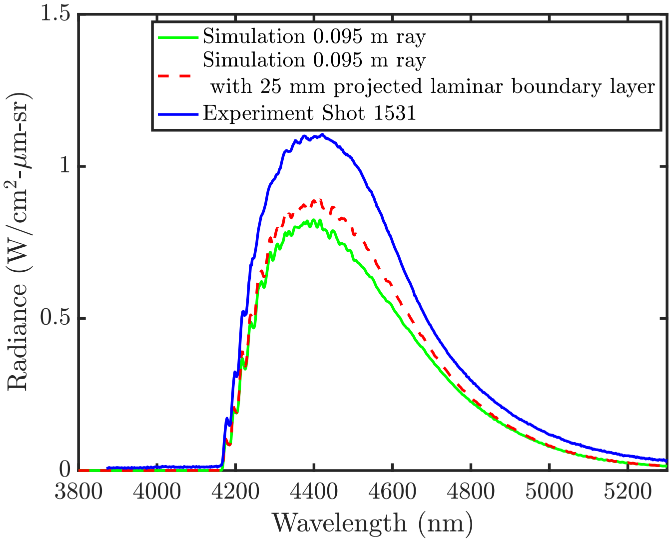

Figure 5.21: Effect of a laminar boundary layer in the line-of-sight of the 16° AOA lee side fiber probe location.

line and the 2.0 m ray length is the approximate length to the primary contact surface, beyond which no radiating gas is expected in the spectral bounds of the experiment.

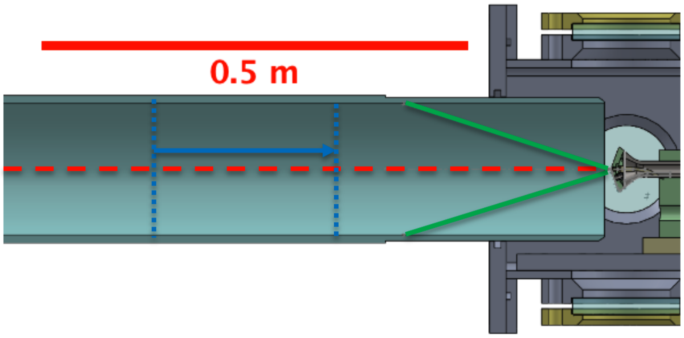

Figure 5.22: Schematic of the fiber collection volume when the probe is mounted at the 0° AOA location on the MSL model.

Results for the MSL1 and MSL2 condition measurements are shown in Figures 5.23 and 5.24, respectively. For the MSL1 condition, the peak radiance of the simulations underpredict the experiment by 30.5%, 19.0%, and 15.6% for the 0.25 m, 1.0 m, and 2.0 m ray length. The radiance at 5000 nm, where shock layer radiance is expected to dominate, is underpredicted by 10.3%. For the MSL2 condition, the

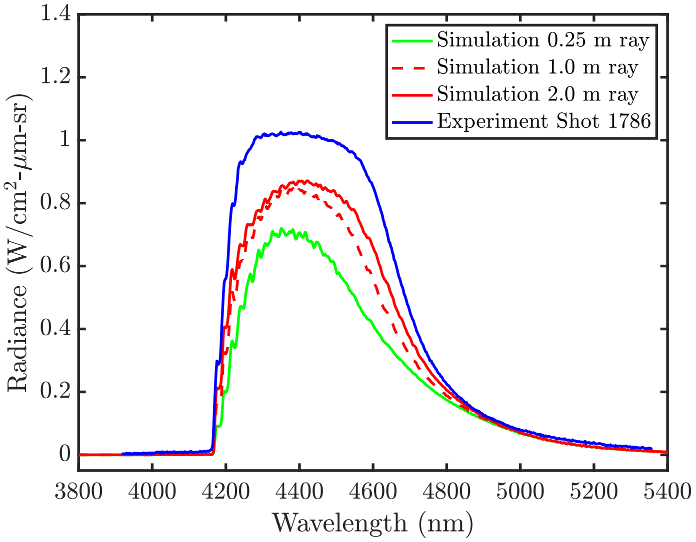

Figure 5.23: MSL1 condition, 0° AOA stagnation point measurements compared with simulations considering three different ray lengths in the probe line-of-sight.

peak radiance of the simulations underpredict the experiment by 59.9%, 47.7%, and 43.2% for the 0.25 m, 1.0 m, and 2.0 m ray length. The peak spectral radiance of the 2 m ray compared to the 1 m and 0.25 m ray shows there is diminishing increase with longer path length due to absorption effects.

The spectral radiance dominated by shock layer radiation at 5000 nm is underpredicted by 10.3% and 18.0% for the MSL1 and MSL2 condition, Figure 5.25. The larger discrepancy for the 0° AOA stagnation measurements compared to the 16° AOA stagnation point measurements (7.1% and 15.2%) can be attributed to less shock layer absorption for the 0° AOA stagnation point measurements, Section 5.9.

5.6.1 0° AOA Shock Layer Chemistry

The presented spectra in this chapter have been calculated assuming Johnston model kinetic rates in the LAURA CFD simulations. The sensitivity of the radiance predictions to the kinetic model is investigated by additional calculations using the Fridman model. Figure 5.26 shows MSL1 and MSL2 0° AOA shock layer simulations calculated with Fridman and Johnston chemistry. The peak radiance calculated assuming the Fridman mechanism are less than the Johnston calculations by 10.9% and 21.9% for the MSL1 and MSL2 conditions, respectively. The spectral radiance of the "tail" at 5000 nm calculated assuming the Fridman model are less than the Johnston calculations by 38.6% and 42.0%. The reason for the decrease in

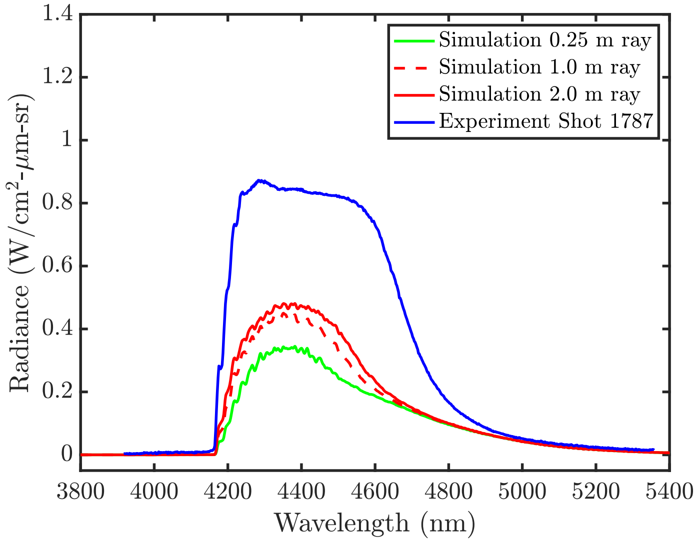

Figure 5.24: MSL2 condition, 0° AOA stagnation point measurements compared with simulations considering three different ray lengths in the probe line-of-sight.

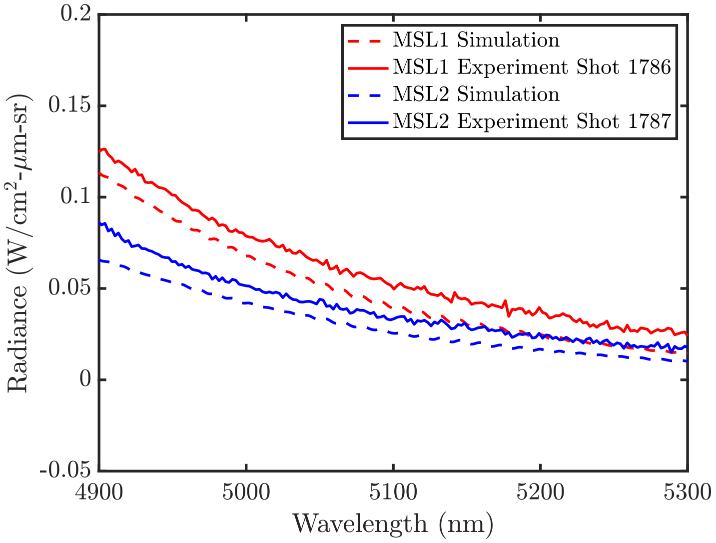

Figure 5.25: 0° AOA stagnation point spectral radiance between 4900 nm to 5300 nm for the MSL1 and MSL2 test condition experiment and simulation (1.0 m ray length).

radiance with Fridman chemistry is due to faster depletion of CO_2 behind the shock wave leading to lower post-shock temperatures and a smaller standoff distance.

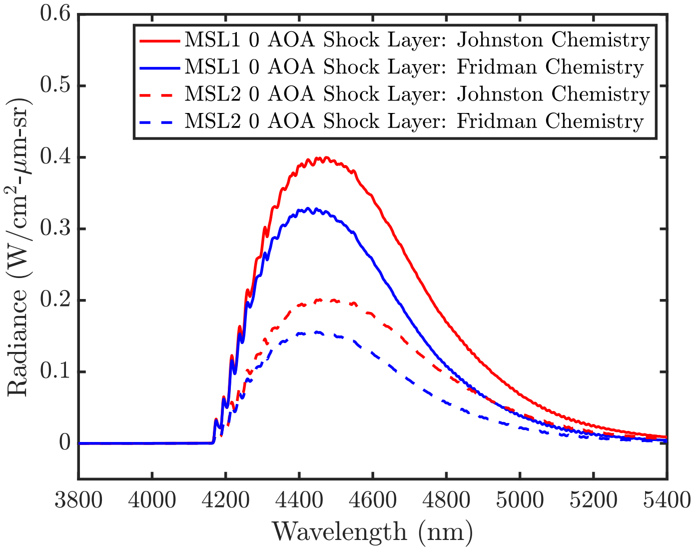

Figure 5.26: Comparison of MSL1 and MSL2 condition shock layer radiation at the 0° AOA probe location implementing two different kinetic mechanisms.

5.7 Expansion Tube Freestream Probe Measurements

Measurements that directly probe the freestream gas are obtained by modifying an existing NPT blank to accommodate a SMA fitting on one side, and a bored out hole with a lip to epoxy a sapphire window on the other side. See Figure 5.27 for a schematic of the freestream probe. The final location of the probe is located 30 cm upstream of the tube exit plane. The green lines represent the outer rays of the fiber collection volume. The red-dashed line is the wall-normal ray perpendicular to the flow.

The measurement is timed as discussed in Section 5.1.3 to expose the IR camera 50 µs after the contact surface arrives at the probe location. The boundary layer developed along the tube is in the probe line-of-sight and is accounted for in the simulations. A laminar boundary layer is assumed and approximated by the Crocco-Busemann relations for the temperature profile and the Blausius velocity profile. A turbulent velocity profile was also considered using a 1/7th power law and produced a spectra that did not significantly vary from the laminar boundary layer profile. Three boundary layer sizes for each condition were considered corresponding to no boundary layer, boundary layer based on Mirels predictions described in Section 2.3.3, and estimates from Figure 3.3 of Sharma [102].

The results for the MSL1 and MSL2 conditions are shown in Figures 5.28 and

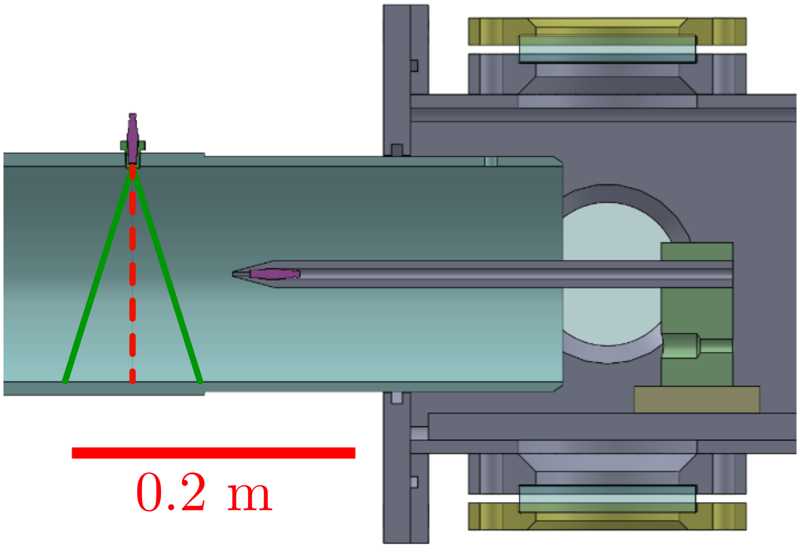

Figure 5.27: Schematic of the fiber collection volume when the freestream probe is mounted in the tube wall. The freestream probe measurement is timed using the pressure trace from the pitot probe extended into the tube.

5.29, respectively. The peak experimental radiance for the MSL1 condition is underpredicted by the no boundary layer, 7 mm boundary layer thickness, and 25 mm boundary thickness simulations by 56.0%, 50.9%, and 42.7% respectively. The peak experimental radiance for the MSL2 condition is underpredicted by the no boundary layer, 7 mm boundary layer thickness, and 25 mm boundary layer thickness simulations by 69.0%, 61.5%, and 44.3% respectively.

5.7.1 Delayed Freestream Measurements

Freestream probe measurements are obtained at a later time window using the timing discussed in Section 5.1.3 and compared to the measurements obtained 50 - 130 μs after the arrival of the contact surface at the probe location. The MSL1 condition experimental spectra obtained 170 - 250 μs after the arrival of the contact surface at the probe location is shown in Figure 5.30 and the MSL2 condition experimental spectra obtained 160 - 240 μs after the arrival of the contact surface at the probe location is shown in Figure 5.31.

The later exposure time window captures part of the less expanded gas observed from pitot traces to start 188 μs and 160 μs after the arrival of the contact surface for the MSL1 and MSL2 conditions, respectively. When the fiber looks upstream, it would see a portion of the less expanded radiating gas obtained at this later time. An 11% increase in peak radiance is observed when exposing later in test time for the

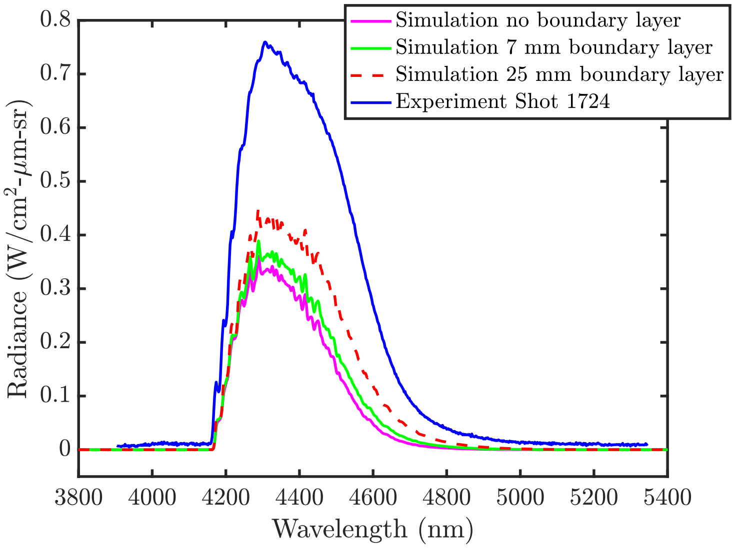

Figure 5.28: MSL1 condition freestream probe measurement compared to simulations implementing different laminar boundary layer thicknesses.

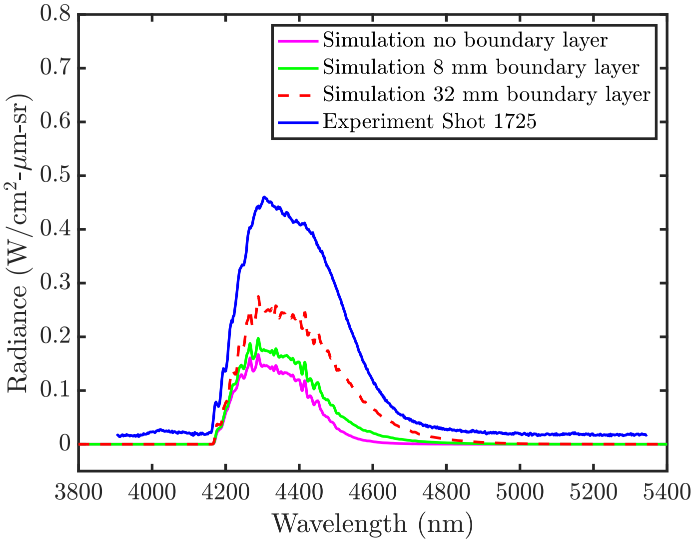

Figure 5.29: MSL2 condition freestream probe measurement compared to simulations implementing different laminar boundary layer thicknesses.

MSL1 condition. The wavelength integrated radiance for the longer delay divided by shorter delay is 8.1% higher for the MSL1 conditions and 3.7% higher for the MSL2 condition.

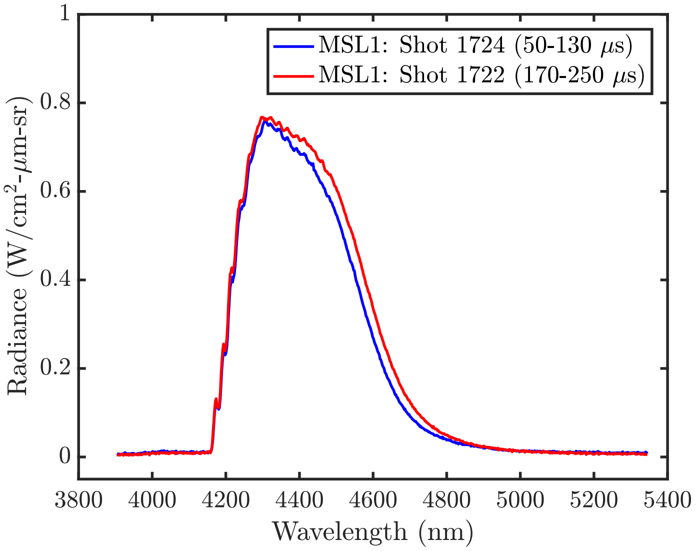

Figure 5.30: MSL1 condition, freestream measurements obtained at different time windows after the arrival of the contact surface at the probe location.

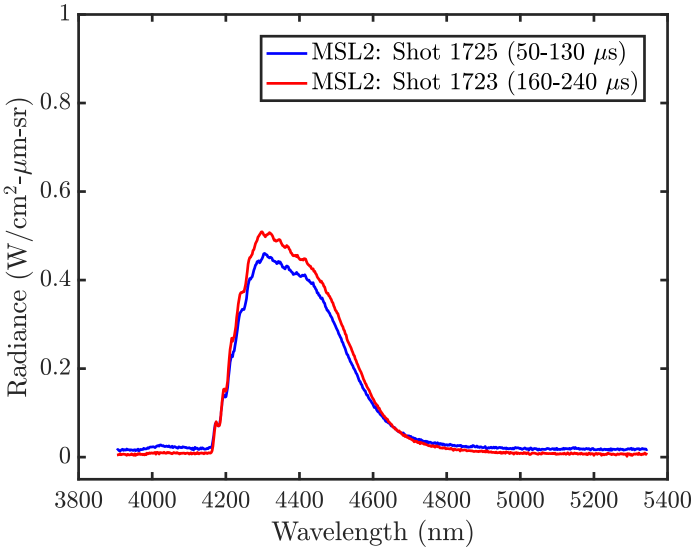

Figure 5.31: MSL2 condition, freestream measurements obtained at different time windows after the arrival of the contact surface at the probe location.

5.7.2 Freestream Radiation Sensitivities to Pressure and Temperature

The freestream pressure is related to the CO_2 number density N_{CO_2} by

$$P = \frac{N_{CO_2} k_B T}{X_{CO_2}} \tag{5.1}$$

where k_B is the Boltzmann constant ($1.381 * 10^{-26}$ J/kg), and the mole fraction of CO_2 for the MSL1 and MSL2 conditions is $X_{CO_2} = 1$. With temperature held constant at the nominal freestream temperature, the sensitivity to freestream pressure is shown in Figures 5.32 and 5.33 for the MSL1 and MSL2 conditions, respectively. In the optically thin limit, pressure is linearly proportional to CO_2 number density and doubling pressure doubles the spectral radiance. In the optically thick limit, doubling pressure has no effect on the spectra. For the MSL1 condition, increasing freestream pressure from 3.3 kPa to 5.0 kPa and 10.0 kPa increases the peak spectral radiance by 16.5% and 31.6%. For the MSL2 condition, increasing freestream pressure from 1.7 kPa to 3.0 kPa and 6.0 kPa increases the peak spectral radiance by 33.6% and 73.2%.

The freestream radiation sensitivity to temperature is shown in Figures 5.32 and 5.33 for the MSL1 and MSL2 conditions, respectively. With pressure held constant at the nominal freestream pressure, performing freestream simulations with increasing temperatures shows there is a much greater dependence of spectral radiance to temperature than there is to pressure. An upper bound on the freestream temperature to match the peak radiance measured in the experiment is shown to be 1700 K for the MSL1 condition and 1600 K for the MSL2 condition, higher than the predicted perfect gas temperature of 1221 K and 1042 K. The free stream calculated assuming the post-shocked test gas is fully processed by a reflected shock predicts a temperature of 1455 K and 1321 K respectively, still 245-279 K below the temperature obtained in experiments.

5.8 Simulations Assuming a Reflected Shock Processed Free Stream

The possibility of a reflected shock from the secondary diaphragm is discussed in Section 2.3.3 and has yet to be directly observed or disproven for the MSL1 and MSL2 conditions. As a limiting case, the reflected shock is assumed to fully process the test gas. The calculated reflected shock processed free stream is shown in Table 2.9. The corresponding simulations for the spectral radiance at the 0° AOA stagnation point for the MSL1 condition (Figure 5.36) and MSL2 condition (Figure 5.37), and the 16° AOA stagnation point for the MSL1 condition, Figure 5.38 and MSL2 condition, Figure 5.39. The experimental spectra are shown on each figure for comparison.

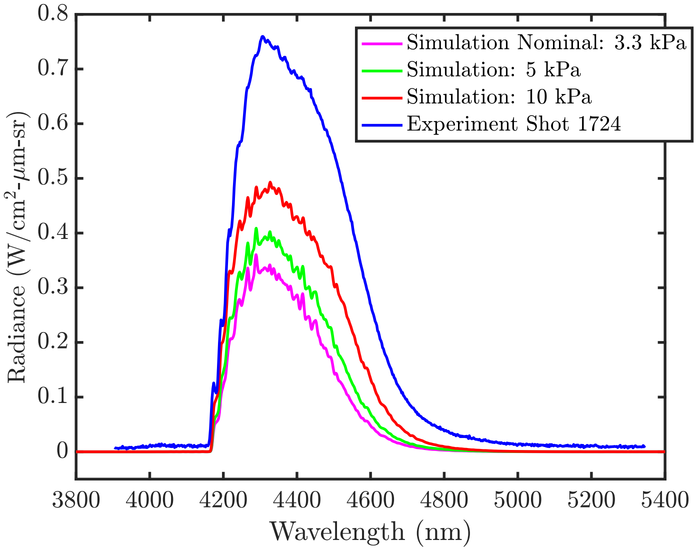

Figure 5.32: MSL1 condition freestream measurement compared to 6" core flow simulations to study sensitivity at different pressures and T_∞ = 1221 K.

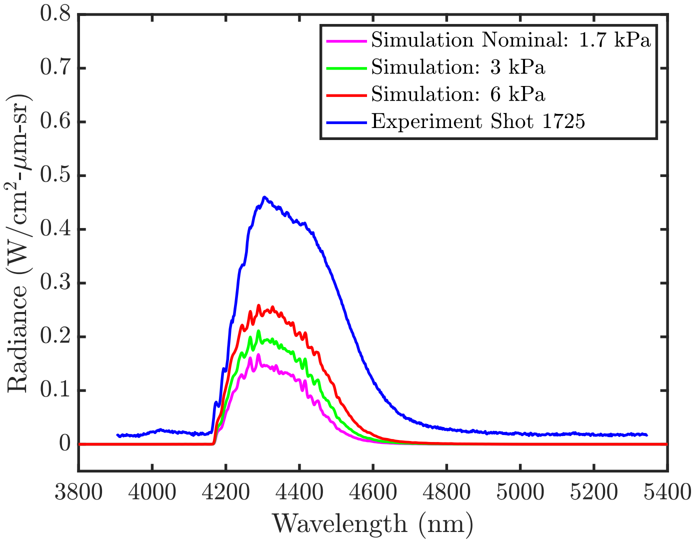

Figure 5.33: MSL2 condition freestream measurement compared to 6" core flow simulations at different pressures to study sensitivity with T_∞ = 1042 K.

5.9 Integrated Measurements

A quantifiable measure of the difference between the experimental and simulated spectra is the ratio of integrated spectra $I_{\text{exp}}/I_{\text{sim}}$. The integrated radiance I is

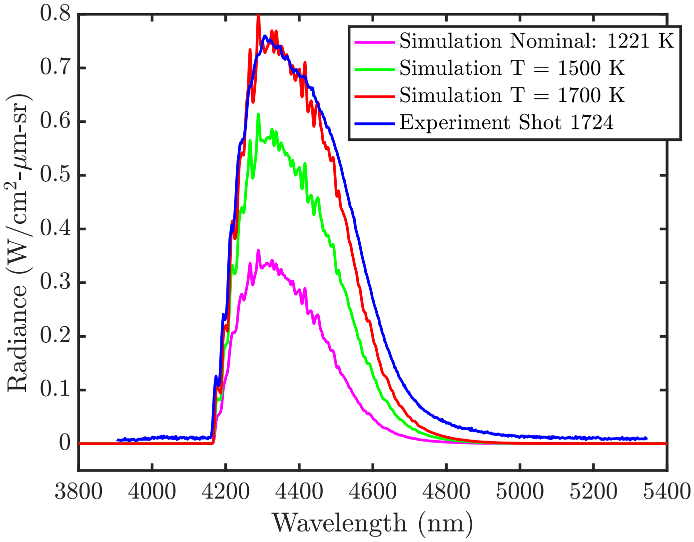

Figure 5.34: MSL1 condition freestream measurement compared to 6" core flow simulations at different temperatures to study sensitivity and P_∞ = 3.35 kPa.

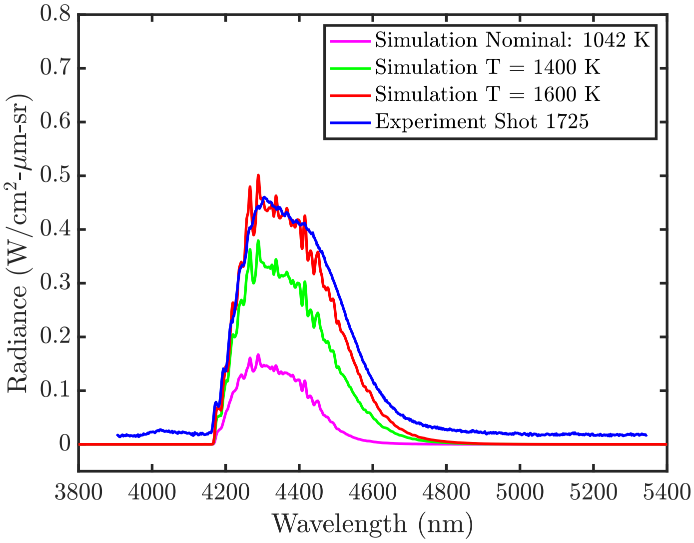

Figure 5.35: MSL2 condition freestream measurement compared to 6" core flow simulations at different temperatures to study sensitivity and P_∞ = 1.66 kPa.

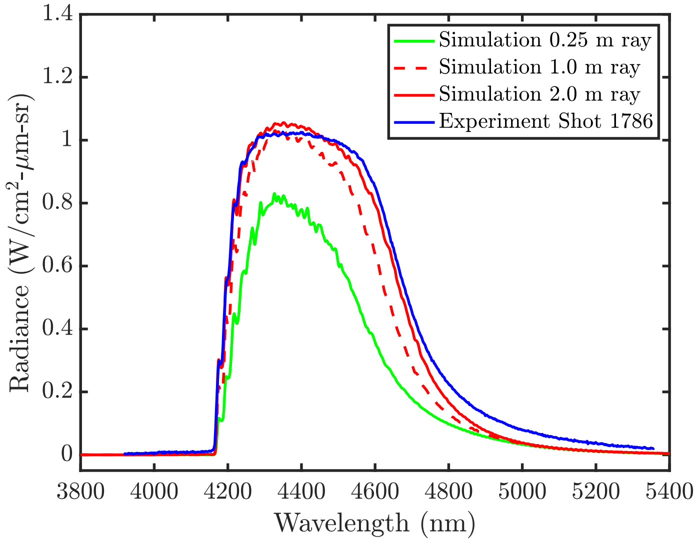

Figure 5.36: 0° AOA stagnation point MSL1 condition measurement compared with simulations assuming a reflected shock processed free stream. Shock layer chemistry is modelled with Fridman chemistry.

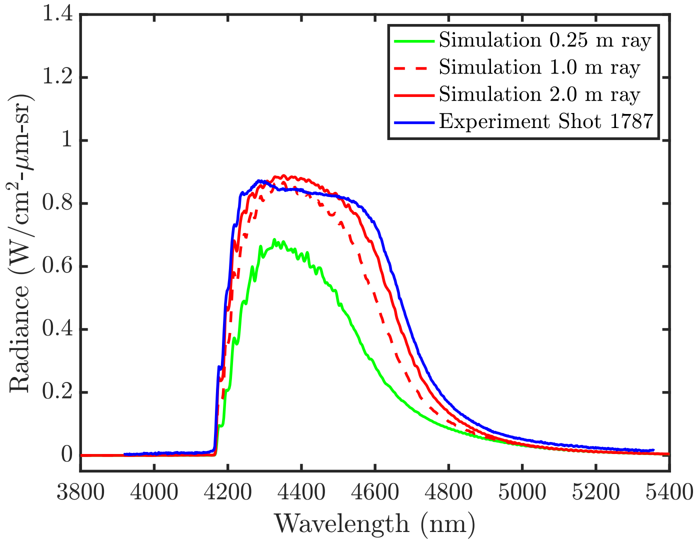

Figure 5.37: 0° AOA stagnation point MSL2 condition measurement compared with simulations assuming a reflected shock processed free stream. Shock layer chemistry is modelled with Fridman chemistry.

calculated by

$$I = \int_{\lambda} I_{\lambda} d\lambda \tag{5.2}$$

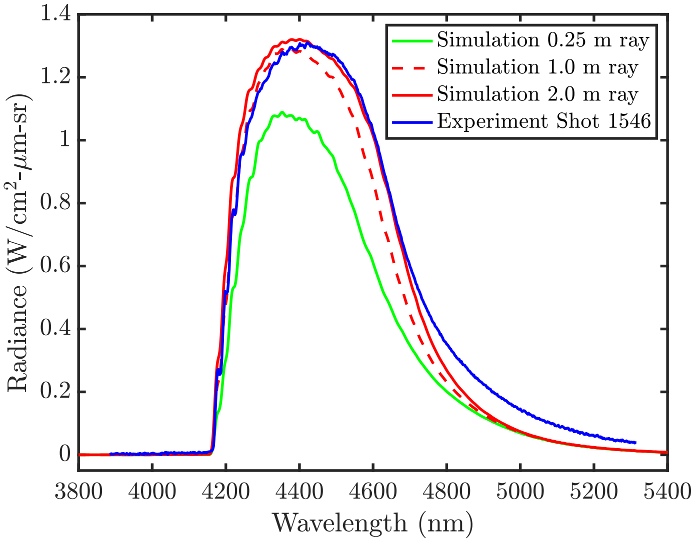

Figure 5.38: 16° AOA stagnation point MSL1 condition measurement compared with simulations assuming a free stream processed by a reflected shock. Shock layer chemistry is modelled with Fridman chemistry.

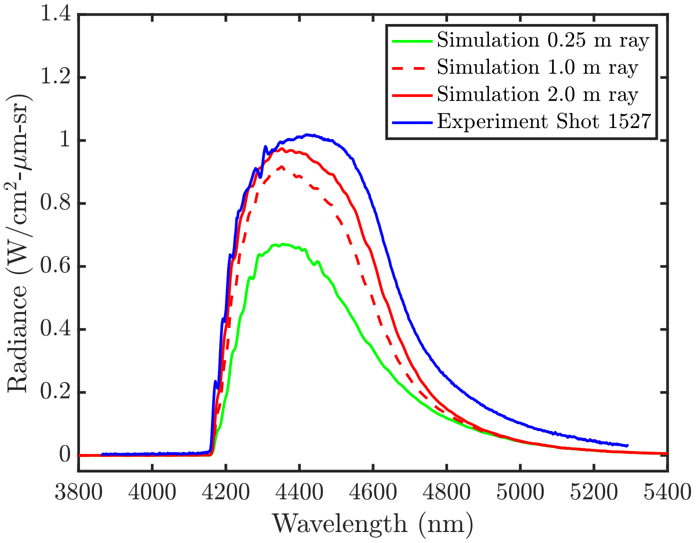

Figure 5.39: 16° AOA stagnation point MSL2 condition measurement compared with simulations assuming a free stream processed by a reflected shock. Shock layer chemistry is modelled with Fridman chemistry.

for the integral bounds 3900 to 5350 nm determined by the range measured on the camera. A summary of $I_{\text{exp}}/I_{\text{sim}}$ for the different orientations and conditions tested are shown in Table 5.3.

Table 5.3: Summary of ratio of experimental to simulated integrated radiance in different configurations. Representative ray lengths are chosen. The distance Δ_n between the body and shock along the normal line-of-sight extracted from simulations is also shown.

	ST0_4	**MSL1**	**MSL1**	**MSL1**	**MSL2**	**MSL2**	**MSL1**	**MSL2**
Orientation	16° Stag.	16° Stag.	16° Lee	0° Stag.	16° Stag.	0° Stag.	FS Probe	FS Probe
Ray (m)	1.00	1.00	0.25	0.10	1.00	1.00	0.15	0.15
$I_{\text{exp}}/I_{\text{sim}}$	0.95	1.07	1.25	1.35	1.49	2.32	2.51	3.41
Δ_n (mm)	7.0	3.7	3.0	1.5	3.2	1.1	N/A	N/A

The integrated radiance for the shock tube condition without observable absorption in the boundary layer at the model surface, ST0_4, is within 5% of the integrated simulated radiance. This is an optically thick condition at significantly higher temperatures and pressures than the expansion tube conditions.

The normal line-of-sight distance from the wall to the shock Δ_n extracted from simulations for the expansion tube conditions and orientations tested are also shown in Table 5.3. For both the MSL1 condition and the MSL2 condition, the discrepancy between experiment and simulation decreases with increasing shock layer thickness Δ_n. The differences in the shock layer thickness also correspond to differences in the post-shock temperature and pressure profiles along the line of sight of the rays, however, these effects on the absorption thickness are not included in this qualitative discussion. The largest discrepancy occurs in the freestream probe measurements and the discrepancy is larger for the MSL2 condition than the MSL1 condition. The initial conditions for the MSL1 and MSL2 conditions vary only in the initial pressure in the accelerator (MSL1: P_5 = 180 mTorr vs. MSL2: P_5 = 75 mTorr).

The larger discrepancies observed in the expansion tube conditions is partially due to freestream flow features such as the expansion fan and the wall boundary layer in the line-of-sight not accounted for in the simulations. A summary of the integrated results for simulations that include these features into the freestream flow field are shown in Table 5.4. The expansion fan is modeled as discussed in Section 5.4.3 and the 16° AOA stagnation point, 1.0 m ray is considered. The projected boundary layer is modeled as discussed in Section 5.5.1 and the lee side, 0.095 m ray is considered. Accounting for flow features decrease the discrepancy between the experiment and simulation.

The possibility of a reflected shock processed free stream is considered and the integrated ratio of experimental to simulated (1.0 m ray) radiance for 0° AOA and

Table 5.4: Summary of $I_{\mathrm{exp}}/I_{\mathrm{sim}}$ when the expansion fan and tube-wall boundary layer flow features are implemented into the simulations. The 1.0 m ray simulations are used for the expansion fan flow feature comparison. The columns Start and End correspond to the expansion fan implemented into the simulation at the start and end of measurement exposure time. The 0.095 m ray is used for the lee side boundary layer feature comparison.

	MSL1 16° AOA Stag.			**MSL2 16° AOA Stag.**			**MSL1 Lee Side**	
Flow Feature	No fan	Start	End	No fan	Start	End	No BL	25 mm BL
$I_{\mathrm{exp}}/I_{\mathrm{sim}}$	1.07	1.02	0.97	1.49	1.35	1.24	1.40	1.29

16° AOA stagnation point free stream is summarized in Table 5.5. The simulations assume Fridman chemistry in the shock layer. In the expansion tube, simulations with Fridman chemistry result in a better match in shock standoff distance compared to simulations with Johnston chemistry discussed in Chapter 4. The shock layer simulations using Fridman chemistry decrease the spectral radiance compared to simulations using Johnston chemistry as discussed in Section 5.6.1.

The better match between integrated experimental and simulated radiance in three of the four cases can be attributed to difference in freestream conditions. For the MSL1 16° AOA case, the agreement is slightly worse with the Fridman kinetic model than the Johnston model ($I_{\mathrm{exp}}/I_{\mathrm{sim}}$ = 1.13 vs. $I_{\mathrm{exp}}/I_{\mathrm{sim}}$ = 1.07).

Table 5.5: Summary of ratio of experimental to simulated integrated radiance for 1.0 m simulation ray length assuming a reflected shock fully processed free stream and Fridman shock layer chemical kinetics. The nominal case assuming perfect gas free stream and Johnston shock layer chemical kinetics is shown for comparison.

Model Orientation	MSL1 0°	MSL2 0°	MSL1 16°	MSL2 16°
$I_{\mathrm{exp}}/I_{\mathrm{sim}}$ reflected shock	1.20	1.21	1.13	1.36
$I_{\mathrm{exp}}/I_{\mathrm{sim}}$ nominal	1.35	2.32	1.07	1.49

5.10 Conclusions

An experiment was successfully designed to measure spectrally resolved radiation measurements of the 4.3 µm CO_2 band using chalcogenide fiber optic probes mounted behind a sapphire window. Surface point measurements at 0° and 16° AOA for three different locations on a scaled MSL model were obtained. Direct measurements of the free stream were obtained with a freestream probe mounted along the tube wall.

The tangent slab approximation was used to conclude that simulating the normal line-of-sight in the shock layer is valid within 2.3% for optically thin conditions and is valid with negligible error for the optically thick conditions. A calibration method was developed that closely followed the methods of Cruden [16]. This method was validated for optically thick conditions by the shock tube measurements that showed good agreement in peak radiance between experiment and simulation (within 2.1%). A strong absorption feature in the spectra between 4200 nm to 4400 nm was identified to be caused by the model wall boundary layer. The optically thick shock tube emission was shown to be blackbody limited, bounded by the Planck curves defined by the post-shock equilibrium and frozen temperatures. For the 16° AOA stagnation point shock tube condition with initial pressure P_1 = 0.4 kPa, the experimental integrated radiance agreed with the HARA simulation integrated radiance within 5%.

For the expansion tube conditions, there is a greater need for the line-of-sight through the freestream gas to be taken into account since the shock layer is closer to the optically thin limit. Different ray lengths determined by the geometry of the fiber acceptance cone were simulated and compared to the experimental measurements. Discrepancy between experiments and simulations was quantified using integrated radiance profiles. When flow-field features were accounted for along the line-of-sight, the discrepancy between the experimental and simulated peak and integrated radiance decreased. It was observed that the discrepancy between experiments and simulations is larger for the MSL2 condition that is closer to the optically thin limit than the MSL1 condition. For both conditions, the discrepancy is larger with decreasing shock standoff distance. This is believed to be due to the increase in photons that get absorbed and reemitted in a longer shock layer distance. The discrepancy is largest for the direct freestream measurements where radiation is highly sensitive to freestream temperatures. The best fits to the freestream measurements occurred when the freestream temperatures for the MSL1 and MSL2 conditions were 1700 K and 1600 K. This is higher than predicted temperatures of 1221 K and 1042 K assuming inviscid facility operation, and also higher than the calculated gas temperatures of 1455 K and 1321 K assuming equilibrium chemistry for the test gas stagnated and completely processed by a reflected shock before expanding.

Chapter 6

T5 CO_2 RADIATION MEASUREMENTS

6.1 Introduction

After developing the spectroscopic calibration technique and making forebody measurements in the expansion tube, the setup was moved to the T5 Reflected Shock Tunnel in order to test a larger test article, enabling wake measurements. Forebody and wake MWIR spectral radiance and shock shape measurements are obtained for CO_2 flow over a 25.3:1 scaled model (177.8 mm base diameter). Two conditions are developed to match the binary scaling parameter vs. total enthalpy flight trajectories of the recent MSL [23] and ExoMars [10] missions, Section 2.1. The model is mounted at a 0° AOA to emulate the ExoMars mission ballistic entry trajectory while the model is mounted at a 16° AOA for the MSL mission lifting entry trajectory. Pitot measurements are presented in Section 2.4.2 and are in agreement with nozzle simulations to within the uncertainty of the position of the pitot rake during firing. A summary of all shots performed in this campaign is shown in Table 6.1. The accompanying simulations needed for radiation predictions are being carried out by NASA Ames.

Table 6.1: T5 Radiation Campaign Summary of Conditions

Shot #	**Condition**	**AOA**	**Fiber Location**	$\Delta \pm \sigma$ **(mm)**
2893	ExoMars	Pitot Measurement		
2891		0°	Stag. Pt.	4.71 ± 0.11
2892				4.71 ± 0.11
2895			Wake	4.99 ± 0.11
2896				4.37 ± 0.11
2894	MSL	Pitot Measurement		
2897		16°	Wake: lee side	AOA Schlieren
2898			Wake: wind side	
2899			NA	
2900			AOA Stag. Pt.	
2901		0°	Stag. Pt.	5.58 ± 0.13
2902	Contour			7.53 ± 0.13

Experimental Setup

The test article mounted in the T5 test section is shown in Figure 6.1. The sting mount can be adjusted to various angles of attacks with the 0° AOA mount and 16° AOA mount utilized. Attached at the end of the sting is a PVC flex tube secured with hose clamps to ensure the fiber is protected during the test. A test section feedthrough flange with three KF-50 vacuum ports is fabricated to accommodate the optical fiber. One of the ports utilized the custom fiber optic feedthrough port used in the HET while the other two ports are blanked off.

Figure 6.1: 7" diameter test article mounted at 0° AOA in the T5 test section.

The fiber optic probes are discussed in Section 3.2.4. The forebody measurements use the same fiber type as the HET experiments, a 500 µm core chalcogenide fiber with a nominal acceptance half angle of 17.5°. Wake measurements are obtained using a 200 µm core indium fluoride fiber that has a smaller bending radius and is less brittle. It is necessary to switch to these fibers to accommodate turning the fiber inside the model towards the afterbody. The indium fluoride fibers have a nominal acceptance half angle of 11.5°.

The blackbody spectral-intensity calibration is performed using a BBS1200 blackbody source at a temperature T = 1473.2 K, rated by the manufacturer to be accurate within ± 0.2 K. Calibration is conducted inside the test section when the fiber is tested at the 0° AOA stagnation point and outside the test section on a optical table for the other fiber locations. To ensure the fiber probe views the back of the blackbody source, the model is mounted on the table and aligned with the blackbody source using a laser level. Consistent calibration between the in situ and optical table methods is checked by comparing the calibration function $S_{\lambda,\mathrm{cal}} = N_{\lambda,\mathrm{cal}} / B_\lambda$ at $\lambda = 3892$ nm where $N_{\lambda,\mathrm{cal}}$ is the number of counts detected on the camera and $B_{\lambda,\mathrm{cal}}$ is the blackbody function. At T=1473.2 K, $B_\lambda = 1.18$ W/cm^2-sr-µm. The four in-situ 0° AOA stagnation point calibration tests taken on separate days resulted in $S_{\lambda,cal} = 795 \pm 72$ counts/(W/cm^2-sr-µm). The single 16° AOA stagnation point bench top calibration resulted in $S_{\lambda,\mathrm{cal}} = 756$ counts/(W/cm^2-sr-µm), within the ± 72 counts/(W/cm^2-sr-µm) scatter of the in-situ measurements. The scatter of the in-situ measurements are a result of the wear on the sapphire window and the variation of the location of the fiber on the slits set by the fiber adapter.

Freestream Conditions

Two nominal test conditions named T5 ExoMars and T5 MSL are chosen to best match the binary scaling parameter vs. total enthalpy trajectory for the flight MSL [23] and ExoMars [10] missions, Figure 6.2. The ExoMars and MSL T5 conditions, the HET conditions, as well as an additional contour nozzle condition are also shown. The freestream conditions are calculated on a shot-to-shot basis by the method described in Section 2.2 and shown in Apppendix B. Freestream conditions for three experiments corresponding to T5 ExoMars, T5 MSL, and contour nozzle initial conditions are shown in Table 6.2.

Experimental Timing

Data acquisition is triggered by the primary shock arrival by the pressure transducer located directly upstream of the nozzle as shown in Figure 2.5. Established flow in the test section is observed approximately one milliseconds after trigger time as shown by the pitot pressure traces for shot T52893, Figure 2.14. Test time typically lasts one to two milliseconds (approximately one to three ms after trigger time), terminated by driver gas contamination [108]. All of the measurements are obtained after flow establishment time and within test time. The ten PCO single shot images and radiation spectra are obtained 1.8 ms after trigger time for all tests except shots T52891 and T52892 that are obtained 1.5 ms after trigger time. The schlieren images have an exposure time of 1.5 µs. The five forebody radiation measurements are obtained with an exposure time of 80 µs on the IR detector, consistent with the

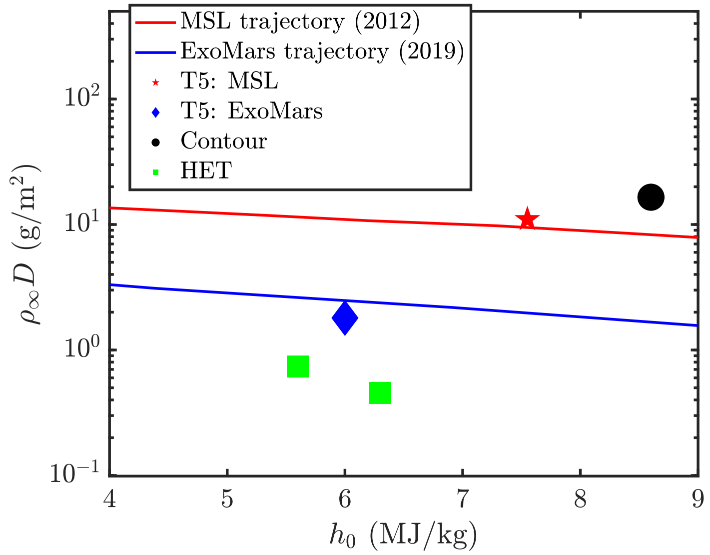

Figure 6.2: Binary scaling parameter $\rho_\infty D$ vs. total enthalpy h_0 comparison of the T5 Exomars and MSL conditions to flight trajectories of the two recent missions. The HET MSL1 and MSL2 conditions and the T5 contour nozzle condition are also plotted.

Table 6.2: Freestream conditions for the sphere-cone tests analyzed.

Shot Condition	**ExoMars T52892**	**MSL T52901**	**Contour T52902**
Nozzle	Conical: 900:1	Conical: 100:1	Contour
$\rho_\infty D$ (g/m^2)	1.8	10.7	16.5
U (m/s)	2937	2967	3160
T (K)	855	1651	1793
T_V (K)	887	1653	1793
P (kPa)	1.5	21.3	35.9
ρ (g/m^3)	8.8	60.4	92.7
h_0 (MJ/kg)	6.1	7.7	8.6
Ma	5.9	4.3	4.3
Y_{CO_2}	0.828	0.745	0.719
Y_{CO}	0.110	0.162	0.179
Y_{O_2}	0.062	0.091	0.100
Y_{O}	2.0E-5	0.002	0.002

HET measurements. The four afterbody radiation measurements are obtained with an exposure time on the IR camera of 200 µs.

6.2 Shock Shape Measurements

The T5 schlieren system used to obtain shock shape measurements is described in Section 3.2.3. For the 0° AOA experiments, the standoff distance is measured and presented in Table 6.1. The ExoMars and MSL tests are conducted with a conical nozzle geometry. 0° AOA schlieren images are shown in Figure 4.16b for T52892 ExoMars condition, Figure 6.3a for T52901 MSL condition, and Figure 4.16d for T52902 contour nozzle condition. A 16° AOA schlieren image is shown in Figure 6.3b for T52900 MSL condition. The uncertainty reported in Table 6.1 for the 0° AOA measurements obtained from the high resolution images is the propagation of error of 1 pixel uncertainty at the body and at the shock. The average and standard deviation of the four repeat 0° AOA measurements is 4.70 ± 0.25 mm. The uncertainty due to shot-to-shot variation is 5.3%, larger than the uncertainty in the measurement of 2.3% and less than the uncertainty observed from the standoff distance unsteadiness during test time (0.8 to 1.8 ms, T52866) of 8.1% presented in Section 4.1.4.

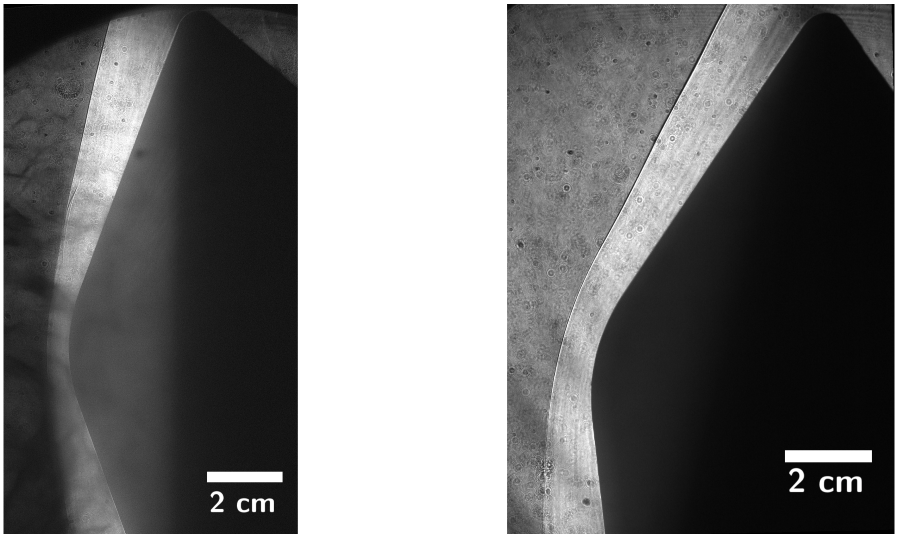

(a) T5 Shot 2901.

(b) T5 Shot 2900.

Figure 6.3: Schlieren images for the MSL condition obtained with the model at 0° and 16° angle of attack.

6.3 Shock Layer Radiation

Simulations of wall-directed radiative intensity for flow over the T5 model geometry are plotted along the 0° AOA stagnation streamline for the T5 ExoMars and MSL conditions, Figure 6.4. The smeared rotational band (SRB) model is used for these computations, applying a simplified and efficient treatment of each molecular band system [1]. This approach does not properly capture wall boundary layer absorption but is useful for evaluating the appropriate optical thickness regime.

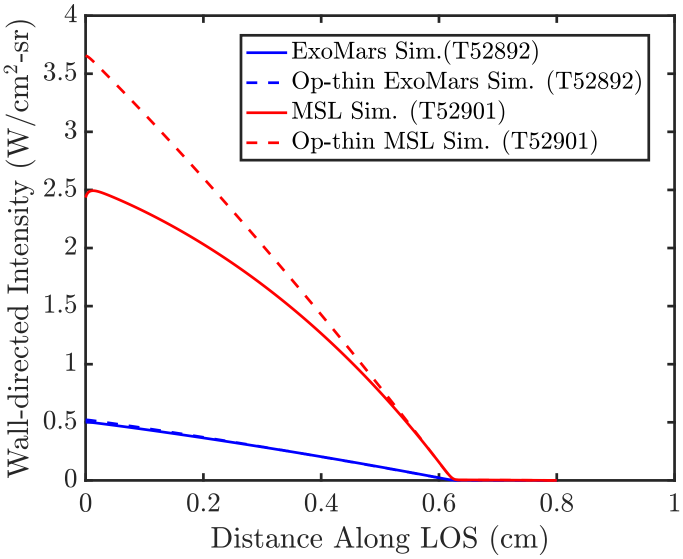

Figure 6.4: T5 ExoMars and MSL condition 0° AOA stagnation point LOS shock layer simulations compared to simulations in the optically thin limit.

The ExoMars condition integrated radiative intensity at the wall is 4.0% below the optically thin limit and can be considered optically thin. The MSL condition integrated radiative intensity at the wall is 33.4% below the optically thin limit and a decrease in radiative intensity next to the wall indicates boundary layer absorption is present in the experiments. Figure 6.5 shows the freestream density vs. enthalpy for the two HET conditions, the ExoMars and MSL T5 conditions and flight trajectories, and contour nozzle condition. For all of the conditions considered in the radiation work, the freestream density is an order of magnitude greater than flight trajectories.

Background Radiation

A background radiation signal can be observed in all of the T5 measurements that is not present in any of the HET expansion tube and shock tube experiments on the spectra between 3850 nm to 4150 nm. In the schlieren images, particles can sometimes be observed as in Figure 6.3a. These particles are a possible source of the background radiation. The particles are believed to be due to soot formed in the CO_2 reservoir at high pressures greater than 300 atm. The soot is mitigated by an extensive cleaning process of the shock tube outlined in the thesis of Jewell [52]. For

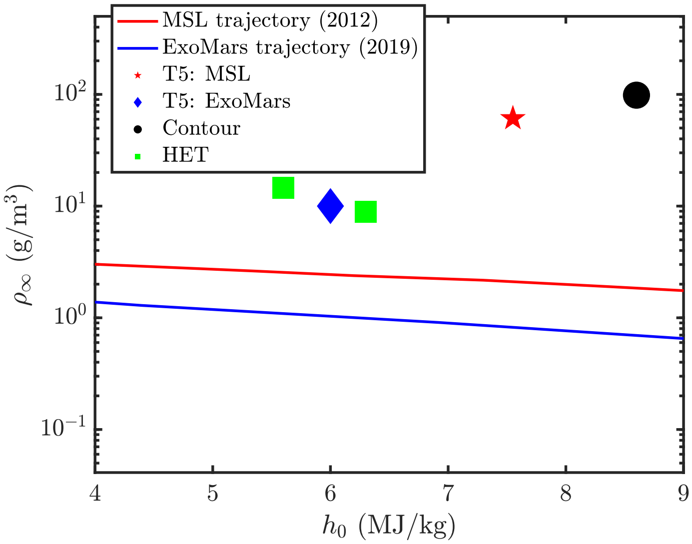

Figure 6.5: Freestream density vs. total enthalpy comparison of the T5 Exomars and MSL conditions to flight trajectories of two recent missions. The HET MSL1 and MSL2 conditions and a contour nozzle condition are also plotted.

future investigations into the source of this experimental artifact, the background signal is fit to be a black body described by Planck's law (Equation 1.37) and the effective temperature ranges from 590 to 1530 K for selected tests.

6.4 0° AOA Radiation Measurements

The coordinates (x/R, y/R) of the two probe locations used when the model is mounted at a 0° AOA are at the nose on the forebody (0,0) and close to the shoulder in the afterbody (0.557, 0.861). The coordinate system is shown in Figure 3.3, where x is the distance into the body and y is the distance in the radial direction. These locations are shown in Figure 6.6 together with the acceptance cones of the forebody and wake probes. The solid lines indicate the outside rays of the acceptance cone and the dashed lines indicate the normal ray.

Forebody Measurements

Two repeat 0° AOA stagnation point measurements are obtained at the ExoMars condition as shown in Figure 6.7. The repeat experiments show good agreement, with the shape matching for the majority of the wavelengths providing confidence in the shot-to-shot repeatability of T5 radiation measurements in the forebody. The largest difference occurs at the peak where there is a 4% difference in radiance.

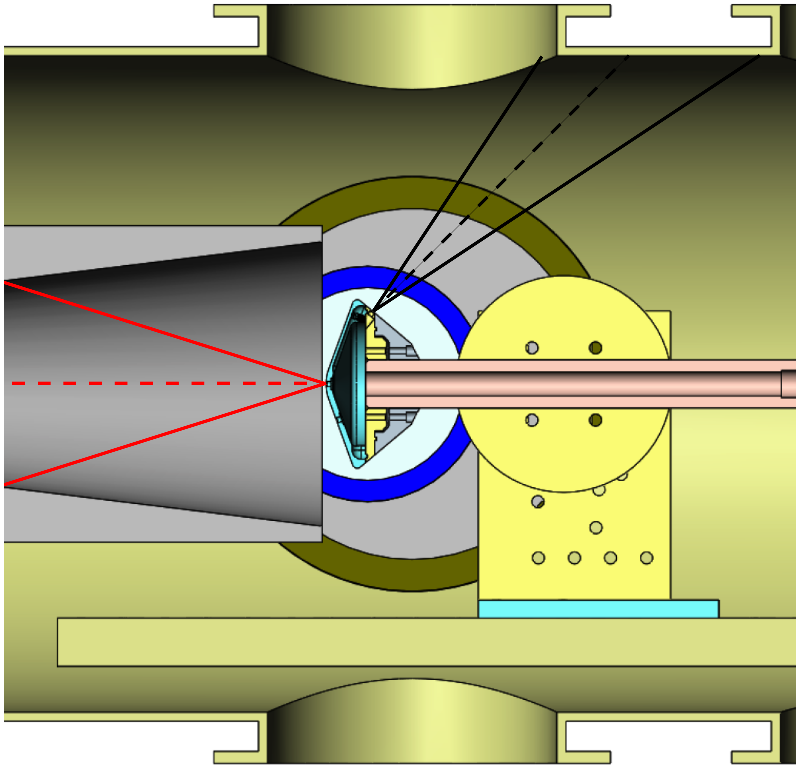

Figure 6.6: 0° AOA T5 MSL model schematic with rays emanating from the fiber probe locations. The forebody and afterbody probes have acceptance cone half angles of 17.5° and 11.5°, respectively.

The 0° AOA stagnation point measurements obtained at the MSL and contour nozzle condition are shown in Figures 6.8 and 6.9, respectively. As predicted in the shock layer simulations, absorption features due to the boundary layer on the model surface appears for these two conditions. The ExoMars, MSL, and contour condition measurements with freestream temperatures of 855 K, 1651 K, and 1793 K, Table 6.2, are fit to blackbody spectra to obtain blackbody curve temperatures at 760 K, 1020 K, and 1530 K.

Wake Measurements

Two repeat 0° AOA wake measurements are obtained for the ExoMars condition as shown in Figure 6.10. The repeat experiments show excellent agreement with the shape matching and the peak radiance differing by 2.0% providing confidence in the shot-to-shot repeatability of T5 radiation measurements in the afterbody. The offset blackbody temperature in the wake is 590 K which is less than 760 K extracted from the forebody measurement.

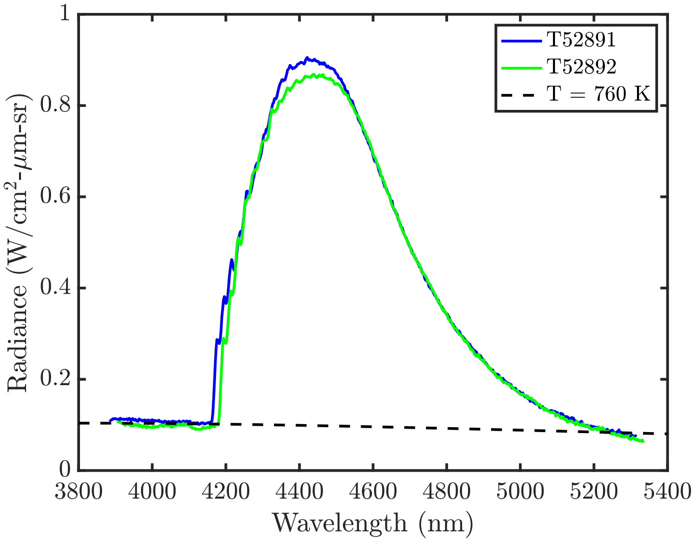

Figure 6.7: T52891 and T52892 ExoMars condition 0° AOA stagnation point measurements. The blackbody curve that best fits the background radiation is indicated by the black-dashed line.

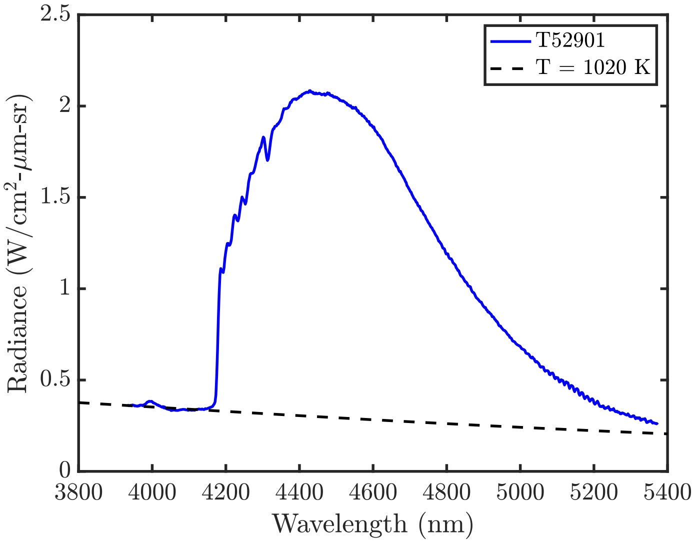

Figure 6.8: T52901 MSL condition 0° AOA stagnation point measurement. The blackbody curve that best fits the background radiation is indicated by the black-dashed line.

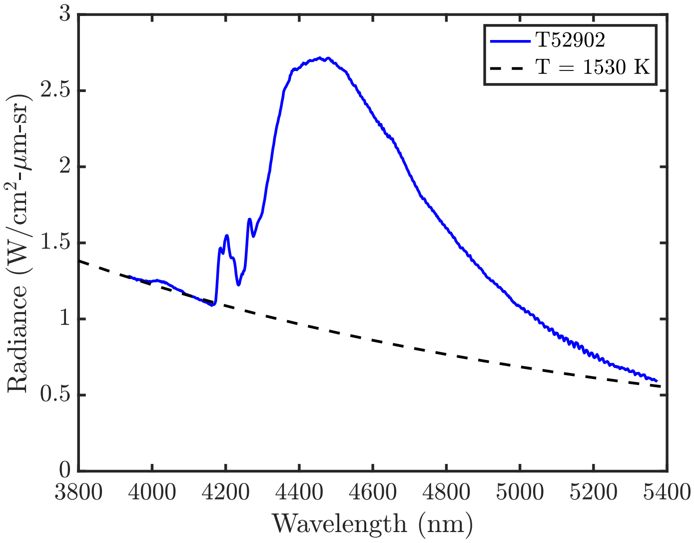

Figure 6.9: T52902 contour nozzle condition 0° AOA stagnation point. The blackbody curve that best fits the background radiation is indicated by the black-dashed line.

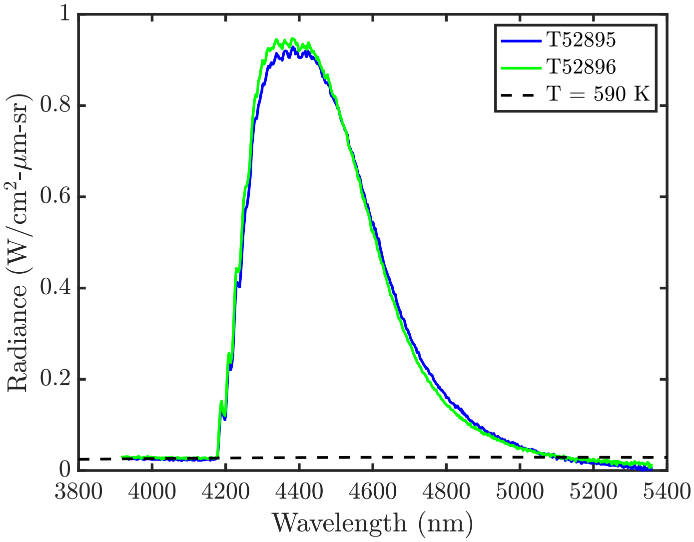

Figure 6.10: T52895 and T52896 ExoMars condition 0° AOA wake measurements. The blackbody curve that best fits the background radiation is indicated by the black-dashed line.

6.5 16° AOA Radiation Measurements

The coordinates of the two 16° probe locations (x/*R*, y/*R*) are at the 16° AOA stagnation point (0.125,0.433) and in the wake (0.557, 0.861). The coordinate system is shown in Figure 3.3, where x is the distance into the body and y is the distance in the radial direction. The two fiber probe locations are used to obtain radiation measurements at three orientations with the model at a 16° AOA as shown in Figure 6.11. The acceptance cones of the forebody and wake probes are also shown with the solid lines indicating the outside rays of the acceptance cone and the dashed lines indicate the normal ray. The red and black lines are on the wind side of the model and the green lines are on the lee side. The two wake orientations are accessible by turning the sting 180° in the mount.

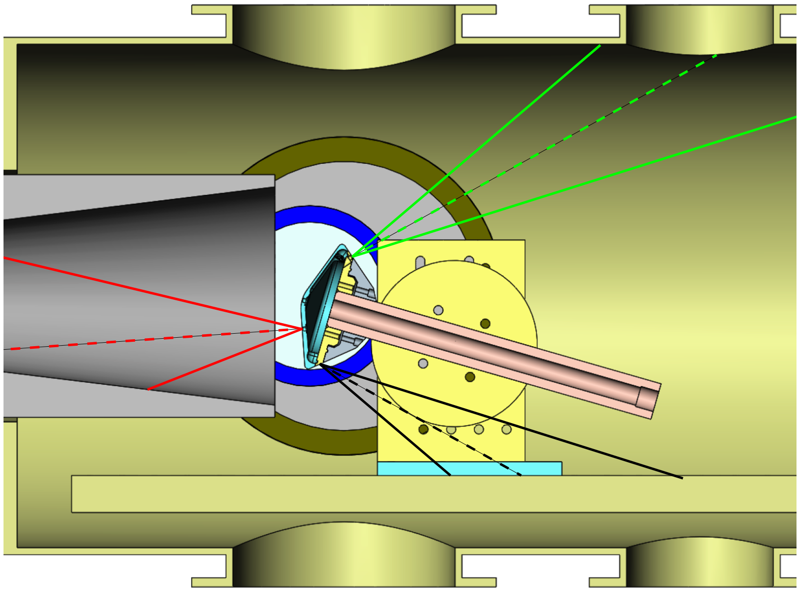

Figure 6.11: 16° AOA T5 MSL model schematic with rays emanating from the fiber probe locations. The forebody and afterbody probes have acceptance cone half angles of 17.5° and 11.5°, respectively.

The three experiments are conducted at the MSL condition at the stagnation point, lee side, and wind side locations. These measurements are shown in Figures 6.12, 6.13, and 6.14, respectively. A boundary layer absorption feature that dips below the estimated blackbody background can be observed for the stagnation point measurement. The background blackbody temperature is 960 K, similar to the value observed for the 0° AOA measurement, 1020 K.

For the wake measurements, the spectra are similar for the wind and lee side with the peak radiance between the wake and lee side measurements only differing by 2.5%. However, the background blackbody temperature is larger on the wind side (1530 K) than on the lee side (720 K).

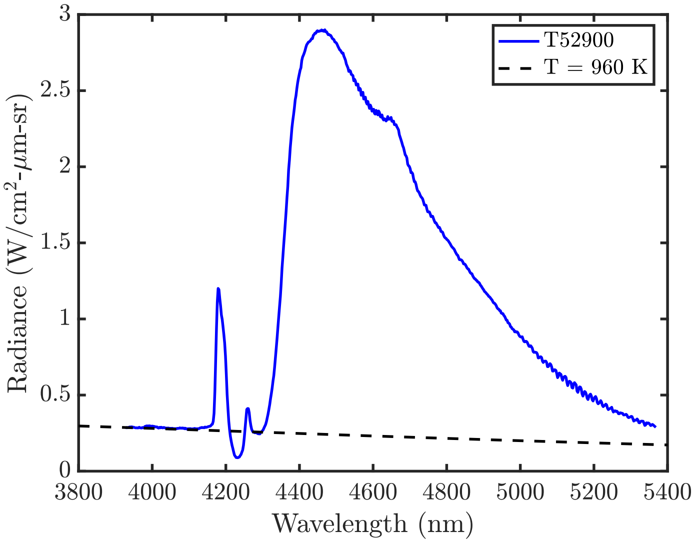

Figure 6.12: T52900 16° AOA MSL condition stagnation point measurement. The blackbody curve that best fits the background radiation is indicated by the black-dashed line.

6.6 Conclusions

The method developed in the HET to obtain spectrally resolved radiation measurements was successfully applied in T5. One of the biggest experimental challenges of being able to probe the wake was overcome by using an indium fluoride fiber optic cable with a small turning radius. Two new conditions were developed that match the binary scaling parameter of the ExoMars and T5 flight trajectories at enthalpies of 6.1 MJ/kg and 7.7 MJ/kg, respectively. The ExoMars shock layer can be considered optically thin while boundary layer absorption occurs for the MSL forebody shock layer measurements.

Repeat 0° AOA stagnation point and wake measurements for the ExoMars condition were obtained that showed good agreement (4.70 ± 0.25 mm) in shot-to-shot variation. 0° AOA stagnation point measurements were also obtained at the MSL and a contour nozzle condition for further comparisons. Background radiation appears in all of the T5 shots. The spectral dependence of the background radiation can

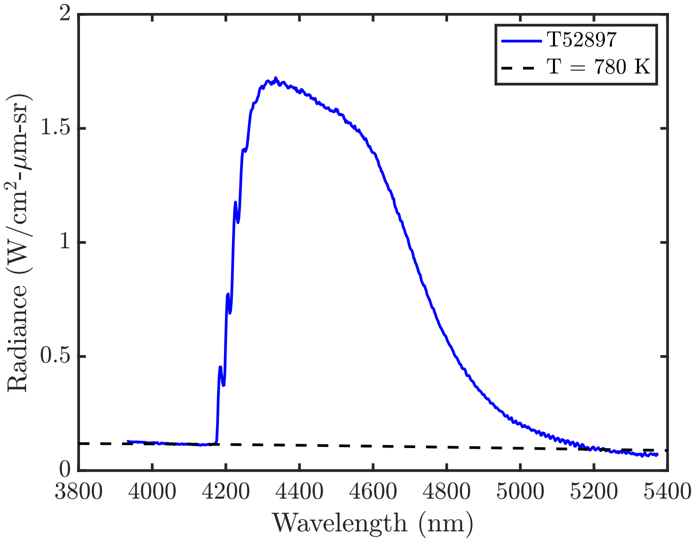

Figure 6.13: T52897 MSL condition 16° AOA wind lee wake measurement. The blackbody curve that best fits the background radiation is indicated by the black-dashed line.

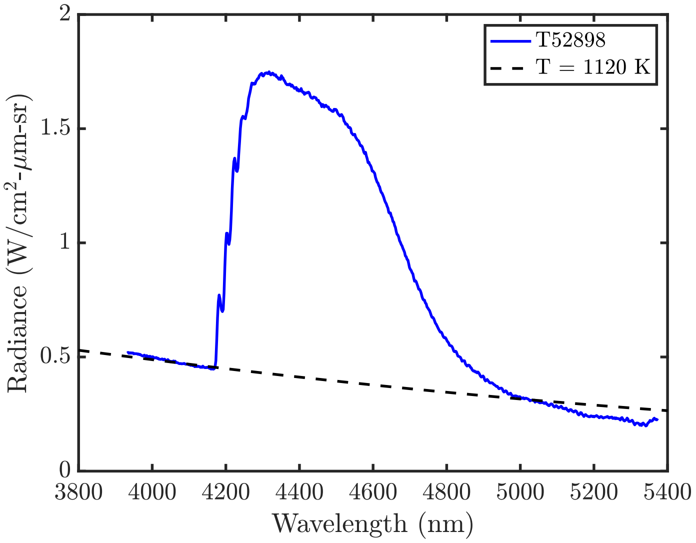

Figure 6.14: T52898 16° AOA MSL condition wind side wake measurement. The blackbody curve that best fits the background radiation is indicated by the black-dashed line.

be fit to a blackbody dependence from wavelengths between 3850 nm to 4150 nm. Three 16° AOA measurements were obtained for the MSL condition. The shape of the 4.3 µm band CO_2 spectra is very similar for both lee side and wind side wake measurements except the background blackbody temperature is much higher on the wind side.

These measurements are provided to the NASA Ames Aerothermodynamics branch who are performing CFD and radiation simulations for this work. Wake simulations of flow over the model and integrated with the conical nozzle flow as shown in Figure 6.15 are in progress. These simulations take into account the interaction of the bow shock with the nozzle shear layer that is in the line-of-sight of the wake probe.

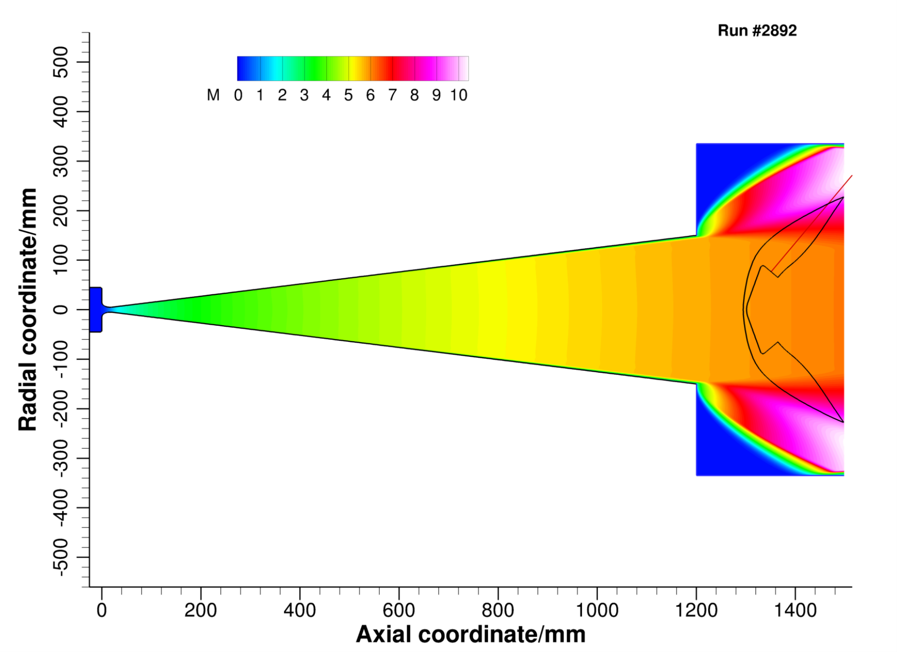

Figure 6.15: Preliminary results from an integrated simulation of the complex shock-boundary layer interactions in the conical nozzle for T52892. Simulation published by permission of Dr. Dinesh Prabhu at NASA Ames [89].

Chapter 7

CONCLUSIONS AND FUTURE WORK

7.1 Concluding Remarks

Hypervelocity testing in shock tunnel facilities is a necessary component in developing models for the heating phenomena experienced by a spacecraft during planetary entry. This thesis examined two issues recently identified as requiring investigation in order to improve heat load prediction for future higher-mass Mars missions.

Previous simulations of flow over sphere-cone geometries underpredicted the shock standoff distance measured in the LENS I Run 8 experiment by a factor of 2.25 and overpredicted previous experiments in T5 by a factor of 1.5 [40]. These comparisons raised concern about the use of reflected shock tunnels for high-enthalpy CO_2 testing. To resolve these discrepancies, bow shock standoff distance was examined through theory, simulations, and experiments in the T5 Reflected Shock Tunnel and compared with a Hypervelocity Expansion Tube experiment to assess facility independence of the results. Experiments spanned the binary scaling and enthalpy of the LENS I Run 8 condition [65] by using different conical nozzle throat sizes, however the large standoff distance anomaly observed in the LENS I facility was not observed. The discrepancy observed in the previous T5 sphere-cone bow shock shape experiments was resolved by accounting for the divergence of streamlines experienced when a conical nozzle geometry was used. A correction factor derived by Hornung [45] for flow over spheres was extended to sphere-cone geometries by accounting for the change in radius of curvature of the bow shock in parallel vs. conical flow.

The theoretical predictions, experiments, and simulations were directly compared to assess each condition tested. There was no evidence that vibrational freezing in the T5 nozzle significantly affects the shock standoff distance in any of the test conditions. The simulation data were analyzed along the stagnation streamline to evaluate the contributions to the total density ratio from vibrational nonequilibrium, convection, chemical nonequilibrium, and the viscous boundary layer region. The sensitivity of the stand-off distance to the chemical contribution was examined by comparing three kinetic models. Simulations with the Johnston or Cruden kinetic model resulted in the best match to the experimental measurements in T5 while simulations with the Fridman kinetic model provided a best match with HET conditions.

An investigation of CO_2 mid-wave infrared radiation in hypervelocity flow fields was motivated by recent work that found that CO_2 radiative heating, which had been previously neglected, is significant, especially in the afterbody where radiative heat loads can exceed convective heat loads. This work examined the strongest emission band of CO_2, the 4.3 μm band, for which existing simulation models were assessed to have a 30% uncertainty in compressive flow [17]. The uncertainty is larger in expanding flow where strong departures from the Boltzmann distribution have been observed from a state-to-state simulation in the backshell region [99].

A diagnostic was successfully designed and implemented to measure mid-wave infrared radiation on the surface of a sphere-cone model using an embedded fiber optic probe. Comparisons were made to reacting flow Navier-Stokes CFD and ray tracing radiation simulations. The experimental technique and method of calibration was validated in optically thick conditions where good agreement in predicted shock shape and peak radiance was obtained in shock tube measurements. The optically thick shock tube emission was shown to be blackbody limited, bounded by the blackbody curves defined by the post-shock equilibrium and frozen temperatures. A strong absorption feature between 4200 to 4400 nm was attributed to absorption in the dense, cold boundary layer next to the model wall.

Expansion tube spectral radiation measurements were made at two test conditions and three orientations. In optically thin conditions, it is necessary to account for the radiation emitted by the freestream gas. The radiation simulations utilized the CFD results for flow properties along the line-of-sight normal to the model surface at the probe location. The obliquely incident ray spectral radiance at the acceptance cone half angle of 17.5° in the shock layer is predicted to be within 2.3% of the normal ray in the tangent slab approximation. To account for freestream radiation in the ray-tracing simulations, the freestream slab was extended to lengths that represented the limiting ray lengths within the acceptance cone of the fiber probe reaching the facility boundary. This method will produce bounding estimates of the radiation incident on the collecting fiber.

The simulations and experiments were quantitatively compared using the ratio of integrated experimental spectra to integrated simulation spectra for representative ray lengths. The optically thick shock tube condition integrated radiance ratio was 0.95. The expansion tube conditions had a systematic increase in differences between measured and simulated radiance with decreasing absorption in the shock layer. For the MSL1 condition measurement at the 16° AOA stagnation point, the integrated radiance ratio for the central ray was 1.07. Direct measurements of the free stream resulted in integrated radiance ratios of 2.51 and 3.41 for the MSL1 condition and MSL2 condition, respectively. The best fits to the freestream measurements occurred when the freestream temperatures for the MSL1 and MSL2 conditions were 1700 K and 1600 K. This is higher than the perfect gas, ideal operation predicted freestream temperatures of 1221 K and 1042 K.

Section 2.3 examined the various processes in the expansion tube and the sensitivity of the radiation measurement to those features. Possible ways for the freestream temperature and pressure to increase relative to ideal operation include thermal nonequilibrium, viscous effects, uncertainty in initial pressures, and diaphragm effects. Vibrational nonequilibrium and possible diaphragm effects had the greatest influence on calculated freestream temperatures. Simulations of the vibrational relaxation through the expansion fan with Camac rates or asymmetric relaxation rates both predicted freestream conditions close to vibrational equilibrium. The possibility that a reflected shock occurs at the secondary diaphragm was investigated. Compared to the ideal diaphragm equilibrium free stream, the free stream predicted by the reflected shock calculations results in a 35% and 36% increase in temperature for the MSL1 and MSL2 conditions but only a 5.0% and 7.2% increase in pressure and a 2.6% and 3.6% increase in velocity, respectively. The resulting temperature of the free stream assuming equilibrium chemistry in all sections and a reflected shock is 1455 K and 1321 K, still 300 K lower than the upper bound on temperature from direct freestream measurements.

The MWIR measurement technique used in HET was employed in T5. Data were gathered for two test conditions that match the binary scaling parameter and stagnation enthalpy for a point on the ballistic entry trajectory of the ExoMars mission and the lifting trajectory of the MSL mission. The spectrum that appeared in all of the T5 shots was fit to a blackbody spectrum from 3850 nm to 4150 nm. Wake measurements were successfully obtained by switching the fiber glass material from chalcogenide to indium fluoride. The T5 data set was provided to the NASA Ames Aerothermodynamics branch where simulations are in progress.

7.2 Future Work

Calculations investigating a possible reflected shock from the secondary diaphragm interaction assumed i) otherwise ideal diaphragm rupture, ii) the reflected shock is unattenuated and uniformly processes the test gas, and iii) equilibrium thermochemistry. Simulations and experiments could be performed to evaluate these assumptions for the more complex, non-ideal diaphragm rupture.

Independent freestream temperature measurement could be made to compare to the temperature extracted from the emission measurements using a tunable diode laser absorption spectroscopy system (TDLAS). TDLAS measurements in the EAST facility extracted ground state number density and temperature from the line shape profile of CO transitions around 4363.86 nm [63, 64].

Obtaining shock time-of-arrival and pressure measurements along the tube wall, especially in the vicinity of the secondary diaphragm would help investigate if a reflected shock is present in the HET facility. In the HYPULSE expansion tube facility, Bakos and Morgan [4] used pressure transducers located 76 mm downstream of the secondary diaphragm to observe a reflected shock.

To obtain a single spectra that simulates the average spectral radiance integrated along the line-of-sight of the collection fiber, a three-dimensional ray-tracing algorithm [71] could be implemented through a viscous simulation of the entire accelerator section accounting for the unsteady expansion fan and boundary layer that develops along the tube.

An investigation into the 2.7 µm CO_2 mid-wave infrared radiation band that was assessed to have 60% uncertainty by Cruden et al. [17] can be conducted using the set up described in this work. A fiber bundle using multiple indium fluoride fibers could be used to obtain measurements in multiple locations, increasing the number of data points gathered in one experiment.

While past and current measurements provide confidence in the predicted T5 Reflected Shock Tunnel conditions, in the future, greater use should be made of probe rakes to characterize the freestream conditions by measuring static and pitot pressure as well as heat flux. The recoil of the nozzle and initial distance from the model to the nozzle should be recorded for each shot.

BIBLIOGRAPHY

[1] M. Alireza, P. A. Gnoffo, C. O. Johnston, and W. L. Kleb. LAURA users manual: 5.5-64987. Technical Report TM-2013-217800, NASA, 2013.

[2] J. D. Anderson Jr. *Computational Fluid Dynamics: The Basics with Applications*. McGraw-Hill, 1995.

[3] J. D. Anderson Jr. *Hypersonic and High-Temperature Gas Dynamics, Second Edition*. AIAA Education Series, 2006.

[4] R. J. Bakos and Morgan R.G. Chemical recombination in an expansion tube. *AIAA Journal*, 32(6), 1994. doi: 10.2514/3.12135.

[5] J. Belanger. *Studies of Mixing and Combustion in Hypervelocity Flows with Hot Hydrogen Injection*. PhD thesis, California Institute of Technology, 1993.

[6] N. Belouaggadia, H. Olivier, and R. Brun. Numerical and theoretical study of the shock stand-off distance in non-equilibrium flows. *Journal of Fluid Mechanics*, 607:167–197, 2008. doi: 10.1017/S0022112008001973.

[7] E. Bethe and E. Teller. Deviations from thermal equilibrium in shock waves. Technical Report X-117, Ballistics Research Lab, 1945.

[8] I. D. Boyd and T. E. Schwartzentruber. *Nonequilibrium Gas Dynamics and Molecular Simulations*. Cambridge University Press, 2017.

[9] A. M. Brandis, D. A. Saunders, C. O. Johnston, B. A. Cruden, and T. R. White. Radiative heating on the after-body of Martian entry vehicles. *Journal of Thermophysics and Heat Transfer*, 34(1), 2015. doi: 10.2514/1.T5613.

[10] A. M. Brandis, T. R. White, D. A. Saunders, J. P. Hill, and C.O. Johnston. Simulation of the Schiaparelli entry and comparison to aerothermal flight data. *AIAA Aviation 2019 Forum*, AIAA Paper 2019-3260, 2019. doi: 10.2514/6.2019-3260.

[11] S. Browne, J. Zeigler, N. Bitter, B. Schmidt, J. Lawson, and J. E. Shepherd. Numerical solution methods for shock and detonation jump conditions. Technical Report GALCIT Report GM2018.001 revised 2019, California Institute of Technology, 2019.

[12] M. Camac. CO_2 relaxation processes in shock waves. In *Fundamental Phenomena in Hypersonic Flow*, pages 195–215. Cornell University Press, 1964.

[13] G. V. Candler. Hypersonic nozzle analysis using an excluded volume equation of state. *38th AIAA Thermophysics Conference*, AIAA Paper 2005-5202, 2005. doi: 10.2514/6.2005-5202.

[14] L. H. Chambers. Predicting radiative heat transfer in thermochemical nonequilibrium flow fields. Technical Report TM-4564, NASA, 1994.

[15] Y. K. Chen, W. D. Henline, D. A. Stewart, and G. V. Candler. Navier-Stokes solutions with surface catalysis for Martian atmospheric entry. *Journal of Spacecraft and Rockets*, 30(1):32–42, 1993. doi: 10.2514/3.25468.

[16] B. A. Cruden. Absolute radiation measurements in Earth and Mars entry conditions. *Radiation and Gas-surface Interaction Phenomena in High-speed Reentry Lecture Series*, NATO TR RTO-EN-AVT-218, 2014.

[17] B. A. Cruden, A. M. Brandis, and D. K. Prabhu. Measurement and characterization of mid-wave infrared radiation in CO_2 shocks. *11th AIAA/ASME Joint Thermophysics and Heat Transfer Conference*, AIAA Paper 2014-2962, 2014. doi: 10.2514/6.2014-2962.

[18] B. A. Cruden, A. M. Brandis, T. R. White, and M. Mahzari. Radiative heating during Mars Science Laboratory entry: Simulation, ground test, and flight. *Journal of Thermophysics and Heat Transfer*, 30(3), 2016. doi: 10.2514/1.T4798.

[19] B. A. Cruden, A. M. Brandis, and M. E. MacDonald. Characterization of CO thermochemistry in incident shockwaves. *2018 Joint Thermophysics and Heat Transfer Conference*, AIAA Paper 2018-3768, 2018. doi: 10.2514/6.2018-3768.

[20] J. P. Davis. *High-enthalpy shock/boundary-layer interaction on a double wedge*. PhD thesis, California Institute of Technology, 1999.

[21] S. Doraiswamy, J. Kelley, and G. V. Candler. Vibrational modeling of CO_2 in high-enthalpy nozzle flows. *Journal of Thermophysics and Heat Transfer*, 24(1), 2010. doi: 10.2514/1.43280.

[22] A. Dufrene, M. Sharma, and J. M. Austin. Design and characterization of a hypervelocity expansion tube facility. *Journal of Propulsion and Power*, 23 (6):1185–1193, 2007. doi: 10.2514/1.30349.

[23] K. T. Edquist, A. A. Dyakonov, M. J. Wright, and Tang C. Y. Aerothermodynamic environments definition for the Mars Science Laboratory entry capsule. *45th AIAA Aerospace Sciences Meeting and Exhibit*, AIAA Paper 2007-1206, 2007. doi: 10.2514/6.2007-1206.

[24] Bakos R. Erdos, J. I. Prospects for a quiet hypervelocity shock-expansion tunnel. *25th Plasmadynamics and Lasers Conference*, AIAA Paper 1994-2500, 1994. doi: 10.2514/6.1994-2500.

[25] J. A. Fay. Theory of stagnation point heat transfer in dissociated air. *Journal of the Aerospace Sciences*, 25(2):73–85, 1958. doi: 10.2514/8.7517.

[26] W. Flaherty. Experimental surface heat flux measurement in hypervelocity flows. Master's thesis, University of Illinois at Urbana-Champaign, 2010.

[27] A. Fridman. *Plasma Chemistry*. Cambridge, 2008.

[28] P. Gnoffo, R. Gupta, and J. Shinn. Conservation equations and physical models for hypersonic air flows in thermal and chemical nonequilibrium. Technical Report TP-2867, NASA, 1989.

[29] P. A. Gnoffo, J. K. Weilmuenster, R. D. Braun, and C. I. Cruz. Influence of sonic-line location on Mars Pathfinder Probe aerothermodynamics. *Journal of Spacecraft and Rockets*, 33(2):169–177, 1996. doi: 10.2514/3.26737.

[30] P. A. Gnoffo, R. D. Braun, J. K. Weilmuenster, R. A. Mitcheltree, W. C. Engelund, and R. C. Powell. Prediction and validation of Mars Pathfinder hypersonic aerodynamic database. *Journal of Spacecraft and Rockets*, 36(3): 367–373, 1999. doi: 10.2514/2.3455.

[31] D. G. Goodwin, R. L. Speth, H. K. Moffat, and B. W. Weber. Cantera: An object-oriented software toolkit for chemical kinetics, thermodynamics, and transport processes, 2018. Version 2.4.0.

[32] R. Goulard. The coupling of radiation and convection in detached shock layers. *Journal of Quantitative Spectroscopy and Radiative Transfer*, 1(3-4): 249–257, 1961. doi: 10.1016/0022-4073(61)90025-5.

[33] W. D. Greenspan and V. H. Blackman. Approach to thermal equilibrium behind strong shock waves in carbon dioxide and carbon monoxide. *Bulletin of American Physical Society*, 217(2):1209–1217, 1957.

[34] W. Griffith, D. Brickl, and V. Blackman. Structure of shock waves in polyatomic gases. *Physical Review*, 102(5):1209–1217, 1956. doi: 10.1103/PhysRev.102.1209.

[35] S. Gu. *Mars entry afterbody radiative heating: an experimental study of nonequilibrium* CO_2 *expanding flow*. PhD thesis, The University of Queensland, 2018.

[36] S. Gu, R. G. Morgan, and T. J. McIntyre. Study of the afterbody radiation during Mars entry in an expansion tube. *55th AIAA Aerospace Sciences Meeting*, AIAA Paper 2017-0212, 2017. doi: 10.2514/6.2017-0212.

[37] R. K. Hanson, R. M. Spearrin, and C. S. Goldenstein. *Spectroscopy and Optical Diagnostics for Gases*. Springer, 2010.

[38] W. D. Hayes and R. F. Probstein. *Hypersonic Flow Theory*. Academic Press, 1959.

[39] B. R. Hollis, 2014. Personal communication.

[40] B. R. Hollis and D. K. Prabhu. Assessment of laminar, convective aeroheating prediction uncertainties for Mars entry vehicles. *Journal of Spacecraft and Rockets*, 50(1):56–58, 2013. doi: 10.2514/1.A32257.

[41] B. R. Hollis, D. K. Prabhu, M. Maclean, and A. Dufrene. Blunt-body aerothermodynamic database from high-enthalpy carbon-dioxide testing in an expansion tunnel. *Journal of Thermophysics and Heat Transfer*, 31(3):712–731, 2017. doi: 10.2514/1.T5019.

[42] H. Hornung. Performance data of the new free-piston shock tunnel at GALCIT. *28th Joint Propulsion Conference and Exhibit*, AIAA Paper 1992-3943, 1992. doi: 10.2514/6.1992-3943.

[43] H. G. Hornung. Non-equilibrium dissociating flow over spheres and circular cylinders. *Journal of Fluid Mechanics*, 53(1):149–176, 1972. doi: 10.1017/S0022112072000084.

[44] H. G. Hornung. AE237 non-steady gas dynamics. Class notes, California Institute of Technology, 2005.

[45] H. G. Hornung. Effect of conical free stream on shock stand-off distance. *AIAA Journal*, 57(9):4115–4116, 2019. doi: 10.2514/1.J058385.

[46] H. G. Hornung, 2019. Personal communication.

[47] H. G. Hornung and B. Valiferdowsi. Development of aeroshell technologies for the Mars Science Laboratory, report on tests in the T5 Hypervelocity Shock Tunnel. Technical report, California Institute of Technology, 2013.

[48] H. G. Hornung, J. M. Schramm, and K. Hannemann. Hypersonic flow over spherically blunted cone capsules for atmospheric entry. part 1. the sharp cone and the sphere. *Journal of Fluid Mechanics*, 871:1097–1116, 2019. doi: 10.1017/jfm.2019.342.

[49] A. F. P. Houwing, S. Nonaka, H. Mizuno, and K. Takayama. Effects of vibrational relaxation on bow shock standoff distance for nonequilibrium flows. *AIAA Journal*, 38(9):1760–1763, 1999. doi: 10.1017/jfm.2019.342.

[50] R. R. Jacobs, K. J. Pettipiece, and S. J. Thomas. Rate constants for the CO_2 02^02 – 10^00 relaxation. *Physical Review A*, 11(1):54–61, 1975. doi: 10.1063/1.555558.

[51] C. M. James, D. E. Gildfind, S. W. Lewis, R. G. Morgan, and F. Zander. Implementation of a state-to-state analytical framework for the calculation of expansion tube flow properties. *Shock Waves*, 29(2):349–377, 2018. doi: 10.1007/s00193-017-0763-3.

[52] J. S. Jewell. *Boundary-Layer Transition on a Slender Cone in Hypervelocity Flow with Real Gas Effects*. PhD thesis, California Institute of Technology, 2014.

[53] N. H. Johannesen, H. K. Zienkiwicz, P. A. Blythe, and J. H. Gerrard. Experimental and theoretical analysis of vibrational relaxation regions in carbon dioxide. *Bulletin of American Physical Society*, 13(2):213–224, 1962. doi: 10.1017/S0022112062000634.

[54] C. O. Johnston and A. M. Brandis. Modeling of nonequilibrium CO fourth-positive and CN violet emission in CO_2–N_2 gases. *Journal of Quantitative Spectroscopy and Radiative Transfer*, 149:303–317, 2014. doi: 10.1016/j.jqsrt.2014.08.025.

[55] C. O. Johnston, B. R. Hollis, and K. Sutton. Non-Boltzmann modeling for air shock-layer radiation at lunar-return conditions. *Journal of Spacecraft and Rockets*, 45(5), 2008. doi: 10.2514/1.33004.

[56] C. O. Johnston, B. R. Hollis, and K. Sutton. Spectrum modeling for air shock-layer radiation at lunar-return conditions. *Journal of Spacecraft and Rockets*, 45(5):865–878, 2008.

[57] C.O. Johnston. Improved exponential integral approximation for tangent-slab radiation transport. *Journal of Thermophysics and Heat Transfer*, 24(3): 659–661, 2010. doi: 10.2514/1.46197.

[58] A. M. Knisely. *Experimental Investigation of Nonequilibrium and Separation Scaling in Double-Wedge and Double-Cone Geometries*. PhD thesis, University of Illinois, 2016.

[59] M. G. Leibowitz and J. M. Austin. Assessment of reflected shock tunnels for Mars entry vehicle ground testing. *2018 AIAA Aerospace Science Meetings*, AIAA Paper 2018-1721, 2018. doi: 10.2514/6.2018-1721.

[60] M. Lino Da Silva and J. Beck. Contribution of CO_2 IR radiation to Martian entries radiative wall fluxes. *49th AIAA Aerospace Sciences Meetings*, AIAA Paper 2011-135, 2011. doi: 10.2514/6.2011-135.

[61] R. K. Lobb. *Experimental measurement of shock detachment distance on spheres fired in air at hypervelocities*, volume 68, chapter 26, pages 519–527. Pergamon, 1964. doi: 10.1016/B978-1-4831-9828-6.50031-X.

[62] M. A. Lopez-Valverde and M. Lopez-Puertas. A non-local thermodynamic equilibrium radiative transfer model for infrared emissions in the atmosphere of Mars. *Journal of Geophysical Research*, 99(E6):13117 – 13132, 1994. doi: 10.1029/94JE01091.

[63] M. E. MacDonald and B. A. Cruden. A tunable laser absorption diagnostic for measurements of CO in shock-heated gases. *46th AIAA Thermophysics Conference*, AIAA Paper 2016-3694, 2016. doi: 10.2514/6.2016-3694.

[64] M. E. MacDonald and B. A. Cruden. Post-shock temperature and CO number density measurements in CO and CO_2. *47th AIAA Thermophysics Conference*, AIAA Paper 2017-4342, 2017. doi: 10.2514/6.2017-4342.

[65] M. MacLean and M. Holden. Numerical assessment of data in catalytic and transitional flows for Martian entry. *9th AIAA/ASME Joint Thermophysics and Heat Transfer Conference*, AIAA Paper 2006-2946, 2006. doi: 10.2514/6.2006-2946.

[66] M. MacLean, T. Wadhams, M. MacLean, E. Mundy, and R. Parker. Experimental studies in LENS I and X to evaluate real gas effects on hypervelocity vehicle performance. *45th AIAA Aerospace Sciences Meeting*, AIAA Paper 2007-204, 2007. doi: 10.2514/6.2007-204.

[67] M. MacLean, A. Dufrene, Z. Carr, R. Parker, and M. Holden. Measurements and analysis of Mars entry, descent, and landing aerothermodynamics at flight-duplicated enthalpies in LENS-XX expansion tunnel. *53rd AIAA Aerospace Sciences Meeting*, AIAA Paper 2015-1897, 2015. doi: 10.2514/6.2015-1897.

[68] E. C. Marineau and Hornung H. G. Modeling and calibration of fast-response coaxial heat flux gages. *47th AIAA Aerospace Science Meetings*, AIAA Paper 2009-737, 2009. doi: 10.2514/6.2009-737.

[69] E. C. Marineau and H. G. Hornung. Study of bow-shock wave unsteadiness in hypervelocity flow from reservoir fluctuations. *48th Aerospace Sciences Meetings*, AIAA Paper 2010-382, 2010. doi: 10.2514/6.2010-382.

[70] L. Massa and J. M. Austin. Spatial linear stability of a hypersonic shear layer with nonequilibrium thermochemistry. *Physics of Fluids*, 20(8):81–104, 2008. doi: 10.1063/1.2972937.

[71] A. Mazaheri, C. O. Johnston, and S. Sefidbakht. Three-dimensional radiation ray-tracing for shock-layer radiative heating simulations. *Journal of Spacecraft and Rockets*, 50(3), 2013. doi: 10.2514/1.A32448.

[72] B. J. McBride, M. J. Zehe, and S. Gordon. NASA glenn coefficients for calculating thermodynamic properties of individual species. Technical Paper TP-2002-211556, NASA, Hampton, Va., 2002.

[73] M. McGilvray, J. M. Austin, M. Sharma, P. A. Jacobs, and R. G. Morgan. Diagnostic modelling of an expansion tube operating condition. *Shock Waves*, 19:59–66, 2009. doi: 10.1007/s00193-009-0187-9.

[74] R. L. McKenzie. An estimate of the chemical kinetics behind normal shock-waves in mixtures of carbon dioxide and nitrogen for conditions typical of Mars entry. Technical Note TN D-3287, NASA, 1966.

[75] R. C. Millikan and D. R. White. Systematics of vibrational relaxation. *The Journal of Chemical Physics*, 39(12):1097–1116, 1963. doi: 10.1063/1.1734182.

[76] H. Mirels. Laminar boundary layer behind shock advancing into stationary fluid. Technical Note 3401, NACA, 1955.

[77] H. Mirels. Test time in low-pressure shock tubes. Technical Note 3712, NACA, 1956.

[78] H. Mirels. Attenuation in a shock tube due to unsteady-boundary-layer action. Technical Report 1333, NACA, 1957.

[79] H. Mirels. Test time in low-pressure shock tubes. *The Physics of Fluids*, 6 (9):1201–1214, 1963. doi: 10.1063/1.1706887.

[80] H. Mirels. Shock tube test time limitation due to turbulent-wall boundary layer. *AIAA Journal*, 2(1), 1964.

[81] R. G. Morgan, T. J. McIntyre, D. R. Buttsworth, P. A. Jacobs, D. F. Potter, A. M. Brandis, R. J. Gollan, C. M. Jacobs, B. R. Capra, M. McGivray, and T. Eichmann. Impulse facilities for the simulation of hypersonic radiating flows. *AIAA 38th Fluids Dynamics Conference and Exhibit*, AIAA Paper 2008-4270, 2008. doi: 10.2514/6.2008-4270.

[82] NASA. Historical log, 2019. URL `https://mars.nasa.gov/mars-exploration/missions/historical-log/`.

[83] A. J. Neely, R. J. Stalker, and Paull A. High enthalpy, hypervelocity flows of air and argon in an expansion tube. *Aeronautical Journal*, 95(946):175–186, 1991. doi: 10.1017/S0001924000023885.

[84] G. Palmer and B. A. Cruden. Experimental validation of CO_2 radiation simulations. *43rd AIAA Thermophysics Conference*, AIAA Paper 2012-3188, 2012. doi: 10.2514/6.2012-3188.

[85] C. Park. *Nonequilibrium Hypersonic Aerothermodynamics*. Wiley, 1990.

[86] C. Park, J. Howe, R. Jaffe, and G. Candler. Review of chemical-kinetic problems of future NASA missions, II: Mars entries. *Journal of Thermophysics and Heat Transfer*, 8(1):9–23, 1994. doi: 10.2514/3.496.

[87] N. J. Parziale, B. E. Schmidt, P. S. Wang, H. G. Hornung, and J. E. Shepherd. Pulsed laser diode for use as a light source for short-exposure, high-frame-rate flow visualization. *53rd AIAA Aerospace Sciences Meeting*, AIAA Paper 2015-0530, 2015. doi: 10.2514/6.2015-0530.

[88] R. H. Pletcher, J. C. Tannehill, and D. A. Anderson. *Computational Fluid Mechanics and Heat Transfer*. CRC Press, 2013.

[89] D. K. Prabhu, 2019. Personal communication.

[90] D. K. Prabhu and D. A. Saunders. On heatshield shapes for Mars entry capsules. *50th AIAA Aerospace Sciences Meeting*, AIAA Paper 2012-399, 2012. doi: 10.2514/6.2012-399.

[91] J. J. Quirk. AMRITA — a computational facility (for CFD modelling). *VKI CFD Lecture Series*, 1998.

[92] S. G. Rock, G. V. Candler, and H. G. Hornung. Analysis of thermochemical nonequilibrium models for carbon dioxide flows. *AIAA Journal*, 31(12): 2255–2262, 1993. doi: 10.2514/3.11923.

[93] P. Roe. Approximate riemann solvers, parameter vectors, and difference schemes. *Journal of Computational Physics*, 43(2):357–372, 2020. doi: 10.1016/0021-9991(81)90128-5.

[94] A. Roshko. On flow duration in low-pressure shock tubes. *The Physics of Fluids*, 3(6):835–842, 1960. doi: 10.1063/1.1706147.

[95] E. M. Rothkopf and W. Low. Diaphragm opening processes in shock tubes. *The Physics of Fluids*, 17(1169), 1974. doi: 10.1063/1.1694860.

[96] B. Rousset. *Calibration and Study of the Contoured Nozzle of the T5 Free-Piston Hypervelocity Shock Tunnel*. PhD thesis, California Institute of Technology, 1995.

[97] O. Rouzaud, L. Tessé, T. Soubrié, A. Soufiani, P. Rivière, and D. Zeitoun. Influence of radiative heating on a Martian orbiter. *Journal of Thermophysics and Heat Transfer*, 22(1):10–19, 2008. doi: 10.2514/1.28259.

[98] G. B. Rybicki and A. P. Lightman. *Radiative Processes in Astrophysics*. Wiley-VCH, 2004.

[99] A. Sahai, B. E. Lopez, C. O. Johnston, and M. Panesi. Novel approach for CO_2 state-to-state modeling and application to multidimensional entry flows. *55th AIAA Aerospace Sciences Meeting*, AIAA Paper 2017-0213, 2017. doi: 10.2514/6.2017-0213.

[100] S. R. Sanderson. *Shock Wave Interaction in Hypervelocity Flow*. PhD thesis, California Institute of Technology, 1995.

[101] G. S. Settles. *Schlieren and Shadowgraph Techniques*. Springer, 1949.

[102] M. Sharma. *Post-Shock Thermochemistry in Hypervelocity CO_2 and Air Flow*. PhD thesis, University of Illinois, 2010.

[103] M. Sharma, A. B. Swantek, W. Flaherty, J. M. Austin, S. Doraiswamy, and G. V. Candler. Experimental and numerical investigation of hypervelocity carbon dioxide flow over blunt bodies. *Journal of Thermophysics and Heat Transfer*, 24(4), 2010. doi: 10.2514/1.49386.

[104] S. P. Sharma and Whiting E. E. Modeling of nonequilibrium radiation phenomena: an assessment. *Journal of Thermophysics and Heat Transfer*, 10 (3):385–396, 1996. doi: 10.2514/3.802.

[105] Bridgman K. B. Simpson, C. M. and T. R. Chandler. Shock-tube study of vibrational relaxation in carbon dioxide. *The Journal of Chemical Physics*, 49(2):513–522, 1968. doi: 10.1063/1.1670105.

[106] B. Stuart. *Infrared Spectroscopy: Fundamentals and Applications*. Wiley, 2004.

[107] V. P. Stulov. Similarity law for supersonic flow past blunt bodies. *Fluid Dynamics*, 4(4):93–96, 1969. doi: 10.1007/BF01094695.

[108] N. Sudani, B. Valiferdowsi, and H. G. Hornung. Test time increase by delaying driver gas contamination for reflected shock tunnels. *AIAA Journal*, 38(9): 1497–1503, 2000. doi: 10.2514/2.1138.

[109] R. Sundberg, J. Duff, and L. Bernstein. Nonequilibrium infrared emission model for reentry vehicles. *27th AIAA Thermophysics Conference*, AIAA Paper 1992-2916, 1992. doi: 10.2514/6.1992-2916.

[110] K. Sutton and A. R. Graves. A general stagnation-point convective-heating equation for arbitrary gas mixtures. Technical report, NASA, 1971.

[111] H. Takayanagi, A. Lemal, S. Nomura, and K. Fujita. Measurements of carbon dioxide nonequilibrium infrared radiation in shocked and expanded flows. *Journal of Thermophysics and Heat Transfer*, 32(2):483–494, 2018. doi: 10.2514/1.T5200.

[112] J. Tamagno, Bakos R., M. Pulsonetti, and J. Erdos. Hypervelocity real gas capabilities of GASL's expansion tube (hypulse) facility. *16th Aerodynamic Ground Testing Conference*, AIAA Paper 1990-1390, 1990. doi: 10.2514/6.1990-1390.

[113] S. A. Tashkun and V. I. Perevalov. CDSD-4000: High-resolution, high-temperature carbon dioxide spectroscopic databank. *Journal of Quantitative Spectroscopy and Radiative Transfer*, 112(9):1403 – 1410, 2011. doi: 10.1016/j.jqsrt.2011.03.005.

[114] S. A. Tashkun, V. I. Perevalov, J. L. Teffo, A. D. Bykov, and N. N. Lavrentieva. CDSD-1000, the high-temperature carbon dioxide spectroscopic databank. *Journal of Quantitative Spectroscopy and Radiative Transfer*, 82(1):165–196, 2003. doi: 10.1016/S0022-4073(03)00152-3.

[115] M. D. Van Dyke. The supersonic blunt-body problem - review and extension. *Journal of Aerospace Sciences*, 25:485–496, 1958. doi: 10.2514/8.7744.

[116] W. G. Vincenti and C. H. Kruger, Jr. *Introduction to Physical Gas Dynamics*. John Wiley and Sons, Inc., 1965.

[117] R. M. Wagnild. *High Enthalpy Effects on Two Boundary Layer Disturbances in Supersonic and Hypersonic Flow*. PhD thesis, University of Minnesota, 2014.

[118] C. Y. Wen and H. G. Hornung. Non-equilibrium dissociating flow over spheres. *Journal of Fluid Mechanics*, 299:389–405, 1995. doi: 10.1017/S0022112095003545.

[119] M. Wright, B. Hollis, M. Barnhardt, C. Johnston, A. Brandis, K. Edquist, and B. Cruden. Aerothermal modeling challenges for entry, descent and landing missions, 2018. URL `https://ntrs.nasa.gov/archive/nasa/casi.ntrs.nasa.gov/20180007849.pdf`.

[120] M. J. Wright, D. Bose, and J. Olejniczak. Impact of flowfield-radiation coupling on aeroheating for titan aerocapture. *Journal of Thermophysics and Heat Transfer*, 19(1):17–27, 2005. doi: 10.2514/1.10304.

[121] M. J. Wright, J. Olejniczak, J. L. Brown, H. G. Hornung, and K. T. Edquist. Modeling of shock tunnel aeroheating data on the Mars Science Laboratory aeroshell. *Journal of Thermophysics and Heat Transfer*, 20(4), 2006. doi: 10.2514/1.19896.

[122] M. J. Wright, Tang C.Y., K. T. Edquist, B. R. Hollis, P. Krasa, and C. A. Campbell. A review of aerothermal modeling for Mars entry missions. *48th AIAA Aerospace Sciences Meeting*, AIAA Paper 2010-443, 2010. doi: 10.2514/6.2010-443.

[123] H. Yee. On symmetric and upwind tvd schemes. Technical Report TM-88325, NASA, 1986.

[124] H. K. Zienkiwicz and N. H. Johannesen. Departures from the linear equation for vibrational relaxation in shock waves in oxygen and carbon dioxide. *Journal of Fluid Mechanics*, 17(4):499–505, 1963. doi: 10.1017/S0022112063001476.

Appendix A

HET SHOT LIST

A.1 All HET Shots

Table A.1: HET shot list part 1.

Shot Number	Date	Model (s)	Diagnostics	Test Condition (Exp. gas)
1421	5/22/16	No model	First shot	MSL1 (Air)
1422	5/24/16	No model	NA	MSL1 (Air)
1423	7/8/16	No model	2 Pitots	MSL1 (Air)
1424	7/11/16	No model	2 Pitots	MSL1 (Air)
1425	7/14/16	No model	2 Pitots	MSL1 (Air)
1426	7/21/16	No model	NA	MSL1 (Air)
1427	7/26/16	MSL	Pitot, Schleiren	MSL1 (Air)
1428	7/27/16	MSL	Pitot, Schleiren	MSL1 (Air)
1429	7/27/16	MSL	Pitot, Schleiren	MSL1 (Air)
1430	7/27/16	MSL	Pitot, Schleiren	MSL3 (He)
1431	7/28/16	MSL	Pitot, Schleiren	MSL3 (He)
1432	7/29/16	MSL	Pitot, Schleiren	(300 mtorr He)
1433	8/1/16	MSL	Pitot, Schleiren	300 (mtorr He)
1434	8/1/16	MSL	Pitot, Schleiren	MSL2 (Air)
1435	8/2/16	MSL	Pitot, Schleiren	MSL4 (He)
1436	8/9/16	MSL, 1" sphere	Pitot, TCs	MSL1 (Air)
1437	8/11/16	MSL, 1" sphere	Pitot, TCs	MSL1 (Air)
1438	8/12/16	MSL, 1" sphere	Pitot, TCs	MSL1 (Air)
1439	8/15/16	MSL, 1" sphere	Pitot, TCs	MSL1 (Air)
1440	8/15/16	MSL, 1" sphere	Pitot, Schleiren	MSL2 (Air)
1441	8/15/16	MSL, 1" sphere	Pitot, Schleiren	MSL3 (He)
1442	8/16/16	MSL, 1" sphere	Pitot, Schleiren	MSL1 (Air)
1443	8/17/16	MSL, 1" sphere	Pitot, Schleiren	MSL4 (He)
1444	8/18/16	MSL 0 AOA	Pitot, Schleiren	MSL1 (Air)
1445	8/31/16	2 spheres	Pitot, TCs	MSL1 (Air)
1446	9/20/16	Sphere and Pitot	High Speed Schlieren/TC	MSL3 (He)
1447	9/22/16	Sphere and Pitot	High Speed Schlieren/TC	MSL3 (He)
1448	9/22/16	Sphere and Pitot	High Speed Schlieren/TC	MSL3 (He)
1449	9/26/16	Sphere and Pitot	High Speed Schlieren/TC	MSL3 (He)

Table A.2: HET shot list part 2.

Shot Number	Date	Model (s)	Diagnostics	Test Condition (Exp. gas)
1450	9/26/16	Sphere and Pitot	High Speed Schlieren/TC	MSL1 (N2)
1451	9/26/16	Sphere and Pitot	High Speed Schlieren/TC	MSL2 (N2)
1452	9/27/16	Sphere and Pitot	High Speed Schlieren/TC	MSL4 (He)
1453	10/3/16	Sphere and PItot	Stagnation Pt. TC/Schlieren	MSL1 (Air)
1454	10/3/16	Sphere and Pitot	Stagnation Pt. TC/Schlieren	MSL1 (Air)
1455	10/4/16	Sphere and Pitot	Stagnation Pt. TC/Schlieren	MSL1 (Air)
1456	10/5/16	Sphere and Pitot	Stagnation Pt. TC/Schlieren	MSL1 (He)
1457	10/6/16	MSL new model 16 AOA	Schlieren/TCs/Pitot	MSL1 (Air)
1458	10/10/16	MSL 16 AOA	Schlieren/TCs/Pitot	MSL1 (N2)
1459	10/13/16	MSL 16 AOA	Schlieren/TCs/Pitot	MSL2 (Air)
1460	10/13/16	MSL 16 AOA	Schlieren/TCs/Pitot	MSL2 (Air)
1461	10/13/16	MSL 16 AOA	Schlieren/TCs/Pitot	MSL2 (N2)
1462	10/14/16	MSL 16 AOA	Schlieren/TCs/Pitot	MSL2 (N2)
1463	10/14/16	MSL 16 AOA	Schlieren/TCs/Pitot	MSL1 (N2)
1464	10/14/16	MSL 16 AOA	Schlieren/TCs/Pitot	MSL1 (Air)
1465	10/17/16	MSL 16 AOA	Schlieren/TCs/Pitot	MSL1 (Air)
1466	10/20/16	MSL 16 AOA	TCs/Pitot	MSL1 (Air)
1467	10/21/16	MSL 0 AOA	Schlieren/TCs/Pitot	MSL1 (Air)
1468	10/26/17	MSL old model 0 AOA	TCs	MSL1 (Air)
1469	10/28/17	MSL 0 AOA	TCs	M7_8
1470	11/6/17	MSL 0 AOA	TCs	MSL1 (Air)
1471	11/6/17	MSL 0 AOA	TCs	MSL1 (Air)
1472	11/9/17	MSL 0 AOA	TCs	MSL1 (Air)
1473	11/9/17	MSL 0 AOA	TCs	MSL1 (Air)
1474	11/10/16	MSL 0 AOA	TCs	MSL1 (Air)
1475	11/10/16	MSL old model 0 AOA	TCs	MSL1 (Air)
1476	11/11/16	MSL new model 0 AOA	TCs	MSL1 (Air)
1477	11/13/16	MSL new model 0 AOA	TCs	MSL1 (Air)
1478	11/14/16	MSL new model 16 AOA	TCs	MSL1 (Air)
1479	11/14/16	MSL new model 16 AOA	TCs	MSL1 (Air)
1480	11/15/16	MSL new model 16 AOA	TCs	MSL1 (Air)
1481	11/15/16	MSL new model 16 AOA	TCs	MSL1 (Air)
1482	11/16/16	MSL new model 16 AOA	TCs	MSL2 (Air)
1483	11/16/16	MSL new model 16 AOA	TCs	MSL2 (Air)
1484	11/16/16	MSL 16 AOA	TCs	MSL3 (He)
1485	11/16/16	MSL 16 AOA	TCs	MSL3 (He)
1486	11/16/16	MSL 16 AOA	TCs	MSL4 (He)
1487	11/16/16	MSL 16 AOA	TCs	MSL4 (He)
1488	3/14/17	Cylinder	TCs	MSL1 (Air)
1489	3/15/17	Cylinder	TCs	MSL1 (Air)
1490	3/20/17	Cylinder	TCs	MSL1 (Air)
1491	3/21/17	Cylinder	TCs	MSL1 (Air)

Table A.3: HET shot list part 3.

Shot Number	Date	Model (s)	Diagnostics	Test Condition (Exp. gas)
1492	3/24/17	MSL 0 AOA	TCs	MSL1 (Air)
1493	3/31/17	Cylinder	TCs	MSL1 (Air)
1494	4/13/17	Cylinder	TCs	MSL1 (Air)
1500	8/1/17	30 and 60 degree wedge	Schlieren (PCO)/pitot	MSL1 (Air)
1503	8/4/17	30 and 60 degree wedge	Schlieren (PCO)/pitot	MSL3 (He)
1504	8/7/17	30 and 60 degree wedge	Schlieren (PCO)/pitot	MSL3 (He)
1520	2/8/18	MSL 16 AOA Stag. Pt Probe	CO2 Radiation	MSL1 (Air)
1521	2/13/18	MSL 16 AOA Stag. Pt Probe	CO2 Radiation	MSL1 (Air)
1522	2/16/18	MSL 16 AOA Stag. Pt Probe	CO2 Radiation	MSL1 (Air)
1523	3/2/18	MSL 16 AOA Stag. Pt Probe	CO2 Radiation	MSL1 (Air)
1524	3/2/18	MSL 16 AOA Stag. Pt Probe	CO2 Radiation	MSL1 (Air)
1525	3/7/18	MSL 16 AOA Stag. Pt Probe	CO2 Radiation	MSL3 (He)
1526	3/8/18	MSL 16 AOA Stag. Pt Probe	CO2 Radiation	MSL2 w Air
1527	3/9/18	MSL 16 AOA Stag. Pt Probe	CO2 Radiation	MSL2 w Air
1528	3/12/18	MSL 16 AOA Stag. Pt Probe	CO2 Radiation	MSL4 w He
1531	3/23/18	MSL: 16AOA Lee side	CO2 Radiation	MSL1 w AIR
1533	3/27/18	MSL: 16AOA Lee side	CO2 Radiation	MSL1 w AIR
1534	3/29/18	MSL: 16AOA Lee side	CO2 Radiation	Shock Tube (1.2 kPa)
1535	3/30/18	MSL: 16AOA Lee side	CO2 Radiation	Shock Tube (1.2 kPa)
1536	4/4/18	MSL: 16AOA Lee side	CO2 Radiation	Shock Tube (1.2 kPa)
1537	4/9/18	MSL: 16AOA Lee side	CO2 Radiation	Shock Tube (1.2 kPa)
1541	4/24/18	MSL 16 AOA Stag. Pt Probe	CO2 Radiation	Shock Tube (1.2 kPa)
1542	4/24/18	MSL 16 AOA Stag. Pt Probe	CO2 Radiation	Shock Tube (Air shot)
1543	4/26/18	MSL 16 AOA Stag. Pt Probe	CO2 Radiation	Shock Tube (14.5 kPa)
1544	4/26/18	MSL 16 AOA Stag. Pt Probe	CO2 Radiation	Shock Tube (0.4 kPA)
1546	5/7/18	MSL 16 AOA Stag. Pt Probe	CO2 Radiation	MSL1 w AIR
1549	5/17/18	Staggered Pitot Rakes	Pitot/transmitted shock	MSL1 (Air)
1551	6/15/18	Staggered Pitot Rakes	Pitot/transmitted shock	MSL1 (Air)
1553	6/18/18	Staggered Pitot Rakes	Pitot/transmitted shock	MSL3 (He)
1590	10/24/18	Staggered Pitot Rakes	Pitot/transmitted shock	MSL1 (Air)
1599	11/15/18	MSL: 0AOA	CO2 Radiation	MSL1
1600	11/16/18	MSL: 0AOA	CO2 Radiation	MSL1
1601	11/16/18	Staggered Pitot Probe	CO2 Radiation	MSL1
1720	10/3/19	Double FLDI	CO2 Radiation	MSL1
1721	10/3/19	Double FLDI	CO2 Radiation	MSL1
1722	10/5/19	Double FLDI	CO2 Radiation	MSL1
1723	10/5/19	Double FLDI	CO2 Radiation	MSL2
1724	10/8/19	Long Pitot Probe	CO2 Radiation	MSL1
1725	10/9/19	Long Pitot Probe	CO2 Radiation	MSL2
1786	11/21/19	MSL 0 AOA	CO2 Radiation	MSL1
1787	11/21/19	MSL 0 AOA	CO2 Radiation	MSL2
1788	11/22/19	MSL 0 AOA	CO2 Radiation	MSL2

A.2 HET Radiation Experiment Shots

Table A.4: HET radiation shot list.

Shot #	**Date**	**Condition**	**Model**	**Fiber Location**	**Useful**	**Slit (μm)**	**Calibration**	**Max Counts**	**Shift**
1520	2/8/18	MSL1	MSL: 16AOA	Stagnation Pt.	Maybe	100	2/2/18	107	28
1521	2/13/18	MSL1	MSL: 16AOA	Stagnation Pt.	Yes	100	2/12/18	1116	-22
1522	2/16/18	MSL1	MSL: 16AOA	Stagnation Pt.	No	100	2/15/18	1138	-15
1523	3/2/18	MSL1	MSL: 16AOA	Stagnation Pt.	No	100	NA	NA	NA
1524	3/2/18	MSL1	MSL: 16AOA	Stagnation Pt.	Yes	100	3/7/18	1144	-15
1525	3/7/18	MSL3	MSL: 16AOA	Stagnation Pt.	Yes	100	3/7/18	1144	-22
1526	3/8/18	MSL2	MSL: 16AOA	Stagnation Pt.	No	100	3/7/18	1144	-22
1527	3/9/18	MSL2	MSL: 16AOA	Stagnation Pt.	Yes	100	3/7/18	1144	-22
1528	3/12/18	MSL4	MSL: 16AOA	Stagnation Pt.	Yes	100	3/7/18	1144	-22
1531	3/23/18	MSL1	MSL: 16AOA	Lee Side	Yes	100	3/21/18	1077	-13
1533	3/27/18	MSL1	MSL:16AOA, 7" back	Lee Side	Yes	100	3/21/18	1077	-13
1534	3/29/18	ST_1.2kPa	MSL: 16AOA	Lee Side	No	100	3/21/18	1077	-13
1535	3/30/18	ST_1.2kPa	MSL: 16AOA	Lee Side	Yes	100	3/21/18	1077	-13
1536	4/4/18	ST_1.2kPa	MSL: 16AOA	Lee Side	Yes	100	3/21/18	1077	-13
1537	4/9/18	ST_1.2kPa	MSL: 16AOA	Lee Side	No LPF	100	3/21/18	1077	-13
1541	4/24/18	ST_1.2kPa	MSL: 16AOA	Stagnation Pt.	Yes	20	4/23/18	1844	8
1542	4/24/18	ST_6kPaAir	MSL: 16AOA	Stagnation Pt.	Yes	20	4/23/18	1844	8
1543	4/26/18	ST_14_5kPa	MSL: 16AOA	Stagnation Pt.	Yes	20	4/26/18	1844	8
1544	4/26/18	ST_0_4kPa	MSL: 16AOA	Stagnation Pt.	Yes	20	4/26/18	1844	8
1546	5/7/18	MSL1	MSL: 16AOA	Stagnation Pt.	Yes	100	5/7/18	1035	0
1599	11/15/18	MSL1:3.7MPa	MSL: 0AOA	0 AOA	Yes	100	11/14/18	269	20
1600	11/16/18	MSL1:2.7μm	MSL: 0AOA	0 AOA	No	100	11/14/18	NA	NA
1601	11/16/18	MSL1:3.7MPa	Staggered Pitot Probe	Freestream Probe	Yes	100	11/16/18	981	17
1720	10/3/19	MSL1	Double FLDI	Freestream Probe	No	100	10/2/19	1058	12
1721	10/3/19	MSL1	Double FLDI	Freestream Probe	Yes	100	10/2/19	1058	12
1722	10/5/19	MSL1	Double FLDI	Freestream Probe	Yes	100	10/3/19	1025	12
1723	10/5/19	MSL2	Double FLDI	Freestream Probe	Yes	100	10/5/19	1011	12
1724	10/8/19	MSL1	Long Pitot Probe	Freestream Probe	Yes	100	10/8/19	988	12
1725	10/9/19	MSL2	Long Pitot Probe	Freestream Probe	Yes	100	10/8/19	988	12
1786	11/21/19	MSL1	MSL: 0 AOA	0 AOA	Yes	100	11/21/19	1128	25
1787	11/21/19	MSL2	MSL: 0 AOA	0 AOA	Yes	100	11/21/19	1128	25
1788	11/22/19	MSL2	MSL: 0AOA	0 AOA	Yes	100	11/21/19	1128	25

Appendix B

T5 SHOT CONDITIONS

Table B.1: T5 900:1 Conical Nozzle Shots

Shot Number	2888	2889	2891	2892	2893	2895	2896
Experiment	1" Sphere	1" Sphere	7" 0 AOA	7" 0 AOA	Pitot	7" 0 AOA	7" 0 AOA
Schlieren Data	High Speed	High Speed	High Res.	High Res.	Na	High Res.	High Res.
Radiation Data	Heat flux	Heat flux	Stag. Pt	Stag. Pt	NA	Wake	Wake
Burst P (MPa)	39.8	39.7	44.6	46.5	40.2	49.0	44.2
Shock Speed (m/s)	2397	2444	2500	2534	2449	2534	2550
Fill P (kPa)	50	50	50	50	50	50	50
Reservoir P (MPa)	32.9	30.8	32.1	33.3	31.7	33.3	32.14
Reservoir ρ (kg/m^3)	45.1	41.6	42.0	42.7	42.0	42.0	41.1
Reservoir T (K)	3475	3503	3575	3623	3512	3575	3628
Y_{CO_2}	0.788	0.774	0.751	0.736	0.772	0.751	0.732
Y_{CO}	0.135	0.144	0.158	0.168	0.145	0.158	0.171
Y_{O_2}	0.074	0.079	0.086	0.091	0.079	0.086	0.092
Y_O	0.003	0.004	0.004	0.005	0.004	0.004	0.005
h_0 (MJ/kg)	5.50	5.63	5.86	6.03	5.63	5.86	6.06
u (m/s)	2819	2840	2892	2926	2847	2892	2929.
ρ (kg/m^3)	0.011	0.010	0.010	0.010	0.010	0.010	0.010
p (Pa)	1841	1717	1800	1874	1744	1800	1802
T (K)	830.8	837.0	866.2	885.8	841.4	866.2	884.7
T_V (K)	861.0	868.8	896.4	914.6	872.9	896.4	914.6
Y_{CO_2}	0.855	0.845	0.835	0.828	0.845	0.835	0.824
Y_{CO}	0.092	0.098	0.105	0.110	0.099	0.105	0.112
Y_{O_2}	0.053	0.056	0.060	0.062	0.056	0.060	0.064
Y_C	0.000	0.000	0.000	0.000	0.000	0.000	0.000
Y_O	0.002	0.000	0.000	0.000	0.000	0.000	0.000
Ma	5.81	5.81	5.80	5.80	5.81	5.80	5.80
$\rho_\infty D$ (g/m^2)	0.3	0.3	1.8	1.8	1.8	1.8	1.8

Table B.2: T5 100:1 Conical Nozzle Shots

Shot Number	2886	2887	2894	2897	2898	2899	2900	2901
Experiment	1" Sphere	1" Sphere	Pitot	7" 16 AOA	7" 16 AOA	7" 16 AOA	7" 16 AOA	7" 0 AOA
Schlieren Data	High Speed	High Speed	NA	High Res.	High Res.	High Res.	High Res.	High Res.
Radiation Data	Heat flux	Heat flux	NA	Lee Wake	Wind Wake	NA	16° Stag.	Stag. Pt.
Burst P (MPa)	41.4	42.2	41.2	47.9	48.9	46	47.3	47.9
Shock Speed (m/s)	2451	2385	2847	2884	2905	2891	2880	2915
Fill P (kPa)	50	50	39	39	39	39	39	39
Reservoir P (MPa)	33.9	33.1	27.5	29.1	28.8	28.5	28.6	28.3
Reservoir ρ (kg/m^3)	45.0	45.6	31.7	31.4	30.8	30.7	31.0	30.2
Reservoir T (K)	3541	3465	3835	3983	4001	3982	3973	4005
$Y_{\mathrm{CO_2}}$	0.767	0.781	0.636	0.580	0.571	0.578	0.582	0.568
Y_{CO}	0.148	0.139	0.232	0.267	0.273	0.269	0.266	0.275
$Y_{\mathrm{O_2}}$	0.081	0.076	0.122	0.138	0.140	0.138	0.137	0.141
Y_{O}	0.004	0.003	0.011	0.015	0.016	0.015	0.015	0.016
h_0 (MJ/kg)	5.73	5.46	7.01	7.62	7.71	7.63	7.59	7.74
u (m/s)	2675.9	2627.1	2884.1	2980.8	2993.2	2981.3	2975.0	2996.9
ρ (kg/m^3)	0.097	0.098	0.063	0.063	0.062	0.061	0.062	0.060
P (Pa)	27540	26818	20615	21927	21703	21434	21532	21310
T (K)	1416.7	1367.3	1552.4	1641.8	1650.5	1639.1	1634.6	1651.0
T_V (K)	1418.3	1369.0	1554.6	1643.9	1652.6	1641.2	1636.7	1653.1
$Y_{\mathrm{CO_2}}$	0.869	0.881	0.785	0.754	0.748	0.752	0.754	0.745
Y_{CO}	0.083	0.076	0.137	0.157	0.160	0.158	0.156	0.162
$Y_{\mathrm{O_2}}$	0.048	0.043	0.077	0.088	0.090	0.089	0.088	0.091
Y_{C}	0.000	0.000	0.000	0.000	0.000	0.000	0.000	0.000
Y_{O}	0.000	0.000	0.001	0.001	0.002	0.002	0.001	0.002
Ma	4.23	4.24	4.27	4.26	4.26	4.27	4.27	4.27
$\rho_\infty D$ (g/m^2)	2.5	2.5	11.3	11.2	11.0	10.9	11.0	10.8

Table B.3: T5 Contour Nozzle Shots

Shot Number	2866	2902
Experiment	2" 0 AOA	7" 0 AOA
Radiation Data	NA	Stag. Pt.
Schlieren Data	High Speed	High Res.
Burst P (MPa)	NA	91.0
Shock Speed (m/s)	3029.0	3063.8
Fill P (kPa)	60	60
Reservoir P (MPa)	47.1	50.6
Reservoir ρ (kg/m^3)	46.7	48.8
Reservoir T (K)	4235.9	4304.3
$Y_{\mathrm{CO_2}}$	0.529	0.510
Y_{CO}	0.300	0.312
$Y_{\mathrm{O_2}}$	0.152	0.156
Y_{O}	0.020	0.022
h_0 (MJ/kg)	8.41	8.61
u (m/s)	3122.6	3160.5
ρ (kg/m^3)	0.088	0.093
P (Pa)	33277	35915
T (K)	1751.4	1793.1
T_v (K)	1751.6	1793.4
$Y_{\mathrm{CO_2}}$	0.728	0.719
Y_{CO}	0.173	0.179
$Y_{\mathrm{O_2}}$	0.097	0.100
Y_{C}	0.000	0.000
Y_{O}	0.002	0.002
Ma	4.30	4.29
$\rho_\infty D$ (g/m^2)	4.5	16.5

Appendix C

MACHINE DRAWINGS

1. 7" diameter MSL model forebody machine drawing with fiber port locations.
2. 7" diameter MSL model assembly drawing.
3. Freestream probe adapter machine drawing modifying an NPT plug.
4. 2" diameter MSL model machine drawing with fiber port locations.
5. 2" diameter MSL sting machine drawing.

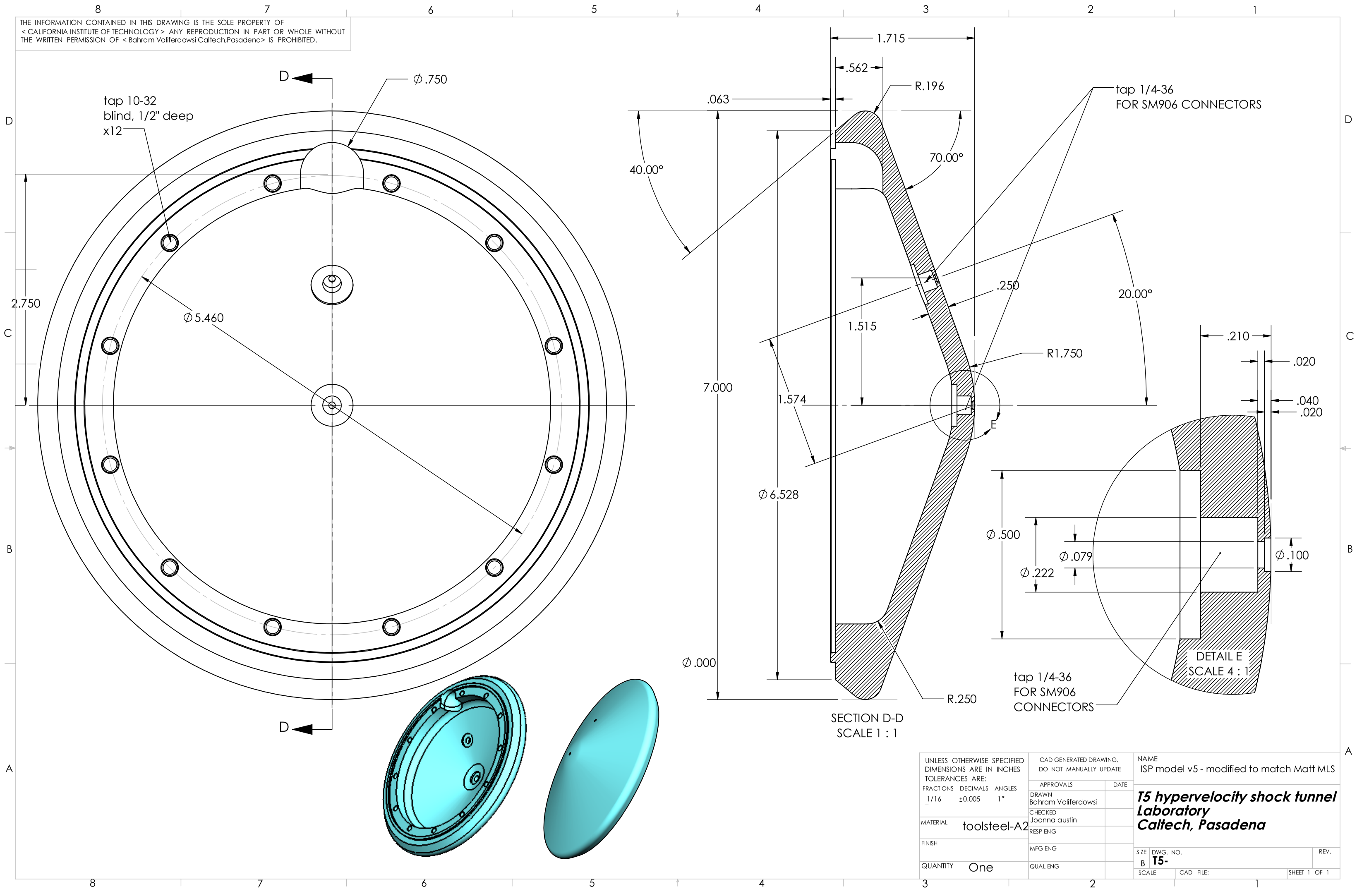

Figure C.1: 7" diameter MSL model forebody machine drawing with fiber port locations.

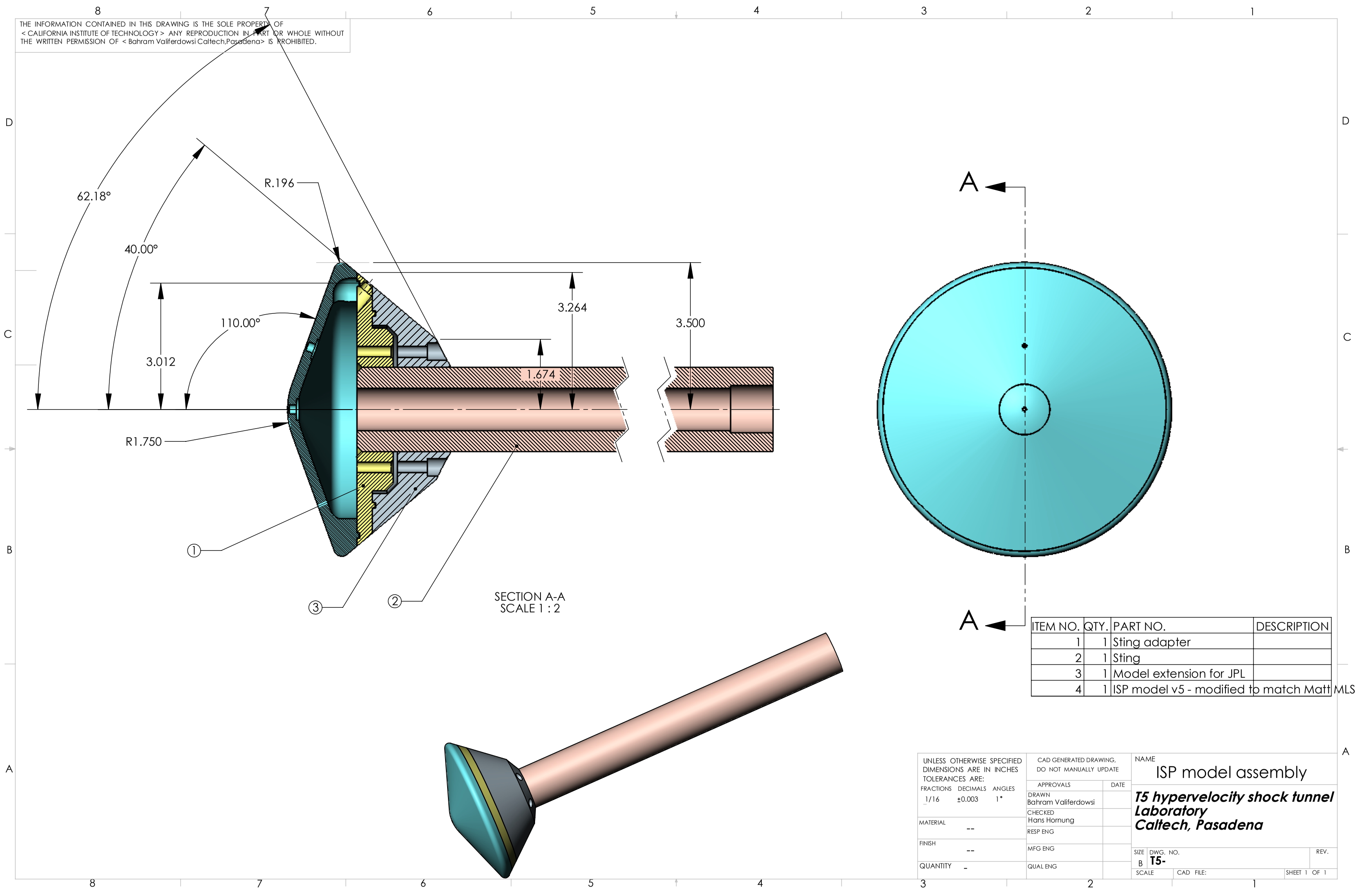

ITEM NO.	QTY.	PART NO.	DESCRIPTION
1	1	Sting adapter	
2	1	Sting	
3	1	Model extension for JPL	
4	1	ISP model v5 - modified to match Matt MLS	

Figure C.2: 7" diameter MSL model assembly drawing.

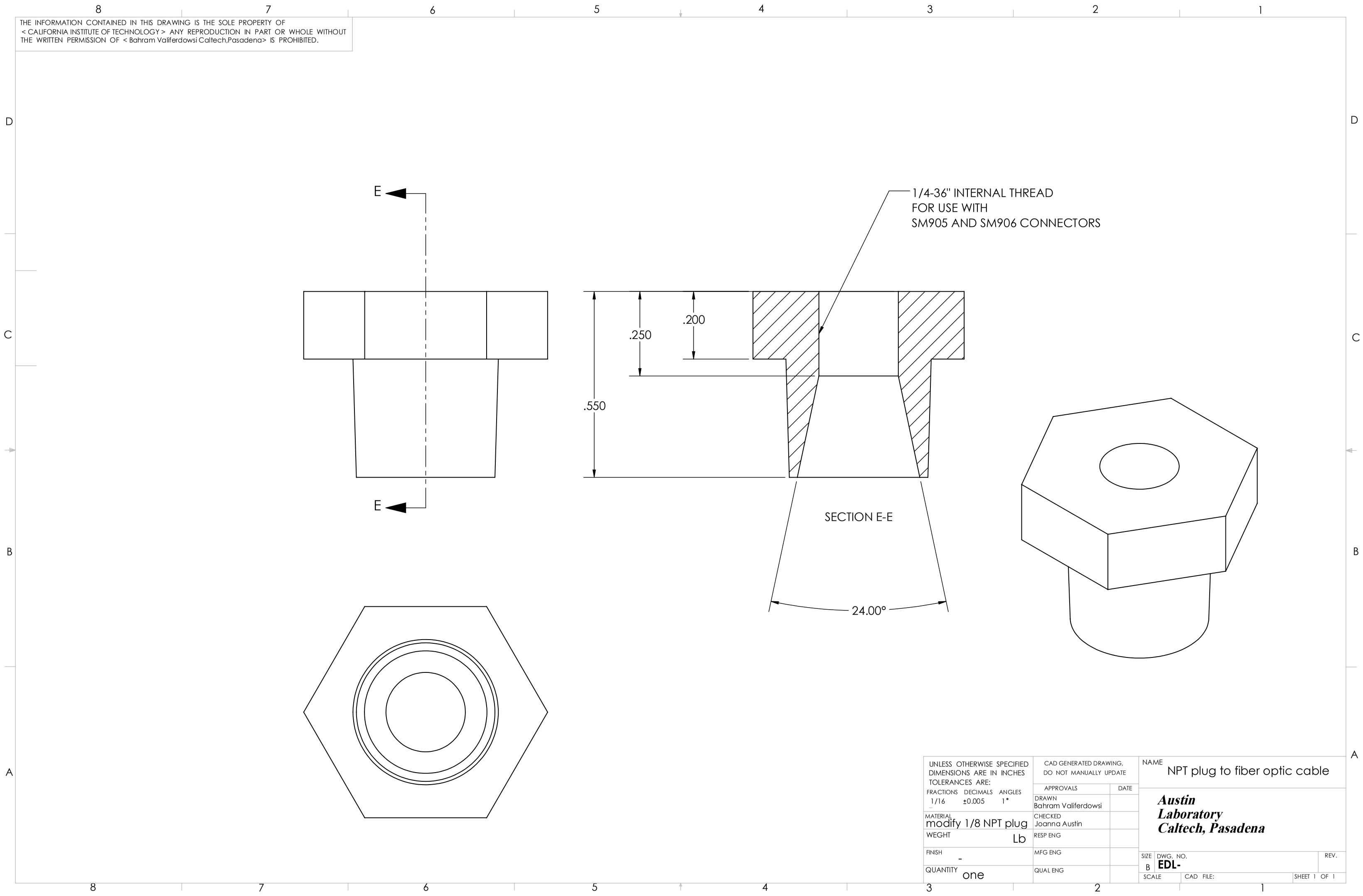

THE INFORMATION CONTAINED IN THIS DRAWING IS THE SOLE PROPERTY OF < CALIFORNIA INSTITUTE OF TECHNOLOGY > ANY REPRODUCTION IN PART OR WHOLE WITHOUT THE WRITTEN PERMISSION OF < Bahram Valiferdowsi Caltech,Pasadena> IS PROHIBITED.

UNLESS OTHERWISE SPECIFIED DIMENSIONS ARE IN INCHES TOLERANCES ARE:

FRACTIONS	DECIMALS	ANGLES
1/16	±0.005	1°

CAD GENERATED DRAWING, DO NOT MANUALLY UPDATE

APPROVALS	DATE
DRAWN Bahram Valiferdowsi	
CHECKED Joanna Austin	
RESP ENG	
MFG ENG	
QUAL ENG	

MATERIAL modify 1/8 NPT plug
WEGHT Lb
FINISH -
QUANTITY one

NAME NPT plug to fiber optic cable

Austin
Laboratory
Caltech, Pasadena

SIZE B
DWG. NO. **EDL-**
REV.
SCALE
CAD FILE:
SHEET 1 OF 1

Figure C.3: Freestream probe adaptor machine drawing modifying an NPT plug.

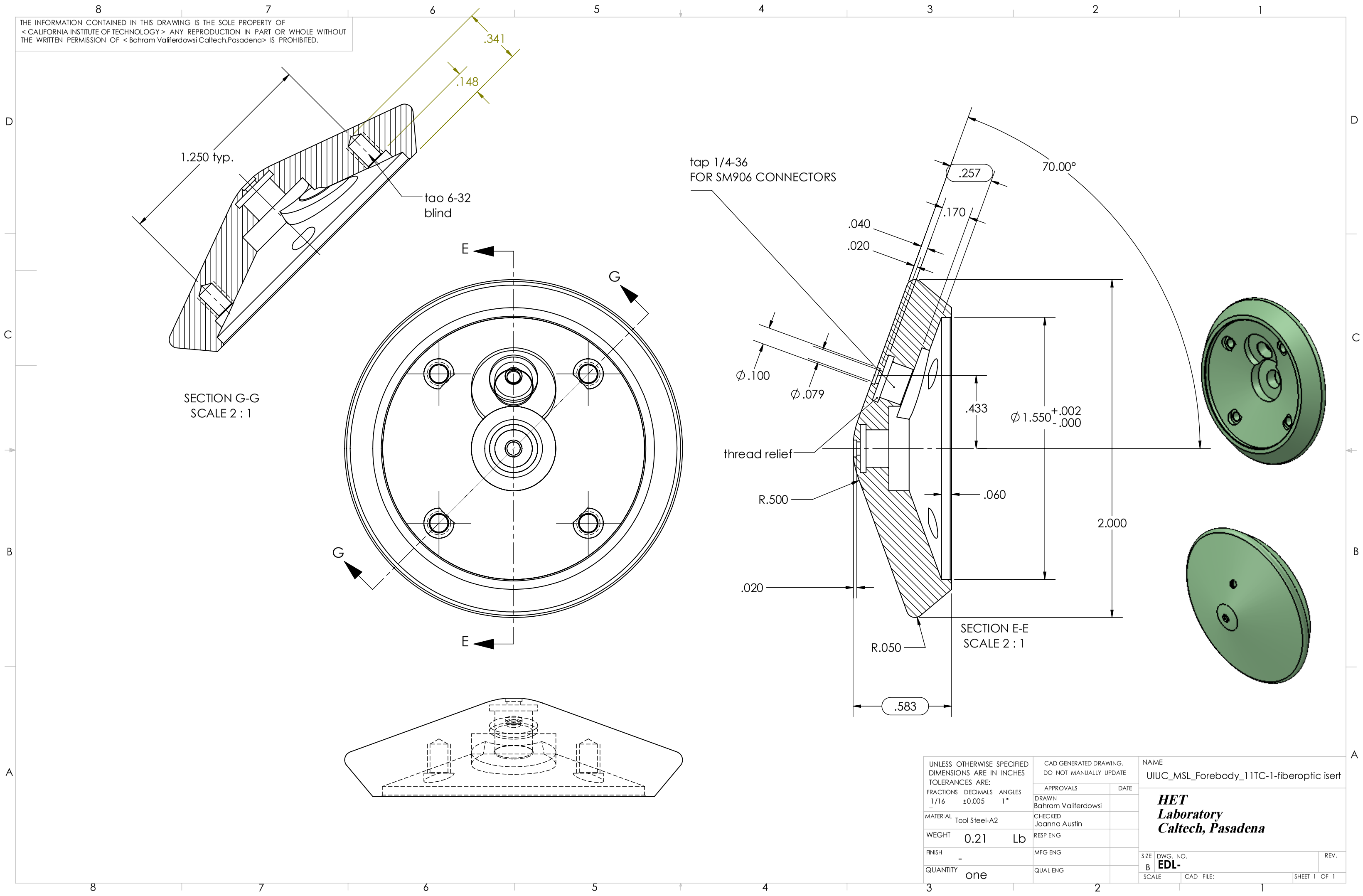

Figure C.4: 2" diameter MSL model machine drawing with fiber port locations.

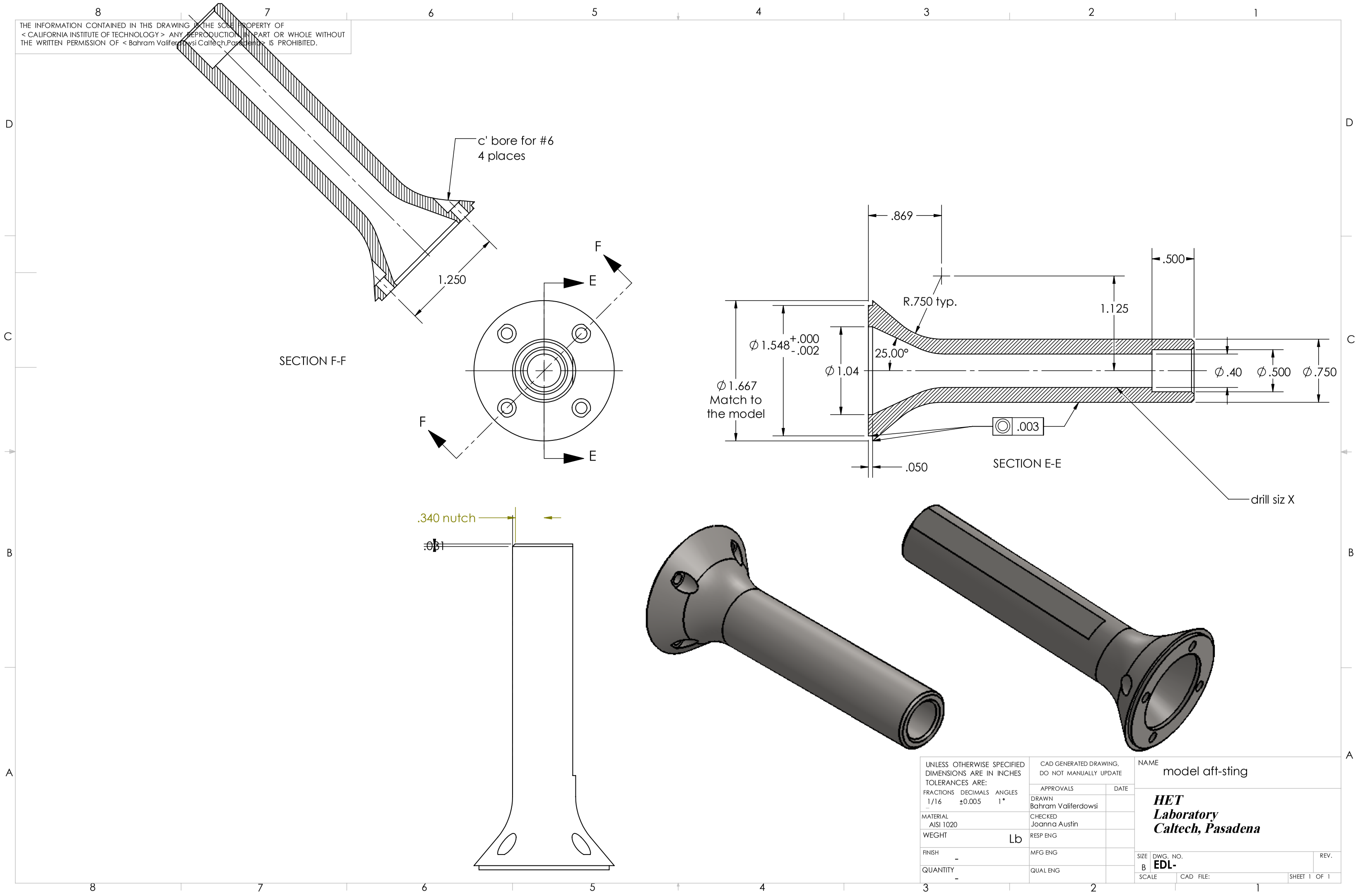

Figure C.5: 2" diameter MSL sting machine drawing.